DESIGN CALCULATIONS ON PROVEN TRAINER AND FIGHTER AIRCRAFT FOR THE VERIFICATION OF A GUST DESIGN PROCEDURE

CHINTSUN HWANG, B. D. KAMBERG,
W. S. PI, A. K. CROSS

NORTHROP CORPORATION

FOREWORD

This report was prepared by Dr. Chintsun Hwang, B. D. Kamberg, Dr. W. S. Pi, and A. K. Cross of the Norair Division, Northrop Corporation. Mr. F. D. Jacobs of the Norair Division also contributed to the portion on real time gust data processing. Mrs. F. H. Perkinson carried out the computer programming work. The work was performed under USAF contract AF33(615)-2625, initiated and administered by the Air Force Flight Dynamics Laboratory, Research and Technology Division, Wright-Patterson Air Force Base, Ohio. The contract was initiated under Project Number 1367, "Structural Design Criteria," Task Number 136702, "Aerospace Vehicle Structural Loads Criteria." The contract was monitored by Mr. P. L. Hasty. Dr. J. C. Houbolt, of Princeton Aeronautical Research Associates, served as technical consultant to the project.

The manuscript was released by the authors May 1966 for publication as an RTD Technical Report.

This report has been assigned Report Number NOR 66-149 for Internal Control.

This report has been reviewed and is approved.

FRANCIS J. JANIK, JR.
Chief, Theoretical Mechanics Branch
Structures Division

ABSTRACT

Design calculations are performed on proven trainer and fighter aircraft for the purpose of verifying a new gust design procedure based on power spectral techniques. The aircraft used in the computation are Northrop Norair T-38 trainer and F-5A fighter. The new gust design procedure uses a gust power spectrum as the input in aircraft response calculation, as against the present discrete gust approach, where the input is a gust velocity profile with a single frequency determined by the aircraft speed and the gust gradient distance. The report describes the specific aircraft weight and flight configurations used in the computation. The choice of stress sensitive locations is explained and illustrated. Also presented is the computation procedure for obtaining the aircraft transfer functions to be used in both the discrete gust and power spectral approaches. Based on the gust input spectrum and the aircraft transfer functions, a number of aircraft gust response power spectra are generated. These latter spectral data are integrated along the frequency band to obtain the mean aircraft response levels and the average zero crossing counts which are the final results of the computation. Through the computation, various scales of turbulence and cut-off frequencies are used to study their effects on the end results of the new gust design procedure. Also presented in the report is a supplementary study on the digital processing of the real time gust data and their conversion into the power spectral data.

CONTENTS

SECTION		PAGE
I	Introduction	1
II	Technical Discussion	2
	1. Weight Configurations and Flight Conditions of the Trainer and Fighter Aircraft Used in the Computation	2
	2. Stress Sensitive Locations and the Stress Influence Coefficients	19
	3. Transfer Function Computation	34
	4. Gust Design Computations Using the Power Spectral Approach	47
III	Conclusions and Recommendations	99
	1. General Discussion	99
	2. Discussion of T-38 Trainer Gust Data	103
	3. Discussion of F-5A Fighter Gust Data	105
	4. Concluding Remarks	107
Appendix I	Method of Frequency Response Calculation	109
Appendix II	Real-Time Gust Data Processing	123
References		157

ILLUSTRATIONS

FIGURE		PAGE
1	Plan and Side View of T-38 Trainer	3
2	Wing, Fuselage and Horizontal Tail Control Point Geometry (T-38)	5
3	T-38 Trainer Wing Outer Panel and Contents (Including Flap and Aileron) Weight Distribution Normal to and Along 35% Wing Chord	6
4	T-38 Wing Outer Panel and Contents (Including Flap and Aileron) C.G. Normal to Elastic Axis	7
5	T-38 Trainer Wing Outer Panel and Contents (Including Flap and Aileron Pitching Moment of Inertia	8
6	T-38 Trainer Wing Flexural and Torsional Stiffness Data	9
7	T-38 Trainer Fuselage and Contents - Weight and Roll Inertia Distribution	10
8	T-38 Trainer Fuel Distribution	11
9	Three View Drawing of F-5A Fighter	13
10	Wing Fuselage and Horizontal Tail Control Point Geometry (F-5)	14
11	F-5A Wing Bending and Torsion Stiffness	17
12	Fuselage Vertical Bending Stiffness About W.L. 92.5	18
13	F-5A Ultimate Wing Load Envelope Wing Station 114.5 Inboard Swept Loads, Shear, V_Z Versus Torsion M_y	20
14	F-5A Ultimate Wing Load Envelope Wing Station 114.5 Inboard Swept Loads, Bending, M_x Versus Torsion M_y	20
15	T-38 Wing Structure Critical Element Coding	22
16	F-5A Wing Structure Critical Element Coding	28
17	F-5A Fighter Wing Stress Sensitive Locations	29
18	Typical F-5A Wing Strength Envelope Plot	32
19	Flexible Modes for the T-38 Trainer Configurations (1), (2)	39

ILLUSTRATIONS (Continued)

FIGURE		PAGE
20	Flexible Modes for the F-5A Fighter Configurations (1), (2),	43
21	Flexible Modes for the F-5A Fighter Configuration (3)	45
22	T-38 Trainer Response Data, Configuration (1)	54
23	Transfer Function H(f), $\bar{A}$ and N_o Data for S-1, T-38 Trainer Configuration (1)	55
24	Transfer Function H(f), $\bar{A}$ and N_o Data for S-2, T-38 Trainer Configuration (1)	56
25	Transfer Function H(f), $\bar{A}$ and N_o Data for S-5, T-38 Trainer Configuration (1)	57
26	Transfer Function H(f), $\bar{A}$ and N_o Data for S-13, T-38 Trainer Configuration (1)	58
27	T-38 Trainer Response Data, Configuration (2)	60
28	Transfer Function H(f), $\bar{A}$ and N_o Data for S-1, T-38 Trainer Configuration (2)	62
29	Transfer Function H(f), $\bar{A}$ and N_o Data for S-5, T-38 Trainer Configuration (2)	63
30	Transfer Function H(f), $\bar{A}$ and N_o Data for S-8, T-38 Trainer Configuration (2)	64
31	Transfer Function H(f), $\bar{A}$ and N_o Data for S-9, T-38 Trainer Configuration (2)	65
32	Transfer Function H(f), $\bar{A}$ and N_o Data for S-12, T-38 Trainer Configuration (2)	66
33	Transfer Function H(f), $\bar{A}$ and N_o Data for S-14, T-38 Trainer Configuration (2)	67
34	T-38 Trainer Response Data, Configuration (3)	68
35	Transfer Function H(f), $\bar{A}$ and N_o Data for S-1, T-38 Trainer Configuration (3)	70
36	Transfer Function H(f), $\bar{A}$ and N_o Data for S-2, T-38 Trainer Configuration (3)	71
37	Transfer Function H(f), $\bar{A}$ and N_o Data for S-5, T-38 Trainer Configuration (3)	72

ILLUSTRATIONS (Continued)

FIGURE		PAGE
38	Transfer Function H(f), $\bar{A}$ and N_o Data for S-13, T-38 Trainer Configuration (3)	73
39	Transfer Function H(f), $\bar{A}$ and N_o Data for S-15, T-38 Trainer Configuration (3)	74
40	F-5A Fighter Response Data, Configuration (1)	76
41	Transfer Function H(f), $\bar{A}$ and N_o Data for S-4, F-5A Fighter Configuration (1)	77
42	Transfer Function H(f), $\bar{A}$ and N_o Data for S-5, F-5A Fighter Configuration (1)	78
43	Transfer Function H(f), $\bar{A}$ and N_o Data for S-7, F-5A Fighter Configuration (1)	79
44	Transfer Function H(f), $\bar{A}$ and N_o Data for S-10, F-5A Fighter Configuration (1)	80
45	Transfer Function H(f), $\bar{A}$ and N_o Data for S-12, F-5A Fighter Configuration (1)	81
46	Transfer Function H(f), $\bar{A}$ and N_o Data for S-23, F-5A Fighter Configuration (1)	82
47	Transfer Function H(f), $\bar{A}$ and N_o Data for S-24, F-5A Fighter Configuration (1)	83
48	Transfer Function H(f), $\bar{A}$ and N_o Data for S-25, F-5A Fighter Configuration (1)	84
49	F-5A Fighter Response Data, Configuration (2)	86
50	Transfer Function H(f), $\bar{A}$ and N_o Data for S-4, F-5A Fighter Configuration (2)	87
51	Transfer Function H(f), $\bar{A}$ and N_o Data for S-7, F-5A Fighter Configuration (2)	88
52	Transfer Function H(f), $\bar{A}$ and N_o Data for S-12, F-5A Fighter Configuration (2)	89
53	F-5A Fighter Response Data, Configuration (3)	91
54	Transfer Function H(f), $\bar{A}$ and N_o Data for S-7, F-5A Fighter Configuration (3)	92
55	Transfer Function H(f), $\bar{A}$ and N_o Data for S-10, F-5A Fighter Configuration (3)	93

ILLUSTRATIONS (Continued)

FIGURE		PAGE
56	Transfer Function H(f), $\bar{A}$ and N_o Data for S-15, F-5A Fighter Configuration (3)	94
57	Transfer Function H(f), $\bar{A}$ and N_o Data for S-23, F-5A Fighter Configuration (3)	95
58	F-5A Transfer Function for C.G. Acceleration	97
59	F-5A Transfer Function for Rigid Pitch Model	98
60	Computer Flow for Processing Gust Flight Data	125
61	Typical Real Time Gust Data, Flight 275	129
62	Comparison of Auto-Correlation Functions Flight 275	130
63	Comparison of Auto-Correlation Functions, Flight 276	131
64	Comparison of Auto-Correlation Functions, Flight 277	132
65	Point Distribution of Vertical Gust Velocity, Flight 275	134
66	Point Distribution of Vertical Gust Velocity, Flight 276	135
67	Point Distribution of Vertical Gust Velocity, Flight 277	136
68	Gamma Filter Transfer Function	137
69	Probability Graph, Flight 275	138
70	Probability Graph, Flight 276	139
71	Probability Graph, Flight 277	140
72	Power Spectral Density of Vertical Gust Velocity, Flight 275	141
73	Power Spectral Density of Vertical Gust Velocity, Flight 276	142
74	Power Spectral Density of Vertical Gust Velocity, Flight 277	143
75	A Seismic System	144
76	Seismic Filter Response Data	147
77	Seismic Filter Response Data	148
78	Seismic Filter Response Data	149

ILLUSTRATIONS (Continued)

FIGURE		PAGE
79	Comparison of the von Kármán Auto Correlation Functions with Experimental Normalized Auto-Correlation Functions	150
80	Comparison of Vertical Gust Velocity Power Spectra for Data Processed Through High Pass Seismic and Gamma Filters	151
81	Comparison of Numerical Filter Characteristics	152
82	Percent Error Versus the Coherence Function $\gamma^2(f)$ for Several Confidence Levels	155
83	Comparison of $H_c(f)$ and $H_s(f)$ for F-5A Normal Acceleration at Fuselage Station 92	156
84	Coherence Function Versus Frequency for F-5A Normal Acceleration at Fuselage Station 92	156

TABLES

TABLE		PAGE
I	T-38 Aircraft Engineering Data	4
II	F-5A Weight and Inertia Data, Overall and Attached Stores	15
III	F-5A Weight and Inertia Data, Wings, Pylons, and Stores; Fuselage and Horizontal Tail	16
IV	T-38 Stress Sensitive Location Identification	21
V	T-38 Wing Stress Influence Coefficients	23
VI	T-38 Fuselage Stress Data	24
VII	T-38 Horizontal Stabilizer Stress Data	25
VIII	F-5A Stress Sensitive Location Identification	26
IX	Stress Influence Coefficients of F-5A Fighter Wing Structure	30
X	Stress Influence Coefficients of F-5A Fighter Horizontal Tail	33
XI	F-5A Fighter Fuselage Stress Influence Coefficients for Location S-23	33
XII	The T-38 Trainer Natural Frequency Mode Data	38
XIII	The F-5A Fighter Natural Frequency Mode Data	41
XIV	Critical Stress Elements of T-38 Trainer	51
XV	Mean Amplitude and Frequency Data, T-38 Trainer, Configuration (1)	52
XVI	Mean Amplitude and Frequency Data, T-38 Trainer, Configuration (2)	61
XVII	Mean Amplitude and Frequency Data, T-38 Trainer, Configuration (3)	69
XVIII	Critical Stress Elements of F-5A Fighter	75
XIX	Mean Amplitude and Frequency Data, F-5A Fighter, Configuration (1)	85
XX	Mean Amplitude and Frequency Data, F-5A Fighter, Configuration (2)	90

TABLES (CONTINUED)

TABLE		PAGE
XXI	Mean Amplitude and Frequency Data, F-5A Fighter, Configuration (3)	96
XXII	Amplitude Ratios as Functions of the Scales of Turbulence, T-38 Trainer	102
XXIII	Amplitude Ratios as Functions of the Scales of Turbulence, F-5A Fighter	102
XXIV	Summary of Flight Gust Data	128

SECTION I

INTRODUCTION

In aircraft gust design, the present day approach is based on a discrete gust input with a fixed gust length. In reality, the air turbulence encountered by the aircraft is a random phenomenon subject to statistical analysis. The aircraft responds to the gust according to its individual dynamic and aerodynamic characteristics. Because of the interaction of the highly complicated factors involving the air turbulence and aircraft response, it is apparent that limitations are involved in using the discrete gust design approach as a universal standard. This need, coupled with the vast knowledge gained in the past on processing random phenomena using spectral and statistical techniques, leads to a search for a more realistic approach in gust design.

The spectral approach is used in the report in the gust computation on two proven aircraft; namely, the Northrop Norair T-38 trainer, and F-5A fighter. The computation is essentially exploratory in nature. The idea behind the spectral approach is to recognize the random gust phenomenon and the individual aircraft response at various frequencies. Through integration along the frequency band of the aircraft response power spectrum, certain mean values are reached which represent the expected response amplitudes as well as the expected rates of exceeding certain stress levels. Due to the scope of the problem, many simplifications and arbitrary conditions are imposed during the computation. The specific conditions, which are not expected to affect the final results in a biased manner, are explained in the report. The data thus obtained for the two aircraft are presented. Hopefully, the approach may eventually lead to a design method which is spectral and statistical in nature, while taking into consideration a substantial number of factors which are either random or individualistic due to the variations in aircraft design, mission, etc.

SECTION II

TECHNICAL DISCUSSION

1. Weight Configurations and Flight Conditions of the Trainer and Fighter Aircraft Used in the Computation

The gust computation is performed for Northrop Norair T-38 trainer and F-5A fighter. Two weight configurations are chosen for each aircraft operating at specific Mach numbers and altitudes. The choice of the configurations which are gust sensitive is based on past experiences in flight tests as well as the design computations using the discrete gust approach.

1.1 T-38 Trainer Configurations

The general arrangement of Northrop Norair T-38, a two seat trainer, is shown in Figure 1. The aircraft geometry and engineering data are given in Table I. The control point geometry and identification are illustrated in Figure 2. The weight distribution, pitching moment of inertia, and stiffness data of the wing structure are given in Figures 3-6. The weight distribution and the rolling moment of inertia distribution for the fuselage are shown in Figure 7. The fuel weight distribution is plotted in Figure 8 corresponding to various stages of fuel consumption.

The T-38 trainer has no wing tank or pylon attached storage. The weight variation is essentially due to the amount of fuel stored in the fuselage cells. For gust computation, the following weight and flight configurations are used:

Configuration	Aircraft Weight (Pounds)	Mach No.	Altitude (Feet)	Remarks
(1)	7,200	.945	Sea Level	Speed brakes closed, zero flap deflection, 5% internal fuel
(2)	7,200	.950	30,000	Weight distribution same as configuration (1)
(3)	10,900	.945	Sea Level	Fuel Tank full

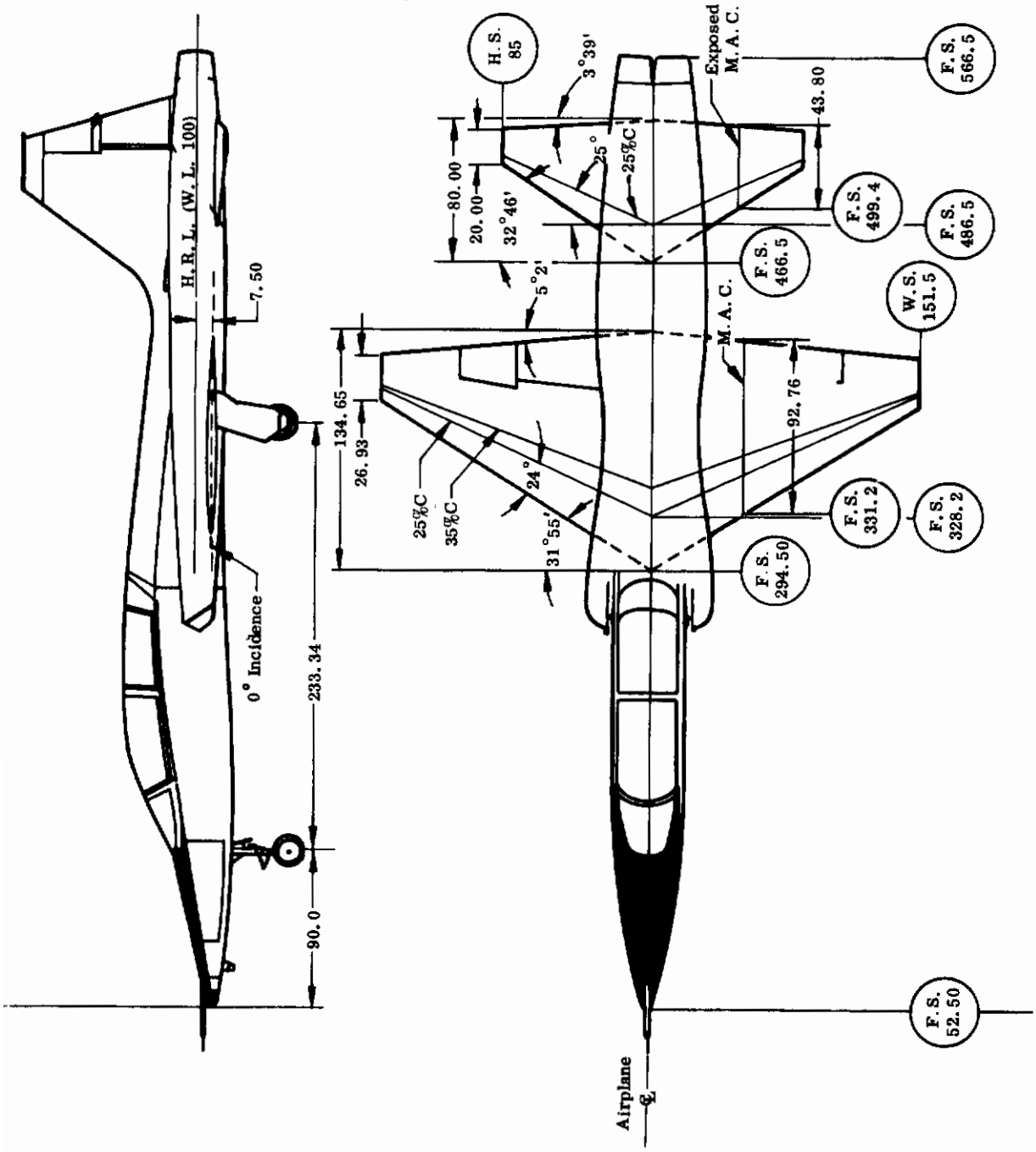

FIGURE 1 PLAN AND SIDE VIEW OF T-38 TRAINER

TABLE I. T-38 AIRCRAFT ENGINEERING DATA

Wing	
Area	170 ft^2
Taper Ratio	0.20
Aspect Ratio	3.75
Sweepback at 25% Chord	24^o
Airfoil Section	NACA 65A-004.8
Horizontal Tail	
Area (Total)	59 ft^2
Area (Exposed)	33.03 ft
Taper Ratio (Exposed)	0.33
Aspect Ratio (Exposed)	2.88
Sweepback at 25% Chord	25^o
Airfoil Section	NACA 65A-004
Vertical Tail	
Area (Exposed)	41.42 ft^2
Taper Ratio (Exposed)	0.25
Aspect Ratio (Exposed)	1.22
Sweepback at 25% Chord	25^o
Airfoil Section	NACA 65A-004
Usable Fuel	
Internal Volume	3790 lbs (583 gal.)
Power Plant	
(2) Turbo jets with afterburners	J85-GE-5

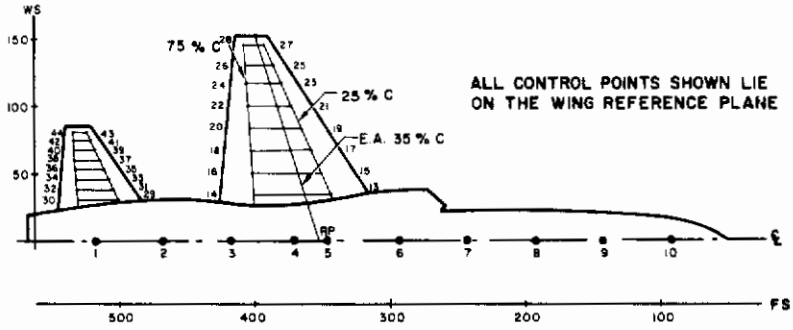

Control Point No. & Direction		Wing Station	Fuselage Station	Elevation	Control Point No. & Direction		Wing Station	Fuselage Station	Elevation
V = Vertical									
Fuselage (Surface 1)					Wing				
1	V	0	517.5	92.5	23	V	116.50	380.01	92.5
2	V	0	467.5	92.5	24	V	116.50	405.91	92.5
3	V	0	417.5	92.5	25	V	131.50	386.68	92.5
4	V	0	371.5	92.5	26	V	131.50	407.26	92.5
5	V	0	345.5	92.5	27	V	144.75	392.58	92.5
6	V	0	292.5	92.5	28	V	144.75	408.45	92.5
7	V	0	242.5	92.5	29	V	31.16	500.98	92.5
8	V	0	192.5	92.5	30	V	31.16	529.98	92.5
9	V	0	142.5	92.5	31	V	38.34	504.38	92.5
10	V	0	92.5	92.5	32	V	38.34	530.88	92.5
11	V	(Dummy)		92.5	Horiz. Tail (Surface 3) 33	V	45.51	507.68	92.5
12	V	(Dummy)		92.5	34	V	45.51	531.68	92.5
Wing (Surface 2) 13	V	34.30	343.41	92.5	35	V	52.69	511.08	92.5
14	V	34.30	398.54	92.5	36	V	52.69	532.48	92.5
15	V	50.50	350.63	92.5	37	V	59.87	514.38	92.5
16	V	50.50	400.00	92.5	38	V	59.87	533.28	92.5
17	V	67.00	357.98	92.5	39	V	67.05	517.78	92.5
18	V	67.00	401.49	92.5	40	V	67.05	534.08	92.5
19	V	83.00	365.09	92.5	41	V	74.23	521.58	92.5
20	V	83.00	402.91	92.5	42	V	74.23	534.88	92.5
21	V	99.50	372.44	92.5	43	V	81.41	524.48	92.5
22	V	99.50	404.39	92.5	44	V	81.41	535.68	92.5

FIGURE 2. WING, FUSELAGE AND HORIZONTAL TAIL CONTROL POINT GEOMETRY (T-38)

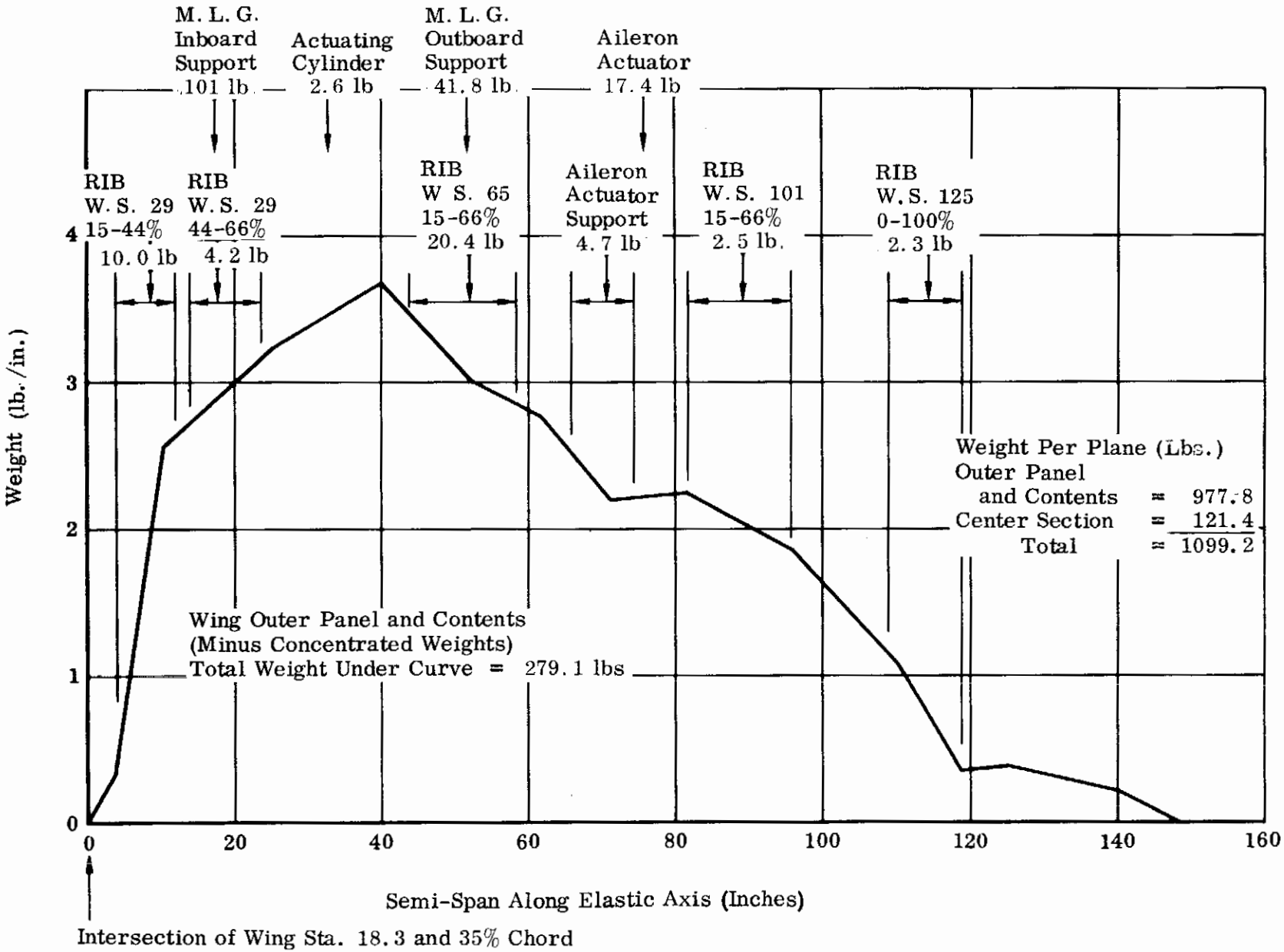

FIGURE 3 T-38 TRAINER WING OUTER PANEL AND CONTENTS (INCLUDING FLAP AND AILERON) WEIGHT DISTRIBUTION NORMAL TO AND ALONG 35% WING CHORD

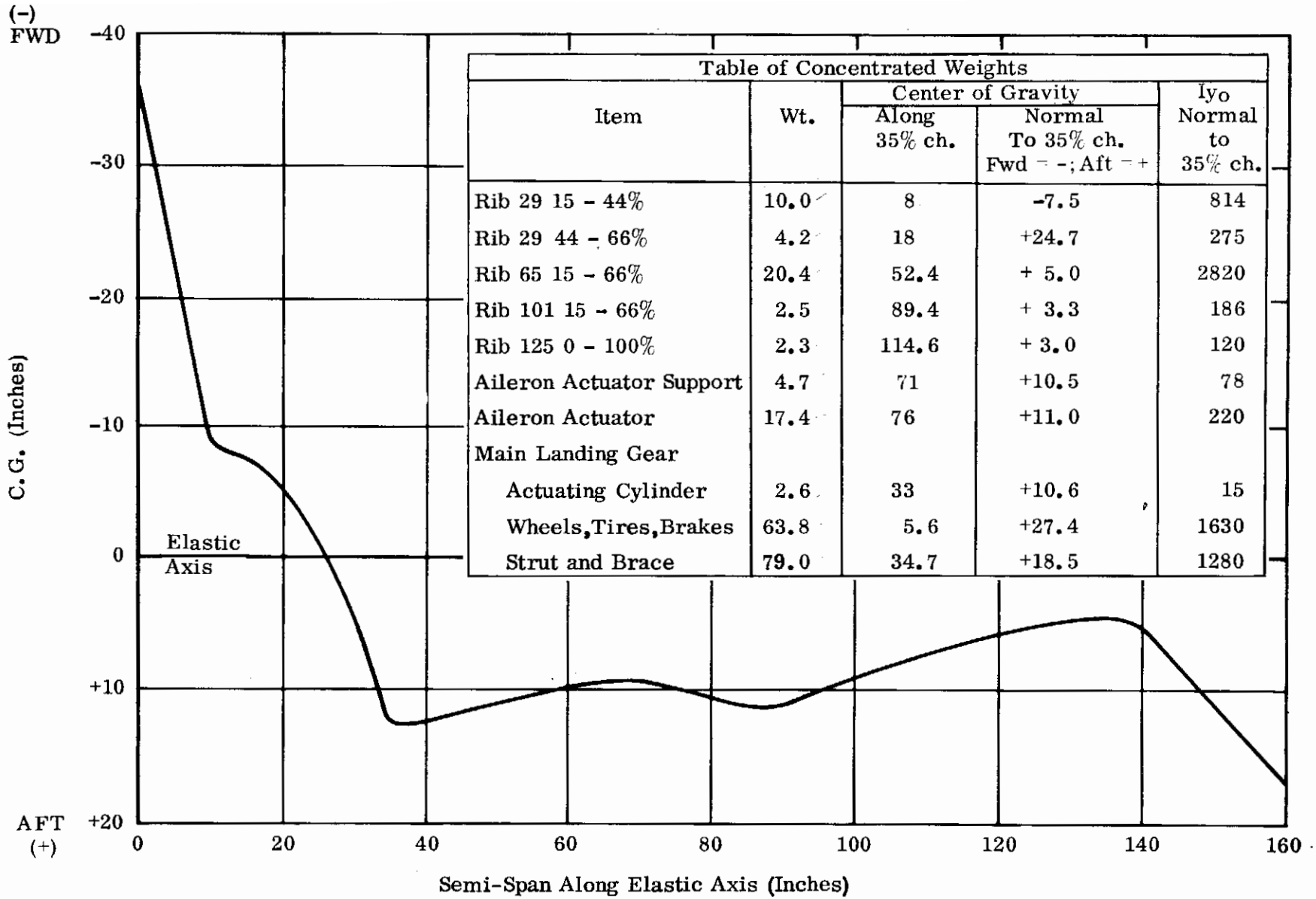

Table of Concentrated Weights

Item	Wt.	Center of Gravity		Iyo Normal to 35% ch.
		Along 35% ch.	Normal To 35% ch. Fwd = -; Aft = +	
Rib 29 15 - 44%	10.0	8	-7.5	814
Rib 29 44 - 66%	4.2	18	+24.7	275
Rib 65 15 - 66%	20.4	52.4	+ 5.0	2820
Rib 101 15 - 66%	2.5	89.4	+ 3.3	186
Rib 125 0 - 100%	2.3	114.6	+ 3.0	120
Aileron Actuator Support	4.7	71	+10.5	78
Aileron Actuator	17.4	76	+11.0	220
Main Landing Gear				
Actuating Cylinder	2.6	33	+10.6	15
Wheels, Tires, Brakes	63.8	5.6	+27.4	1630
Strut and Brace	79.0	34.7	+18.5	1280

FIGURE 4 T-38 TRAINER WING OUTER PANEL AND CONTENTS (INCLUDING FLAP AND AILERON) C.G. NORMAL TO ELASTIC AXIS

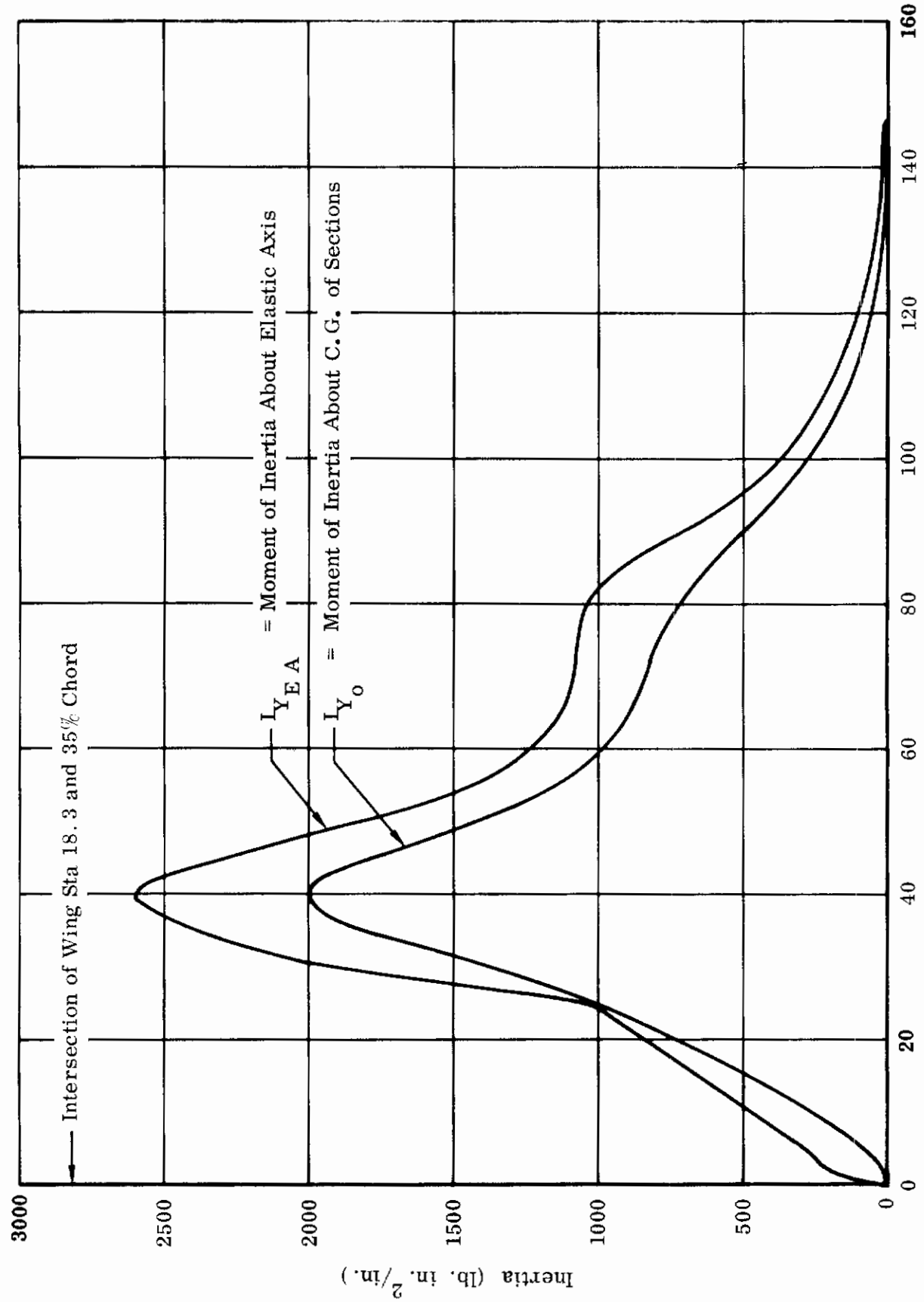

FIGURE 5 T-38 TRAINER WING OUTER PANEL AND CONTENTS (INCLUDING FLAP AND AILERON) PITCHING MOMENT OF INERTIA

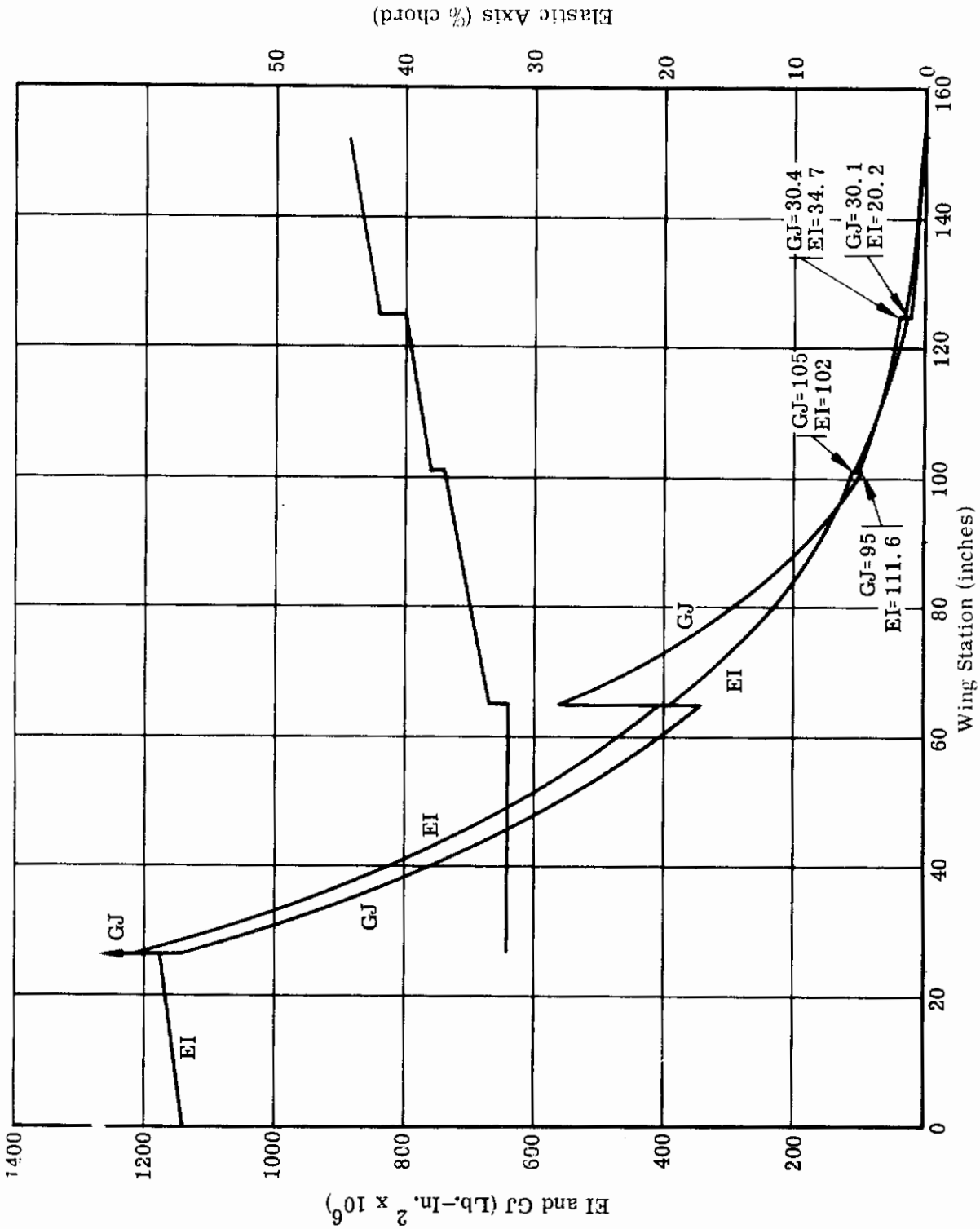

FIGURE 6 T-38 TRAINER WING FLEXURAL AND TORSIONAL STIFFNESS DATA

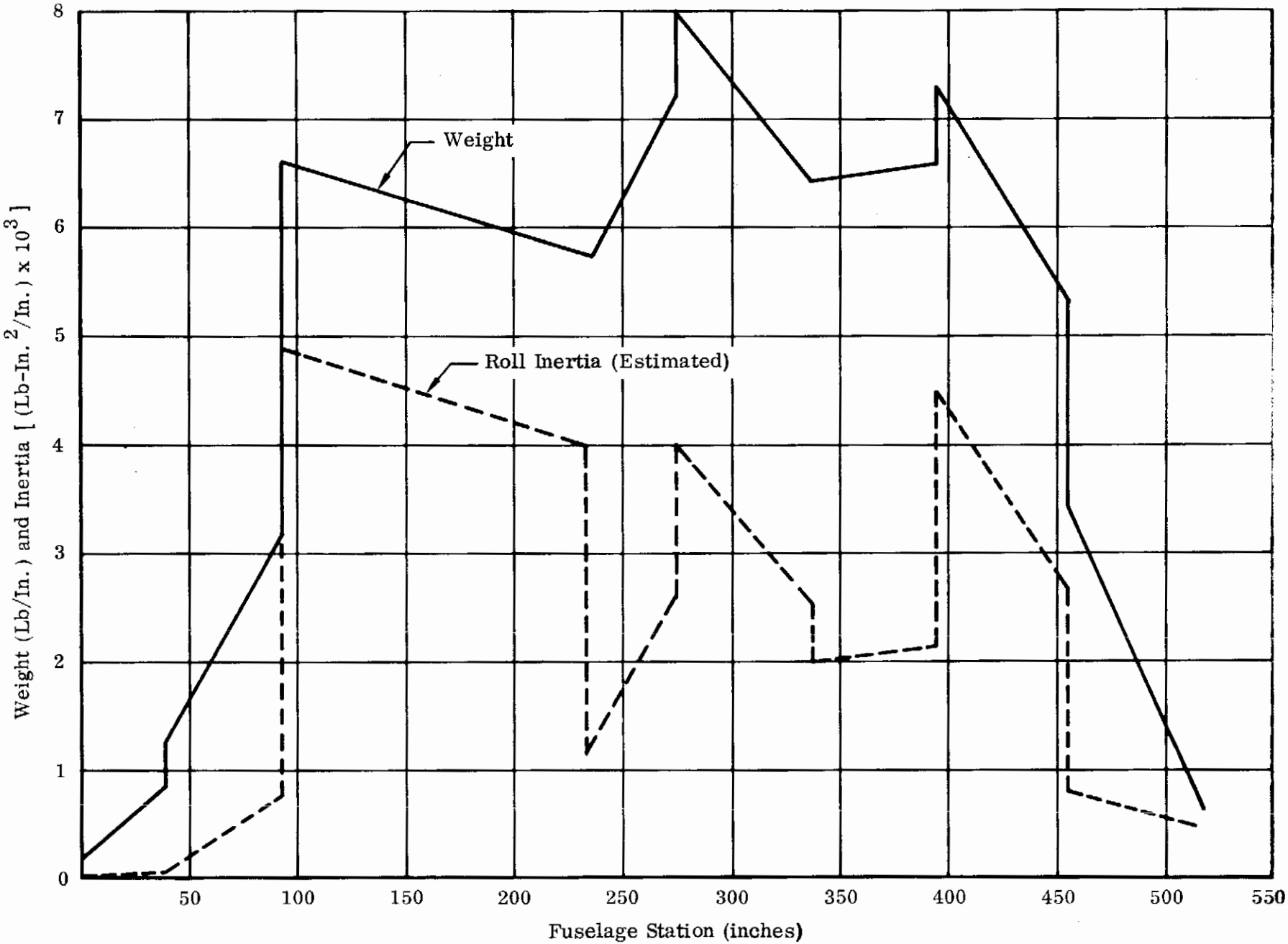

FIGURE 7 T-38 TRAINER FUSELAGE AND CONTENTS-WEIGHT AND ROLL INERTIA DISTRIBUTION

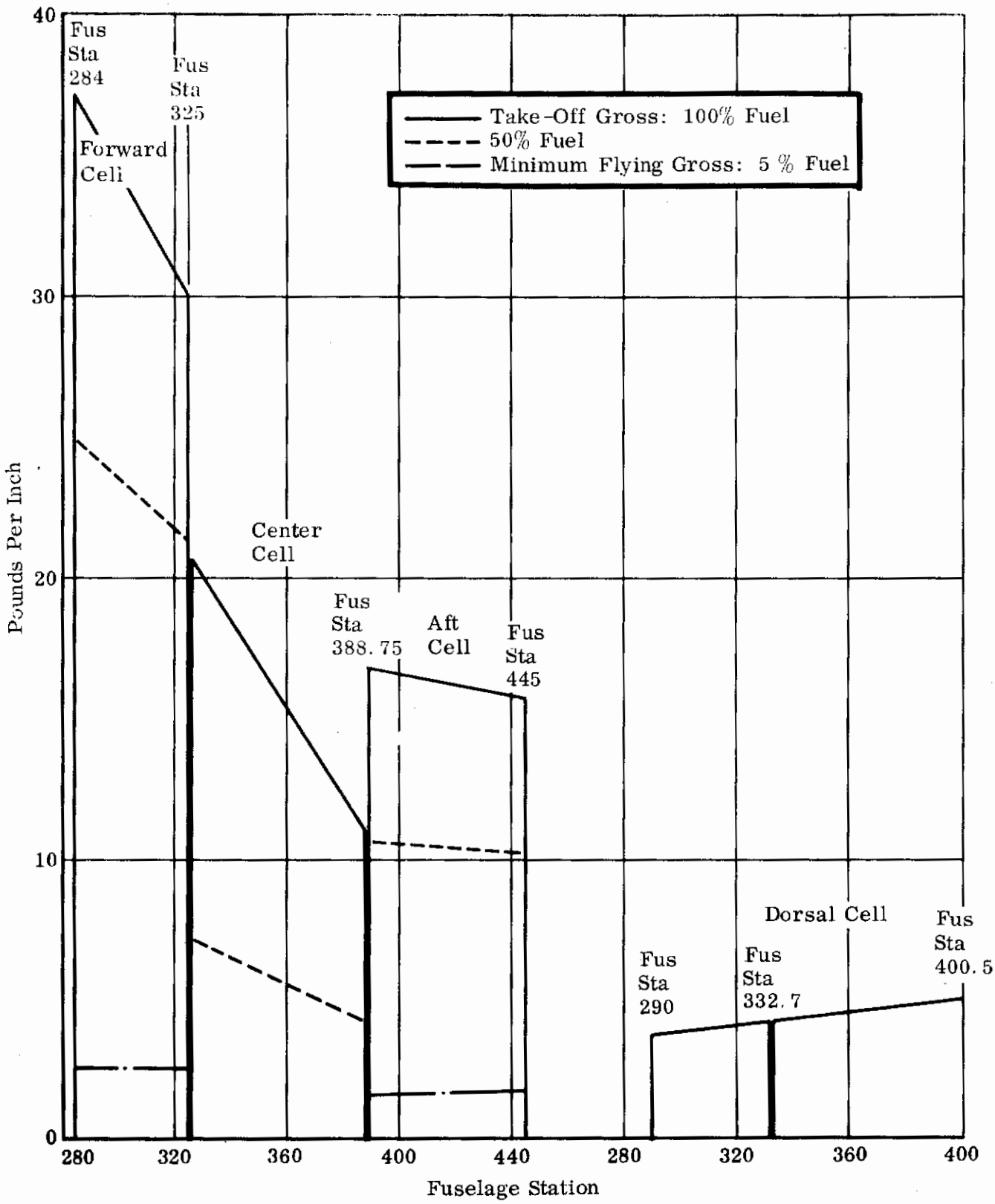

FIGURE 8 T-38 TRAINER FUEL DISTRIBUTION

1.2 F-5A Fighter Configurations

The Northrop Norair F-5A is a 1.7 Mach-number fighter aircraft. It may accommodate various combinations of pylon attached armament and external fuel tanks. The external geometry and engineering data are essentially identical to those of the T-38 trainer (Table I) with the following exceptions:

Wing area	173.82 ft^2
Airfoil section	NACA65A-004.8 modified
Power plant	
(2) Turbo-jets with afterburners	J85-GE-13

A three-view drawing of the aircraft is given in Figure 9. The weight configurations and flight conditions chosen for the gust computation are as follows:

Configuration	Aircraft Weight (Pounds)	Mach No.	Altitude (Feet)	Remarks
(1)	15,000	.81	Sea Level	Full internal fuel, MK-84 under fuselage. Empty wing tip and station 85 fuel tanks.
(2)	15,000	.81	30,000	Weight configuration same as case (1)
(3)	13,118	.90	Sea Level	Basic configuration, full fuselage tank, wing tip attached GAR-8.

In the gust transfer function computation, a total of 76 control points are used. The detailed control point geometry is given in Figure 10. The overall weight data is given in Table II, while Table III gives the detail weight and inertia data. The fuselage fuel distribution of F-5A is the same as that of T-38 which is shown in Figure 8. The wing and fuselage stiffness data of F-5A are plotted in Figures 11 and 12.

It may be appropriate at this point to illustrate an historical background under which the gust computation configurations are chosen. The structure of a fighter designed to a maneuver load factor of 7.33, as required by current military specifications, is not affected appreciably by the current design up-gust velocities.

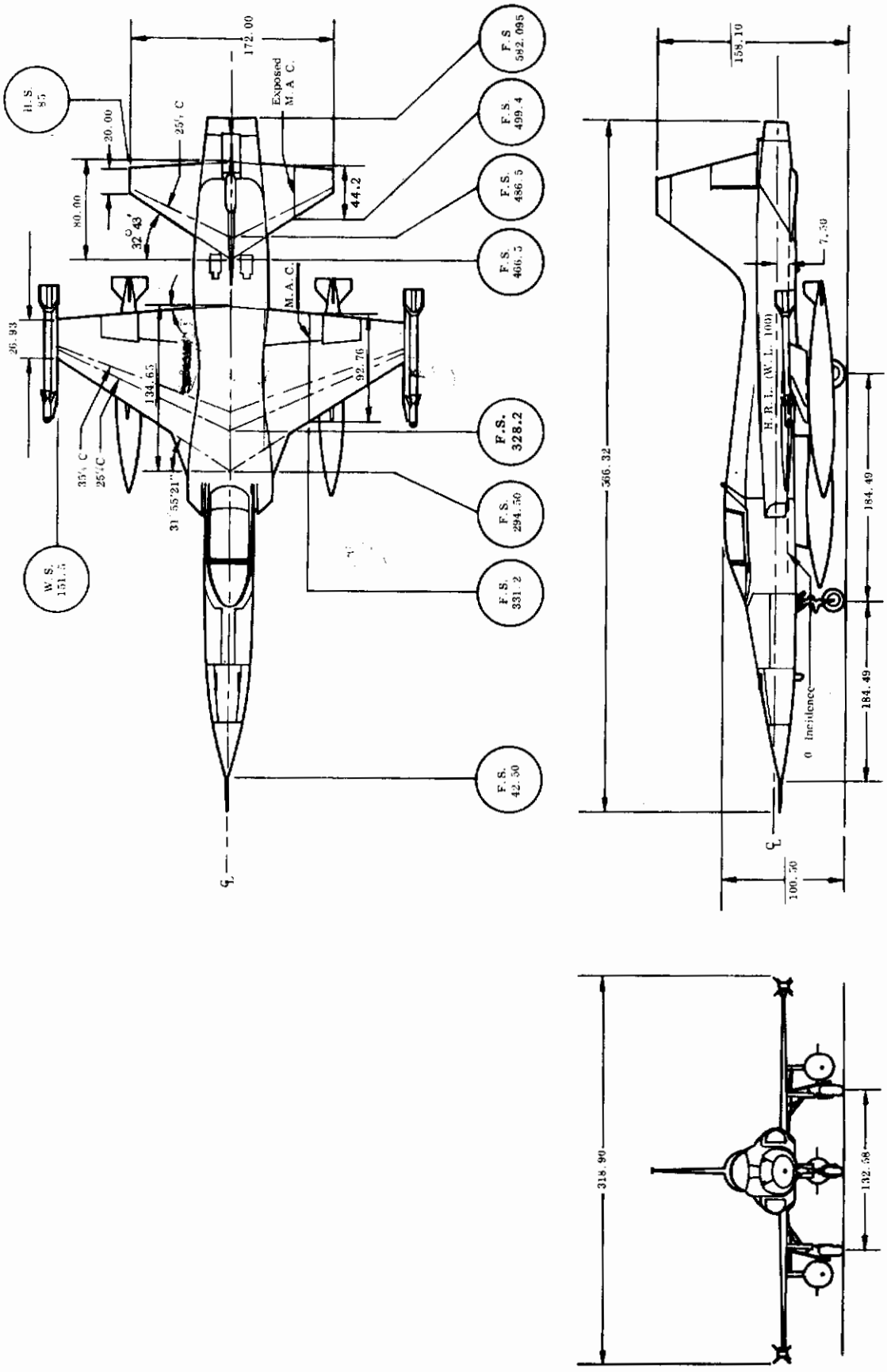

FIGURE 9 THREE VIEW DRAWING OF F-5A FIGHTER

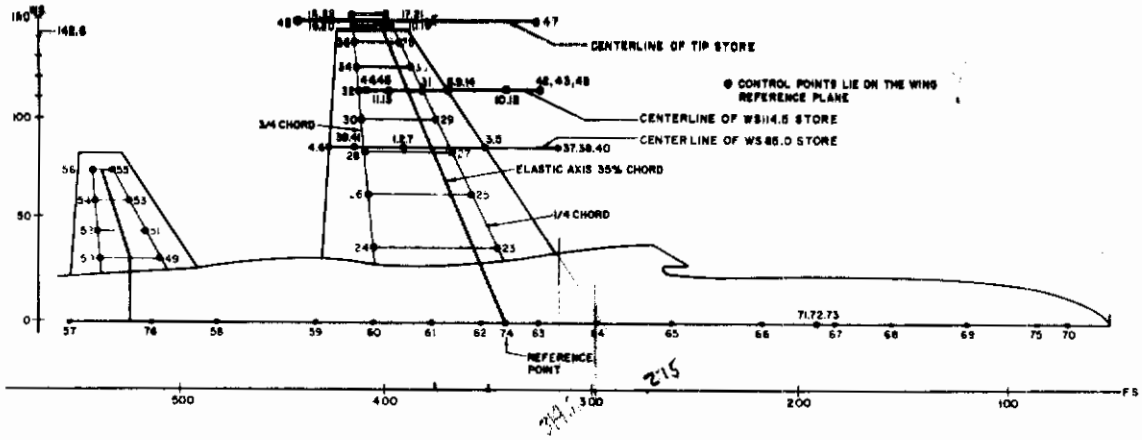

48 & 76 CONTROL POINT LOCATIONS

	CONTROL POINT NO. & DIRECTION L - LONG. V - VERT S - SIDE		W.S.	F.S.	W.L.		CONTROL POINT NO. & DIRECTION L - LONG. V - VERT S - SIDE		W.S.	F.S.	W.L.		CONTROL POINT NO. & DIRECTION L - LONG. V - VERT S - SIDE		W.S.	F.S.	W.L.
PYLON	1	L	85.0	364.00	77.95	WING STRIPS	28	V	85.5	402.98	92.50	HORIZ TAIL	55	V	77.75	522.60	92.50
	2	L		384.00	82.50		29		89.5	372.46			56		77.75	535.16	
	3	V		346.00	77.95		30		99.5	404.41			57		0	548.12	
	4	V		422.00	77.95		31		114.5	379.14			58			479.38	
	5	S		346.00	77.95		32		114.5	405.76			59			430.94	
	6	S		422.00	77.95		33		128.0	384.26			60			402.81	
	7	S	85.0	384.00	62.50		34		128.0	406.79			61			376.97	
PYLON	8	L	114.5	386.54	78.45		35		137.3	389.29			62			353.41	
	9	L		386.54	63.50		36	V	137.3	401.81	92.50		63			327.23	
	10	V		338.44	78.45	FLIGHT TEST ACCELEROMETER W.S. 85.0 STORE	37	L	85.0	315.00	68.50		64			298.41	
	11	V		394.64	78.45		38	S		315.00	68.50		65			261.50	
	12	S		338.44	78.45		39	S		407.30	71.80		66			216.50	
	13	S		394.64	78.45		40	V		315.00	68.50		67			179.88	
	14	S	114.5	386.54	63.50		41	V	85.0	407.30	71.80		68			151.63	
MISSILE LAUNCH	15	V	146.0	393.18	92.50		42	L	114.5	322.30	67.30		69			113.75	
	16		146.0	408.59			43	S		322.30	67.30	FORWARD FUSELAGE	70	V		66.25	92.50
	17		151.5	395.81			44	S		404.10	70.20		71	L		190.00	72.25
	18		151.5	409.08		W.S. 114.5 STORE	45	V		322.30	70.20	NOSE GEAR	72	V		190.00	72.25
TIP TANK	19		146.0	393.16			46		114.5	404.10	67.30		73	L		190.00	50.50
	20		146.0	408.59			47		147.75	328.34	92.50	REFL PT	74	V		341.626	92.50
	21		151.5	395.81		TIP TANK	48		147.75	432.34		FWD FUS	75	V		82.00	92.50
	22		151.5	409.08			49		34.25	502.31		AFT FUS	76	V	0	510.00	92.50
WING STRIPS	23		39.8	345.88			50		34.25	530.22			77				
	24		39.8	398.06			51		48.75	509.07			78				
	25		64.5	356.88			52		48.75	531.87			79				
	26		64.5	401.27			53		63.25	515.84			80				
	27	V	83.5	365.34	92.50	HORIZ. TAIL	54	V	63.25	533.51	92.50		81				

WING, FUSELAGE AND HORIZONTAL TAIL CONTROL POINT GEOMETRY (F-5)

FIGURE 10 WING, FUSELAGE AND HORIZONTAL TAIL CONTROL POINT GEOMETRY (F-5)

TABLE II. F-5A WEIGHT AND INERTIA DATA, OVERALL AND ATTACHED STORES

ITEM	C.G. LOCATION				STREAMWISE C.G. INERTIA		
	WEIGHT LB	W.S	F.S.	W.L.	ROLL LB-IN^2	PITCH LB-IN^2	YAW LB-IN^2
Configuration (3) 100% Fuel (No Ammo)	13,118	0	349.8	102.6	0	140,948,720	----
GAR-8-Missile	158.6	151.5	376.08	92.50	0	193,000	Same as Pitch
GAR-8-Launcher	52.6	146.0	372.70	92.50	0	26,216	Same as Pitch
Empty Tip 50 Gal. Tank	117.5	147.74	374.84	92.5	3557	174,476	174,476
Empty W.S. 85 150 Gal. Tank	163	85	369.7	65.28	12067	281,947	281,947

TABLE III. F-5A WEIGHT AND INERTIA DATA

WING, PYLONS AND STORES

ITEM	WEIGHT LB	C.G. LOCATION W.S.	C.G. LOCATION F.S.	C.G. LOCATION Elevation	STREAMWISE INERTIA I_{ox} LB-IN^2	STREAMWISE INERTIA I_{oy} LB-IN^2
Wing Strip						
W.S. 26.6 - W.S. 53.0	372.42	33.13	367.68	92.50	-	155,357
W.S. 53.0 - W.S. 76.0	126.41	64.50	371.48		-	42,811
W.S. 76.0 - W.S. 91.0	98.92	84.91	378.51		-	21,335
W.S. 91.0 - W.S. 108.0	48.71	99.22	382.15		-	8,908
W.S. 108.0 - W.S. 120.0	40.04	113.86	386.30		-	4,669
W.S. 120.0 - W.S. 132.0	19.38	125.39	378.77		-	1,731
W.S. 132.0 - W.S. 142.6	27.46	139.39	396.41		-	1,524

FUSELAGE AND HORIZONTAL TAIL

Horizontal Tail Strip (1/2 Airplane)						
H.T.S. 27.00 - 41.40	18.02	33.30	511.66	92.50	350	3,375
41.50 - 56.00	12.38	46.71	516.59		192	1,601
56.00 - 70.50	8.10	62.65	521.87		142	773
70.50 - 85.00	5.07	76.93	527.28		86	315
Fuselage Section (Total Airplane)						
F.S. 42.50 - 137.50	382.80	0	115.41		-	211,144
137.50 - 194.00 (Gear Up)	836.90		168.91		-	357,393
194.00 - 284.00	1429.20		241.74		-	1,061,006
284.00 - 341.63 5% Fuel	767.95		310.66		-	277,142
341.63 100% Fuel	2569.60		310.60		-	276,385
341.63 - 388.75 5% Fuel	434.80		364.25		-	128,491
388.75 100% Fuel	1320.70		364.17		-	128,494
388.75 - 445.00 5% Fuel	749.80		417.85		-	310,005
445.00 100% Fuel	1620.00		416.29		-	309,917
445.00 - 582.50	2468.20		498.07		-	3,071,019

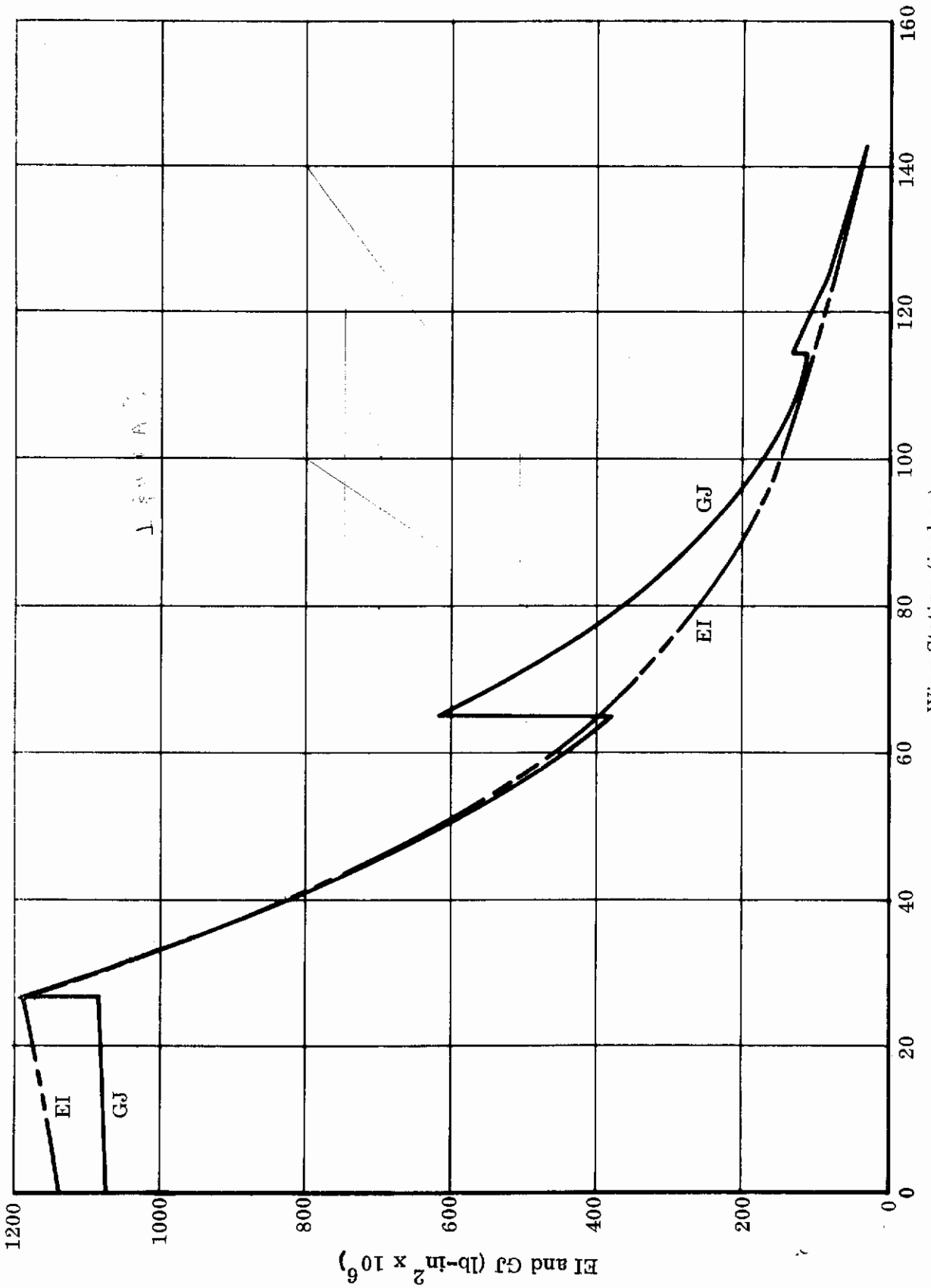

FIGURE 11 F-5A WING BENDING AND TORSION STIFFNESS

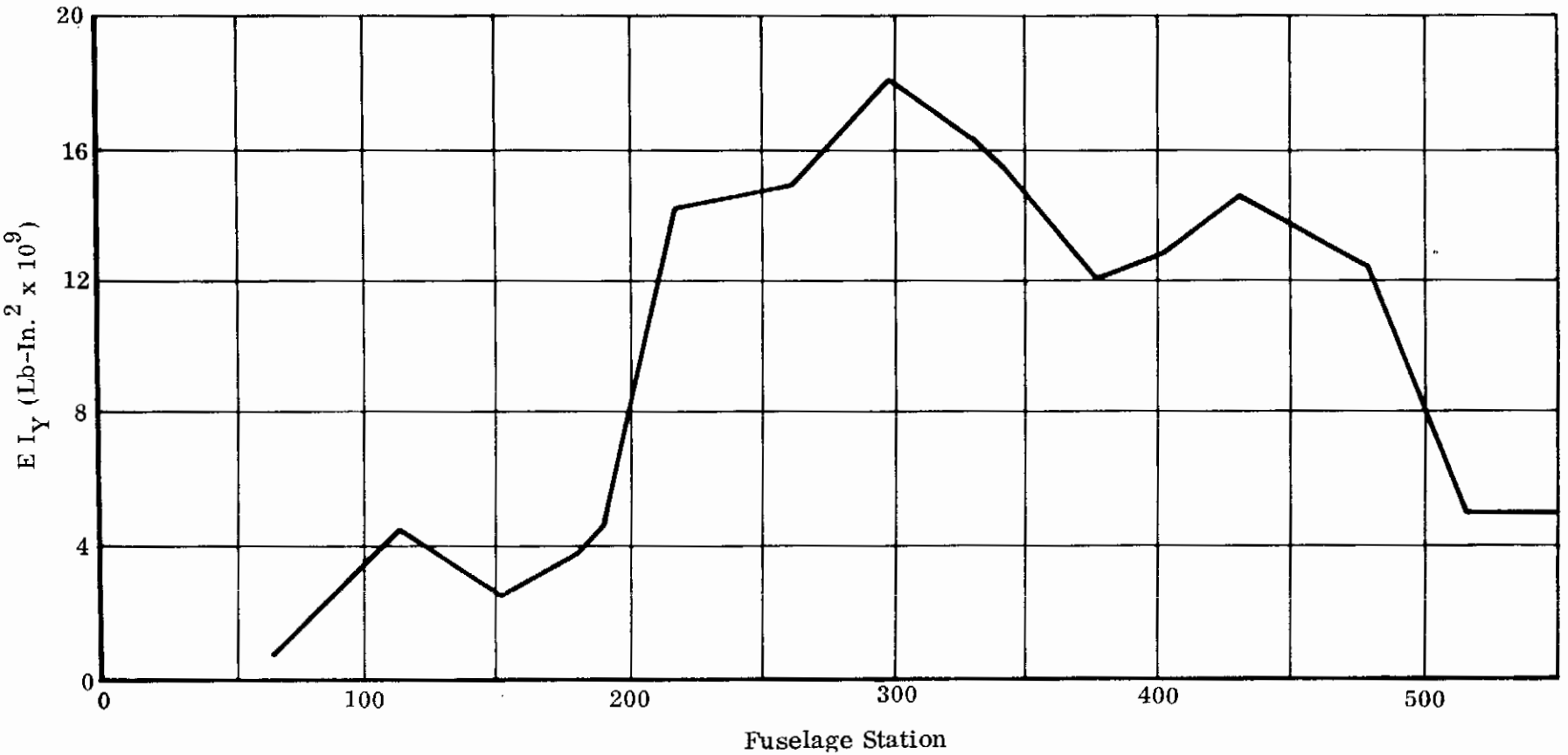

FIGURE 12 FUSELAGE VERTICAL BENDING STIFFNESS ABOUT W.L. 92.5

Down-gusts sometimes produce critical conditions. A quasi-steady down-gust is a critical, downward bending condition, on the F-5A airplane, at the wing root, and over most of the span. Since various external stores are carried on the wing, it appears possible that dynamic gusts may also be critical. For this reason, an extensive investigation of dynamic gust loads was instigated, using a discrete (1-cosine) gust shape with gust lengths varying from 40 to 70 wing reference semi-chords. The most critical responses were obtained. Design load envelopes for the F-5A are shown in Figures 13 and 14 for the section just inboard of the outboard pylon station, Wing Station 114.5. The most critical loads for a 45-fps gust are superimposed on the diagrams. It is seen that the negative bending moment is outside the design envelope, but it is within the strength capability of the wing. This condition is for a configuration defined as Configuration (1) above.

2. Stress Sensitive Locations and the Stress Influence Coefficients

The gust computation is carried out in terms of various types of stresses in the critical locations of the aircraft. For this purpose, a number of stress sensitive locations are chosen for T-38 and F-5A aircraft based on existing test and analytical data. The chosen locations are used as the base points for gust computation. Corresponding to each stress sensitive location, a row of stress influence coefficients are established which are the induced stresses due to unit loads applied at the various control points.

As explained later in the report, the gust input-output transfer function is generated for each stress sensitive location corresponding to a specific gust frequency. The stress data are obtained by converting the dynamic forces at the control points into the stress at the chosen location through the use of the stress influence coefficients. In this manner, a set of frequency-dependent stress transfer functions are generated which are used in the final gust computation.

2.1 Stress Influence Coefficients of the T-38 Trainer

In this section, T-38 wing, fuselage, and horizontal stabilizer stress influence coefficients are presented. The most critical structural members under gust loading conditions, together with the associated allowable stresses, are tabulated in Table IV. The data for the wing structure may be compared with the data of Figure 15 which gives the wing structure critical element coding. The

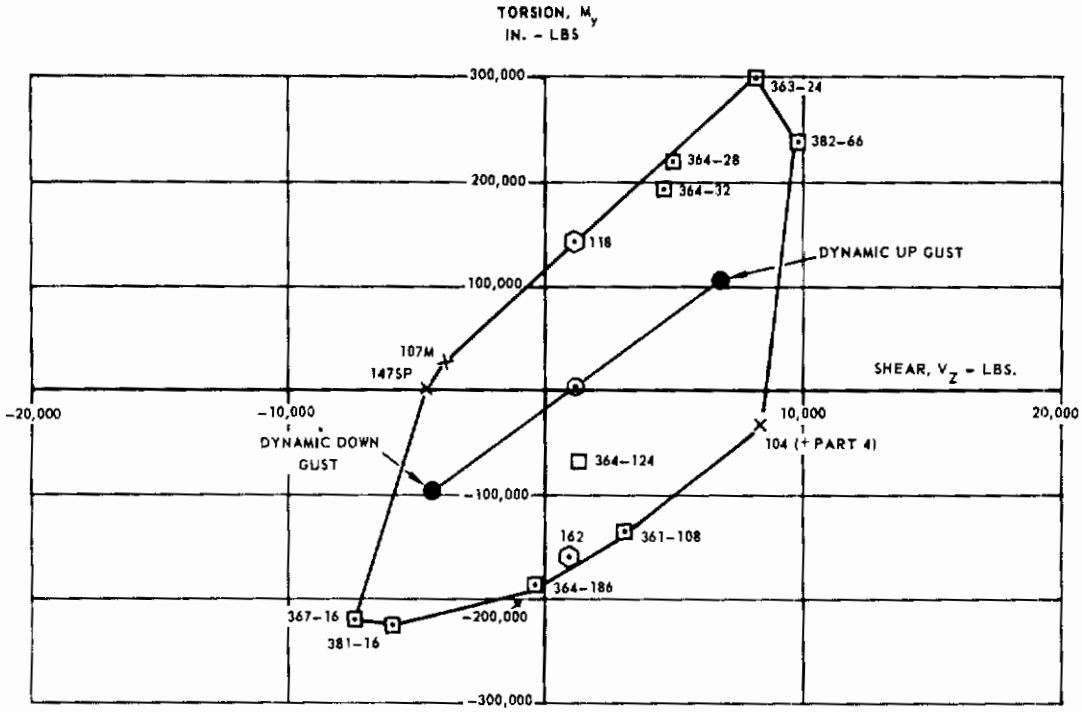

FIGURE 13 F-5A WING LOAD ENVELOPE WING STA. 114.5 INBOARD SWEPT LOADS SHEAR, V_Z VS. TORSION, M_Y

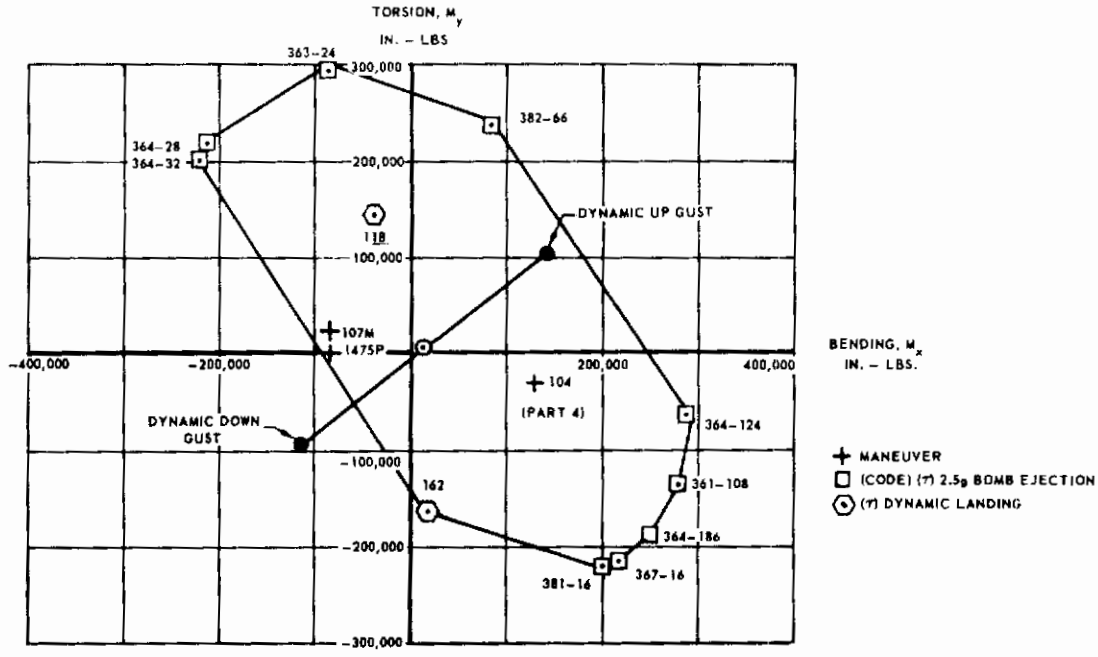

FIGURE 14 F-5A WING LOAD ENVELOPE WING STA. 114.5 INBOARD SWEPT LOADS BENDING, M_x VS. TORSION, M_y

TABLE IV. T-38 STRESS SENSITIVE LOCATION IDENTIFICATION

Dynamic Stress Index	I IBM Index	Location	Stress Type	Stress Element	Description of Stress Element	1-G Limit	Increm. Limit All. Non-Inter.	Increm. Limit All. Interact
S-1	46	F.S. 284	σ_t	1	Tension failure of lower longeron bolt at F.S. 284	-2089	122090	
S-2	47	F.S. 284	τ	2	Shear failure at side panel attach of F.S. 284 bulkhead		8534	
S-3	21	WS-27	τ	2	29% spar web stability comb.	3333	11534	6000
S-4	22	WS-27	σ_c	2	bending, shear, crushing	-6000	-43000	-29340
S-5	23	WS-27	σ_c	1	27-33% Upper panel stability comb. compression and shear	-6666	-28670	-28340
S-6	24	WS-65	σ_t	2	39% chord-lower skin axial stress	5334	40340	40000
S-7	25	WS-65	τ	1	27-33% upper panel stability	4000	24670	2933
S-8	26	WS-65	σ_c	1	combined compression & shear	-5333	-28670	-26690
S-9	39	WS-101	σ_t	2	W.S. 101 rib-attachment lower door in rib flange	2000	18000	18000
S-10	40	WS-101	τ	1	22.8% spar web stability		11267	7667
S-11	41	WS-101	σ_c	1	Comb. bending, shear, crushing.	-2667	-36670	-20660
S-12	42	WS-125	σ_c	2	Rib-attach. skin to rib flange		-18530	-18000
S-13	43	WS-125	τ	1	23-30% upper panel stability		8600	3867
S-14	44	WS-125	σ_c	1	Comb. compression & Shear		-17000	-13330
S-15	28	HSS-27.7	τ	1	Shear in bond between skin and root rib HSS-27.7		1666	
S-16	29	HSS-25.07	σ_t	2	Bending of torque tube H.S.S.-25.07		197340	

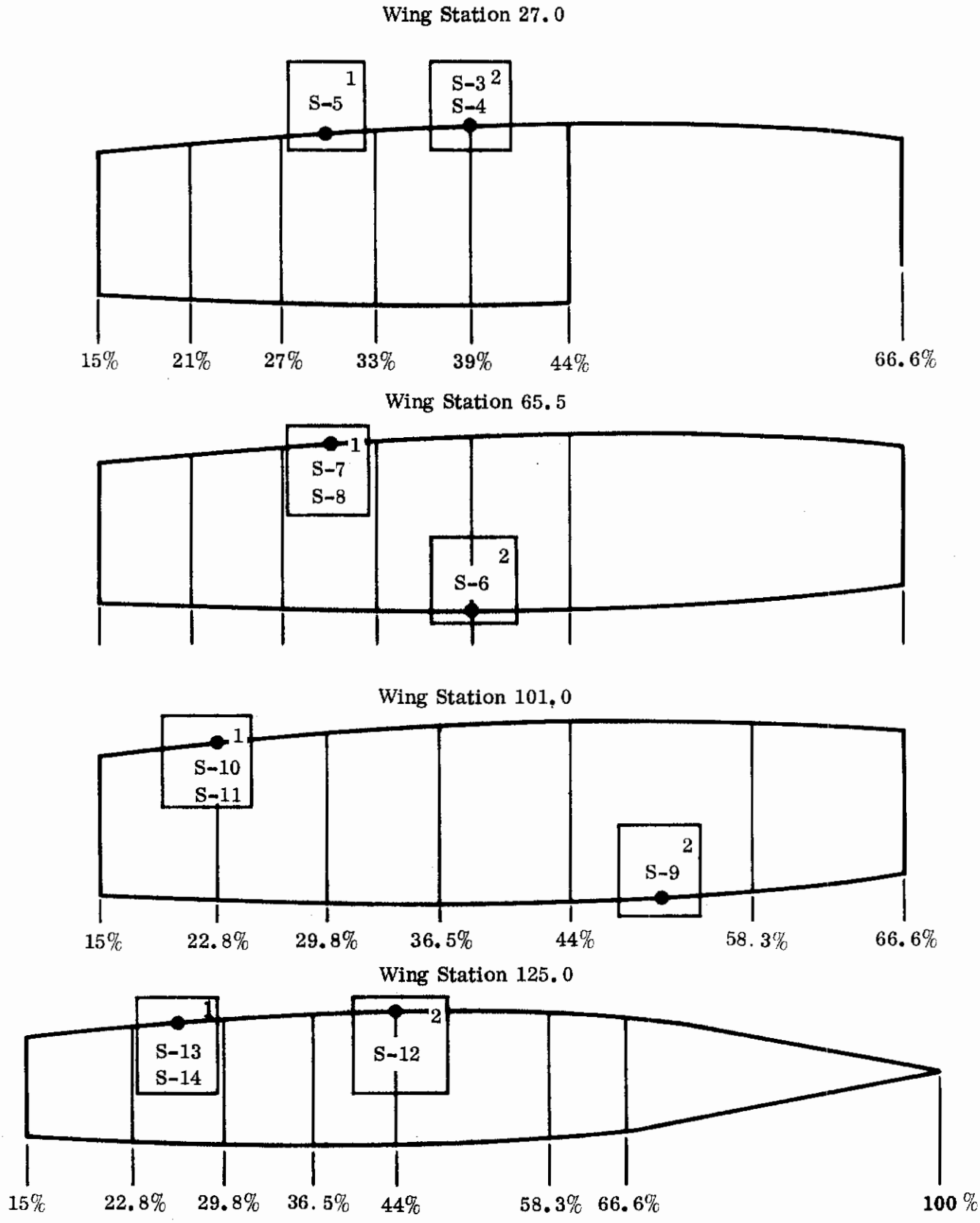

FIGURE 15 T-38 WING STRUCTURE CRITICAL ELEMENT CODING

TABLE V. T-38 WING STRESS INFLUENCE COEFFICIENTS

W.S.	Dynamic Stress Index	Stress	Control Points															
			13	14	15	16	17	18	19	20	21	22	23	24	25	26	27	28
27	S-3	σ	1291	2921	4904	6364	8586	9873	12154	13273	15836	16780	19627	20394	22974	23581	25932	26400
27	S-4	τ	-2351	-4785	-2768	-5642	-2443	-4976	-2129	-4330	-1805	-3664	-1471	-2980	-1175	-2373	-915	-1838
27	S-5	σ	-1370	-3101	-5204	-6755	-9113	-10478	-12899	-14087	-16808	-17809	-20831	-21645	-24383	-25029	-27522	-28019
65	S-6	σ	0			0	-573	8619	10089	18172	21094	27914	32422	34526	42413	46811	51106	54497
65	S-7	σ	0			0	493	-7404	-8667	-15610	-18120	-23978	-27851	-29658	-36434	-40212	-43901	-46814
65	S-8	τ	0			0	482	-2948	-1703	-6023	-2257	-4274	2827	-3215	3329	-878	3740	498
101	S-9	σ	0									0	16170	26147	34188	42119	50116	56232
101	S-10	σ	0									0	-18375	-29713	-38850	-47863	-56950	-63900
101	S-11	τ	0									0	-9199	-10582	-8487	-9586	-7858	-8706
125	S-12	σ	0											0	-22127	-51400	-80916	-103489
125	S-13	σ	0											0	-17495	-40639	-63975	-81823
125	S-14	τ	0											0	7987	-31246	3436	-26839

σ and τ are in units of psi.
The data are based on control point load of 10,000 pounds, positive upward

TABLE VI. T-38 FUSELAGE STRESS INFLUENCE COEFFICIENTS

Dynamic Stress Index	Stress psi	Control Points			
		7	8	9	10
S-1	(σ)	106,500	235,000	363,000	492,000
S-2	(τ)	8,886	5,808	10,730	11,650

TABLE VII. T-38 HORIZONTAL STABILIZER STRESS INFLUENCE COEFFICIENTS

CONTROL POINT	ELEMENTS	
	S-15(τ)	S-16 (σ)
29	5082	77,950
30	-4154	77,950
31	4619	169,860
32	-3821	169,860
33	4186	261,630
34	-3458	261,630
35	3721	353,280
36	-3095	353,280
37	3291	445,440
38	-2728	445,440
39	2827	537,340
40	-2364	537,340
41	2236	629,250
42	-1745	629,250
43	1772	721,150
44	-1635	721,150

stress influence coefficients for stress sensitive locations of the wing structure are tabulated in Table V. Stress influence coefficients for the critical elements of the fuselage together with the allowable stresses are presented in Table VI. The two elements selected are at Fuselage Station 284 and control point influence coefficients are given for control points forward of Fuselage Station 284. Influence coefficients for the critical horizontal stabilizer elements are presented in Table VII. In Tables V - VII, all the stress influence coefficients are computed based on a 10,000 pound upward (positive) force applied at each control point.

2.2 Stress Influence Coefficients of the F-5A Fighter

Similar stress sensitive locations and stress influence coefficients data are organized for the F-5A fighter. The gust stress sensitive locations are identified and indexed in Table VIII. The corresponding critical element coding is given in Figure 16. Figure 17 gives the specific wing section orientations as well as the stress sensitive locations corresponding to different weight and flight configurations described in subsection 1.2. The critical element coding of Figure 16 may be cross-checked against the data of Figure 17. In Table VIII, it is noted that various types of stress conditions are used including tensile and shear stresses, (σ, τ), shear flow (q) and bending moment (M_y). The shear flow and the bending moment are selected for intricate structural parts where a detailed stress analysis is not feasible because of the localized nature of the internal stresses. The data are based on test results and empirical formulas in these cases. As will be shown later, the final result of the gust computation is represented in terms of a ratio of the response stress and the allowable stress. As long as the two stress data are of the same units, a non-dimensional ratio may be established irrespective of the actual units used.

2.2.1 F-5A Wing Structure Stress Influence Coefficients

Wing influence coefficients for the elements shown in Figure 16 are tabulated on Table IX. These influence coefficients are determined by the flexure formula using standard tapered beam analysis.

The most critical members of the wing under gust loading conditions, together with the associated allowable stresses, are tabulated in Table VIII. Discrete gust conditions corresponding to configurations (1-3) are selected as representative of the particular airplane store configurations specified and are used in determining the stress critical locations. The procedure and results are summarized below.

TABLE VIII. F-5A STRESS SENSITIVE LOCATION IDENTIFICATION

Dynamics Stress Index	I IBM Index	Location	Stress Type	Stress Element	Description of Stress Element	1-G Limit	Increm. Limit All. Non-Inter	Increm. Limit All. Interact.
S-1	14	WS-27	τ	58	39% spar web stability for	-627	13627	3093
S-2	15	WS-27	σ_c	58	combined axial-shear stress	-6407	-33593	-31593
S-3	16	WS-27	τ	10	27-33% upper panel stability	5034	18966	3299
S-4	17	WS-27	σ_c	10	for combined axial-shear stress	-6484	-30185	-24851
S-5	18	WS-85	q	29	66% spar buckling	66		741
S-6	19	WS-85	τ	10	27-33% upper panel stability	169	14231	1584
S-7	20	WS-85	σ_c	10	for combined axial-shear stress	-6021	-28310	-27777
S-8	28	WS-101	q	78	21% spar to skin attach	73	640	640
S-9	29	WS-101	τ	40	44-66% lower panel attach for	420	11714	2713
S-10	30	WS-101	σ_t	40	combined axial-shear stress	2593	16341	15541
S-11	38	WS-114	q	78	21% spar to skin attach	60	653	653
S-12	39	WS-114	τ	67	27-33% lower panel stability	233	8167	480
S-13	40	WS-114	σ_c	67	combined axial-shear stress	1589	-44250	-43591
S-14	41	WS-114	τ	40	44-66% lower panel attach to	413	16054	6034
S-15	42	WS-114	σ_t	40	rib for comb. axial-shear stress	1460	20274	18450
S-16	43	WS-114	σ_c	39	55% spar web stab. for axial stress	1313	-44648	-44648
S-17	44	WS-114	σ_c	31	66% skin fastener-tension	873	-44873	-44873
S-18	45	WS-142.6	τ	40	51%-58.25% lower panel stab.	773	31095	29495
S-19	46	WS-142.6	σ_c	40	comb. axial-shear stress	-82	-46000	-4685
S-20	47	WS-142.6	τ	19	51-58% upper panel stability	807	27200	23200
S-21	48	WS-142.6	σ_c	19	for combined axial-shear	143	-46140	-12470

TABLE VIII. F-5A STRESS SENSITIVE LOCATION IDENTIFICATION (Continued)

Dynamics Stress Index	I IBM Index	Location	Stress Type	Stress Element	Description of Stress Element	1-G Limit	Increm. Limit All. Non-Inter.	Increm. Limit All. Interact.
S-22	49	WS-142.6	q	1	15% spar to skin attach	88	3267	3267
S-23	33	FS-284	My		Section bending moment	-81440	548840	
S-24	22	HSS-27.7	τ	1	Bond shear between skin and root		1666	
S-25	32	HSS-25.07	σ_t	2	Bending at torque tube		197340	

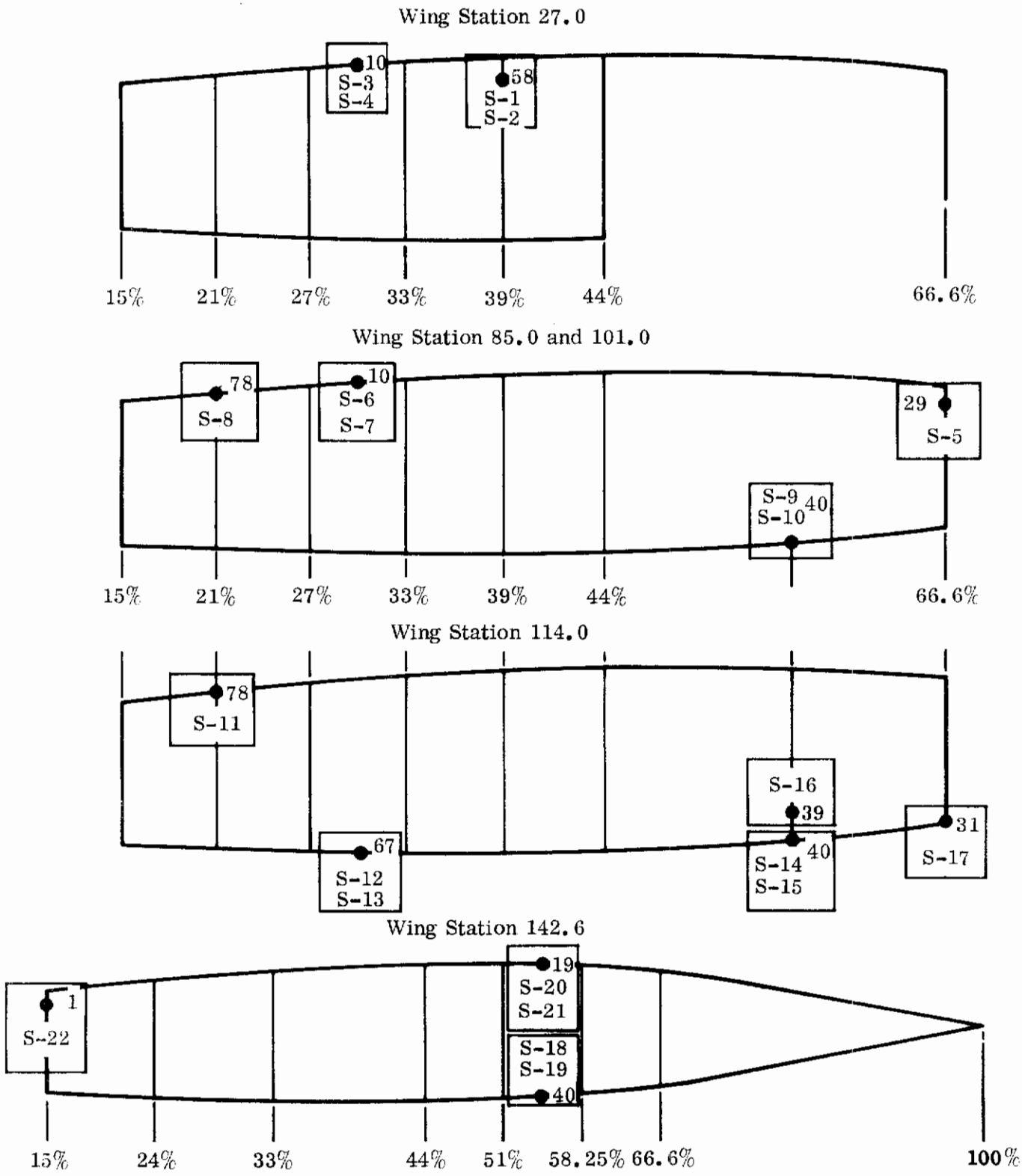

FIGURE 16 F-5A WING STRUCTURE CRITICAL ELEMENT CODING

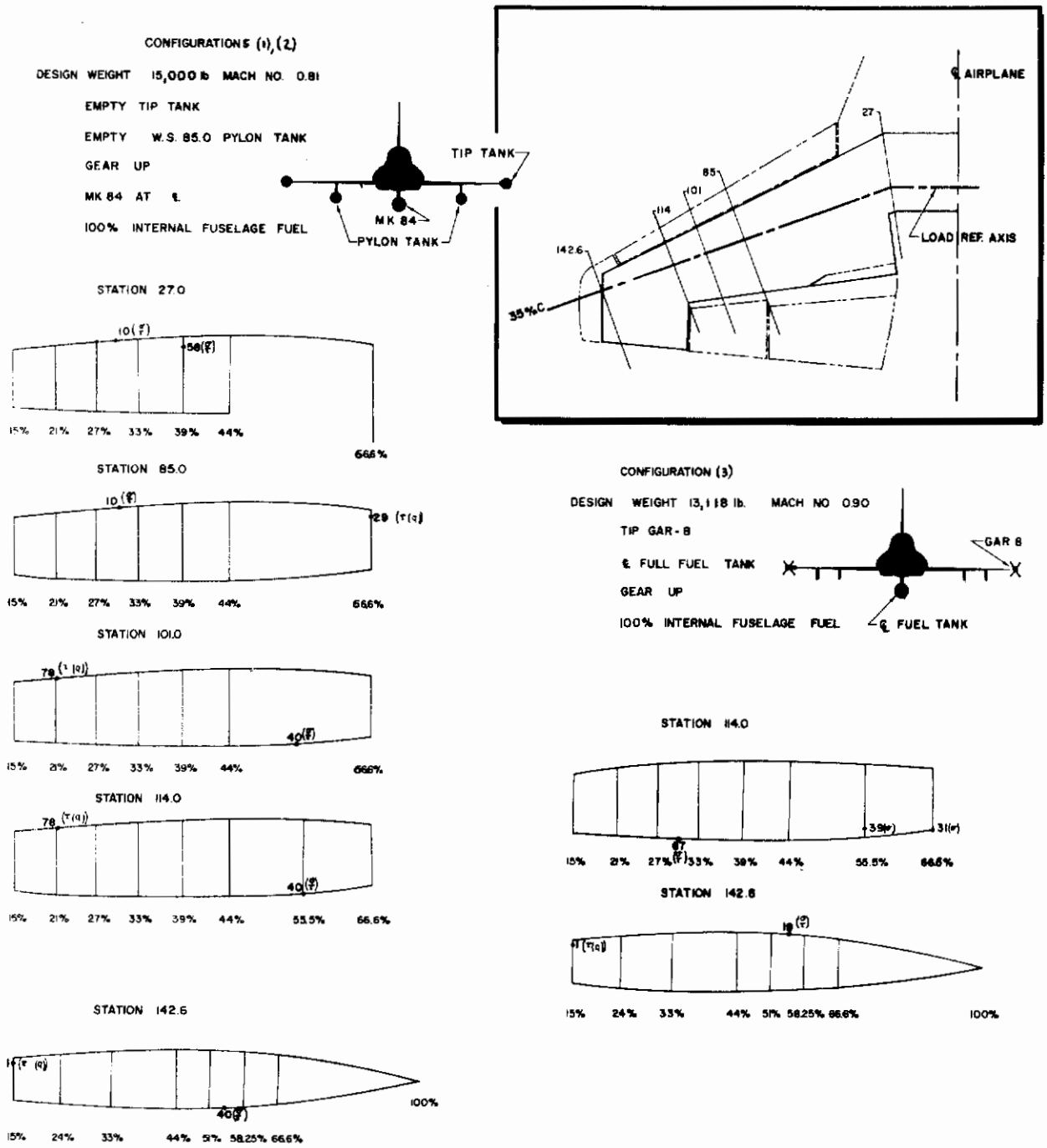

FIGURE 17 F-5A FIGHTER WING STRESS SENSITIVE LOCATIONS

TABLE IX. STRESS INFLUENCE COEFFICIENTS OF F-5A FIGHTER WING STRUCTURE

W.S.	Dynamic Stress Index	Stress	Control Points 1	2	3	4	5	6	7	13, 19	16, 20	17, 21	18, 22	23	24	25	26	27	28	29	30	31	32	33	34	35	36	37	38
27	S-1	τ	- 684	- 1421	- 1105	- 4695	589	589	1221	- 843	- 1580	- 737	- 1388	-2940	-5455	-9455	- 4550	- 2085	- 3850	- 1760	- 3275	- 1462	- 2725	- 1241	- 2306	- 1021	- 1895	2380	2620
	S-2	σ	- 459	- 944	-12890	-15280	- 3256	- 3256	- 6792	-24021	-28510	-29330	-29750	-2774	-4418	-9546	-10045	-13162	-14348	-16967	-17970	-20530	-21372	-23630	-23930	-25954	-26340	- 26310	-29650
	S-3	τ	-2031	- 4188	3678	- 6929	961	961	1984	1125	- 1027	1149	- 733	706	-6718	504	5392	878	- 4378	945	- 3518	1000	- 2714	1047	- 2098	1090	- 1494	10565	- 4227
	S-4	σ	- 464	- 956	-13041	-15460	- 3294	- 3294	- 6792	-28353	-28444	-29676	-30100	-2807	-4401	-8148	-10163	-13319	-14518	-17170	-19190	-20730	-21630	-23540	-24280	-26360	-26830	- 26620	-30000
85	S-5	τ(Q)	- 418	- 861	516	- 1629	296	296	610	438	- 4	479	93	0	←				→ 0	97	- 430	201	- 536	257	- 359	372	- 159	2392	- 951
	S-6	τ	-5962	-12290	9846	-21315	1562	1562	3231	- 2938	- 9254	- 3354	- 6869	0	←				→ 0	538	-12546	- 577	-11485	- 1438	-10677	- 2285	- 9677	24640	-14910
	S-7	σ	-4668	- 9882	7743	-15670	-12560	-12560	-25890	-59010	-63990	-64543	-68890	0	←				→ 0	-12197	-22508	-27297	-35690	-38840	-46150	-50250	-55224	- 38960	-73190
101	S-8	τ(Q)	0	←						→ 0	- 265	- 1	- 237	- 7	0	←						→ 0	- 425	31	- 366	19	- 309	7	1412	401
	S-9	τ	0	←						→ 0	- 3115	-10375	- 4983	-10427	0	←						→ 0	2448	-10060	417	-10178	- 1533	-10292	25406	-21586
	S-10	σ	0	←						→ 0	36730	40958	41427	45120	0	←						→ 0	9815	17100	19630	25800	29297	34374	18708	45740
114	S-11	τ(Q)	0	←						→ 0	- 399	- 68	- 364	- 84	0	←						→ 0	- 528	23	- 480	- 10	- 429	- 43	1791	429
	S-12	τ	0	←						→ 0	2531	- 9231	1654	- 8615	0	←						→ 0	7735	-12770	3700	-11490	3506	-10215	32420	-27050
	S-13	σ	0	←						→ 0	34970	40768	41423	46480	0	←						→ 0	- 2139	4003	11484	19960	24750	31720	11590	51470
	S-14	τ	0	←						→ 0	508	- 6776	35	- 5888	0	←						→ 0	3800	- 8512	2206	- 7694	1247	- 6894	20049	-16330
	S-15	σ	0	←						→ 0	32120	37449	38050	42700	0	←						→ 0	- 2500	7352	10549	18330	22740	29140	13647	47290
	S-16	σ	0	←						→ 0	28890	33677	34218	38400	0	←						→ 0	- 2364	6611	9486	16490	20450	26210	9575	42320
	S-17	σ	0	←						→ 0	31610	36860	37450	42020	0	←						→ 0	- 3113	7235	10362	18040	22360	28680	13456	46530
142.6	S-18	τ	0	←						→ 0	12350	-14450	10696	-12720	0	←												→ 0	12930	-34250
	S-19	σ	0	←						→ 0	6386	19961	21520	33360	0	←												→ 0	48320	45000
	S-20	τ	0	←						→ 0	9400	- 8200	6977	16077	0	←												→ 0	123600	-57960
	S-21	σ	0	←						→ 0	- 6451	-20160	-21740	-33700	0	←												→ 0	48811	-43460
	S-22	τ(Q)	0	←						→ 0	1826	- 1021	1373	- 914	0	←												→ 0	14233	- 5340

σ and τ are in units of psi, τ(Q) is in units of pounds per inch.

The data are based on control point load of 10,000 pounds. Sign convention: positive upward, outboard and aft.

The critical gust loads are obtained by linearly extrapolating the discrete gust loads corresponding to configuration (1) until the maximum allowable loads are obtained. The maximum allowable loads (V_z, M_x, M_y) at each wing station are determined by considering the failure of the most critical members as defined by the wing strength envelopes. The wing strength envelope for a particular wing station consists of families of curves which define the wing loads with zero margin of safety for the critical structural members. Each family of curves represents one structural member. Families of curves are necessary in order to represent two dimensionally the three load variables.

A typical example of the above mentioned load envelopes is shown in Figure 18, obtained in a discrete gust analysis corresponding to configuration (1) with a gust length of 150 feet. In the figure the three dimensional envelope for three stresses on the section (Wing Station 101) is plotted in two dimensional form. This is accomplished by means of projecting onto the V_z - M_y plane the intercepts of the envelope with planes of constant M_x. The line $\overline{0A}$ indicates the load vector. Point (A) corresponds to a derived gust velocity of 45 feet per second. The vector increases in amplitude with increasing gust velocity. The figure indicates that the lower panel rib attachment is most critical (Point B) as compared to the other stress sensitive locations of the wing section (Point C).

The allowable axial and shear stresses for the critical members are found directly from the maximum allowable loads utilizing the tapered beam analysis. The stresses for each member are derived such that their interaction impends failure of the member, and are therefore designated the interaction allowable stresses. These interaction allowable stresses are valid only for load conditions which approximate the condition for which they are derived, since significantly different load conditions produce different ratios of the interacting stresses.

The critical members consist of three groups: (1) attachment failure, (2) panel stability, (3) spar web stability. The members at the wing tip (Wing Station 142.6) are critical primarily for shear stress, while those inboard are critical mainly for axial stress. The allowable axial and shear stresses for no interaction are tabulated for the purpose of indicating the relative importance of axial and shear stresses. Members critical for attachment shear or bearing have allowable shear flows given rather than allowable stresses. This is done both for clarity in defining the allowables and for reduction of the computation required.

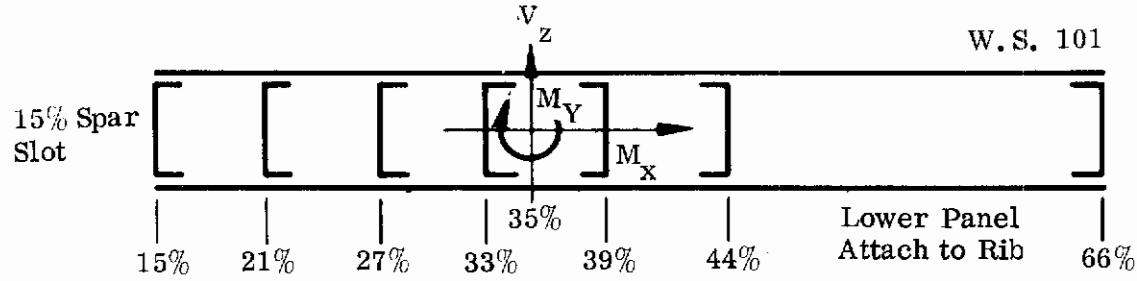

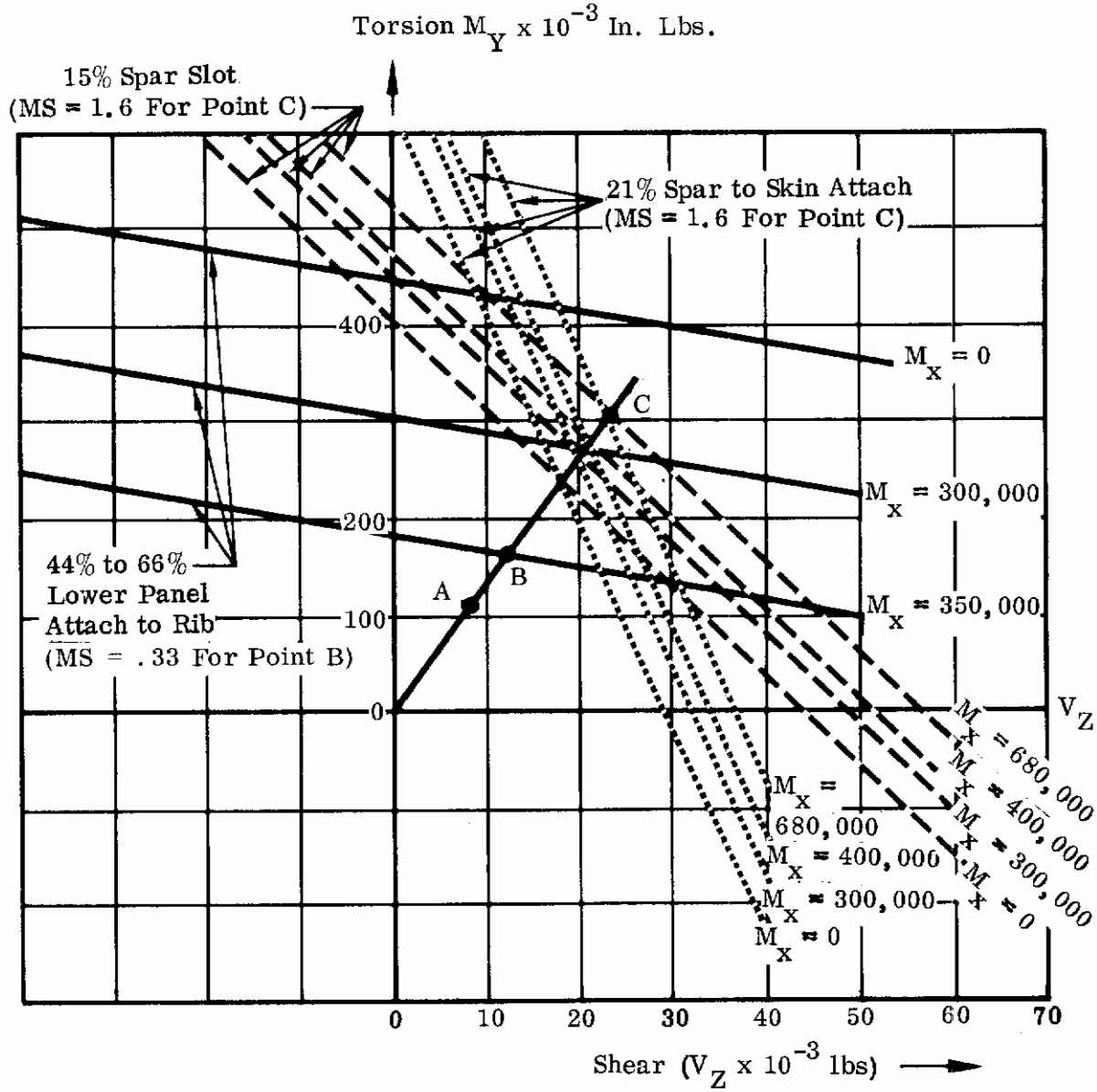

FIGURE 18 TYPICAL F-5A WING STRENGTH ENVELOPE PLOT

Configuration (1) is investigated only for the outboard two wing stations (Figure 16) as the load conditions are not critical for the inboard stations.

2.2.2 Stress Influence Coefficients for the Horizontal Stabilizer and the Fuselage

Stress influence coefficients for the critical horizontal stabilizer elements together with the allowable stresses are presented in Table X. Critical items are determined using a discrete gust condition similar to those used for the wing structure.

TABLE X. STRESS INFLUENCE COEFFICIENTS OF F-5A FIGHTER HORIZONTAL TAIL

Dynamic Stress Index	Type of Stress	Control Point							
		49	50	51	52	53	54	55	56
S-24	(τ)	4,900	-3,970	4,020	-3,240	3,120	-2,510	2,210	-1,790
S-25	(σ)	117,500	117,500	303,100	303,100	488,700	488,700	674,300	674,300

The stress influence coefficients for location S-23 in the fuselage of the F-5A fighter are given in Table XI.

TABLE XI. F-5A FIGHTER FUSELAGE STRESS INFLUENCE COEFFICIENTS FOR LOCATION S-23

Control Point	S.I.C. ($M_{y/F}$)
65	225,000
66	675,000
67	1,041,200
68	1,323,700
69	1,702,500
70	2,177,500

3. Aircraft Transfer Function Computation

The aircraft transfer functions are computed for a number of frequencies within the band of interest. For a gust profile with a specific frequency, the overall aircraft response is computed using a modal approach. The data are then converted into stresses at selected sensitive locations based on the stress influence coefficients described in the previous section.

The dynamic equations used in the response computation are typical matrix equations for a damped elastic system considering aerodynamic forces due to motion and gust. Approximate solutions minimizing the degrees of freedom are obtained applying the Galerkin method. For this purpose, the basic elastic modes of the aircraft are generated, which are used as the normal modes in the response formulation. For a given vertical gust at a discrete frequency, the resulting generalized coordinates yield the aircraft response data.

Several methods are available to determine the elastic mode patterns and the corresponding natural frequencies for the aircraft. In one approach, the collocation method is used which gives the deformation data at the control points. The solution is reached through an iteration scheme. In cases where the control points are too numerous to execute the collocation program efficiently, or the elastic vibration modes for the major sub-assemblies (wing, fuselage, tail surfaces) are available, then the modal approach of the dynamic equations may be used. The elastic mode formulation is essentially a special case of the general dynamic equations where the external excitation terms such as those representing aerodynamic forces are dropped. In this case, the frequency is an unknown parameter to be determined together with the elastic mode pattern.

The equations of motion for the determination of frequency response functions are programmed using both the cantilever and the free-free modal solutions. The frequency response functions are determined for deflection, acceleration, control point load, shear, bending moment, torque, and stress at specified locations.

The following considerations are incorporated in the development of the equations of motion:

1. Lift on wing and tail due to gust penetration, accounting for wing and tail sweep.
2. Lift on a fuselage (slender body) due to gust penetration.

3. Aerodynamic lift on wing and tail due to motion using lifting surface theory. Other aerodynamic theories may be employed (e.g., piston theory) for the derivation of the aerodynamic influence coefficients (AIC's). Hence, Mach number range is not restricted by the formulation of the problem if one uses appropriate AIC's.

4. Aerodynamic lift on fuselage (slender body) due to motion.

5. Items (1) to (4) may be adjusted for wind tunnel or flight aerodynamic data, including wing and tail carryover to the fuselage through the use of weighting matrices.

6. The effect of downwash due to wing lift on tail airloads for either gust or motion terms is accounted for by weighting matrices.

7. Modes of vibration and corresponding frequencies may be modified to provide consistency with ground vibration data.

8. Structural damping may be varied in each mode.

9. Loads may be determined by either the mode acceleration or the mode deflection method.

Typical formulations of the aircraft gust response and mode computation are given in Appendix I.

3.1 Mass Stiffness Model

The aircraft is represented by a system of control point masses with intermediate masses suspended on rigid massless bars connecting the control points which are shown in Figures 2, 10. The control point and intermediate masses are calculated such that the mass and inertia properties of the system are matched with those of the aircraft. The control point and intermediate masses are then used to derive the coupled mass matrix for a dynamically equivalent system. Additional control points with no associated masses are added at locations which are required to correlate the response data with measured flight test data. The elastic axis of the wing is the 35 percent local chord, and the control points are located at the 25 percent and 75 percent local chord locations as shown in Figures 2, 10.

The flexibility matrix is calculated using the elastic energy method for each of the three main sections of the model: left wing panel plus optional pylon-store combination, forward fuselage, and aft fuselage plus horizontal-tail combination.

3.2 Aerodynamics

This subsection describes the approach employed to compute the oscillatory aerodynamic influence coefficients (AIC's). The AIC's relate the control point deflections whose derivatives are the downwash velocities. Aerodynamic forces expressed in terms of AIC's for gust and motion are given in Equations (I-10), (I-11) of Appendix I. The resulting AIC's are functions of planform, Mach number, and reduced frequency.

The AIC's for wing and tail motion are based on lifting surface theory. The basis of the lifting surface theory is found in the aerodynamic integral equation which relates the pressures on the surface to the downwash at the surface. A number of solutions to this integral equation have been proposed by collocation methods. The methods are based on certain approximate treatments of the kernel of the integral equation. In the subsonic range, the kernel of Watkins, Runyan and Woolston is used (Reference 1). The method of solution is based on the expansion of the kernel function into a fifth order power series in reduced frequency and was originated by Runyan and Woolston (References 2, 3 and 4). It consists of adjusting the amplitudes of an assumed series of modes for the pressure corresponding to the downwash produced at the control points by a system of chordwise replacement loads. The AIC's for gust based on lifting surface theory are derived as a modification to Reference 4. This has been accomplished by replacing the substantial derivative operator matrix $V(\partial/\partial x + i\omega/V)$ by the sinusoidal gust operator matrix [exp. (-ikx/b)] and appropriately accounting for the scale factors in the lift equation. The AIC's due to gust are also derived for the wing and tail using the strip theory, Reference 5.

Tail downwash due to wing lift is accounted for (Reference 6). The wing and tail AIC matrices are assumed to be decoupled.

The AIC's for the fuselage and tip tank due to motion are derived from the slender body theory (References 3 and 7). The method employs the momentum theory of Munk and Jones (Reference 8). The disturbance flow

component considered in the momentum computation is two dimensional and is located in a plane normal to the direction of flight. These AIC's are independent of Mach number. The AIC's for the fuselage and tip tank due to gust are also derived using the momentum theory (Reference 9).

The theoretically derived AIC's for all surfaces are modified to agree with measured steady state wind tunnel or flight test spanwise lift and aerodynamic center distributions. This is accomplished by use of the weighting matrices.

3.3 Modal Data for the T-38 Trainer

The natural vibration mode data are obtained theoretically and are checked against the ground vibration data. Table XII gives the modal and frequency data for the T-38 trainer corresponding to configurations (1), (2), and configuration (3). Also listed in the table are the frequencies at which the mode responses are the highest when the aerodynamic forces are considered. This latter frequency is denoted as F_1 and is given at various altitudes corresponding to the design configurations. The detailed mode shapes of the aircraft are plotted in Figure 19 for configurations (1), (2).

3.4 Modal Data for the F-5A Fighter

Similar natural frequency mode data are computed for the F-5A fighter corresponding to various weight and attachment configurations. The frequency and mode description are tabulated in Table XIII. In the table, the frequencies F_1 are also listed at which the mode responses are at their peaks when the aerodynamic forces are considered. The detail flexible mode data are plotted in Figures 20, 21.

3.5 Stress Transfer Function Data

Applying the techniques described in the previous subsections, the stress transfer functions are computed for all the stress sensitive locations for each aircraft corresponding to the various design configurations defined in Section 1. The data, plotted as a function of the gust frequency, are applied in gust design computation using the spectral approach. Since the amplitude and distribution of each transfer function play a dominant role in determining the corresponding spectral data for each stress sensitive location, it is found convenient to present the transfer function data side by side with the corresponding spectral data in the following section.

TABLE XII. THE T-38 TRAINER NATURAL FREQUENCY MODE DATA

CONFIGURATIONS (1), (2)

MODE	F(CPS)	DESCRIPTION OF MOTION	Aeroelastic Modes F_1 (CPS)	
			S. L.	30, 000 Ft.
1	9.49	1st Fuselage Bending - 1st Wing Bending	11.0	10.5
2	12.96	1st Wing Bending - 1st Fuselage Bending	17.5	14.5
3	18.01	1st Horizontal Tail Bending	18.0	19.0
4	26.27	2nd Fuselage Bending - 2nd Wing Bending	26.3	26.3
5	33.0	2nd Wing Bending - 2nd Fuselage Bending	32.2	33.0
6	44.69	1st Wing Torsion	32.2	42.0

CONFIGURATION (3)

MODE	F(CPS)	DESCRIPTION OF MOTION	Aeroelastic Modes F_1 (CPS)
			S. L.
1	8.62	1st Fuselage Bending - 1st Wing Bending	9.0
2	11.97	1st Wing Bending - 1st Fuselage Bending	13.0
3	17.89	1st Horizontal Tail Bending	19.0
4	23.06	2nd Fuselage Bending - 2nd Wing Bending	23.5
5	33.0	2nd Wing Bending - 2nd Fuselage Bending	39.2
6	40.84	1st Wing Torsion	39.2

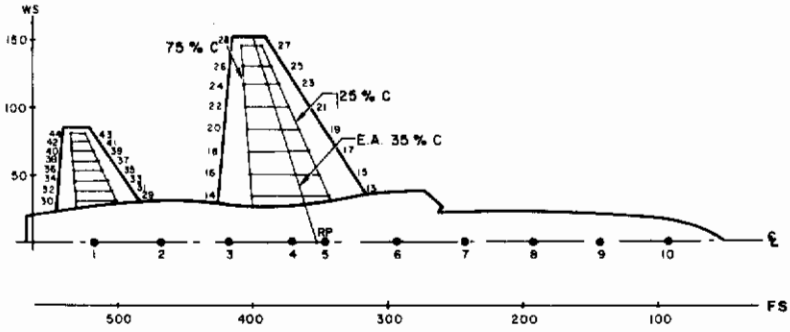

T-38 TRAINER CONTROL POINT GEOMETRY

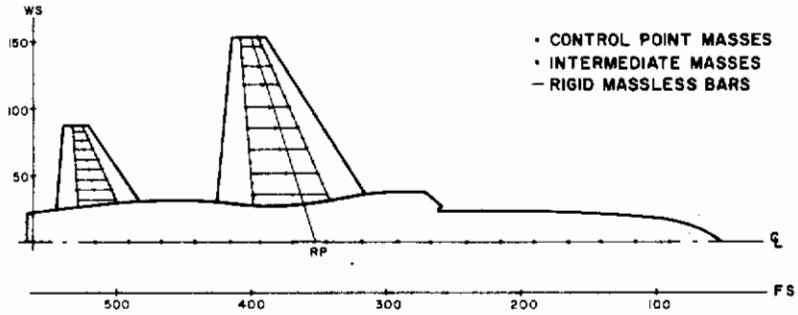

IDEALIZED MASS DISTRIBUTION FOR T-38

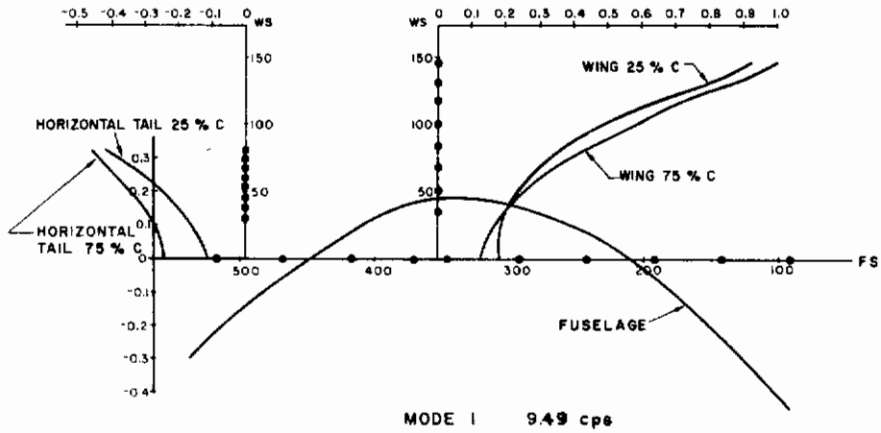

MODE 1 9.49 cps

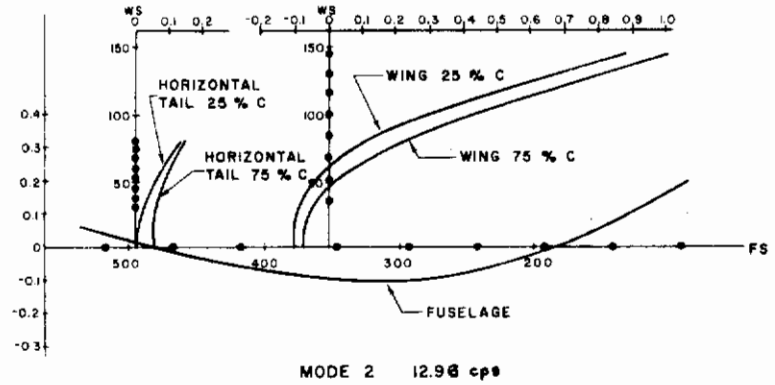

MODE 2 12.96 cps

FIGURE 19 FLEXIBLE MODES FOR THE T-38 TRAINER, CONFIGURATIONS (1), (2)

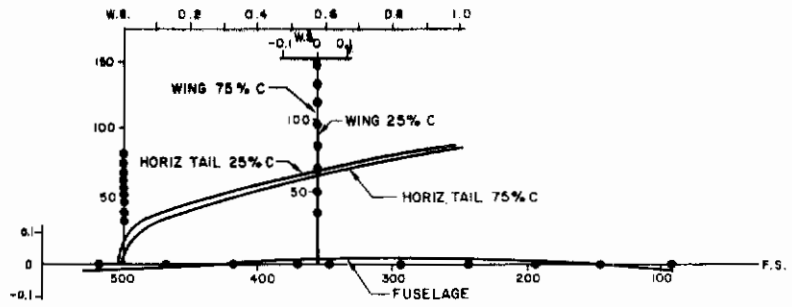

MODE 3 18.01 CPS

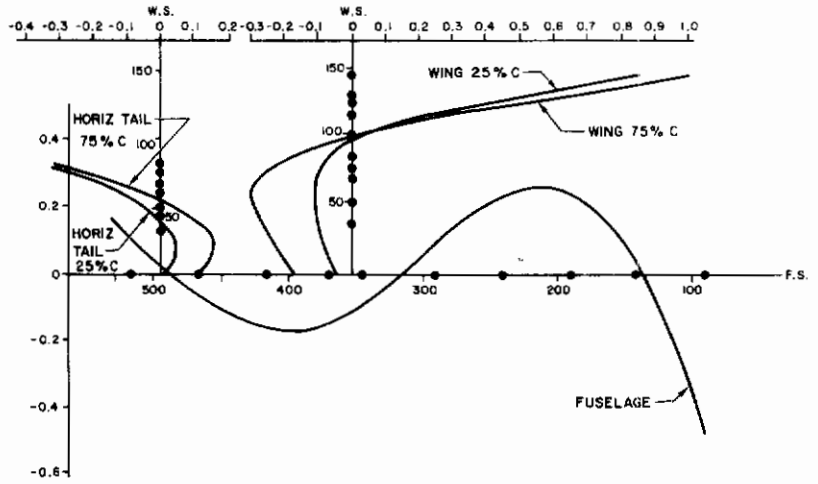

MODE 4 26.27 CPS

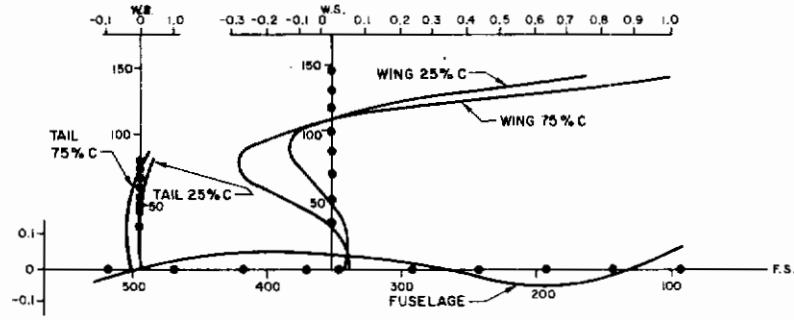

MODE 5 33.00 CPS

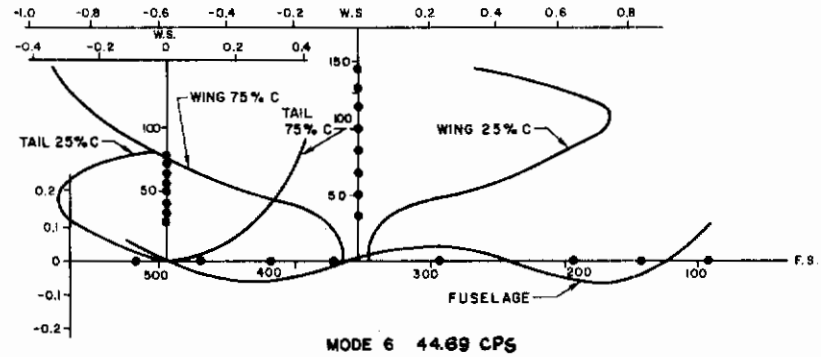

MODE 6 44.69 CPS

FIGURE 19 FLEXIBLE MODES FOR THE T-38 TRAINER, CONFIGURATIONS (1), (2) (CONTINUED)

TABLE XIII. THE F-5A FIGHTER NATURAL FREQUENCY MODE DATA

CONFIGURATIONS (1), (2)

MODE	F(CPS)	DESCRIPTION OF MOTION	Aeroelastic Modes F_1 (CPS)	
			S.L.	30,000 Ft.
1	4.96	Wing 1st Bending, Forward and Aft Fuselage Bending. (Fuselage-Wing out of phase)	5.3	5.3
2	7.00	Wing 1st Torsion-Bending, Aft Fuselage Bending	7.3	7.3
3	8.02	Fuselage Bending, Wing Bending (Fuselage-Wing in phase)	8.5	8.3
4	13.14	Wing 2nd Torsion-Bending, Fuselage 2nd Bending	12.6	13.0
5	15.13	W.S. 85 Store Yaw, Wing 2nd Bending-Torsion	15.1	15.1
6	16.59	Horizontal Tail Bending, Forward Fuselage Bending, Slight Wing Bending	16.6	17.0
7	17.20	Horizontal Tail Bending, Slight Fuselage and Wing Bending	18.0	18.0
8	19.20	Horizontal Tail Bending, Fuselage and Wing Bending-Torsion (all moderate motion)	19.5	19.0
9	22.20	W.S. 85 Store Roll-Yaw, Slight Wing-Fuselage Motion. Forward Fuselage Bending	22.0	22.0

TABLE XIII. THE F-5A FIGHTER NATURAL FREQUENCY MODE DATA (Continued)

CONFIGURATION (3)

MODES	F(CPS)	DESCRIPTION OF MOTION	Aeroelastic Modes F_1 (CPS) S.L.
1	4.31	1st Wing Bending, Fuselage Bending (Wing tip and fuselage nose are out of phase)	4.7
2	6.51	1st Wing Torsion - Bending, Forward Fuselage Bending	8.5
3	7.94	1st Fuselage Bending, Wing Bending (Wing tip and fuselage nose are in phase)	8.5
4	17.0	1st Horizontal Stabilizer Bending	18.0
5	17.32	2nd Wing Bending, Fuselage Bending (Wing tip and fuselage nose are out of phase)	18.6
6	20.54	2nd Fuselage Bending, Wing Bending (Wing tip and fuselage nose are in phase)	21.5
7	30.96	3rd Fuselage (Forward Fuselage) Bending	—
8	34.81	2nd Wing Torsion, Forward Fuselage Bending, Wing Bending (Wing tip and fuselage nose are out of phase)	—

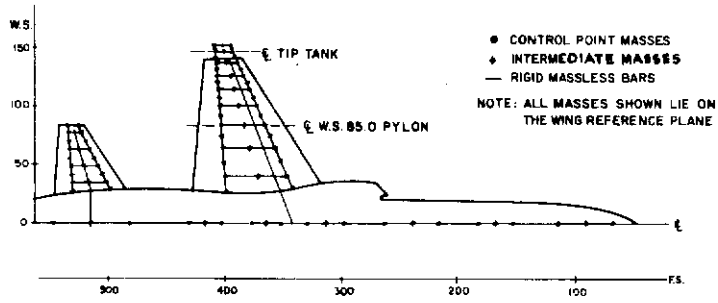

IDEALIZED MASS DISTRIBUTION FOR F-5A CONDITION 397

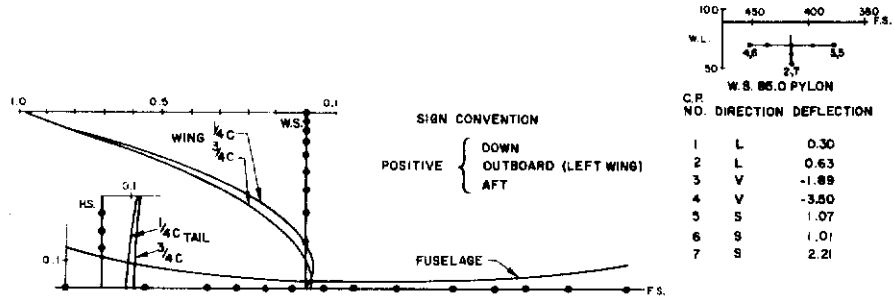

C.P. NO.	DIRECTION	DEFLECTION
1	L	0.30
2	L	0.63
3	V	-1.89
4	V	-3.50
5	S	1.07
6	S	1.01
7	S	2.21

MODE 1 4.96 cps

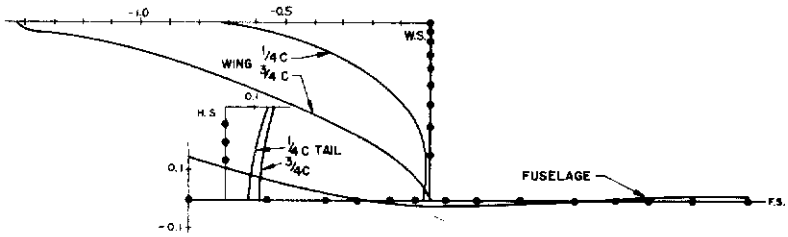

1	L	1.76
2	L	3.70
3	V	1.56
4	V	-8.02
5	S	0.12
6	S	0.10
7	S	0.24

MODE 2 7.00 cps

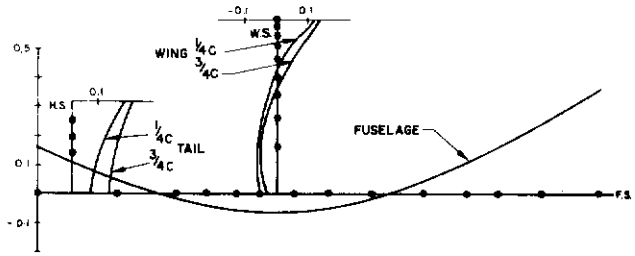

1	L	-0.11
2	L	-0.22
3	V	-0.48
4	V	0.10
5	S	-0.20
6	S	-0.17
7	S	-0.41

MODE 3 8.02 cps

FIGURE 20 FLEXIBLE MODES FOR THE F-5A FIGHTER, CONFIGURATIONS (1), (2)

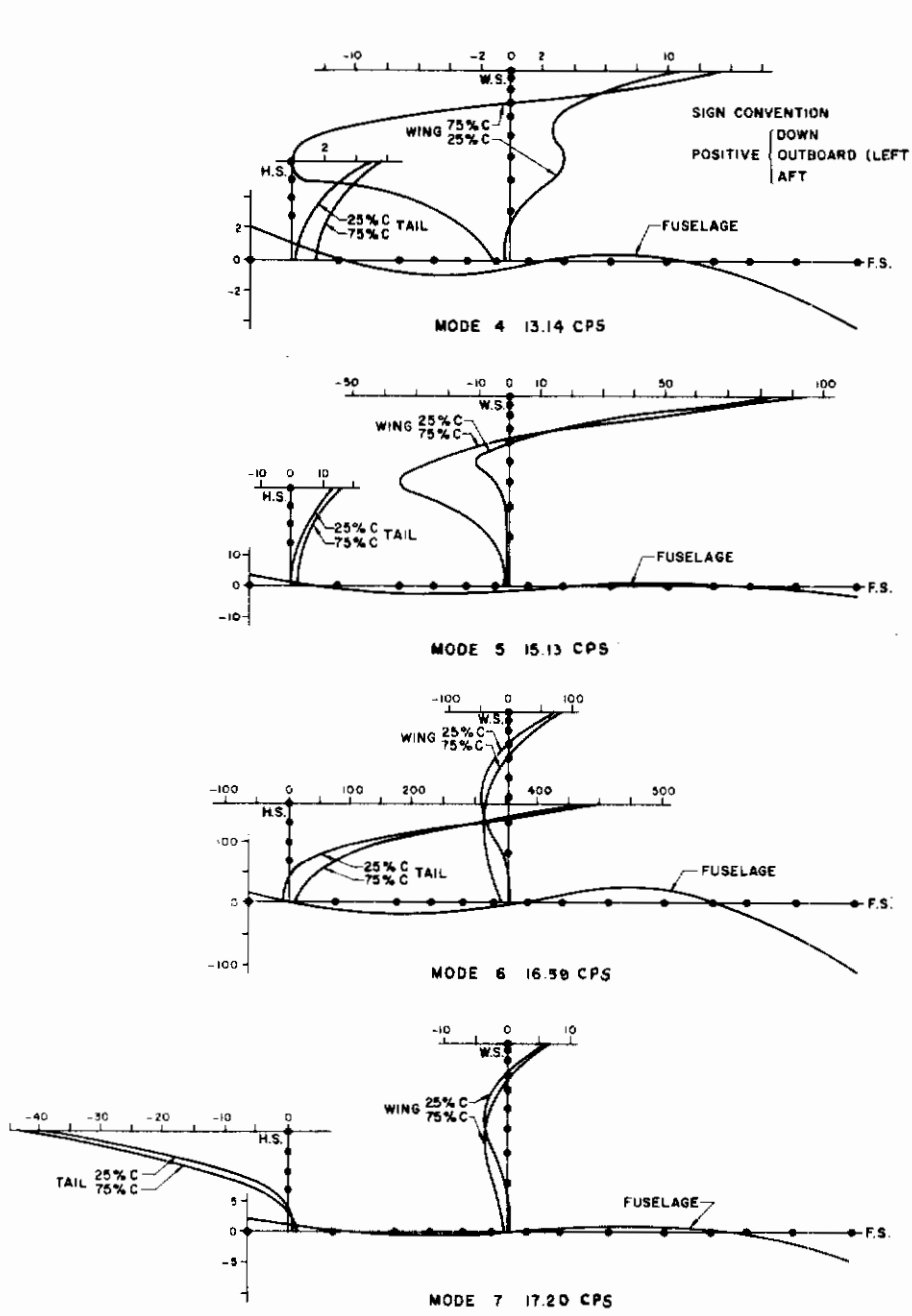

FIGURE 20 FLEXIBLE MODES FOR THE F-5A FIGHTER, CONFIGURATIONS (1), (2) (CONTINUED)

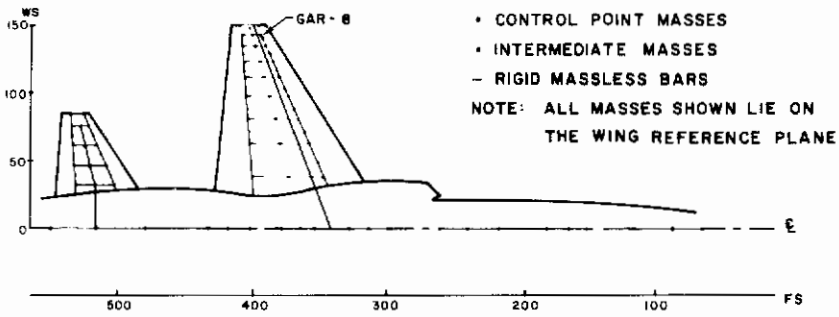

IDEALIZED MASS DISTRIBUTION FOR F-5A CONDITION 489

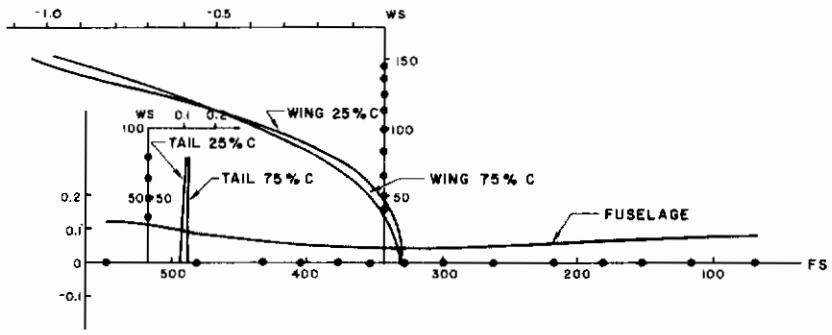

MODE 1 4.31 cps

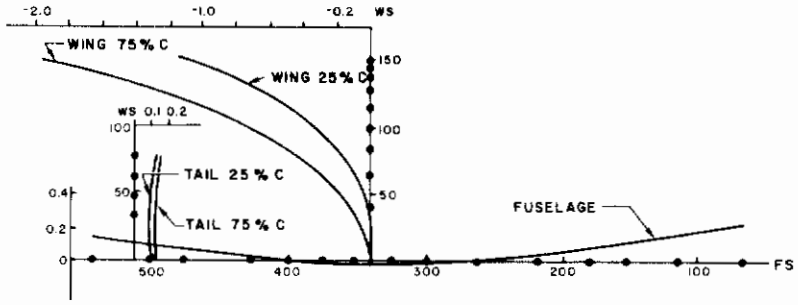

MODE 2 6.51 cps

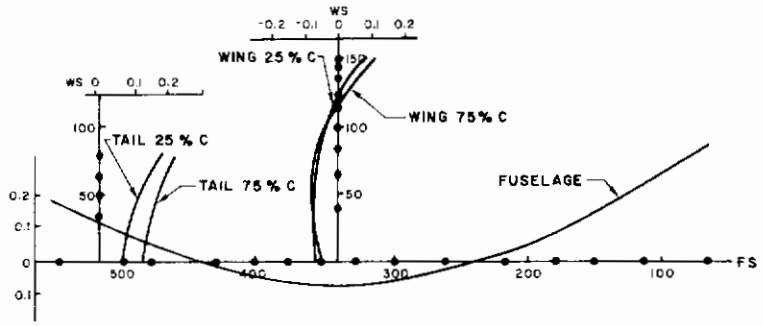

MODE 3 7.94 cps

FIGURE 21 FLEXIBLE MODES FOR THE F-5A FIGHTER, CONFIGURATION (3)

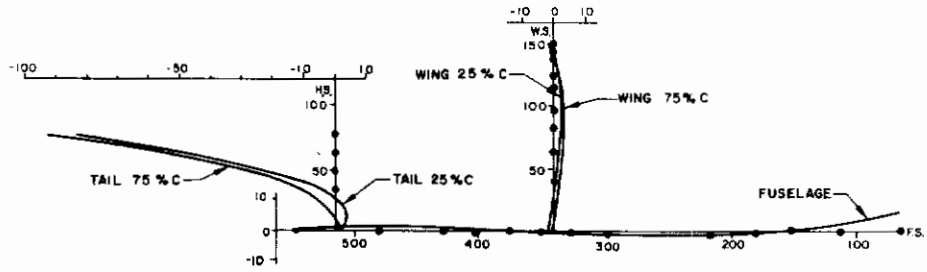

MODE 4 17.00 CPS

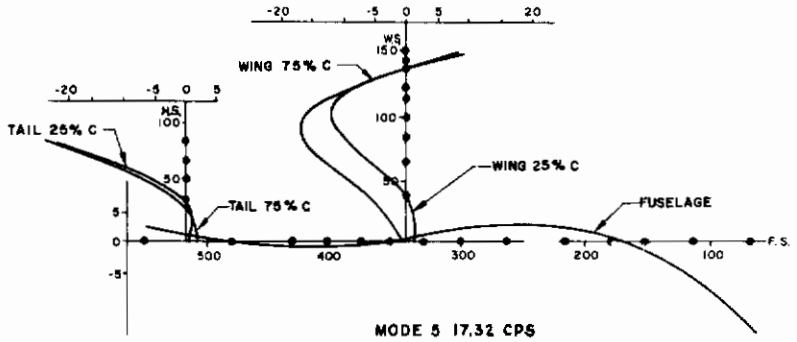

MODE 5 17.32 CPS

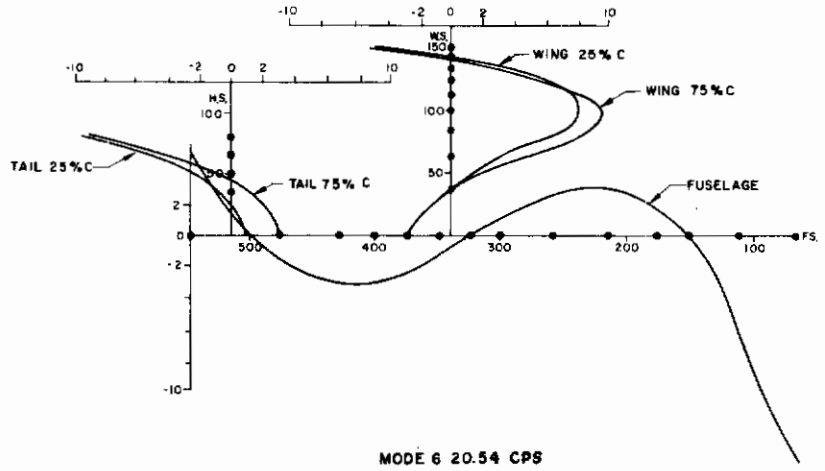

MODE 6 20.54 CPS

FIGURE 21 FLEXIBLE MODES FOR THE F-5A FIGHTER, CONFIGURATION (3) (CONTINUED)

4. Gust Design Computations Using the Power Spectral Approach

The gust design computation presented in this section uses the power spectral approach as described in Reference 10. The basic philosophy behind the spectral approach recognizes the randomness of the air turbulence phenomenon and the random characteristics of the corresponding responses of different aircraft. The gust power spectrum extends along a certain frequency band which may be represented analytically based on the theory of isotropic turbulence using a number of parameters. An aircraft subject to the random gust excitation responds in a highly complicated manner depending on the inherent flexible modes, the aerodynamic and structural damping characteristics, etc. The discrete gust design approach does not take into proper consideration the randomness of the gust data as well as the individual aircraft response characteristics at various frequencies.

In the power spectral approach, the gust response data is processed in a statistical manner to reach a rational gust design procedure considering the overall response along the frequency band, the corresponding stress statistics and the mean rate of zero crossing, etc. The ultimate goal of the approach is to develop a method which can be applied to various aircraft operating under different mission profiles with reasonable uniformity. Specifically, the probabilities of encountering certain levels of air turbulence are considered based on available air data, the flight mission and flight contours, as well as the availability of certain storm-warning devices, etc. In this manner, statistical data representing a composite response of the aircraft may be obtained. The computation given in the present report represents a preliminary step toward this goal.

4.1 Gust and Response Power Spectra

The gust spectrum used in the computation is the von Kármán spectrum based on isotropic turbulence. The actual fit of the von Kármán spectrum with available empirical gust data will be discussed in a latter section of the report. The autocorrelation function of the gust is in this case:

$$R(r) = \sigma_w^2 \frac{\sqrt[3]{4}}{\Gamma(1/3)} \left(\frac{r}{1.339L}\right)^{1/3} \left[K_{1/3}\left(\frac{r}{1.339L}\right) - \frac{1}{2}\left(\frac{r}{1.339L}\right) K_{2/3}\left(\frac{r}{1.339L}\right)\right] \quad (4\text{-}1)$$

where r is the space coordinate, σ_w^2 is the mean square of the vertical gust, L is the scale of turbulence, $K_{1/3}(x)$ and $K_{2/3}(x)$ are the modified Bessel functions of the second kind. The corresponding gust power spectrum is:

$$\Phi_w(\Omega) = \frac{\sigma_w^2 L}{\pi} \frac{1 + \frac{8}{3}(1.339L\,\Omega)^2}{\left[1 + (1.339L\,\Omega)^2\right]^{11/6}} \tag{4-2}$$

where $\Omega = \frac{2\pi}{\lambda}$ is the spatial frequency where λ is the gust component wave length. With regard to other empirical curve fit formulas, some remarks are in order. Fundamental considerations of turbulent fluid mechanics strongly favor the von Kármán spectrum. From the results of homogeneous, isotropic turbulence theory, the $\Omega^{-5/3}$ behavior of the (wave number-energy) spectrum at high wave numbers is valid for any turbulent motion at sufficiently high Reynolds numbers. This is based on the universal equilibrium hypotheses of Kolmogoroff (Reference 11) and depends only on dimensional arguments, using length and velocity scales appropriate to the dissipation range of the energy spectrum. The required conditions are well fulfilled for the meteorological scale of turbulence and Reynolds numbers for much of the Ω range under consideration.

In the gust design using the power spectral approach, after the gust spectrum has been defined, the stress frequency response functions $H(\Omega)$ are generated as explained in Section 3. The power spectrum of the stress response is given as:

$$\Phi_{x,w}(\Omega) = |H(\Omega)|^2 \Phi_w(\Omega) \tag{4-3}$$

If for a specific patch of gust where the power spectrum is defined as $\Phi_n(\Omega)$ and the mean velocity σ_n, then the rms value of the aircraft response x is:

$$\sigma_{x,n} = \left[\int_0^\infty |H(\Omega)|^2 \Phi_n(\Omega)\, d\,\Omega\right]^{1/2} = \bar{A}\sigma_n \tag{4-4}$$

where

$$\bar{A} = \left[\frac{\int_0^\infty |H(\Omega)|^2 \Phi_n(\Omega)\, d\,\Omega}{\int_0^\infty \Phi_n(\Omega)\, d\,\Omega}\right]^{1/2} \tag{4-5}$$

In order to account for the frequency at which the aircraft exceeds a certain stress level per unit flying distance, the statistical distributions of the gust and the response have to be considered. For instance, the probabilities of encountering certain levels of air turbulence are considered based on available meteorological data, the flight missions and flight contours, the availability of certain storm-warning devices, etc. In this manner, a composite response of the aircraft may be obtained.

For each individual patch of turbulence, a Gaussian distribution is assumed. The number of peaks per unit distance for a specific patch is given as:

$$G_n(w) = G_o e^{-(w^2/2\sigma_n^2)} = \frac{1}{2\pi\sigma_n}\left[\int_o^\infty \Omega^2 \Phi_n(\Omega)\, d\Omega\right]^{1/2} e^{-(w^2/2\sigma_n^2)} \qquad (4\text{-}6)$$

where

$$\sigma_n^2 = \int_o^\infty \Phi_n(\Omega)\, d\,\Omega \qquad (4\text{-}7)$$

In the above integrations, the upper limit of integration is infinity; for practical purposes, the integrations are carried out to an appropriate limit depending on the range of the gust response power spectrum. Consider a continuous variation of the rms value of σ_n, corresponding to an infinite number of patches each of which has the probability of $p(\sigma_n)$ of being encountered during the life span of the aircraft, then the number exceeding a certain gust level w per unit flying distance is called G(w). The value of G(w) for a specific flying altitude is given

$$G(w) = G_o \int_o^\infty p(\sigma)\, e^{-(w^2/2\sigma^2)}\, d\sigma \qquad (4\text{-}8)$$

Furthermore, assuming Gaussian distribution for the response amplitude of the aircraft, the mean number of response peaks exceeding a certain level x per unit flight distance in the nth gust patch is:

$$N_n(x) = \frac{1}{2\pi\sigma_{x,n}}\left[\int_o^\infty \Omega^2 |H(\Omega)|^2 \Phi_n(\Omega)\, d\Omega\right]^{1/2} e^{-(x^2/2\sigma_{x,n}^2)} = N_o\, e^{-(x^2/2\sigma_{x,n}^2)} \qquad (4\text{-}9)$$

so that

$$N_o = \frac{1}{2\pi}\left[\frac{\int_o^\infty \Omega^2 |H(\Omega)|^2 \Phi_n(\Omega)\, d\Omega}{\int_o^\infty |H(\Omega)|^2 \Phi_n(\Omega)\, d\Omega}\right]^{1/2} \tag{4-10}$$

The mean number of peaks exceeding a certain level x per unit flight distance at a certain altitude h during the life of the aircraft is:

$$N(x) = N_o \int_o^\infty p(\sigma)\, e^{-(x^2/2\sigma^2\bar{A}^2)}\, d\sigma \tag{4-11}$$

which may be plotted as generalized curves for each major aircraft modification in the following form:

$$\frac{N}{N_o} = f\left(\frac{x}{\bar{A}}, h\right) \tag{4-12}$$

Subsection 4.2 illustrates an important class of curves (4-12) for the case of the T-38 trainer.

In the above approach, it is assumed that both the gust in a specific patch and the response level of the aircraft have Gaussian distributions so that the number of exceedances can be computed explicitly to give an acceptable probability of failure.

In the gust computation data presented below, the independent variable $f = V/\lambda$ (cps) is used instead of the spatial frequency Ω. In order to reconcile the differences, $\Phi(\Omega)$ as discussed above, is multiplied by $\Omega/f = 2\pi/V$ to obtain $\Phi(f)$. $H(\Omega)$ is identical to $H(f)$. The other quantities are essentially unchanged. Furthermore, throughout the numerical process, a parametric cutoff frequency f_{co} is used for the upper limit of integration. Thus, instead of Equations (4-5), (4-10), the following equations are used in the computation:

$$\bar{A} = \left[\frac{\int_o^{f_{co}} |H(f)|^2 \Phi_n(f)\, df}{\int_o^\infty \Phi_n(f)\, df}\right]^{1/2} \tag{4-13}$$

$$N_o = \left[\frac{\int_o^{f_{co}} |H(f)|^2 \Phi_n(f) f^2 \, df}{\int_o^{f_{co}} |H(f)|^2 \Phi_n(f) \, df} \right]^{1/2} \qquad (4\text{-}14)$$

4.2 T-38 Trainer Gust Computation Data

Based on the von Kármán gust spectrum, the mean amplitude and frequency response values $\bar{A}$ and N_o are computed for all the stress sensitive locations listed in Table IV and corresponding to three design configurations defined in Section 1. For the input gust spectrum, four (4) scales of turbulence are used, i.e., L = 500 feet, 1000 feet, 3000 feet, and 5000 feet. A brief summary of the more critical stress elements for L = 500 feet is given in Table XIV.

TABLE XIV. CRITICAL STRESS ELEMENTS FOR T-38 TRAINER

CONFIGURATION	$(x/\bar{A})_{minimum}$	STRESS ELEMENT FOR $(x/\bar{A})_{minimum}$	ADDITIONAL CRITICAL ELEMENTS
(1)	41 fps	S-1: Tension Failure of lower longeron at F.S. 284: σ_c applied	S-2, S-5, S-13
(2)	92 fps	S-1: Tension failure of lower longeron at F.S. 284: σ_c applied	S-5, S-8 S-9, S-12 S-14
(3)	68 fps	S-1: Tension failure of lower longeron at F.S. 284: σ_c applied	S-2, S-5 S-13, S-15

Configuration (1)

The computed data are presented in three groups corresponding to the three design configurations. Starting with Configuration (1), Table XV gives the computed $\bar{A}$, N_o and $(x/\bar{A})$ data for all stress sensitive locations and corresponding to the four (4) scales of turbulence listed above. An arbitrary cutoff frequency (48.4 cps) has been chosen based on the spread of the flexible modes of the aircraft. In Figure 22,

TABLE XV. MEAN AMPLITUDE AND FREQUENCY DATA, T-38 TRAINER, CONFIGURATION (1)

f_{co} = 48.4 cps

STRESS INDEX	IBM INDEX I	$\bar{A}$				N_o (cps)				$x \cdot \bar{A}$ ~ NON-INTERACTING			
		L = 500 ft.	L = 1000 ft.	L = 3000 ft.	L = 5000 ft	L = 500 ft.	L = 1000 ft	L = 3000 ft.	L = 5000 ft	L = 500 ft.	L = 1000 ft.	L = 3000 ft.	L = 5000 ft.
1	46	2978	2365	1705	1471	10.41	10.31	10.28	10.27	41.0	51.6	71.6	82.9
2	47	52.76	41.84	30.14	26.00	19.68	19.53	19.48	19.47	80.88	102.0	141.6	164.1
3	21	71.49	57.25	41.68	36.03	18.45	18.14	17.89	17.85	161.3	201.5	276.7	320.1
4	22	293.5	237.5	174.2	150.7	5.62	5.48	5.37	5.35	146.5	181.0	246.9	285.3
5	23	311.5	252.1	184.9	160.0	5.63	5.48	5.37	5.35	92.0	113.7	155.1	179.2
6	24	339.1	274.2	200.9	173.9	6.35	6.18	6.07	6.04	119.0	147.1	200.7	232.0
7	25	84.55	67.03	48.40	41.75	25.05	24.86	24.74	24.71	291.8	368.0	509.6	590.4
8	26	291.3	235.5	172.6	149.4	6.35	6.18	6.07	6.04	98.42	121.7	166.1	191.9
9	39	193.5	155.8	113.8	98.41	13.62	13.51	13.29	13.25	93.03	115.5	158.2	182.9
10	40	56.84	45.8	33.46	28.94	12.67	12.38	12.17	12.14	198.2	246.0	336.7	389.4
11	41	219.9	177.1	129.3	111.8	13.82	13.51	13.29	13.25	166.8	207.1	283.6	327.9
12	42	174.4	140.1	102.1	88.26	17.48	17.13	16.88	16.84	106.3	132.3	181.5	210.0
13	43	62.34	49.43	35.70	30.81	25.19	25.01	24.87	24.85	138.0	174.0	240.9	279.1
14	44	137.9	110.7	80.71	69.78	17.48	17.13	16.88	16.84	123.3	153.5	210.6	243.6

the mean frequency N_o is plotted versus the nominal velocity $(x/\bar{A})$ for all stress sensitive locations on a semilog scale. Essentially, $(x/\bar{A})$ is a ratio between the local allowable stress x and the rms response at the same location due to a gust spectrum of unit rms velocity. The ratio is a measure of the capacity of the local structure to stand a composite mean gust of certain intensity. Analytically, consider a particular composite rms gust velocity σ_c experienced a fraction P of the service lift. Substituting the probability function:

$$p(\sigma) = \frac{P}{\sigma_c}\sqrt{\frac{2}{\pi}}\, e^{-\frac{\sigma^2}{2\sigma_c^2}} \qquad (4\text{-}15)$$

into Equation (4-11) yields the mean rate of exceedance of an allowable stress x:

$$N(x) = P N_o e^{-\frac{x}{\sigma_c \bar{A}}} \qquad (4\text{-}16)$$

Equation (4-16) can be rewritten as:

$$\ln\left[\frac{N_o P}{N(x)}\right] = \frac{1}{\sigma_c}\left(\frac{x}{\bar{A}}\right) \qquad (4\text{-}17)$$

For a given N(x) value determined according to design requirement, etc., Equation (4-17) as plotted in semilog scale on Figure 22 defines a straight line with slope $(1/\sigma_c)$. The straight line establishes a criterion for the aircraft to withstand a certain composite rms gust velocity level. All stress members with equal exceedance rates N(x) lie on the straight line. All underdesigned members are plotted above this line, while the overdesigned members are below this line. It is understood that the line plotted on Figure 22 representing Equation (4-17) is arbitrary and is for illustrative purposes only.

Figures 23-26 include plots of transfer functions, mean response $\bar{A}$ and mean zero crossing data N_o versus the frequency. The four (4) figures are for stress sensitive locations S-1, S-2, S-5, and S-13. The data are selected either because they are most critical stresswise or due to some special interest in the response behavior.

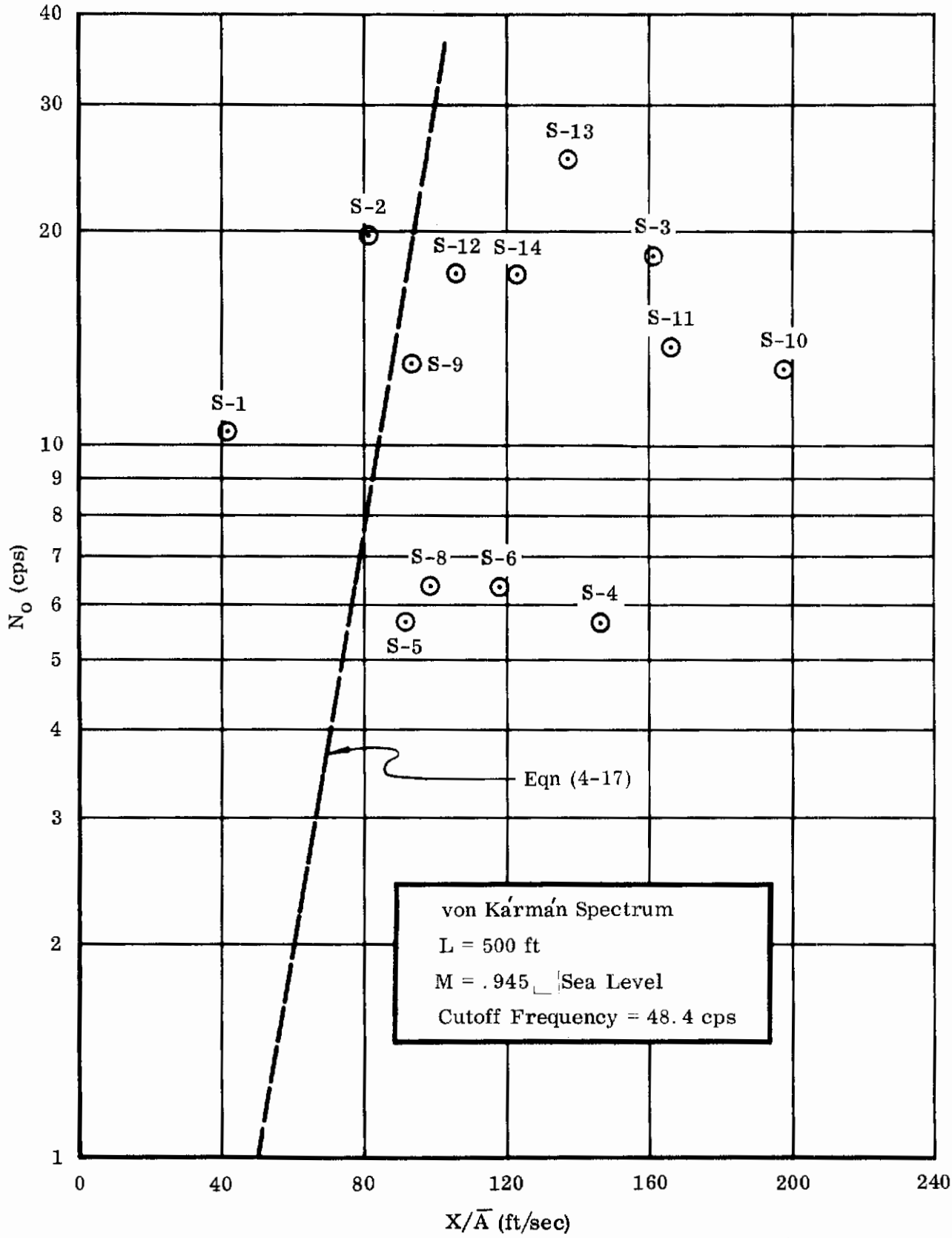

FIGURE 22 T-38 TRAINER RESPONSE DATA, CONFIGURATION (1)

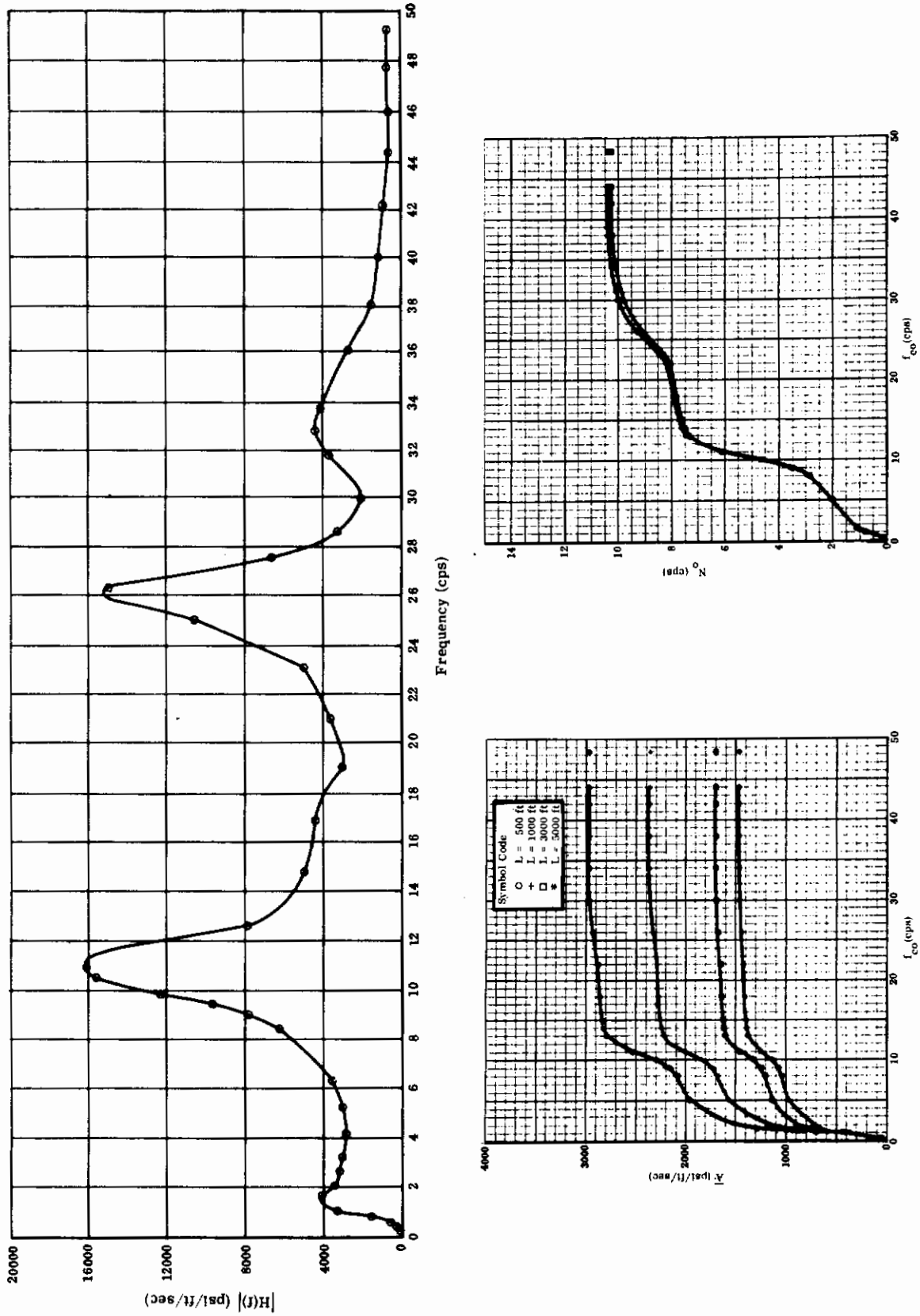

FIGURE 23 TRANSFER FUNCTION H(f), $\bar{A}$ AND N_o DATA FOR S-1, T-38 TRAINER, CONFIGURATION (1)

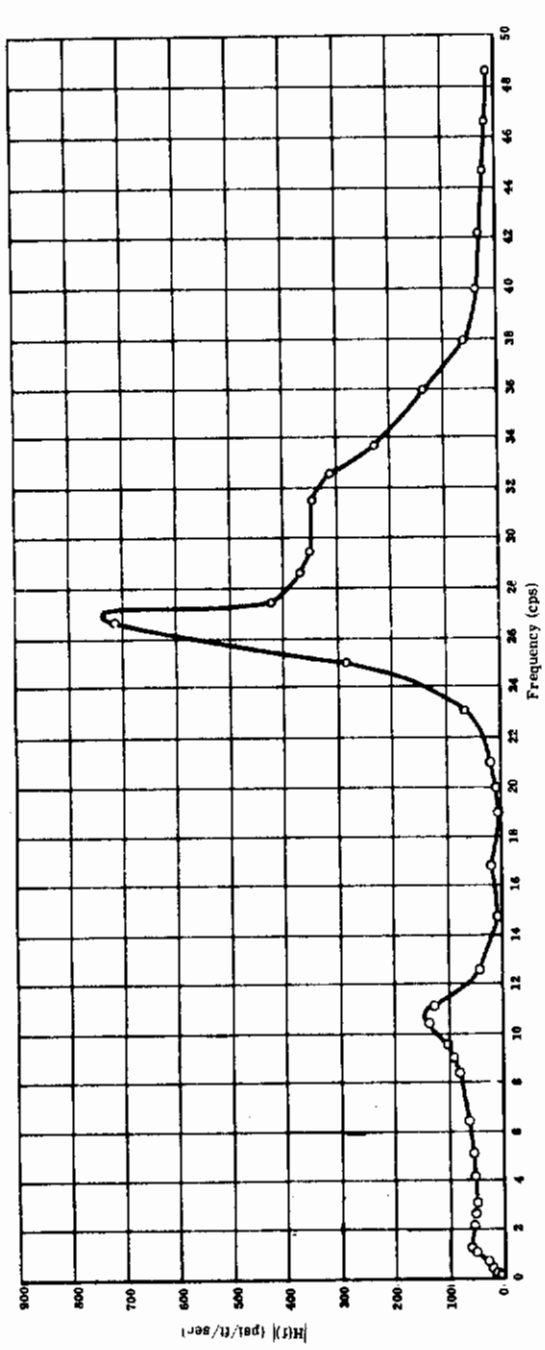

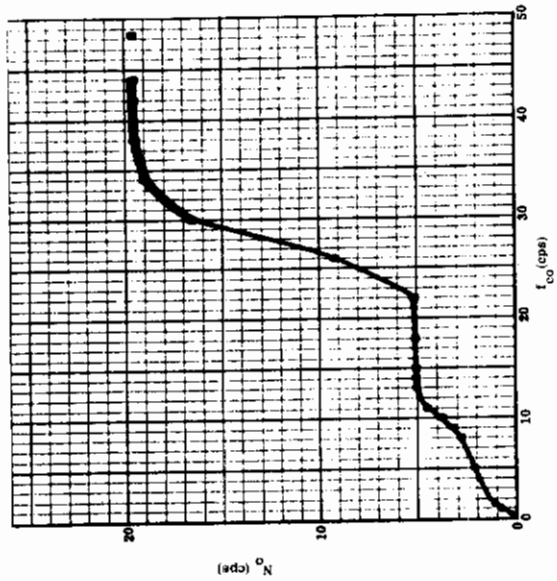

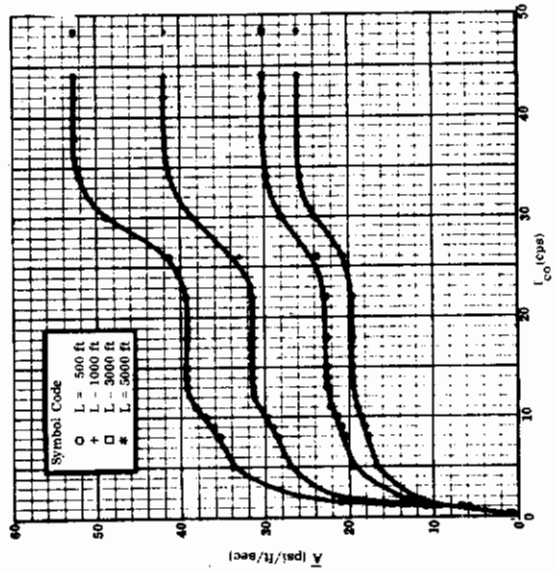

FIGURE 24 TRANSFER FUNCTION H(f), $\overline{A}$ AND N_o DATA FOR S-2, T-38 TRAINER, CONFIGURATION (1)

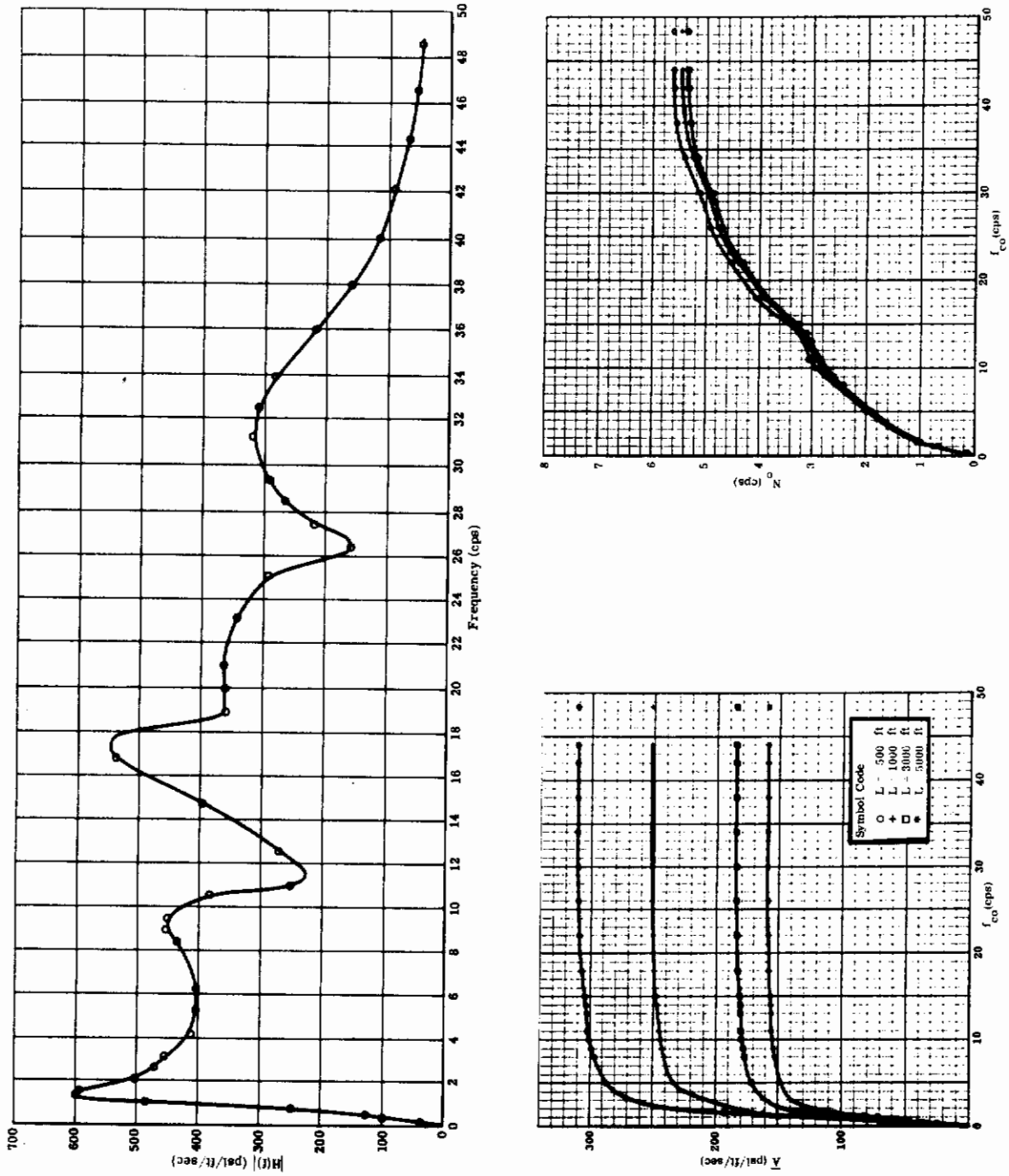

FIGURE 25 TRANSFER FUNCTION H(f), $\bar{A}$ AND N_o DATA FOR S-5, T-38 TRAINER, CONFIGURATION (1)

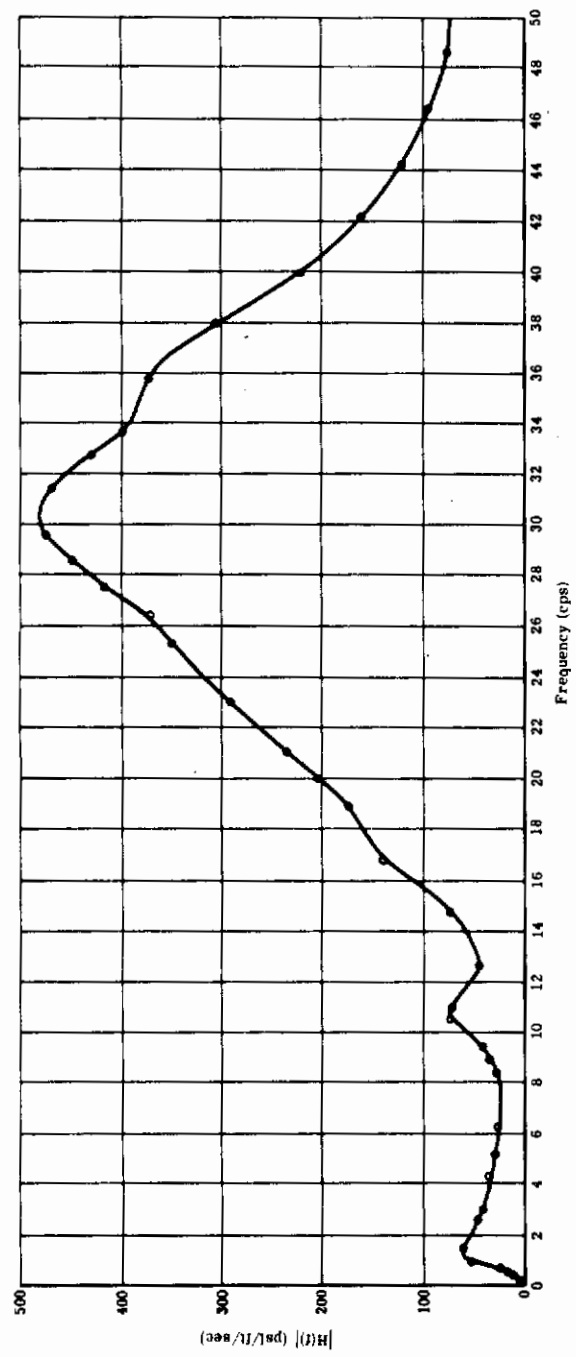

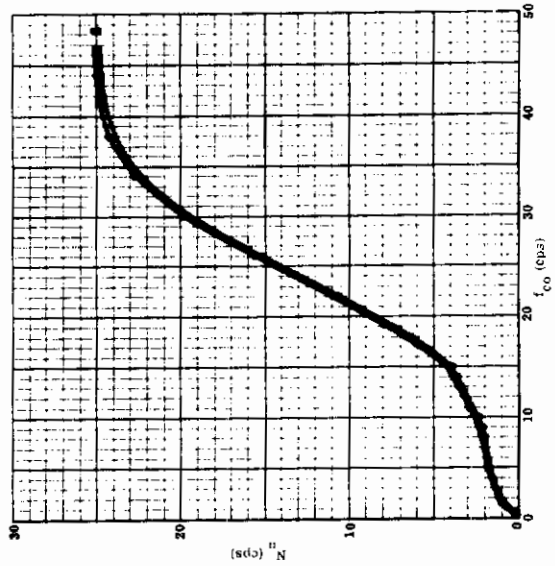

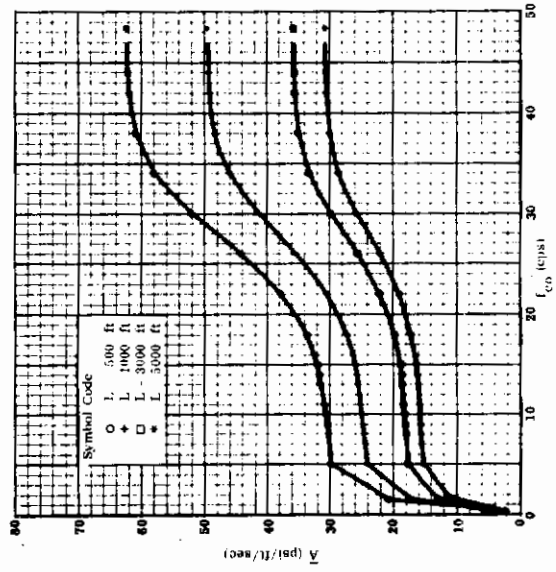

FIGURE 26 TRANSFER FUNCTION H(f), $\bar{A}$ AND N_o DATA FOR S-13, T-38 TRAINER, CONFIGURATION (1)

In the following pages, similar gust response data are plotted and tabulated for the T-38 trainer corresponding to configurations (2) and (3). Figure 27 is the overall response plot for configuration (2). For the same configuration, Table XVI gives the detailed $\bar{A}$ and N_o, $(x/\bar{A})$ data for various scales of turbulence. Figures 28-33 give the transfer functions as well as $\bar{A}$ and N_o plotted against the cut-off frequency (f_{co}) for the more critical locations of the aircraft.

For configuration (3) of the T-38 trainer, Figure 34 gives the overall response data. The detailed $\bar{A}$, N_o and $(x/\bar{A})$ data are tabulated in Table XVII, while the stress transfer functions as well as the $\bar{A}$ and N_o versus f_{co} data are plotted in Figures 35-39.

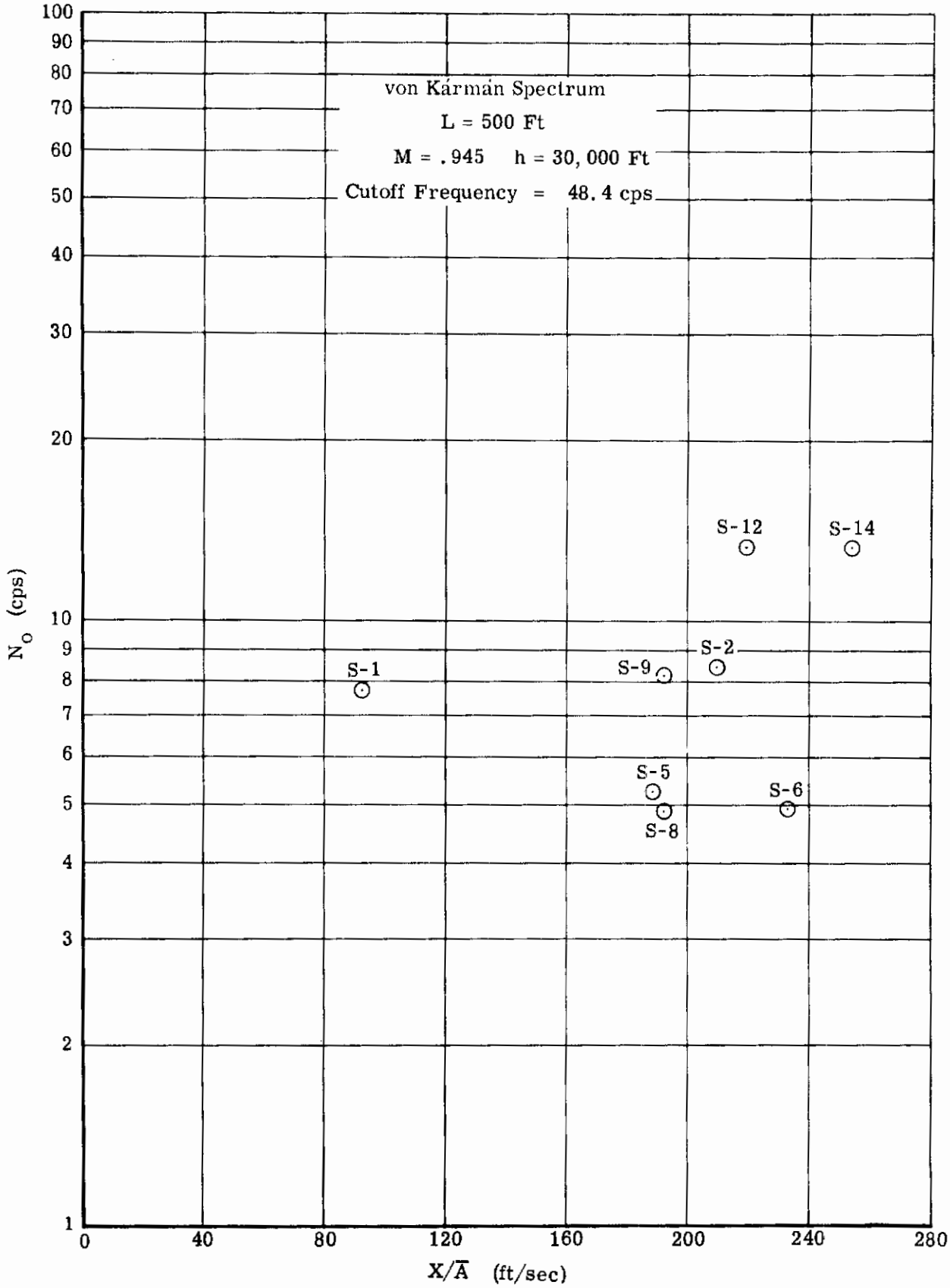

FIGURE 27 T-38 TRAINER RESPONSE DATA, CONFIGURATION(2)

TABLE XVI. MEAN AMPLITUDE AND FREQUENCY DATA, T-38 TRAINER, CONFIGURATION (2)

f_{co} = 48.4 cps

STRESS INDEX	IBM INDEX I	$\bar{A}$				N_o (cps)				$x/\bar{A}$ ~ NON-INTERACTING			
		L = 500 ft.	L = 1000 ft.	L = 3000 ft.	L = 5000 ft.	L = 500 ft.	L = 1000 ft.	L = 3000 ft.	L = 5000 ft.	L = 500 ft.	L = 1000 ft.	L = 3000 ft.	L = 5000 ft.
1	46	1325	1066	777.6	665	7.74	7.57	7.52	7.51	92.13	114.6	157.0	183.5
2	47	20.29	16.41	12.00	10.27	8.43	8.21	8.13	8.12	210.3	260.0	355.7	415.5
3	21	25.67	20.97	15.48	13.27	7.57	7.28	7.14	7.12	450.2	549.9	744.9	868.9
4	22	143.1	117.4	86.74	74.36	5.23	5.02	4.93	4.91	300.5	366.1	495.8	578.3
5	23	151.9	124.6	92.06	78.92	5.23	5.03	4.93	4.91	188.7	230.0	311.4	363.2
6	24	173.5	142.2	104.9	89.95	4.89	4.69	4.61	4.60	232.5	283.7	284.4	446.4
7	25	25.12	20.42	15.00	12.85	19.18	18.56	18.29	18.26	982.1	1208	1644	1919
8	26	149.0	122.1	90.14	77.26	4.89	4.69	4.61	4.60	192.4	234.7	318.0	371.0
9	39	93.55	76.68	56.58	48.50	8.17	7.84	7.69	7.68	192.4	234.7	318.1	371.2
10	40	27.11	22.24	16.41	14.07	5.71	5.47	5.37	5.36	415.6	506.7	686.4	800.8
11	41	106.3	87.14	64.29	55.11	8.17	7.84	7.69	7.68	344.9	420.8	570.3	665.3
12	42	84.20	68.80	50.69	43.44	13.40	12.90	12.68	12.65	220.1	269.4	365.6	426.6
13	43	247.8	19.91	14.55	124.6	27.37	26.80	26.55	26.52	347.1	432.0	590.9	690.2
14	44	66.57	54.39	40.08	34.35	13.40	12.90	12.68	12.65	255.4	312.5	424.2	494.9

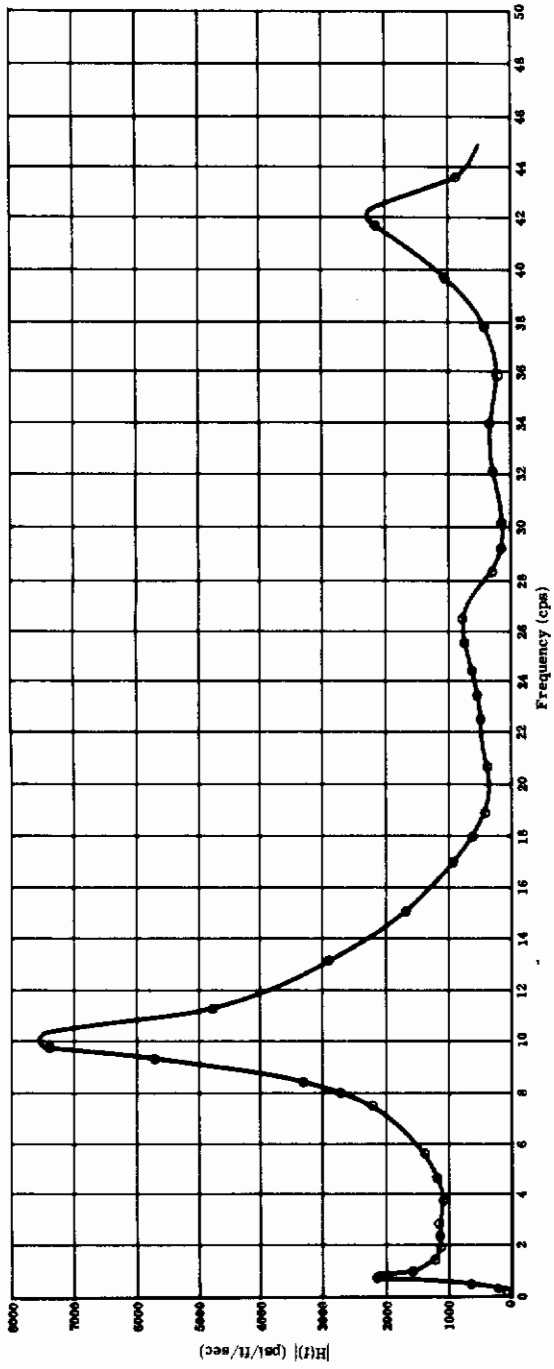

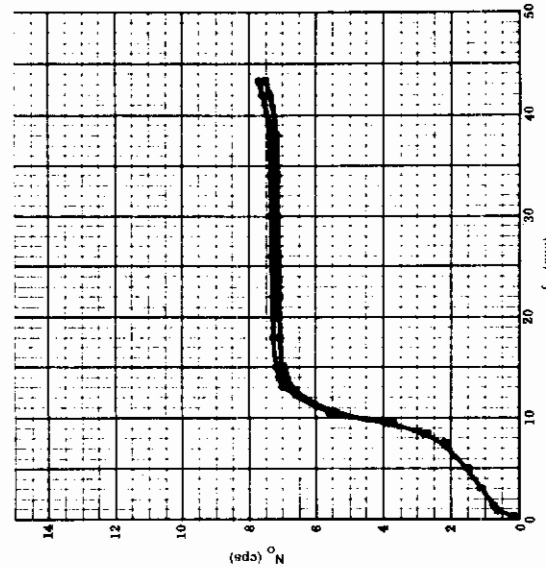

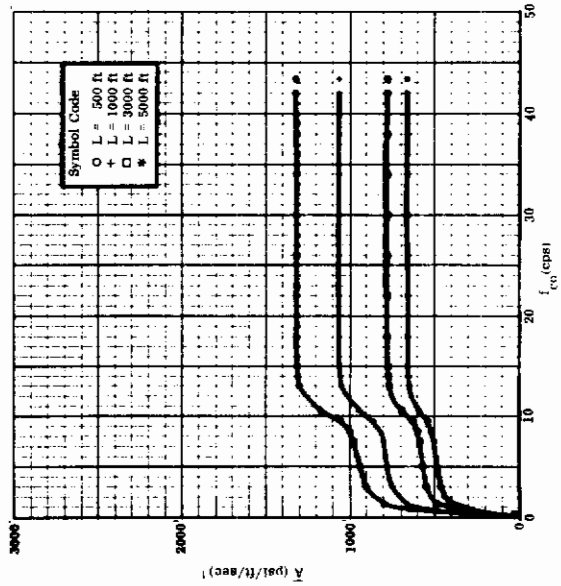

FIGURE 28 TRANSFER FUNCTION H(f), $\bar{A}$ AND N_o DATA FOR S-1, T-38 TRAINER, CONFIGURATION (2)

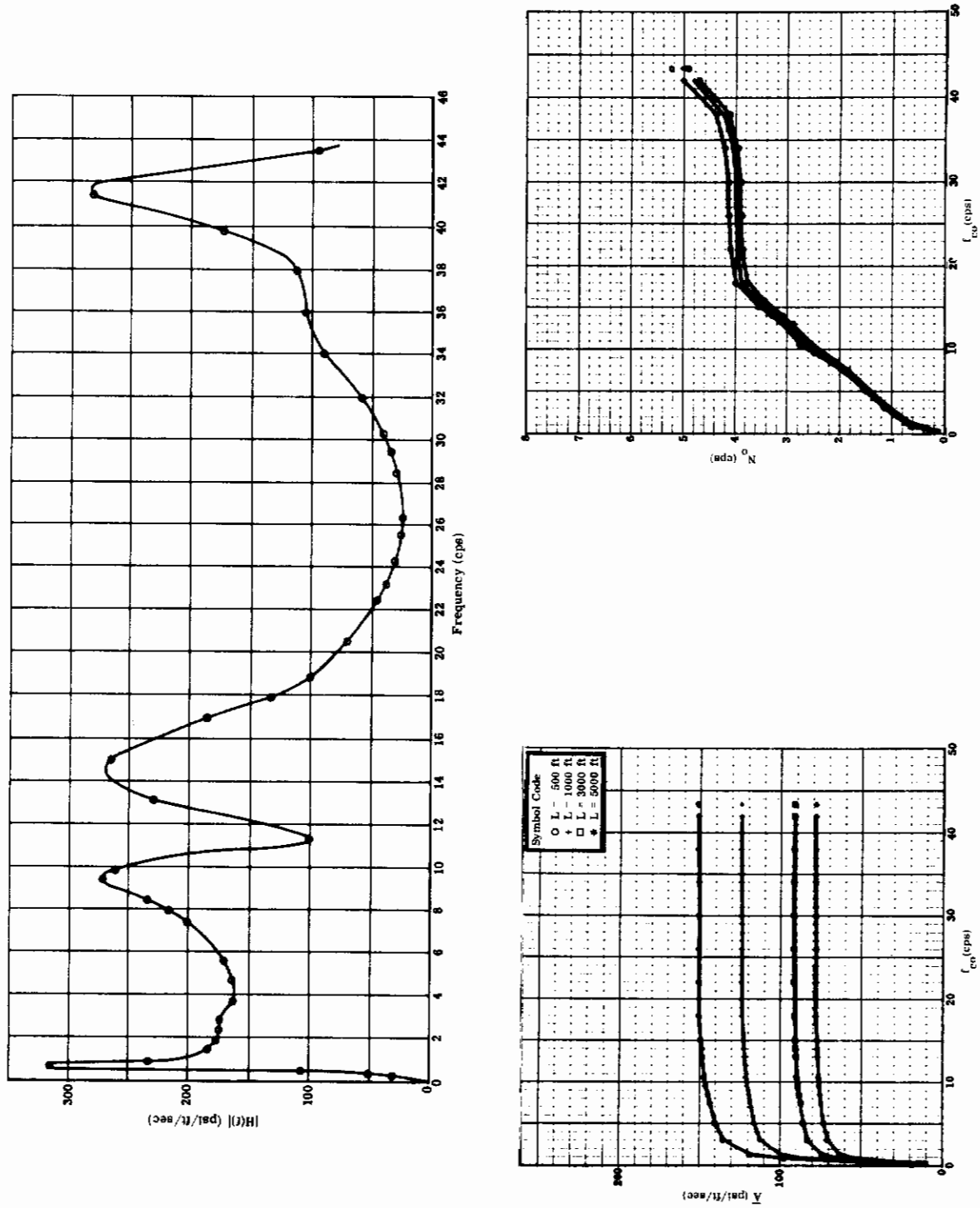

FIGURE 29 TRANSFER FUNCTION H(f), $\overline{A}$ AND N_o DATA FOR S-5, T-38 TRAINER, CONFIGURATION (2)

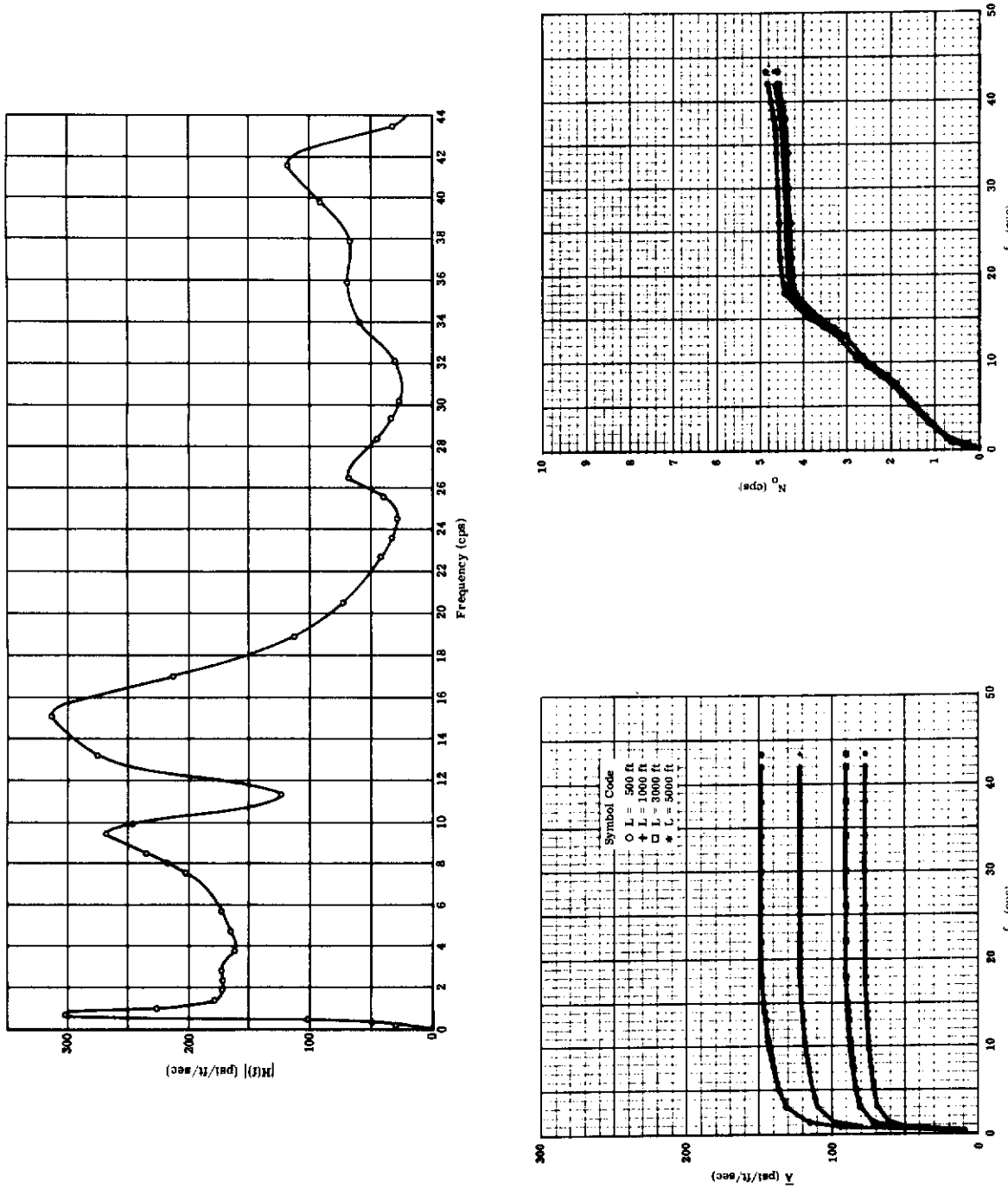

FIGURE 30 TRANSFER FUNCTION H(f), $\bar{A}$ AND N_o DATA FOR S-8, T-38 TRAINER, CONFIGURATION (2)

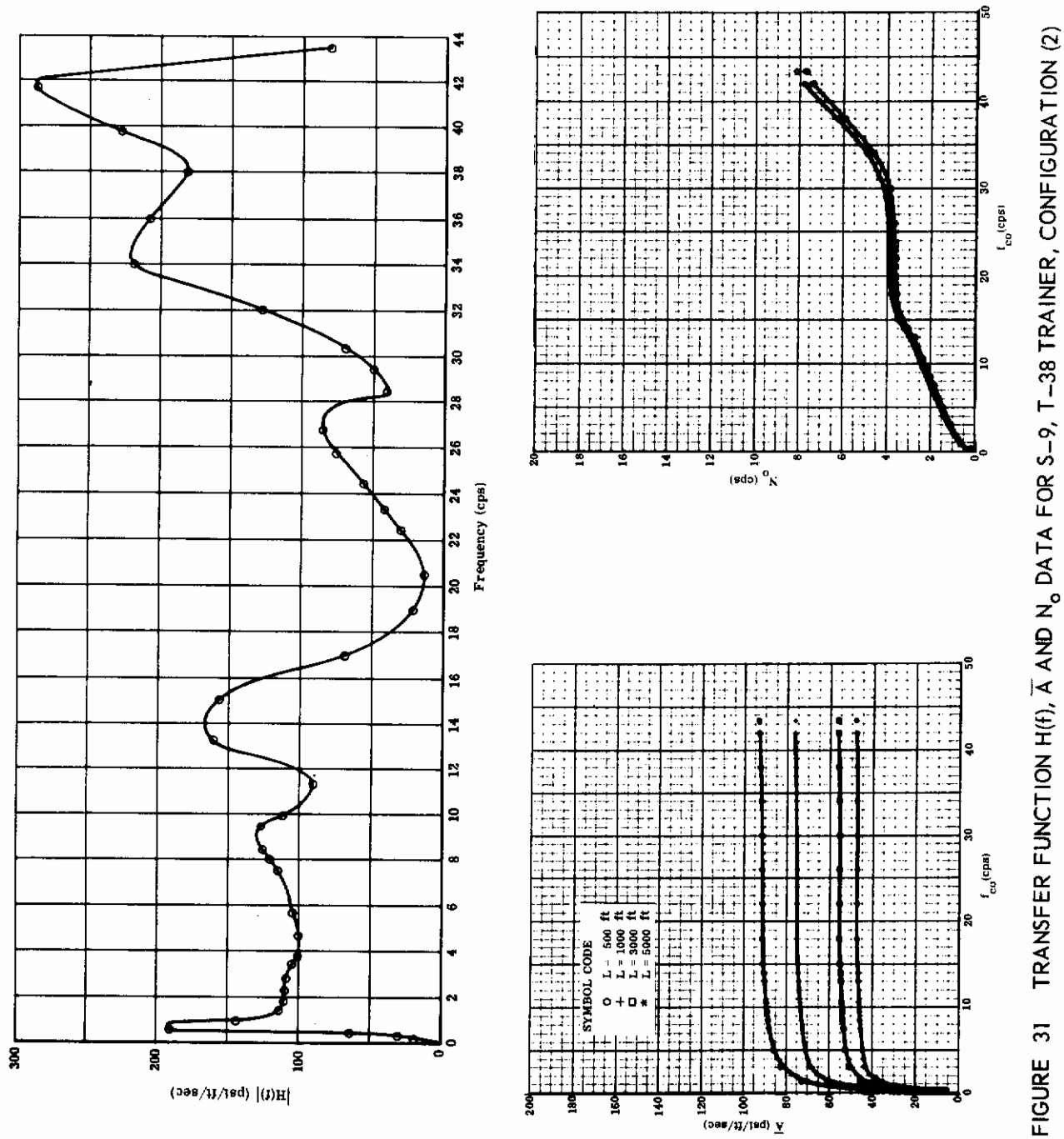

FIGURE 31 TRANSFER FUNCTION H(f), $\overline{A}$ AND N_o DATA FOR S-9, T-38 TRAINER, CONFIGURATION (2)

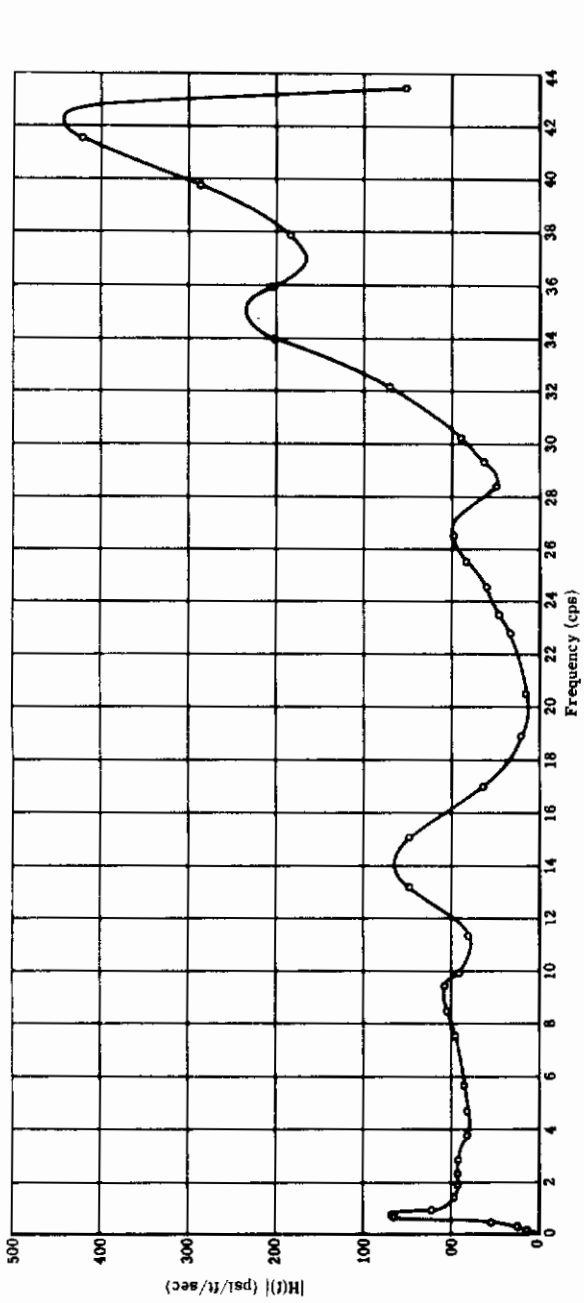

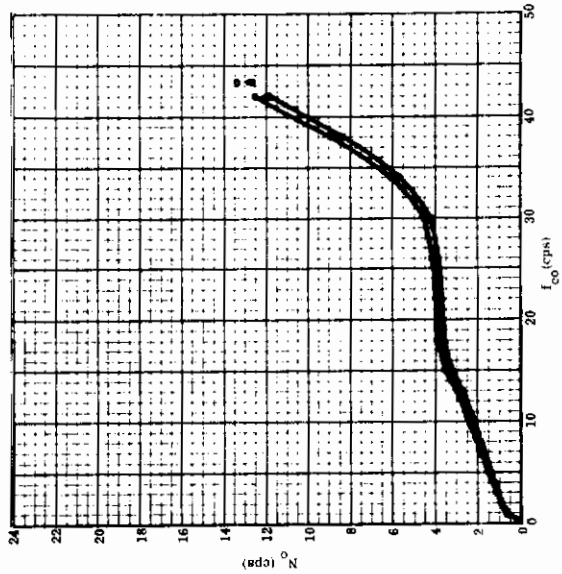

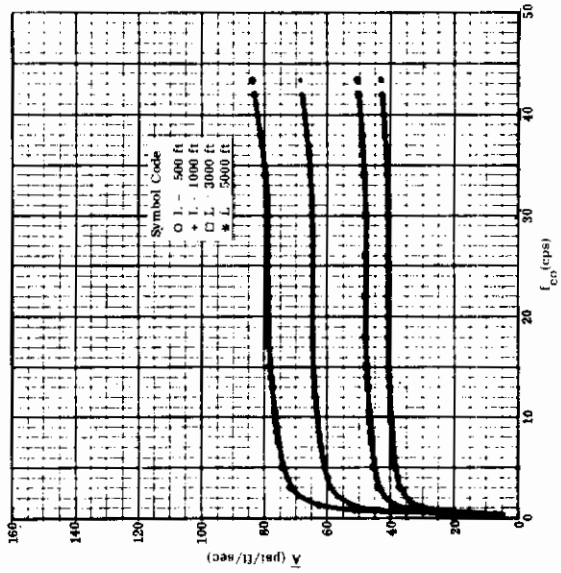

FIGURE 32 TRANSFER FUNCTION H(f), $\bar{A}$ AND N_o DATA FOR S-12, T-38 TRAINER, CONFIGURATION (2)

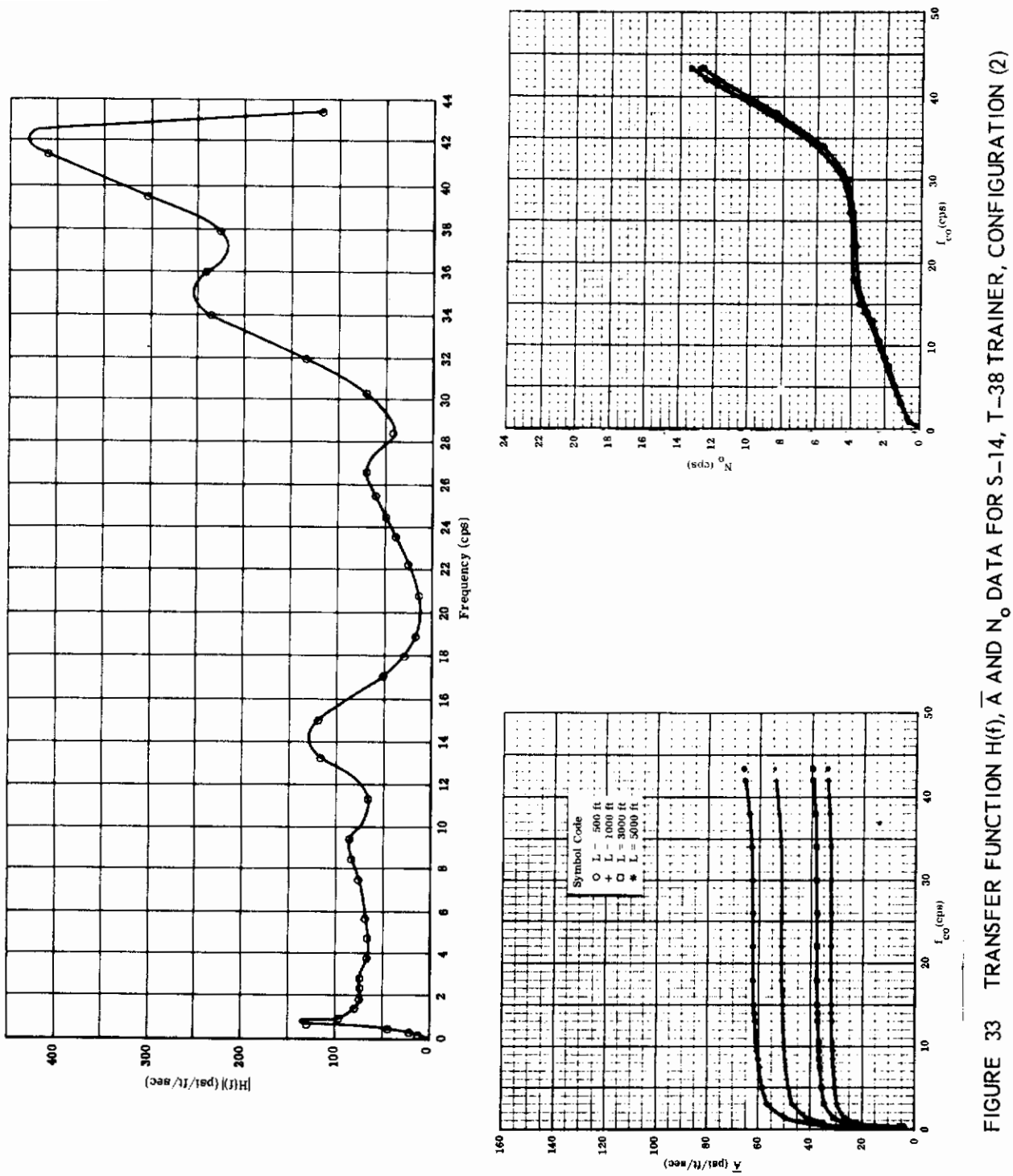

FIGURE 33 TRANSFER FUNCTION H(f), $\bar{A}$ AND N_o DATA FOR S-14, T-38 TRAINER, CONFIGURATION (2)

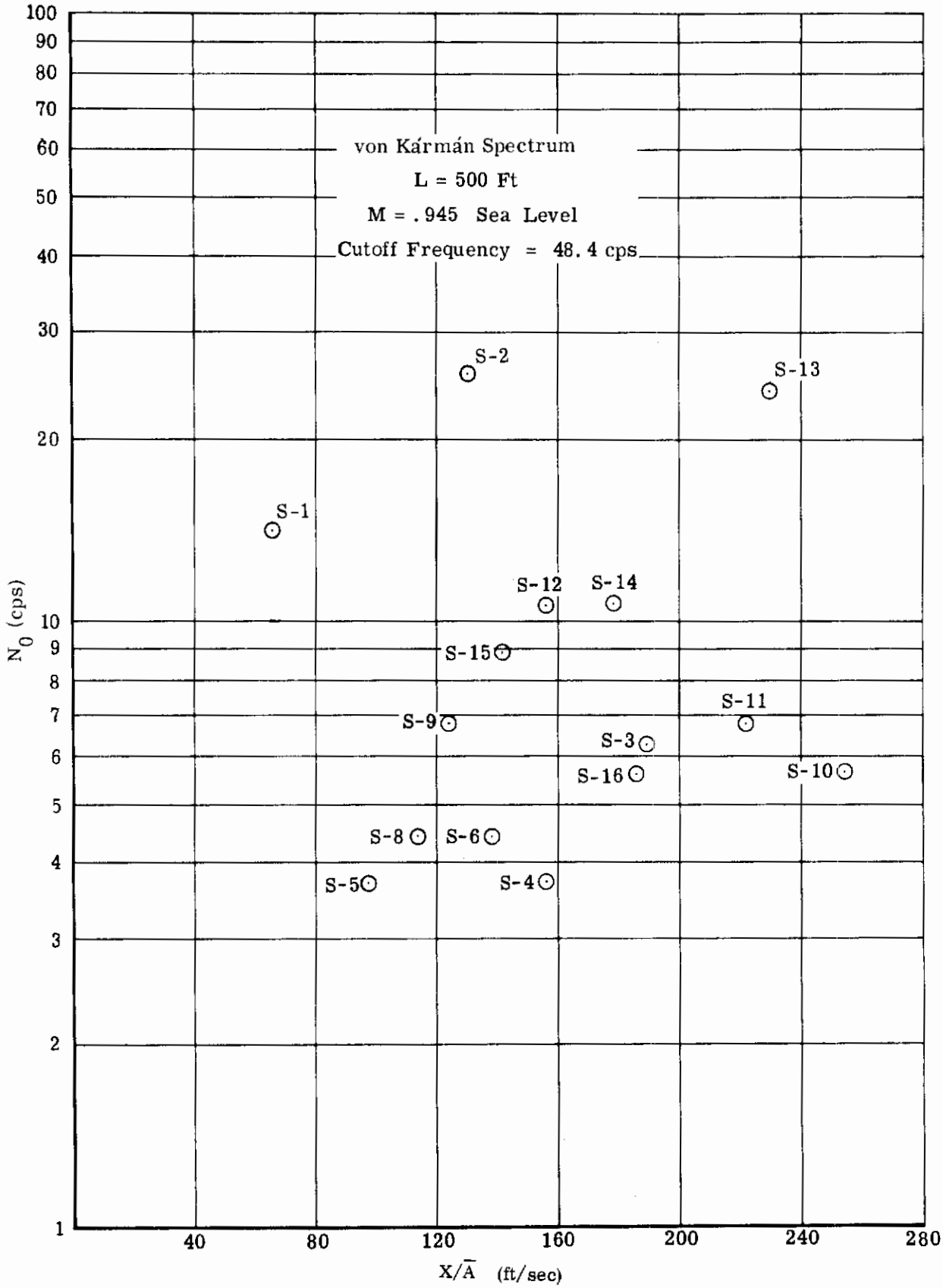

FIGURE 34 T-38 TRAINER RESPONSE DATA, CONFIGURATION (3)

TABLE XVII. MEAN AMPLITUDE AND FREQUENCY DATA, T-38 TRAINER, CONFIGURATION (3)

f_{co} = 48.4 cps

STRESS INDEX	IBM INDEX I	$\bar{A}$				N_o (cps)				x/$\bar{A}$ NON-INTERACTING			
		L = 500 ft.	L = 1000 ft.	L = 3000 ft.	L = 5000 ft.	L = 500 ft.	L - 1000 ft.	L = 3000 ft.	L = 5000 ft.	L = 500 ft.	L = 1000 ft.	L = 3000 ft.	L = 5000 ft.
1	46	1790	1428	1031	890.2	14.01	13.82	13.75	13.74	68.2	85.51	118.4	137.1
2	47	32.97	26.22	18.92	16.32	26.07	25.79	25.68	25.67	129.4	162.7	225.6	261.4
3	21	60.61	49.40	36.27	31.39	6.62	6.39	6.26	6.24	190.3	233.5	317.9	367.4
4	22	275.5	224.7	165.0	142.8	3.78	3.66	3.58	3.57	156.1	191.4	260.7	301.2
5	23	292.4	238.5	175.1	151.5	3.78	3.66	3.58	3.57	98.0	120.2	163.7	189.2
6	24	292.2	238.0	174.6	151.5	4.54	4.39	4.30	4.29	138.0	169.5	231.0	267.0
7	25	44.77	36.21	26.4	22.85	12.73	12.39	12.20	12.17	550.9	681.2	933.4	1080.0
8	26	251.0	204.4	150.0	129.8	4.54	4.39	4.30	4.29	114.2	140.2	191.2	220.9
9	39	145.2	118.2	86.7	75.01	7.62	7.37	7.22	7.20	123.9	152.2	207.6	240.0
10	40	44.29	36.1	26.5	22.88	6.08	5.88	5.76	5.75	254.4	312.4	426.0	492.3
11	41	165.1	134.11	98.52	85.24	7.62	7.37	7.23	7.20	222.2	272.9	372.2	430.2
12	42	121.6	98.8	72.4	62.59	12.03	11.65	11.43	11.39	152.5	187.6	256.1	296.1
13	43	37.37	29.9	21.7	18.73	23.72	23.3	23.1	23.08	230.1	287.7	396.6	459.1
14	44	96.10	78.1	57.2	49.49	12.03	11.7	11.4	11.39	176.9	217.7	297.2	393.5
15	28	11.81	9.57	6.98	6.04	8.66	8.62	8.49	8.47	141.1	174.2	238.8	276.3
16	29	1057.0	858.2	627.1	592.2	5.71	5.54	5.45	5.43	186.7	229.9	314.7	364.0

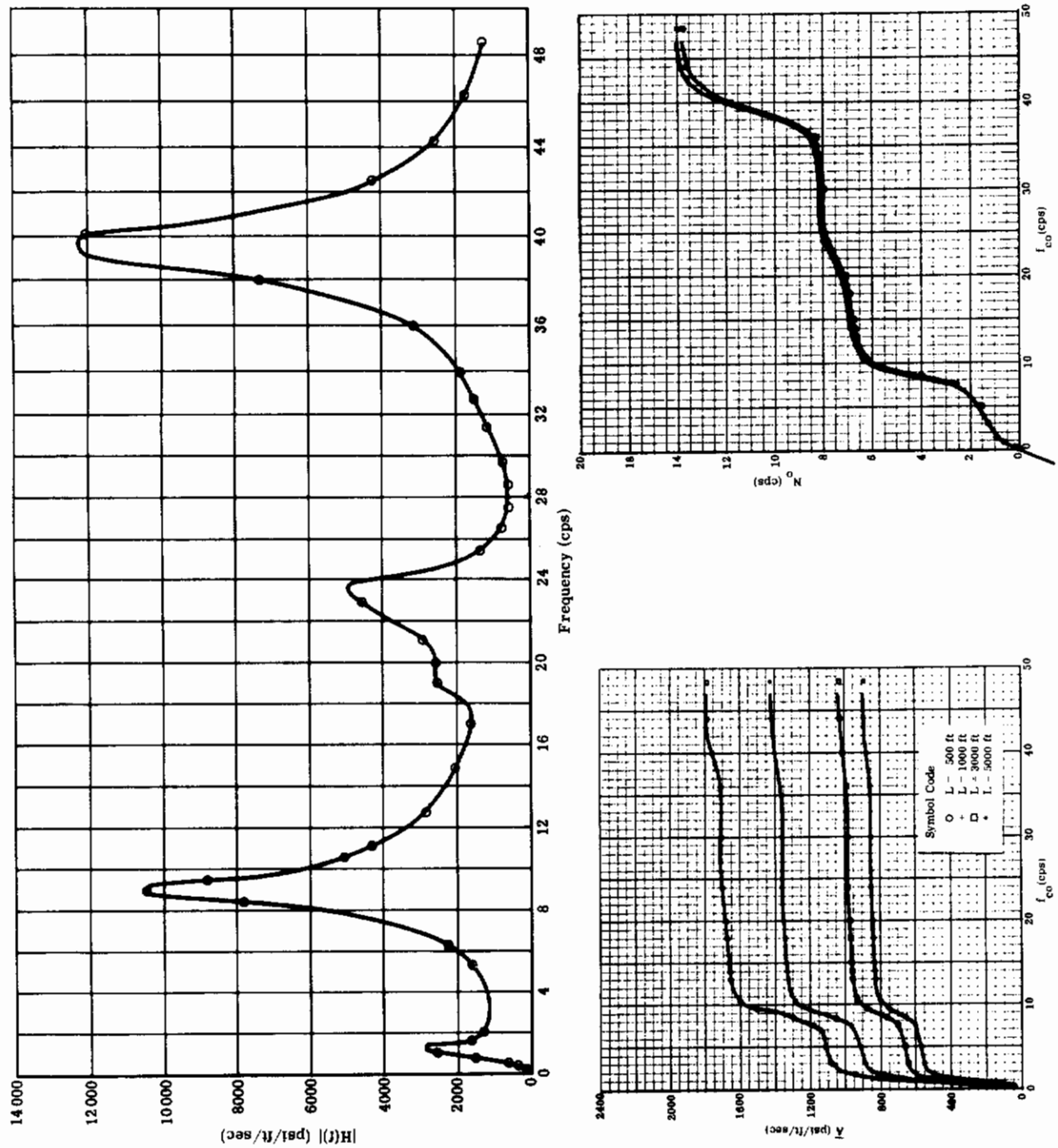

FIGURE 35 TRANSFER FUNCTION H(f), $\bar{A}$ AND N_o DATA FOR S-1, T-38 TRAINER, CONFIGURATION (3)

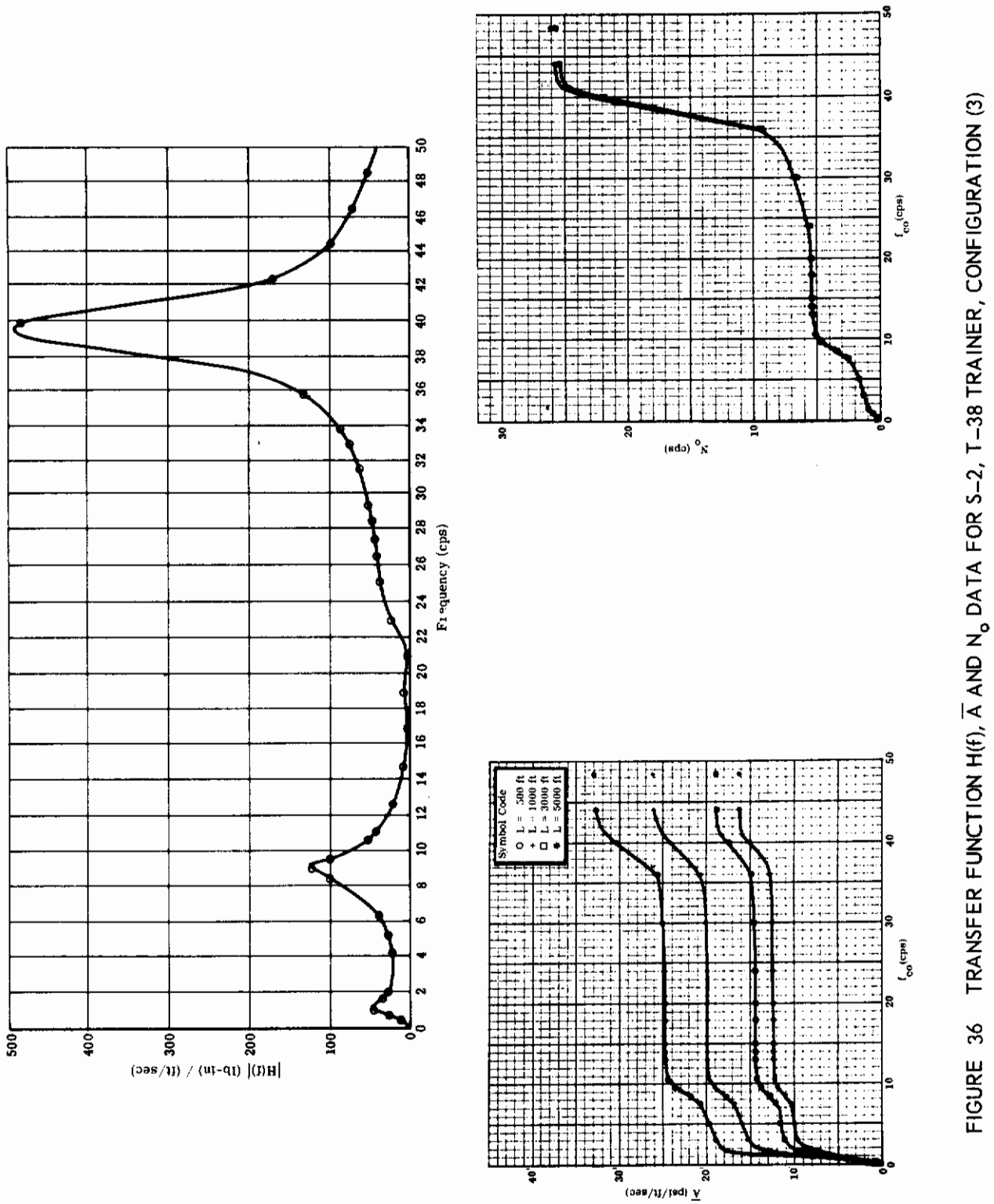

FIGURE 36 TRANSFER FUNCTION H(f), $\bar{A}$ AND N_o DATA FOR S-2, T-38 TRAINER, CONFIGURATION (3)

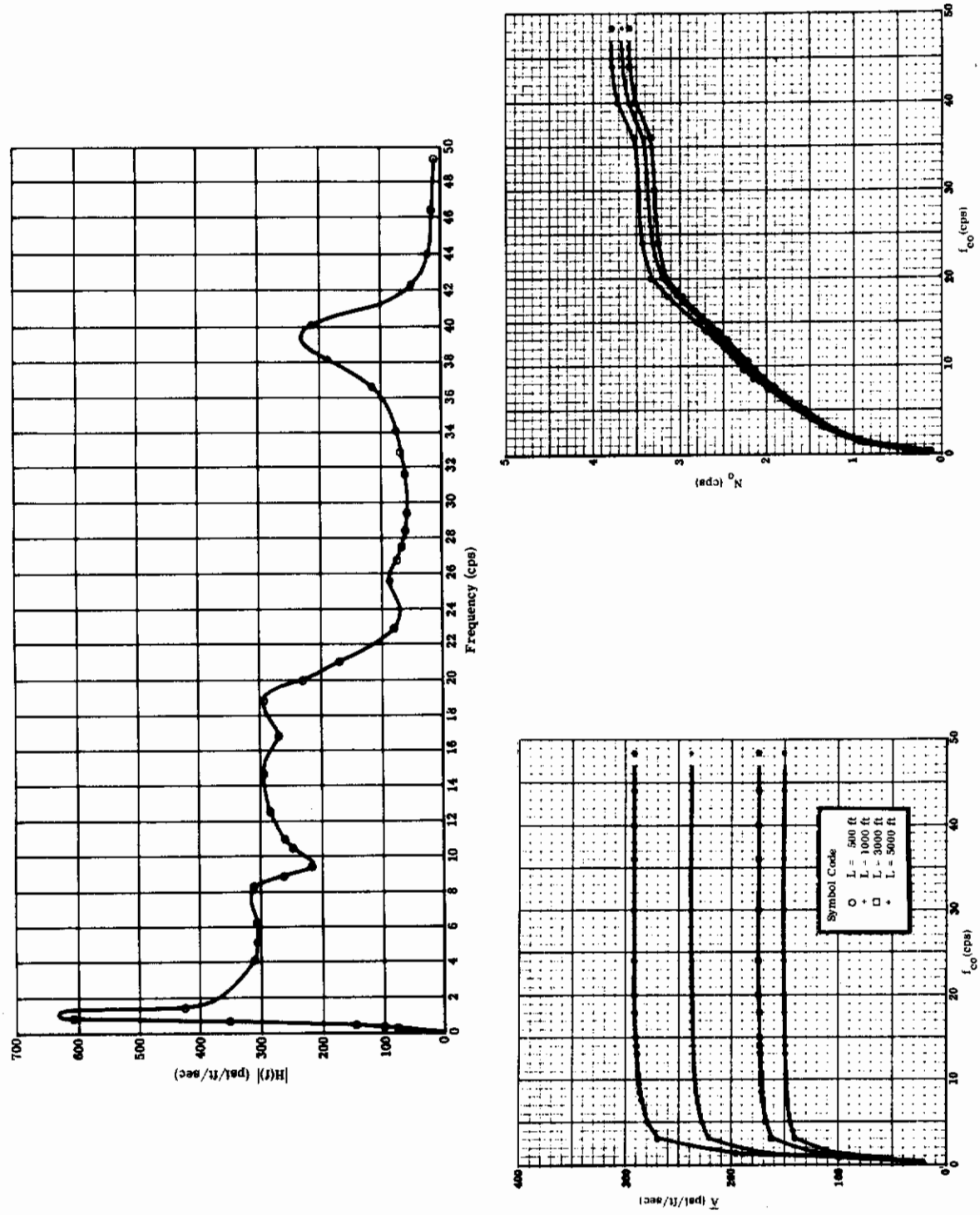

FIGURE 37 TRANSFER FUNCTION H(f), $\overline{A}$ AND N_o DATA FOR S-5, T-38 TRAINER, CONFIGURATION (3)

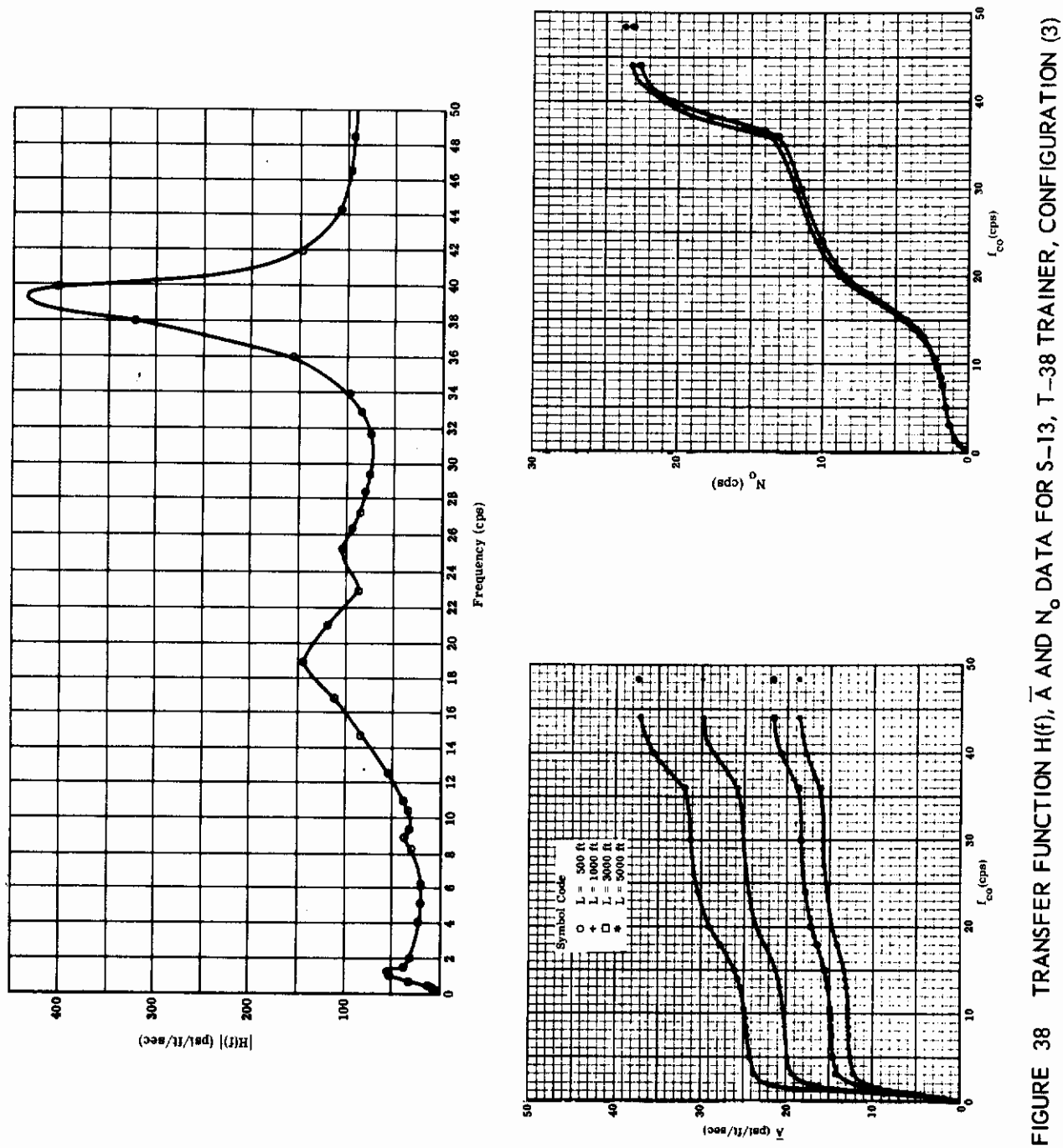

FIGURE 38 TRANSFER FUNCTION H(f), $\bar{A}$ AND N_o DATA FOR S-13, T-38 TRAINER, CONFIGURATION (3)

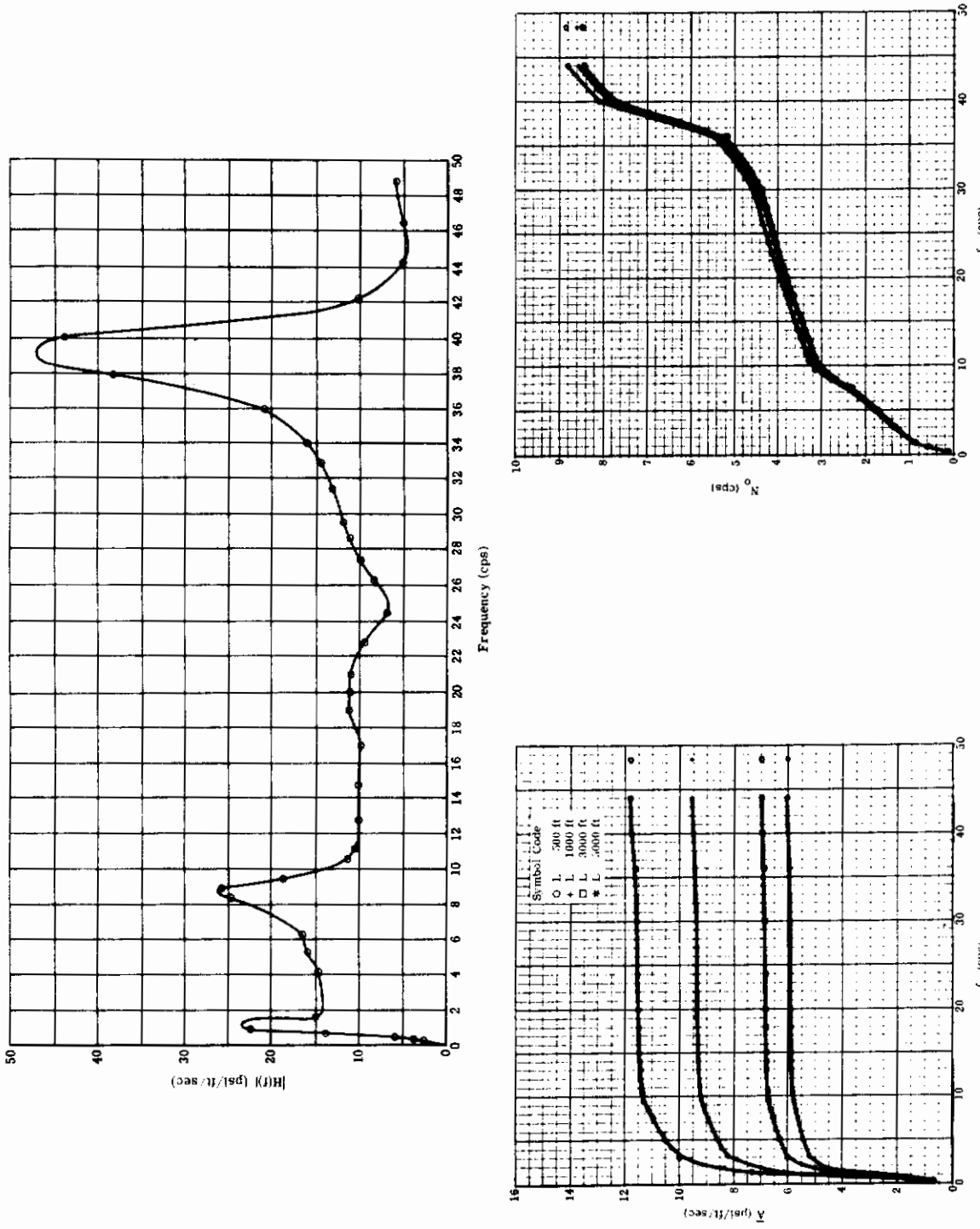

FIGURE 39 TRANSFER FUNCTION H(f), $\bar{A}$ AND N_o DATA FOR S-15, T-38 TRAINER, CONFIGURATION (3)

4.3 F-5A Fighter Gust Computation Data

F-5A fighter gust computation data are presented in the following figures and tables. They are arranged in the order of the three (3) configurations as defined in sub-section (1.2). It is noted that for the F-5A fighter, lower cutoff frequencies (around 28.0 cps) are used in obtaining the tabulated $\bar{A}$, N_o values as well as the overall response plots. The selection of a lower F-5A cutoff frequency is due to the fact that the major flexible modes are grouped in a relatively lower frequency region as compared to the T-38 trainer. A brief summary for the more critical elements of F-5A corresponding to L = 500 feet is given in Table XVIII.

TABLE XVIII. CRITICAL STRESS ELEMENTS OF F-5A FIGHTER

Configuration	($x/\bar{A}$ Minimum)	Stress Element for ($x/\bar{A}$) Minimum	Additional Critical Elements
(1)	98 fps	S-7: 27-33 percent upper panel stability for combined axial-shear stress: σ_c applied	S-4, S-5, S-10, S-12, S-23, S-24, S-25
(2)	205 fps	S-7: 27-33 percent upper panel stability for combined axial-shear stress: σ_c applied	S-4, S-12
(3)	101 fps	S-10: 44-66 percent lower panel attach for combined axial-shear stress: σ_t applied	S-7, S-15, S-23

Gust computation data corresponding to Configuration (1) are presented in Figures 40-48 and Table XIX.

Gust computation data corresponding to Configuration (2) are presented in Figures 49-52 and Table XX.

The same gust data for Configuration (3) are given in Figures 53-57 and Table XXI. The center of gravity normal acceleration transfer function plot for the same configuration is shown in Figure 58. Also plotted on the same figure is the analytical transfer function data for a similar configuration identical to Configuration (3) except that 5 percent fuel is present. The corresponding flight test data for an F-5A with 50 percent internal fuel is also plotted for comparison purpose. A transfer function plot for the rigid pitch motion of F-5A is shown in Figure 59.

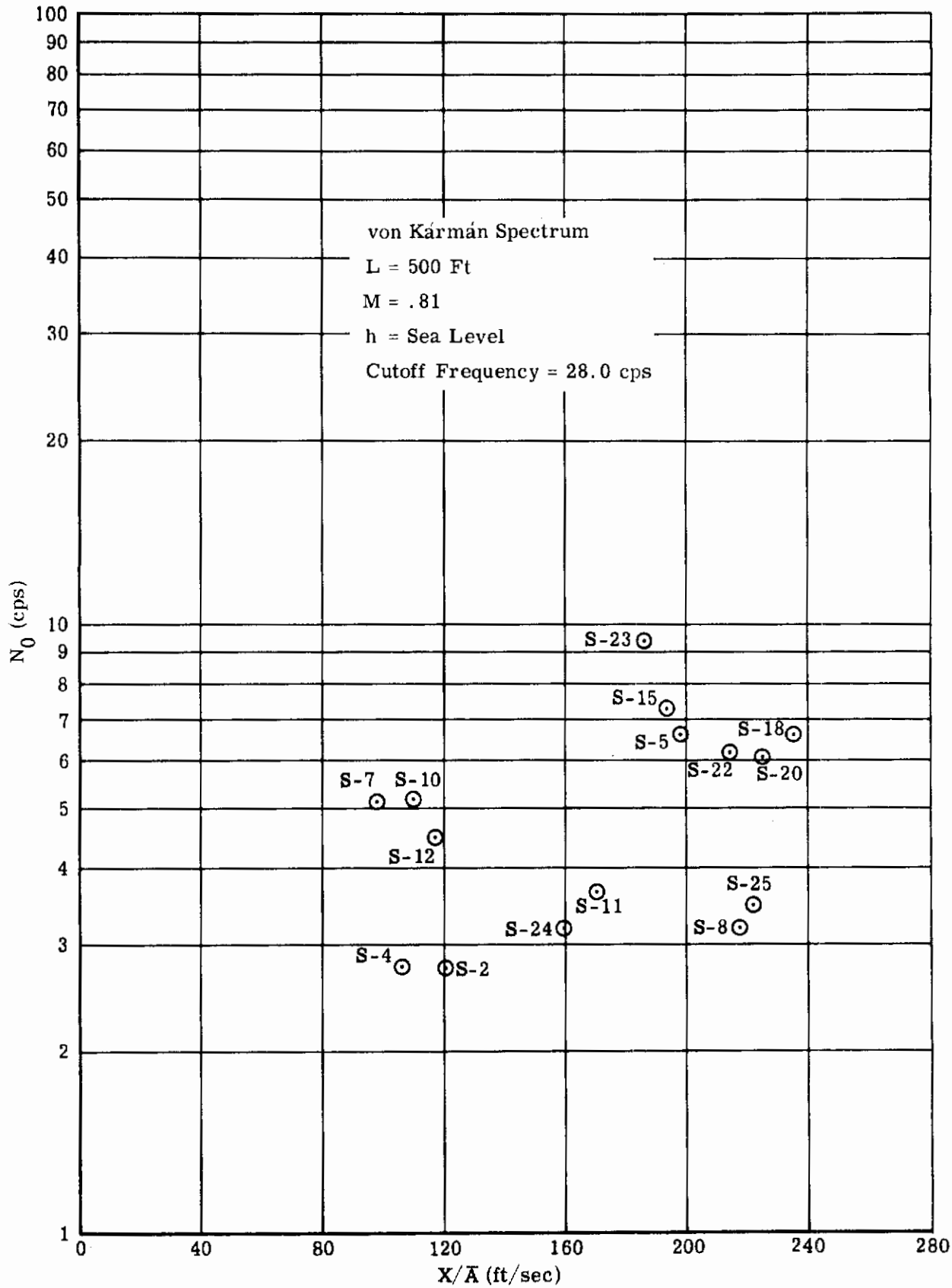

FIGURE 40 F-5A FIGHTER RESPONSE DATA, CONFIGURATION (1)

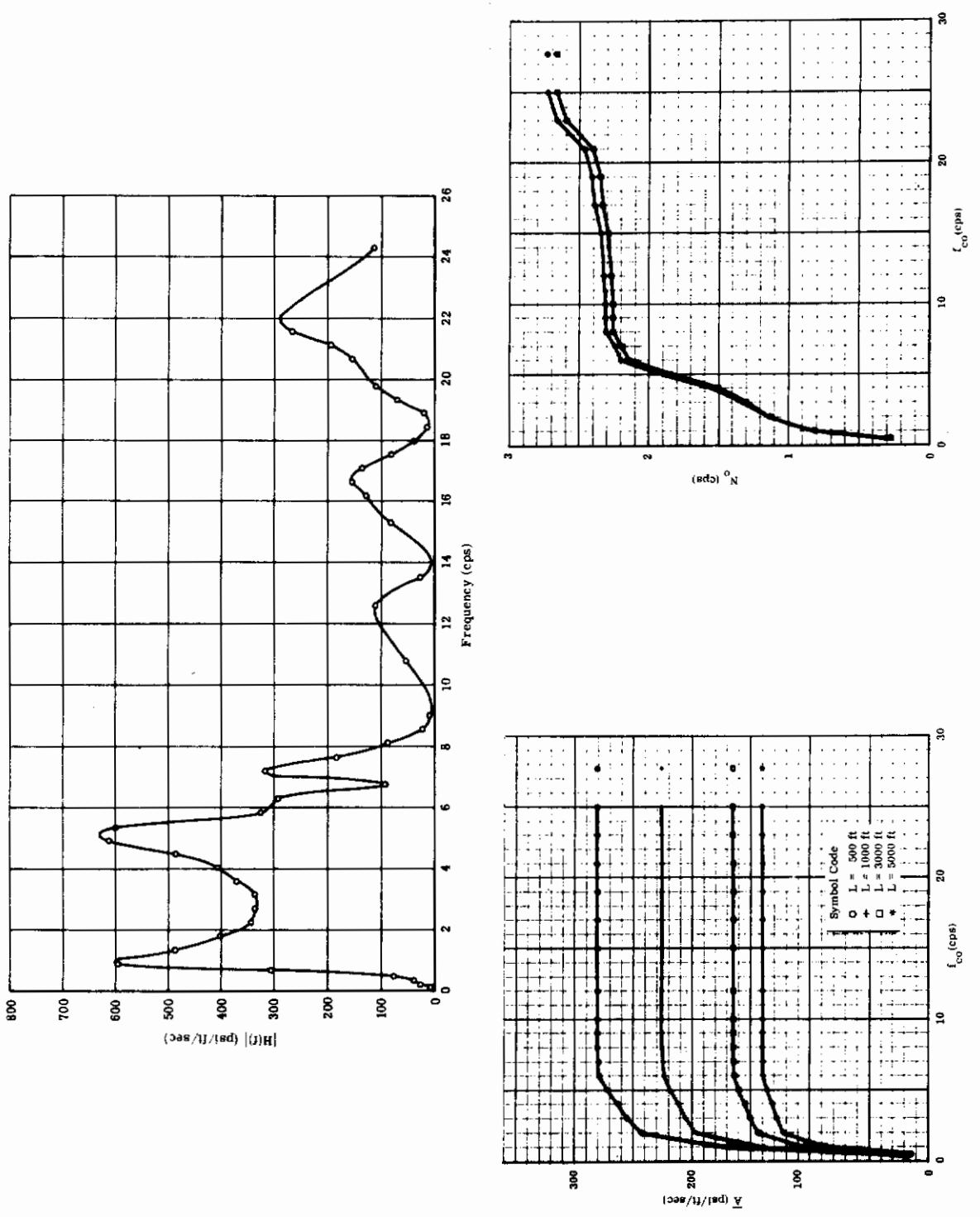

FIGURE 41 TRANSFER FUNCTION H(f), $\bar{A}$ AND N_o DATA FOR S-4, F-5A FIGHTER, CONFIGURATION (1)

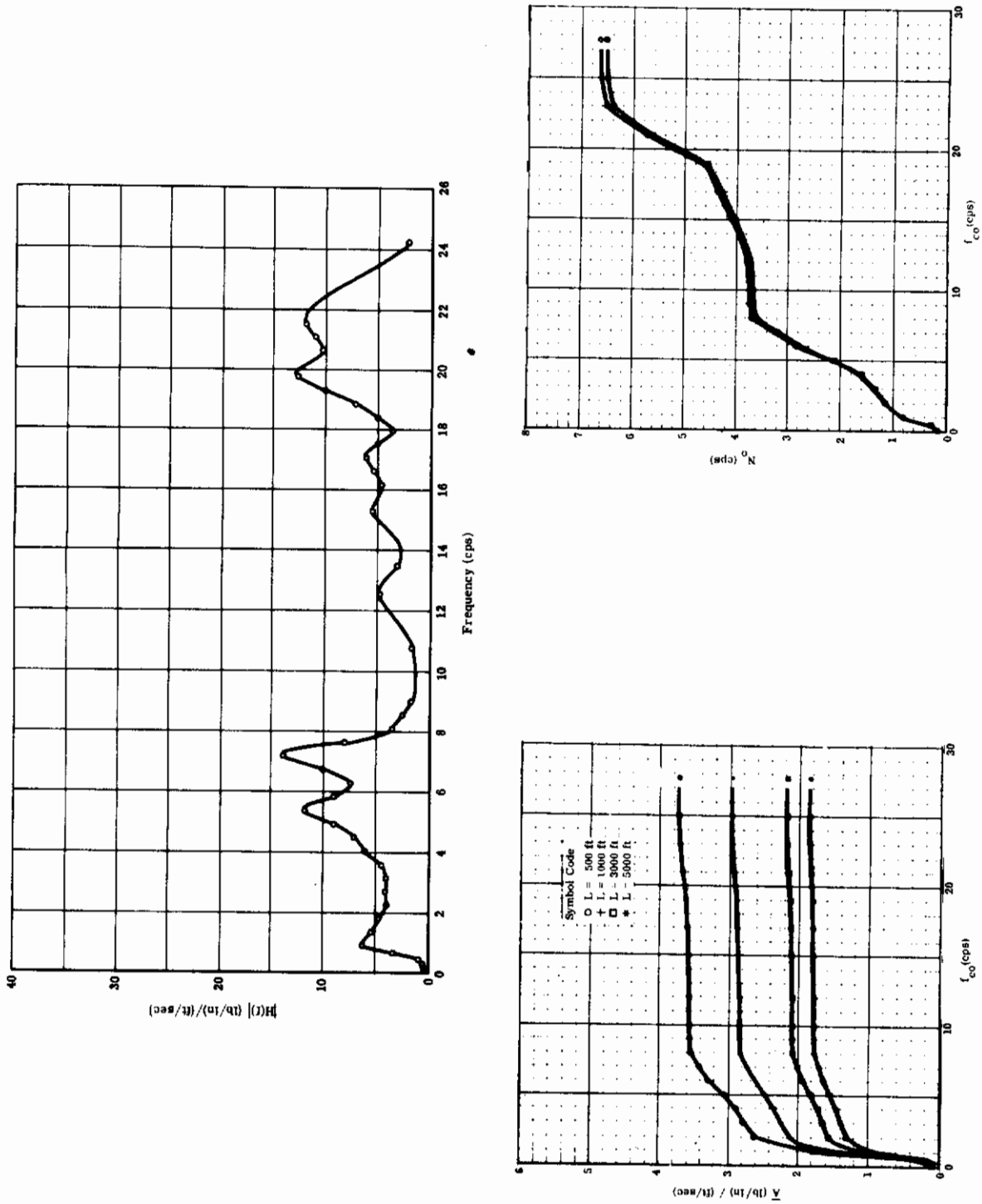

FIGURE 42 TRANSFER FUNCTION H(f), $\overline{A}$ AND N_o DATA FOR S-5, F-5A FIGHTER, CONFIGURATION (1)

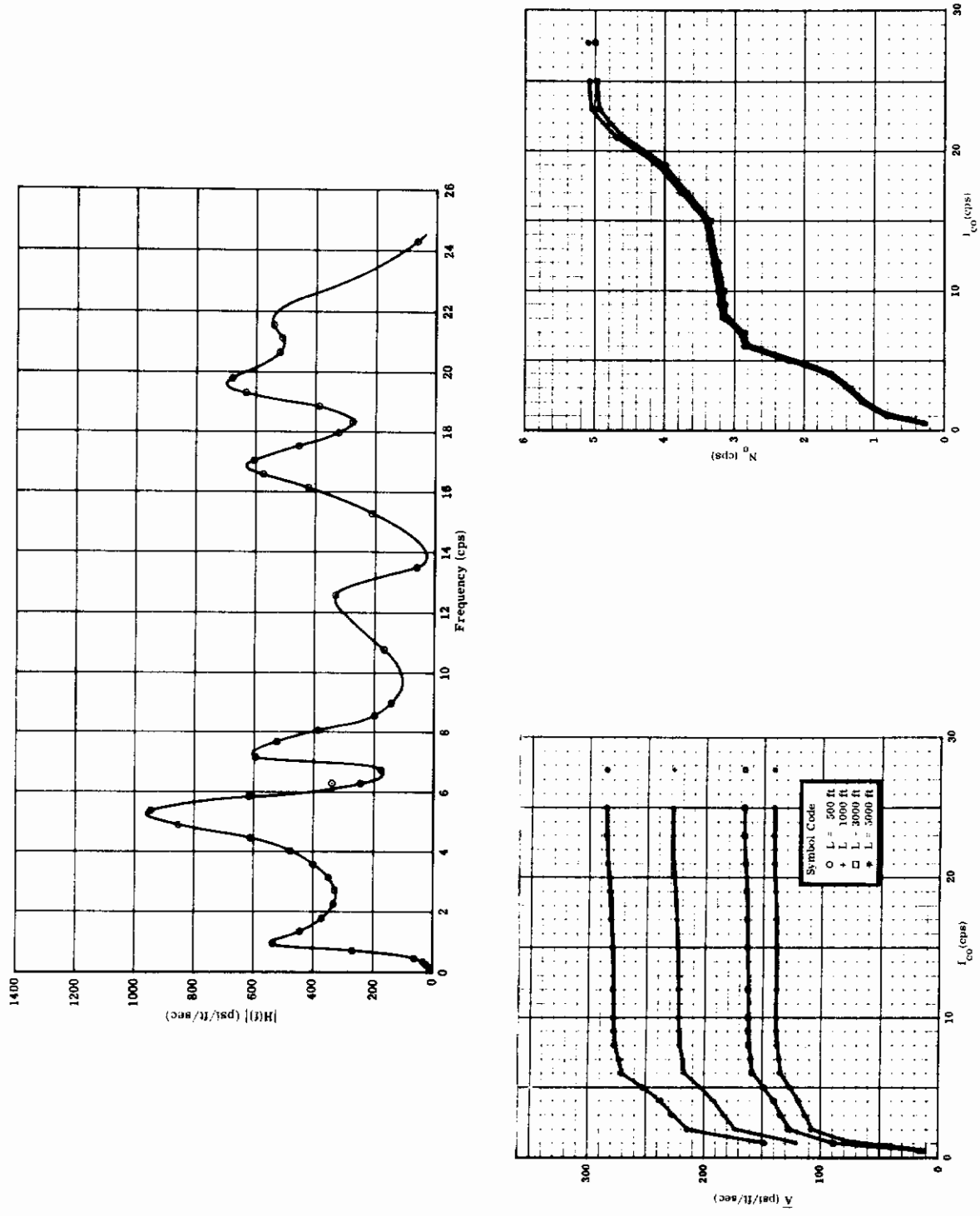

FIGURE 43 TRANSFER FUNCTION H(f), $\bar{A}$ AND N_o DATA FOR S-7, F-5A FIGHTER CONFIGURATION (1)

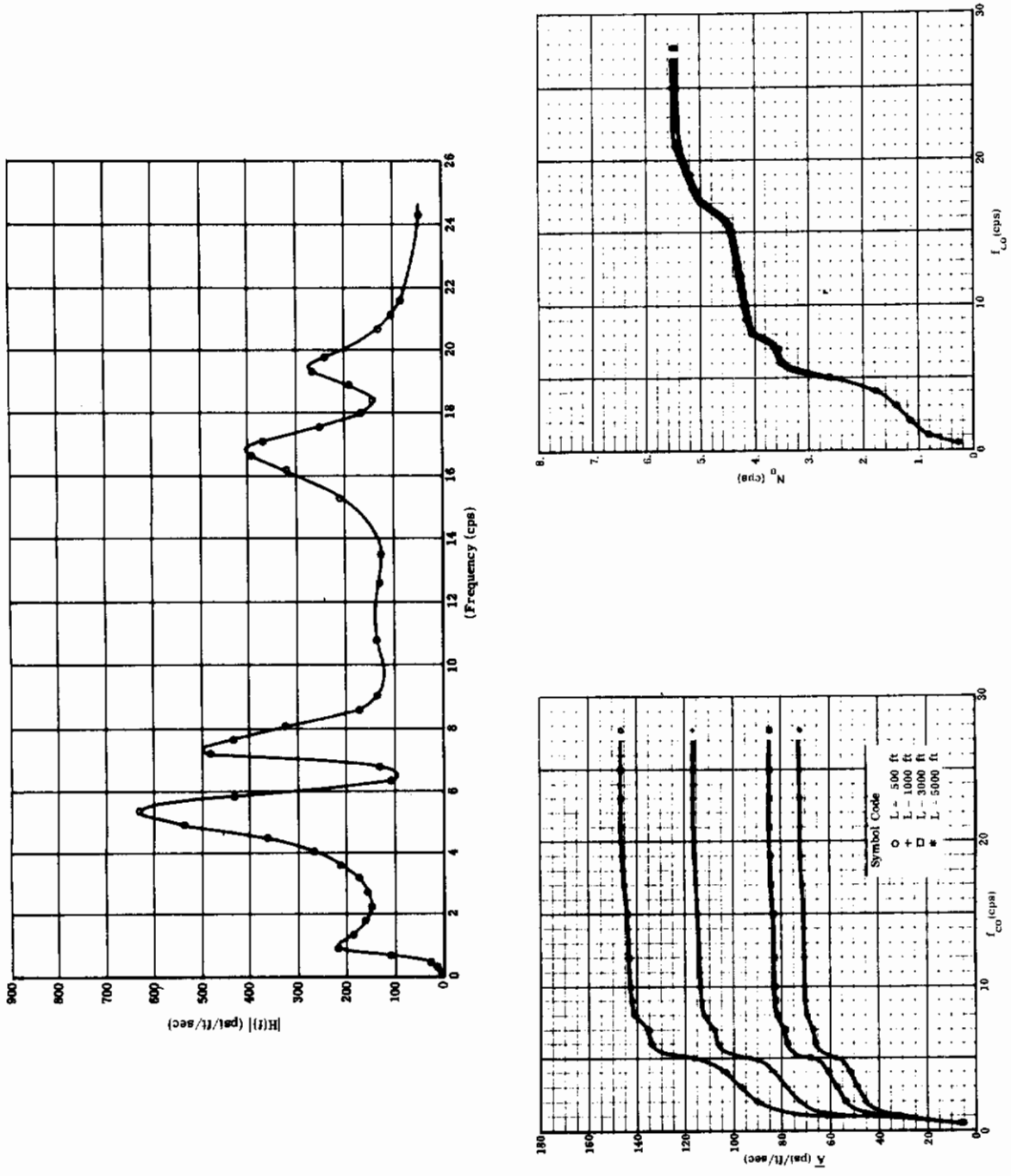

FIGURE 44 TRANSFER FUNCTION H(f), $\bar{A}$ AND N_o DATA FOR S-10, F-5A FIGHTER, CONFIGURATION (1)

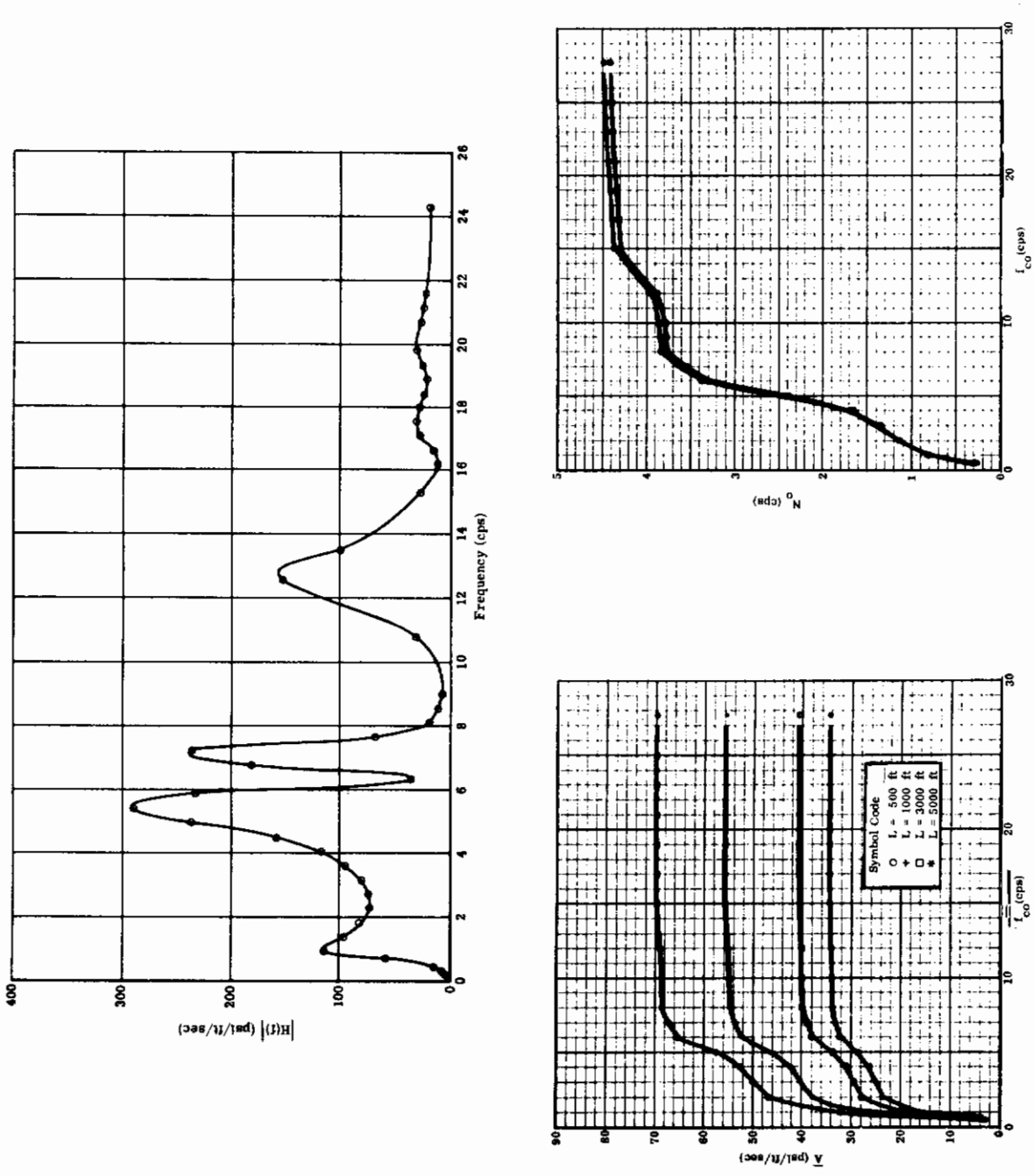

FIGURE 45 TRANSFER FUNCTION H(f), $\overline{A}$ AND N_o DATA FOR S-12, F-5A FIGHTER, CONFIGURATION (1)

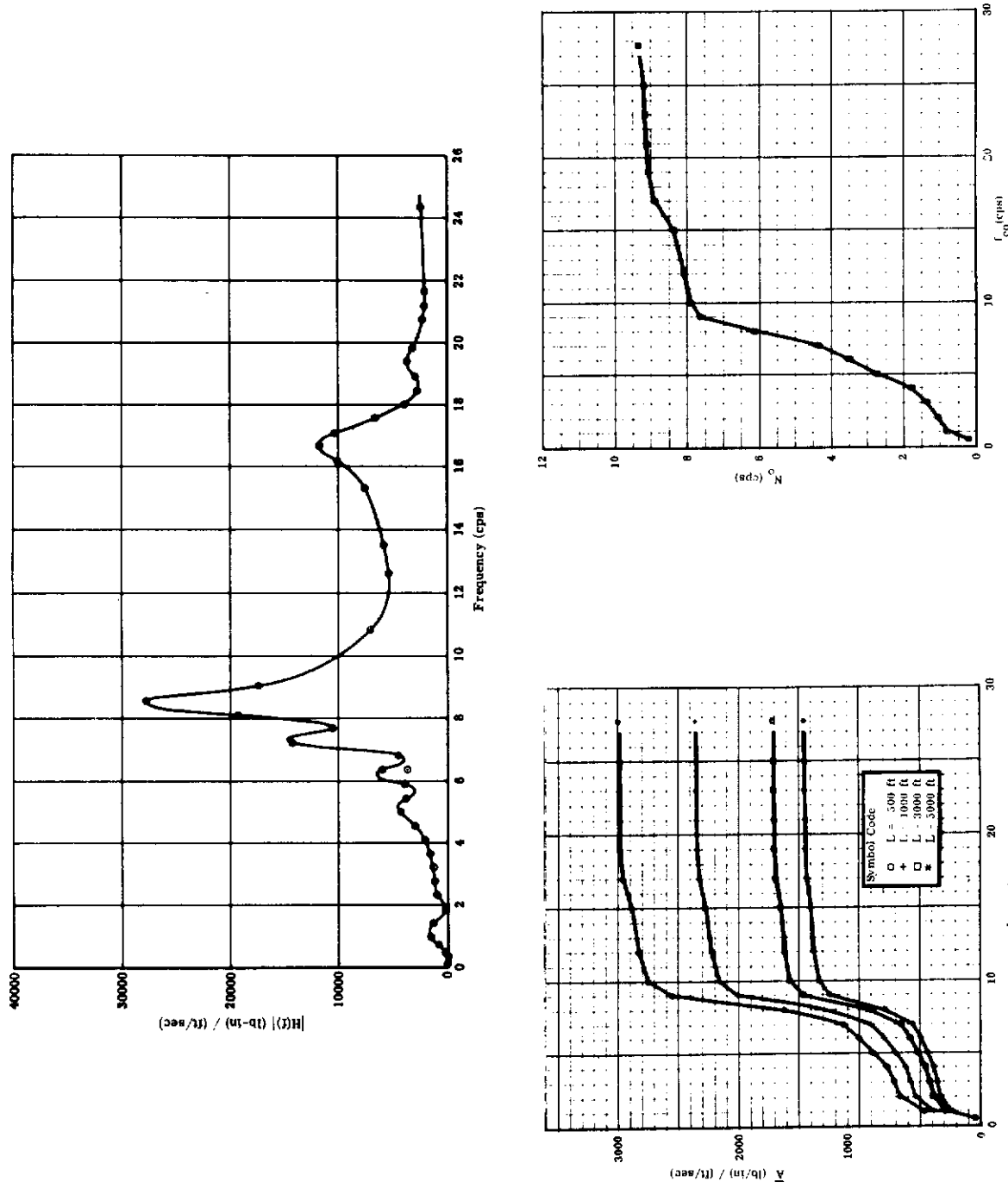

FIGURE 46 TRANSFER FUNCTION H(f), $\bar{A}$ AND N_o DATA FOR S-23, F-5A FIGHTER, CONFIGURATION (1)

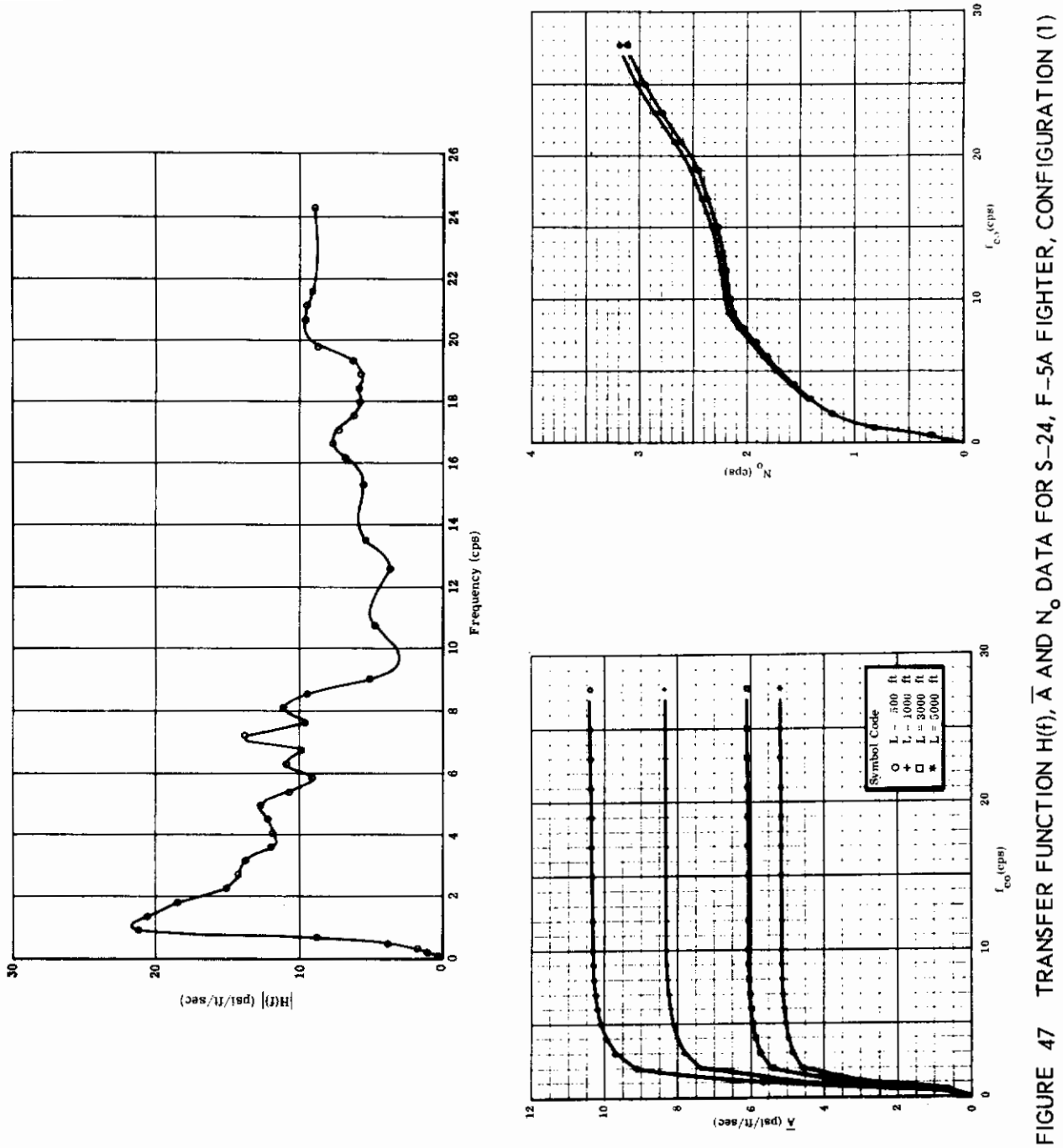

FIGURE 47 TRANSFER FUNCTION H(f), $\bar{A}$ AND N_o DATA FOR S-24, F-5A FIGHTER, CONFIGURATION (1)

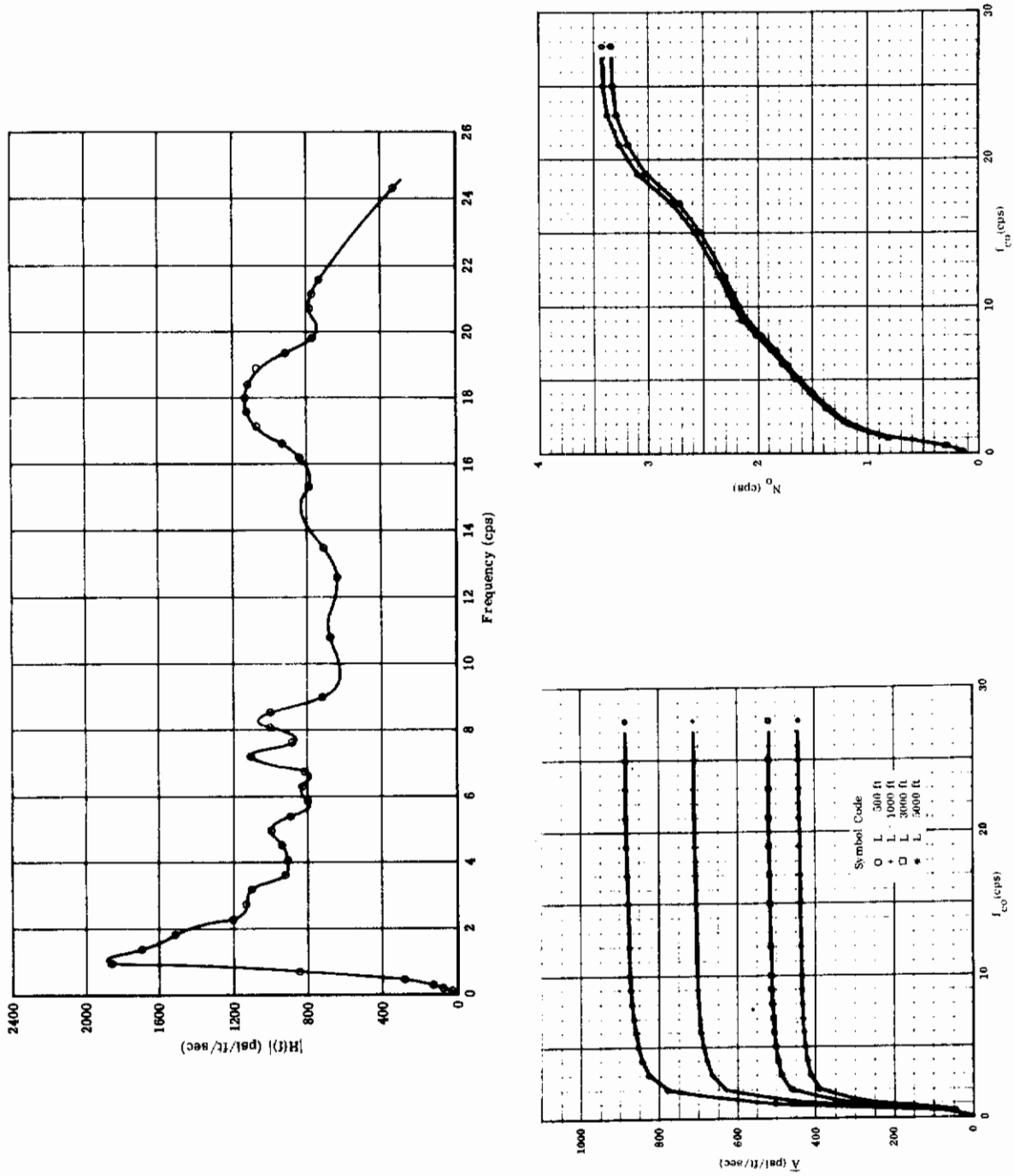

FIGURE 48 TRANSFER FUNCTION H(f), $\bar{A}$ AND N_o DATA FOR S-25, F-5A FIGHTER, CONFIGURATION (1)

TABLE XIX. MEAN AMPLITUDE AND FREQUENCY DATA, F-5A FIGHTER, CONFIGURATION (1)

f_{co} = 28.0 cps

STRESS INDEX	IBM INDEX I	$\bar{A}$				N_o (cps)				$x/\bar{A} \sim$ NON-INTERACTING			
		L = 500 ft.	L = 1000 ft.	L = 3000 ft.	L = 5000 ft.	L = 500 ft.	L = 1000 ft.	L = 3000 ft.	L = 5000 ft.	L = 500 ft.	L = 1000 ft.	L = 3000 ft.	L = 5000 ft.
1	14	37.32	30.02	21.95	18.70	3.845	3.762	3.733	3.730	365.1	453.9	620.5	728.5
2	15	279.1	224.1	163.8	139.5	2.733	2.682	2.664	2.663	120.3	149.9	205.1	240.7
3	16	43.06	34.64	25.33	21.59	3.733	3.651	3.623	3.620	440.4	547.5	748.7	878.7
4	17	281.7	226.3	165.3	140.9	2.734	2.683	2.665	2.663	107.3	133.6	182.8	214.5
5	18	3.726	2.971	2.166	1.845	6.643	6.547	6.541	6.511	198.6	249.1	341.7	401.1
6	19	24.01	18.92	13.73	11.69	9.129	9.104	9.095	9.094	592.8	752.3	1036	1217
7	20	286.4	228.8	166.9	142.2	5.106	5.026	4.998	4.995	98.74	123.6	169.4	198.9
8	28	2.930	2.342	1.708	1.455	3.564	3.510	3.491	3.489	218.4	273.3	374.6	439.7
9	29	25.04	19.85	14.44	12.30	6.547	6.492	6.473	6.471	467.6	590.0	811.1	952.3
10	30	146.7	116.6	84.88	72.29	5.530	5.471	5.451	5.449	111.4	140.0	192.5	226.0
11	38	3.820	3.051	2.226	1.896	3.626	3.572	3.553	3.552	171.0	214.0	293.4	344.4
12	39	69.85	55.63	40.53	34.53	4.488	4.432	4.413	4.411	116.9	146.8	201.5	236.5
13	40	114.1	90.12	65.47	55.76	7.169	7.133	7.121	7.120	388.2	491.5	676.4	794.4
14	41	35.14	27.96	20.36	17.35	4.808	4.753	4.733	4.732	456.6	574.0	788.0	925.2
15	42	104.4	82.43	59.89	51.00	7.217	7.182	7.170	7.169	194.2	245.9	338.5	397.5
16	43	93.78	74.06	53.80	45.81	7.228	7.194	7.182	7.181	476.0	602.8	829.8	974.4
17	44	102.2	80.71	58.63	49.93	7.275	7.242	7.230	7.229	438.9	556.0	765.4	898.8
18	45	131.8	103.7	75.22	64.05	6.575	6.568	6.566	6.565	235.9	299.8	413.3	485.4
19	46	37.16	29.26	21.24	18.08	8.744	8.725	8.719	8.718	1236	1569	2162	2539
20	47	120.7	94.94	68.88	58.65	6.553	6.546	6.544	6.544	225.4	286.4	394.8	463.7
21	48	37.54	29.56	21.45	18.27	8.744	8.725	8.719	8.718	1229	1561	2151	2526
22	49	15.19	11.95	8.669	7.382	6.610	6.603	6.601	6.601	214.8	273.0	376.3	441.9
23	33	3004	2364	1716	1461	9.367	9.352	9.346	9.346	186.6	237.1	326.7	383.7
24	22	10.41	8.351	6.101	5.198	3.189	3.131	3.110	3.108	160.4	200.0	273.7	321.3
25	32	888.1	712.7	520.7	443.6	3.429	3.364	3.341	3.339	222.2	276.8	378.9	444.8

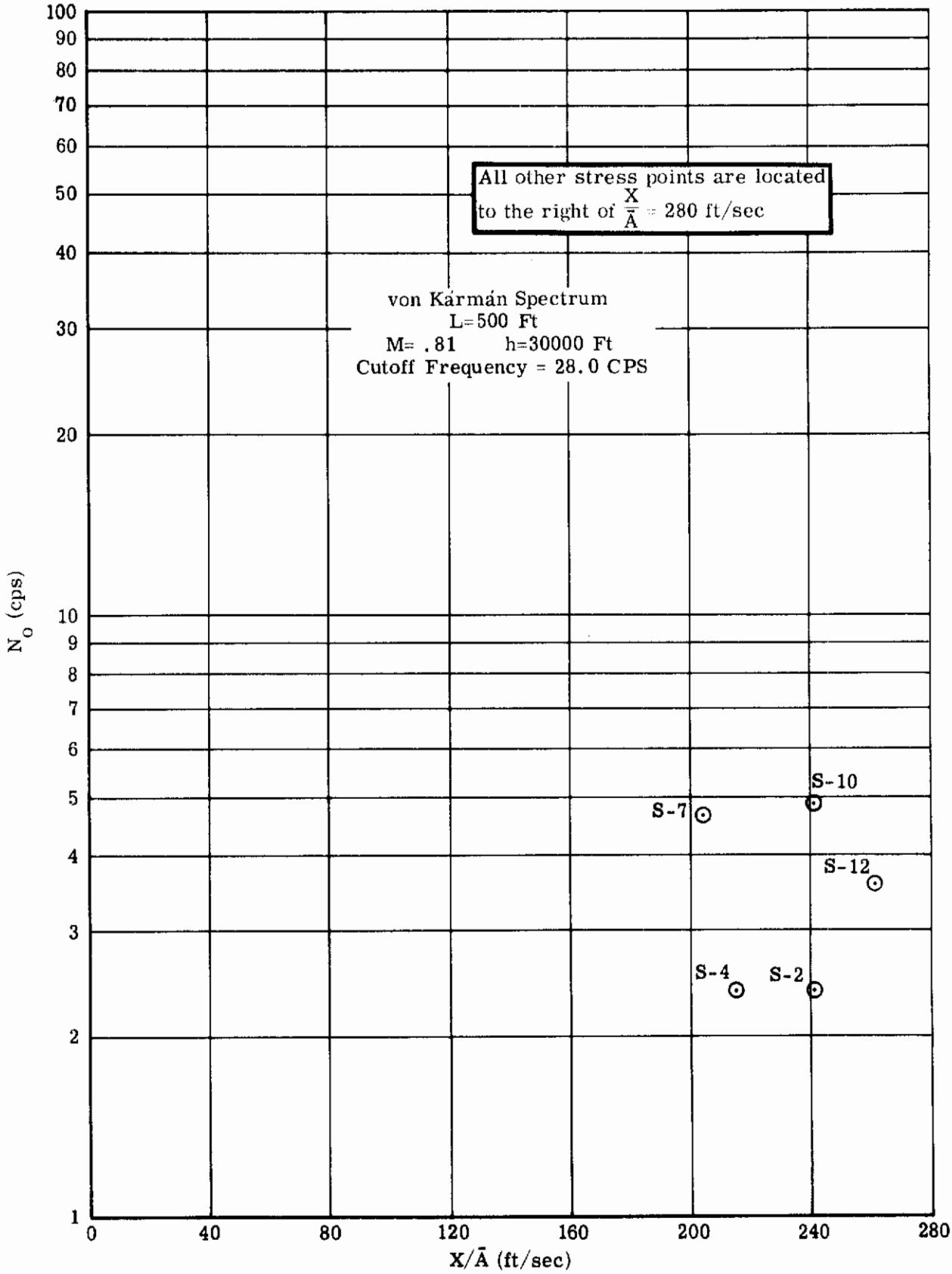

FIGURE 49 F-5A FIGHTER RESPONSE DATA, CONFIGURATION (2)

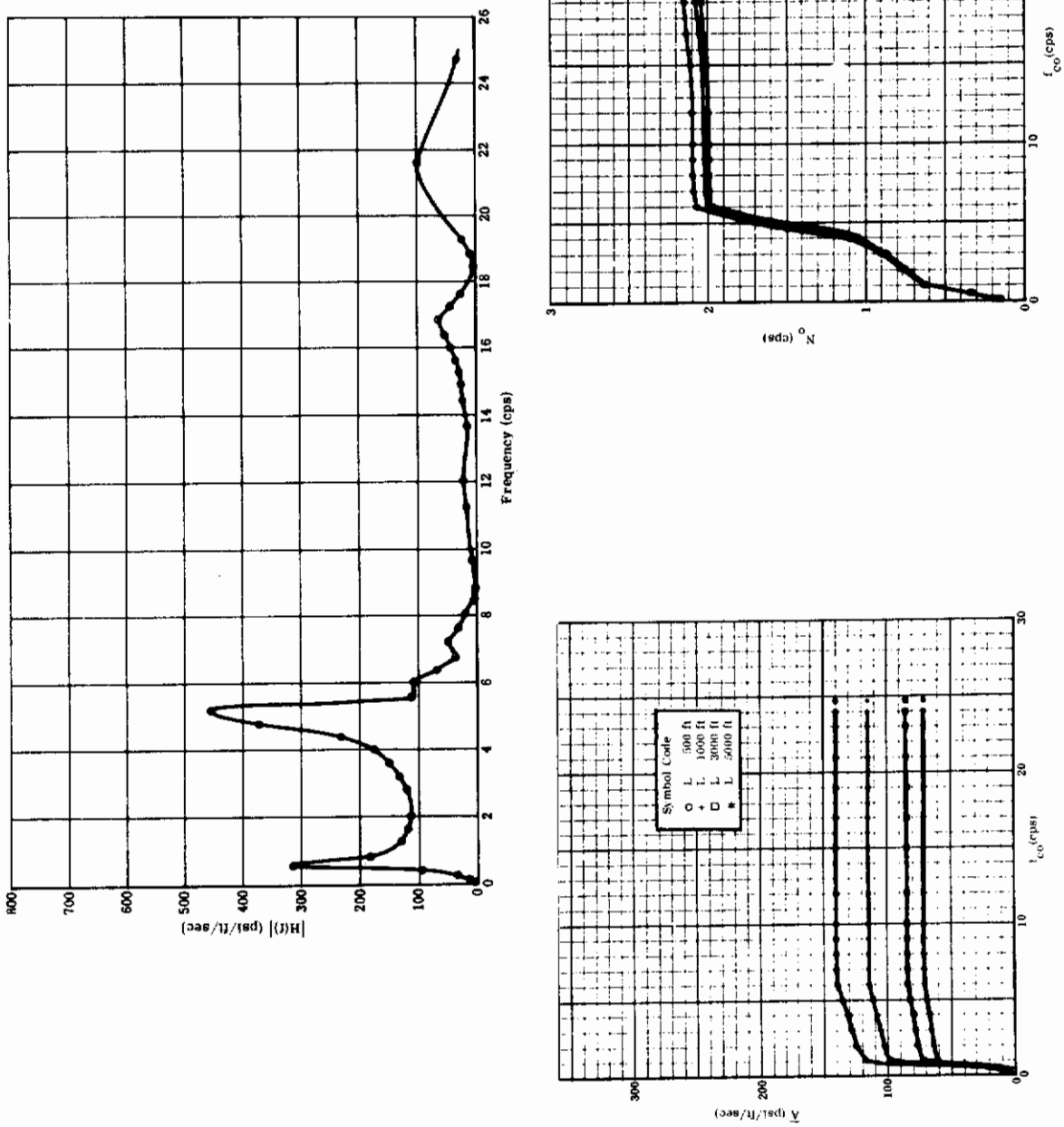

FIGURE 50 TRANSFER FUNCTION H(f), $\bar{A}$ AND N_o DATA FOR S-4, F-5A FIGHTER, CONFIGURATION (2)

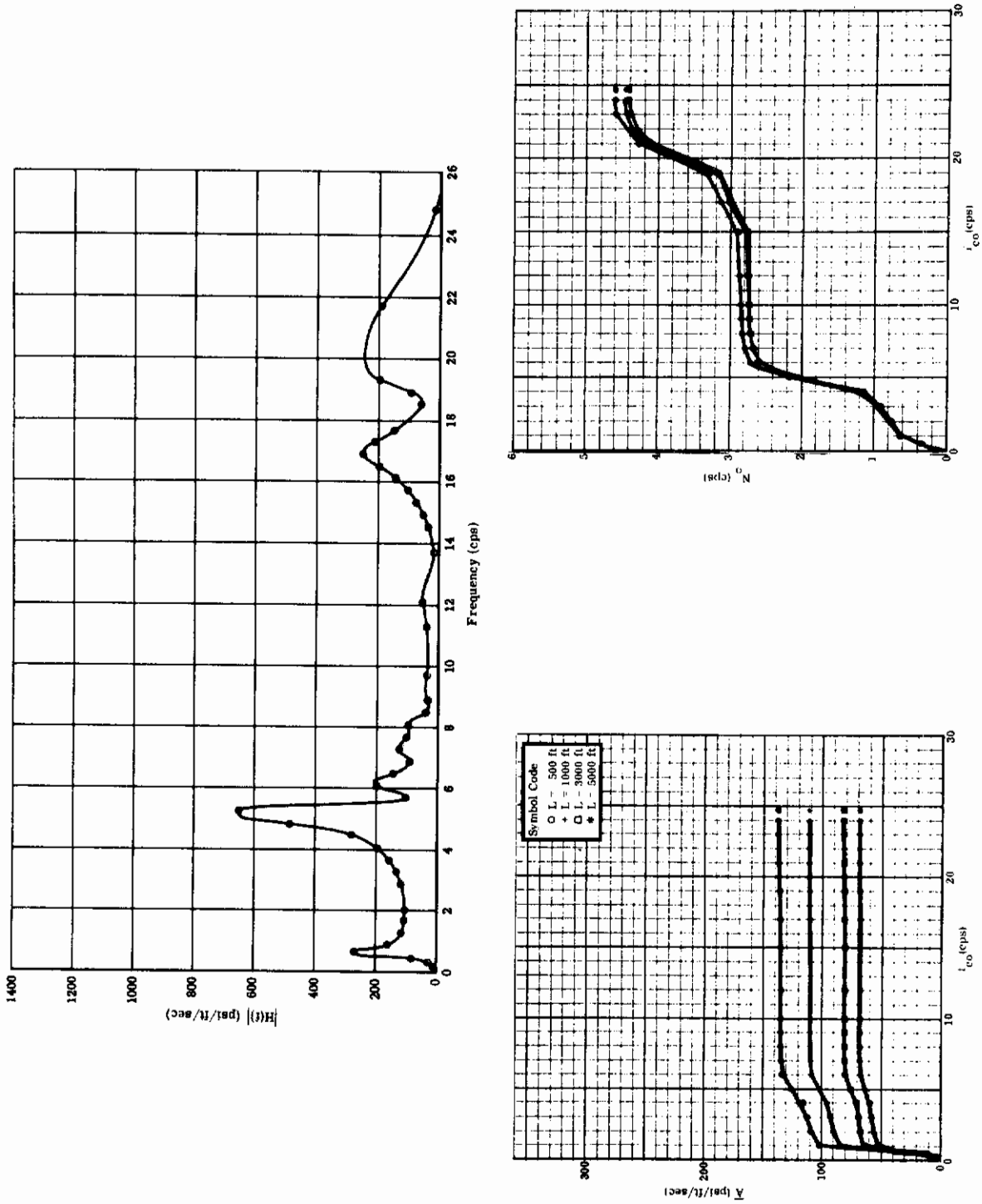

FIGURE 51 TRANSFER FUNCTION H(f), $\bar{A}$ AND N_o DATA FOR S-7, F-5A FIGHTER, CONFIGURATION (2)

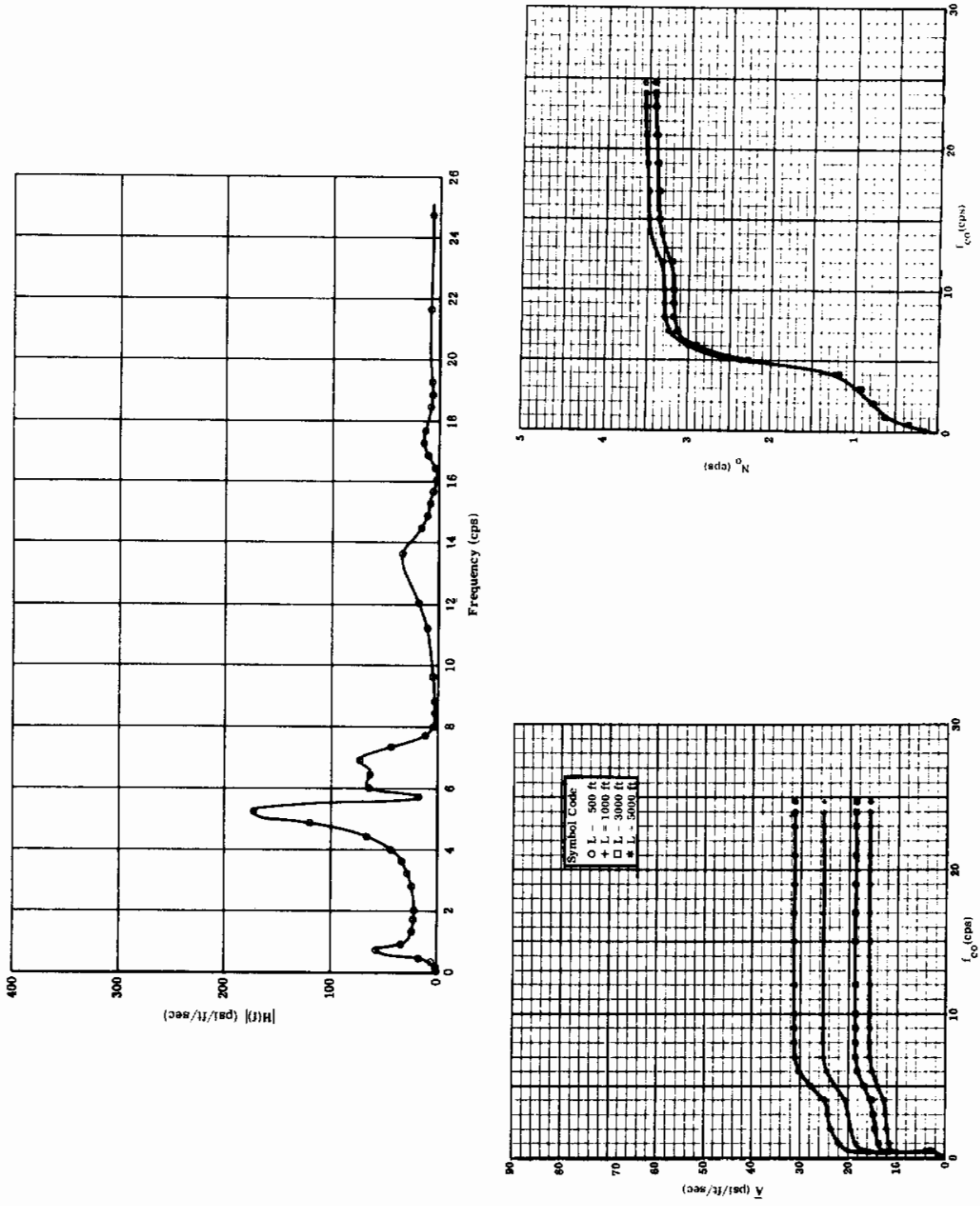

FIGURE 52 TRANSFER FUNCTION H(f), $\bar{\lambda}$ AND N_o DATA FOR S-12, F-5A FIGHTER, CONFIGURATION (2)

TABLE XX. MEAN AMPLITUDE AND FREQUENCY DATA, F-5A FIGHTER CONFIGURATION (2)

f_{co} = 28.0 cps

STRESS INDEX	IBM INDEX I	$\bar{\lambda}$				N_o (cps)				x/$\bar{A}$ NON-INTERACTING			
		L – 500 ft.	L = 1000 ft.	L = 3000 ft.	L = 5000 ft.	L = 500 ft.	L = 1000 ft.	L = 3000 ft.	L = 5000 ft.	L – 500 ft.	L = 1000 ft.	L = 3000 ft.	L = 5000 ft.
1	14	18.26	15.02	11.13	9.371	2.904	2.783	2.743	2.739	746.1	907.0	1225	1454
2	15	139.3	114.1	84.38	71.05	2.391	2.303	2.274	2.271	241.2	294.5	398.1	472.8
3	16	20.77	17.11	12.68	10.68	2.520	2.413	2.378	2.375	913.2	11109	1496	1776
4	17	140.6	115.1	85.17	71.72	2.393	2.305	2.275	2.273	215.0	262.4	354.8	421.3
6	19	6.198	4.963	3.644	3.066	9.237	9.073	9.016	9.011	2296	2867	3906	4641
7	20	137.9	112.0	82.64	69.57	4.616	4.472	4.423	4.418	205.1	252.4	342.1	406.4
8	28	1.398	1.137	.8391	.7064	3.085	2.989	2.957	2.954	457.8	562.9	762.8	906.0
9	29	9.348	7.551	5.560	4.680	5.074	4.943	4.898	4.894	1253	1551	2106	2502
10	30	67.06	53.99	39.70	33.41	4.830	4.722	4.685	4.681	243.6	302.6	411.5	488.9
11	38	1.821	1.480	1.092	.9192	3.187	3.090	3.057	3.054	358.6	441.2	598.1	710.4
12	39	31.28	25.34	18.67	15.72	3.555	3.457	3.424	3.42[illegible]	261.0	322.3	437.4	519.6
13	40	48.10	38.27	28.03	23.58	6.410	6.339	6.314	6.312	920.7	1157	1580	1878
14	41	15.35	12.42	9.147	7.699	3.742	3.642	3.609	3.606	1045	1292	1754	2084
15	42	43.87	34.89	25.55	21.49	6.462	6.393	6.369	6.367	462.0	581.0	793.4	943.0
16	43	39.39	31.32	22.93	19.29	6.475	6.407	6.383	6.381	1133	1425	1947	2314
17	44	42.80	34.02	24.91	20.95	6.527	6.461	6.438	6.436	1048	1319	1802	2142
18	45	53.20	41.92	30.06	25.73	5.721	5.714	5.711	5.711	584.3	741.6	1016	1208
19	46	11.08	8.783	6.425	5.405	8.991	8.922	8.897	8.894	4145	5228	7147	8496
20	47	48.34	38.09	27.81	23.39	5.689	5.680	5.678	5.677	562.5	713.9	978.0	1163
21	48	11.19	8.872	6.490	5.46	8.991	8.922	8.897	8.895	4123	5201.	7110	8452
22	49	6.173	4.863	3.550	2.986	5.767	5.759	5.756	5.756	528.5	670.7	918.9	1093
23	33	1077	852.3	622.9	524	8.904	8.854	8.837	8.835	520.2	657.6	899.7	1070
24	22	4.922	4.058	3.009	2.535	2.053	1.968	1.938	1.936	339.3	411.5	554.9	65.9
25	32	416.1	342.4	253.7	213.7	3.671	3.513	3.460	3.456	474.2	576.2	777.6	923.4

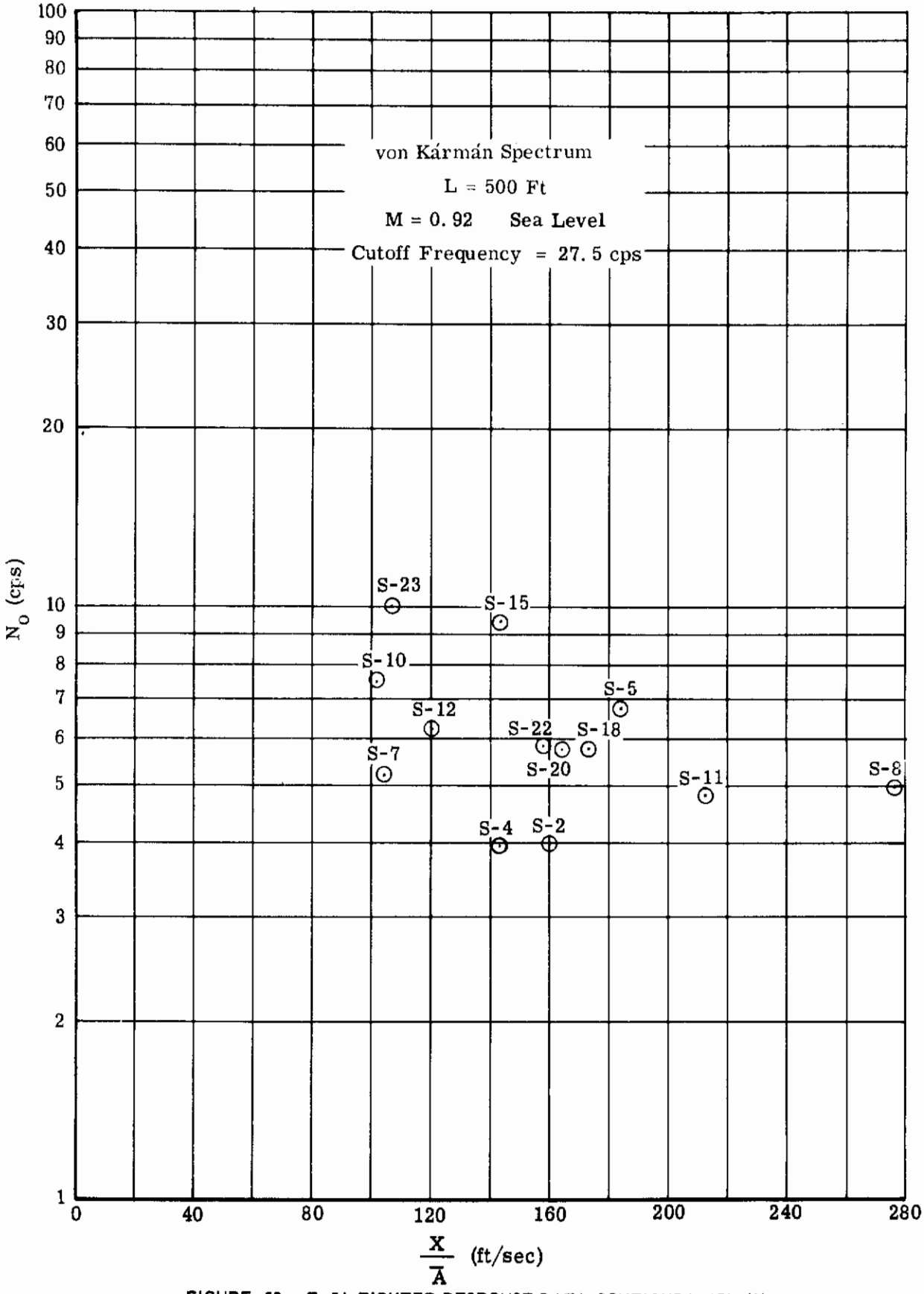

FIGURE 53 F-5A FIGHTER RESPONSE DATA CONFIGURATION (3)

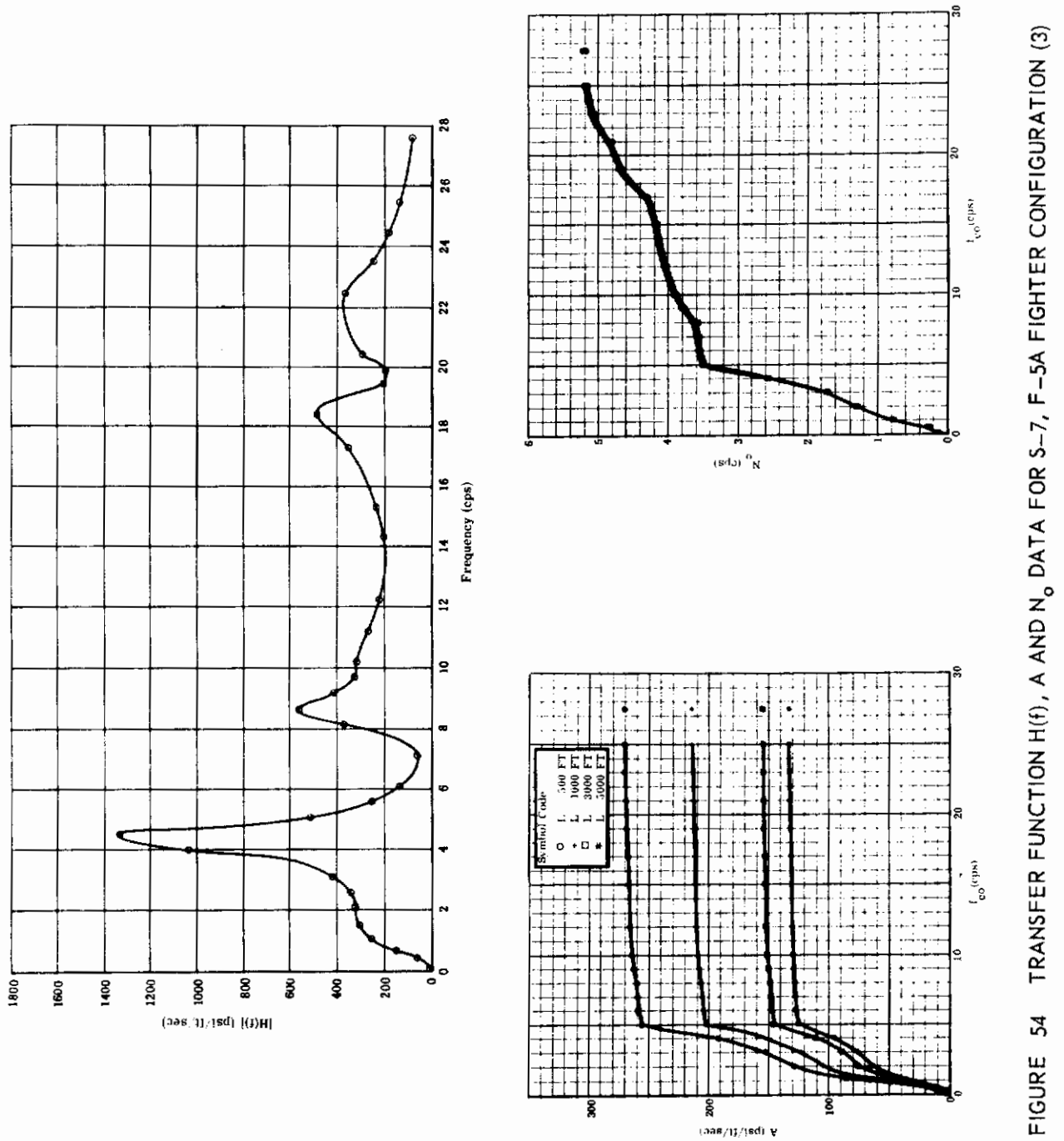

FIGURE 54 TRANSFER FUNCTION H(f), A AND N_o DATA FOR S-7, F-5A FIGHTER CONFIGURATION (3)

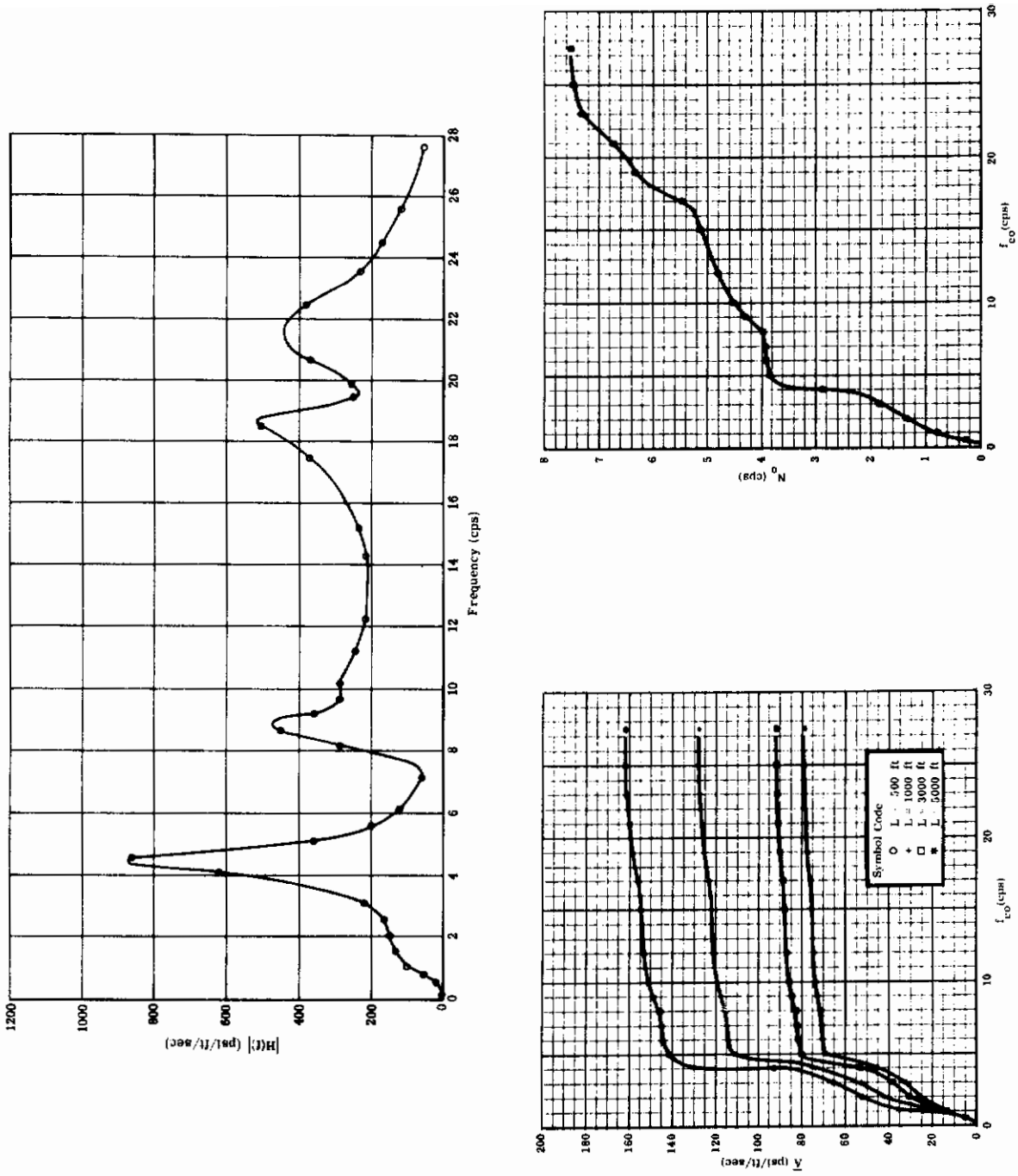

FIGURE 55 TRANSFER FUNCTION H(f), $\bar{A}$ AND N_o DATA FOR S-10, F-5A FIGHTER, CONFIGURATION (3)

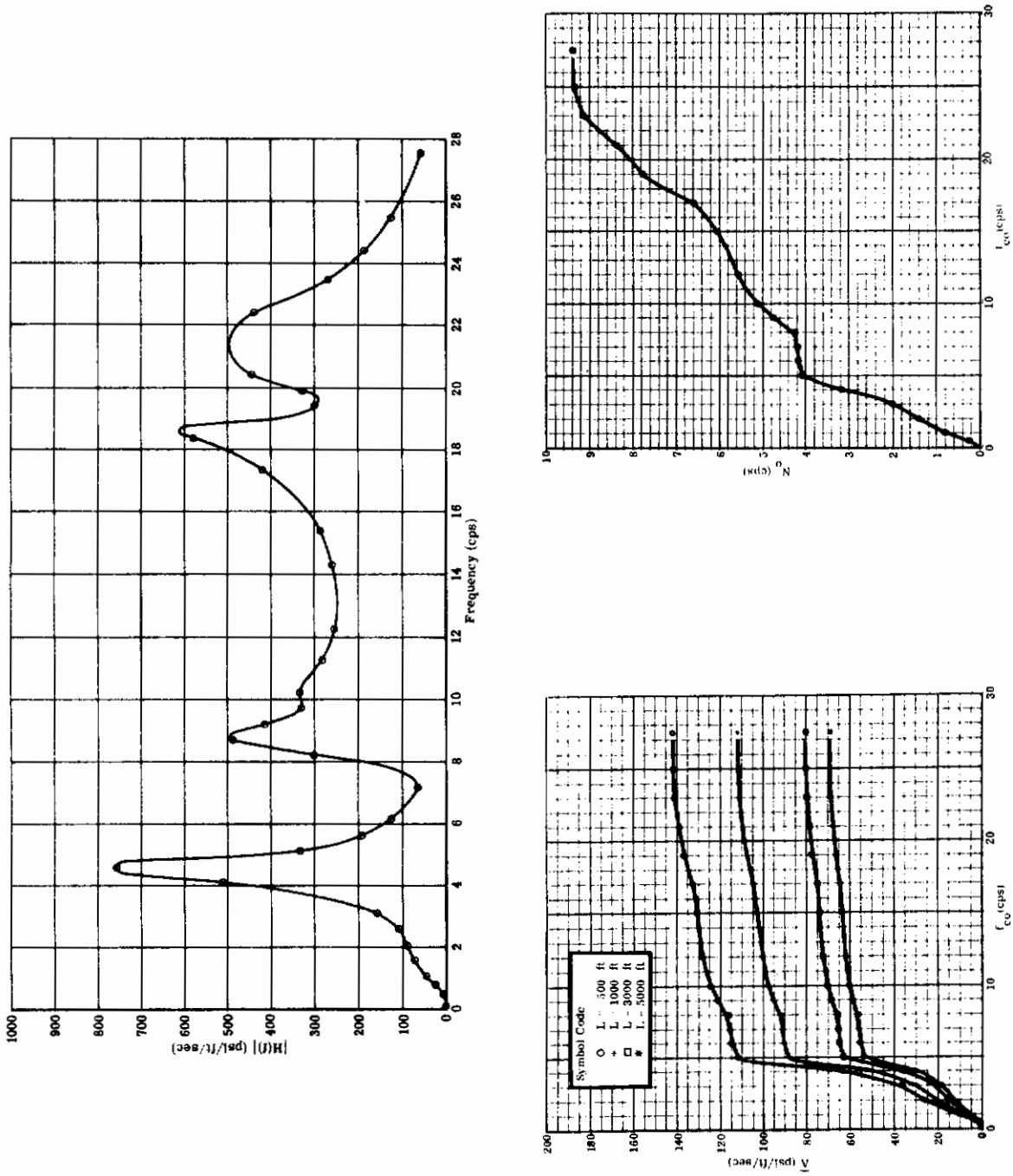

FIGURE 56 TRANSFER FUNCTION H(f), $\bar{A}$ AND N_o DATA FOR S-15, F-5A FIGHTER, CONFIGURATION (3)

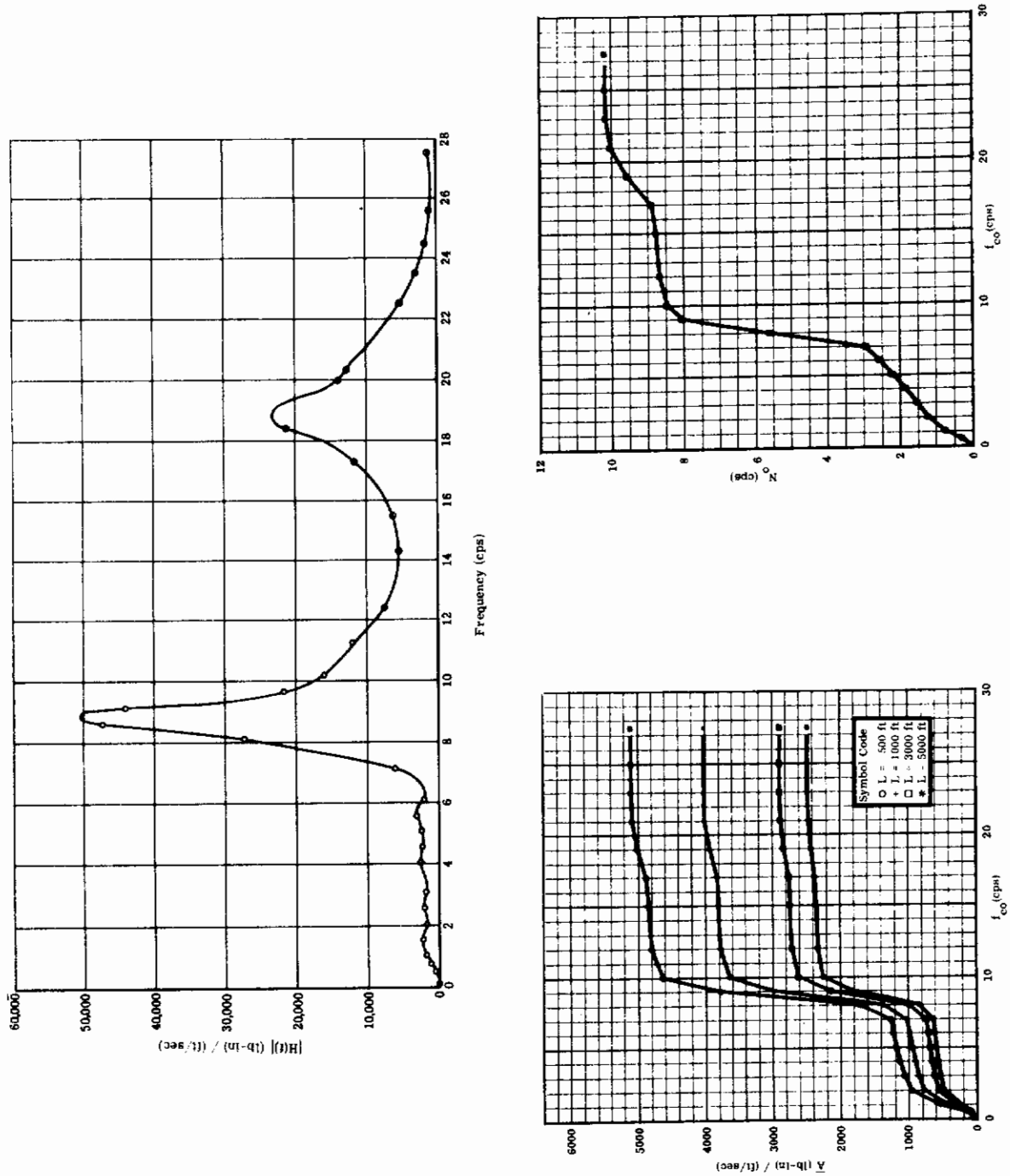

FIGURE 57 TRANSFER FUNCTION H(f), $\bar{A}$ AND N_o DATA FOR S-23, F-5 FIGHTER, CONFIGURATION (3)

TABLE XXI. MEAN AMPLITUDE AND FREQUENCY DATA, F-5A FIGHTER, CONFIGURATION (3)

f_{co} = 27.5 cps

STRESS INDEX	IBM INDEX I	$\bar{A}$				N_o (cps)				x/$\bar{A}$ NON-INTERACTING			
		L = 500 ft.	L = 1000 ft.	L = 3000 ft.	L = 5000 ft.	L = 500 ft.	L - 1000 ft.	L - 3000 ft.	L = 5000 ft.	L = 500	L = 1000	L = 3000	L = 5000
1	14	34.20	27.33	19.79	17.05	9.717	9.548	9.472	9.463	398.4	498.6	688.4	799.3
2	15	209.7	167.9	121.6	104.8	3.948	3.880	3.849	3.845	160.2	200.1	276.2	320.6
3	16	32.12	25.42	18.33	15.78	11.31	11.22	11.18	11.18	590.6	746.1	1035.	1202.
4	17	211.8	169.5	122.8	105.8	3.947	3.880	3.849	3.845	142.7	178.3	246.0	285.6
5	18	4.022	3.162	2.274	1.956	6.751	6.743	6.740	6.740	184.0	234.0	325.5	378.2
6	19	32.10	25.43	18.35	15.80	7.144	7.084	7.053	7.049	443.3	559.7	775.5	900.7
7	20	271.2	214.8	154.9	133.4	5.244	5.203	5.186	5.183	104.2	131.6	182.5	212.9
8	28	2.309	1.819	1.309	1.127	4.982	4.970	4.964	4.964	277.2	351.8	488.9	568.1
9	29	33.31	26.23	18.88	16.25	8.312	8.289	8.277	8.276	351.5	446.4	620.3	720.8
10	30	162.1	127.8	92.01	79.19	7.544	7.514	7.502	7.501	100.8	127.8	177.6	206.3
11	38	3.068	2.417	1.739	1.497	4.825	4.813	4.808	4.808	212.9	270.1	375.4	436.3
12	39	68.04	53.48	38.44	33.08	6.23	6.226	6.224	6.22	120	152.7	212.4	246.8
13	40	154.7	121.7	87.53	75.32	9.369	9.351	9.345	9.344	286.2	363.8	506.0	588.0
14	41	36.77	28.91	20.79	17.89	6.502	6.496	6.493	6.493	436.4	555.0	772.0	897.1
15	42	142.2	111.8	80.42	69.20	9.408	9.391	9.385	9.385	142.6	181.2	252.1	292.9
16	43	127.9	100.6	72.32	62.24	9.418	9.401	9.395	9.394	349.1	443.8	617.3	717.3
17	44	140.0	110.1	79.17	68.13	9.457	9.441	9.435	9.434	320.6	407.5	566.8	658.7
18	45	179.7	141.5	101.8	87.62	5.771	5.759	5.753	5.752	173.0	219.7	305.3	354.8
19	46	74.99	58.94	42.37	36.46	12.21	12.20	12.19	12.19	612.3	779.0	1084.	1259
20	47	166.0	130.7	94.02	80.91	5.768	5.755	5.749	5.749	163.9	208.1	289.2	336.1
21	48	75.75	59.54	42.80	36.83	12.21	12.20	12.19	12.19	609.1	775.0	1078.	1253.
22	49	20.56	16.19	11.64	10.02	5.842	5.830	5.825	5.824	158.0	200.7	279.0	324.2
23	33	5119	4025	2894	2490	10.21	10.20	10.19	10.19	107.2	136.3	189.7	220.4

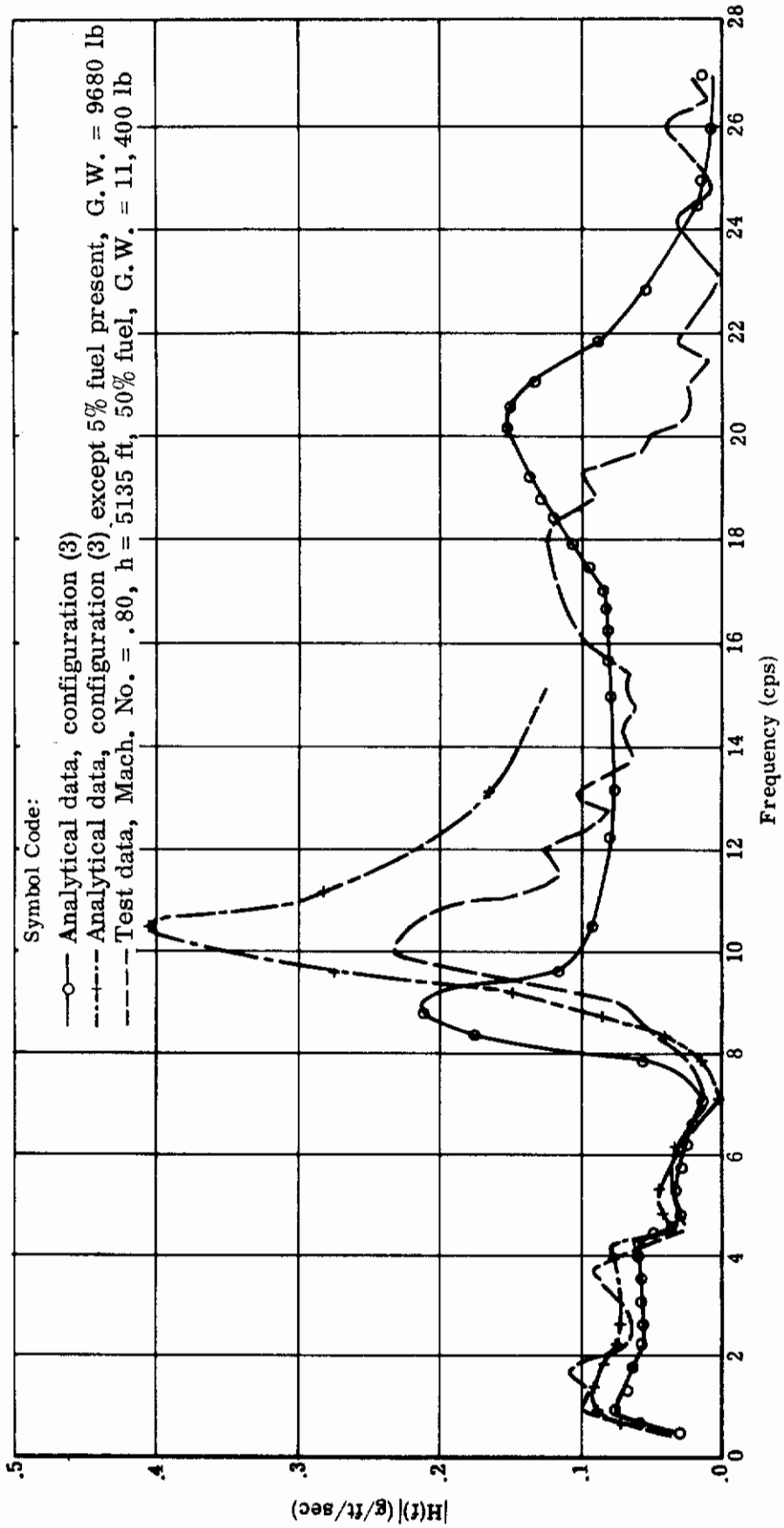

FIGURE 58 F-5A TRANSFER FUNCTION FOR C. G. ACCELERATION

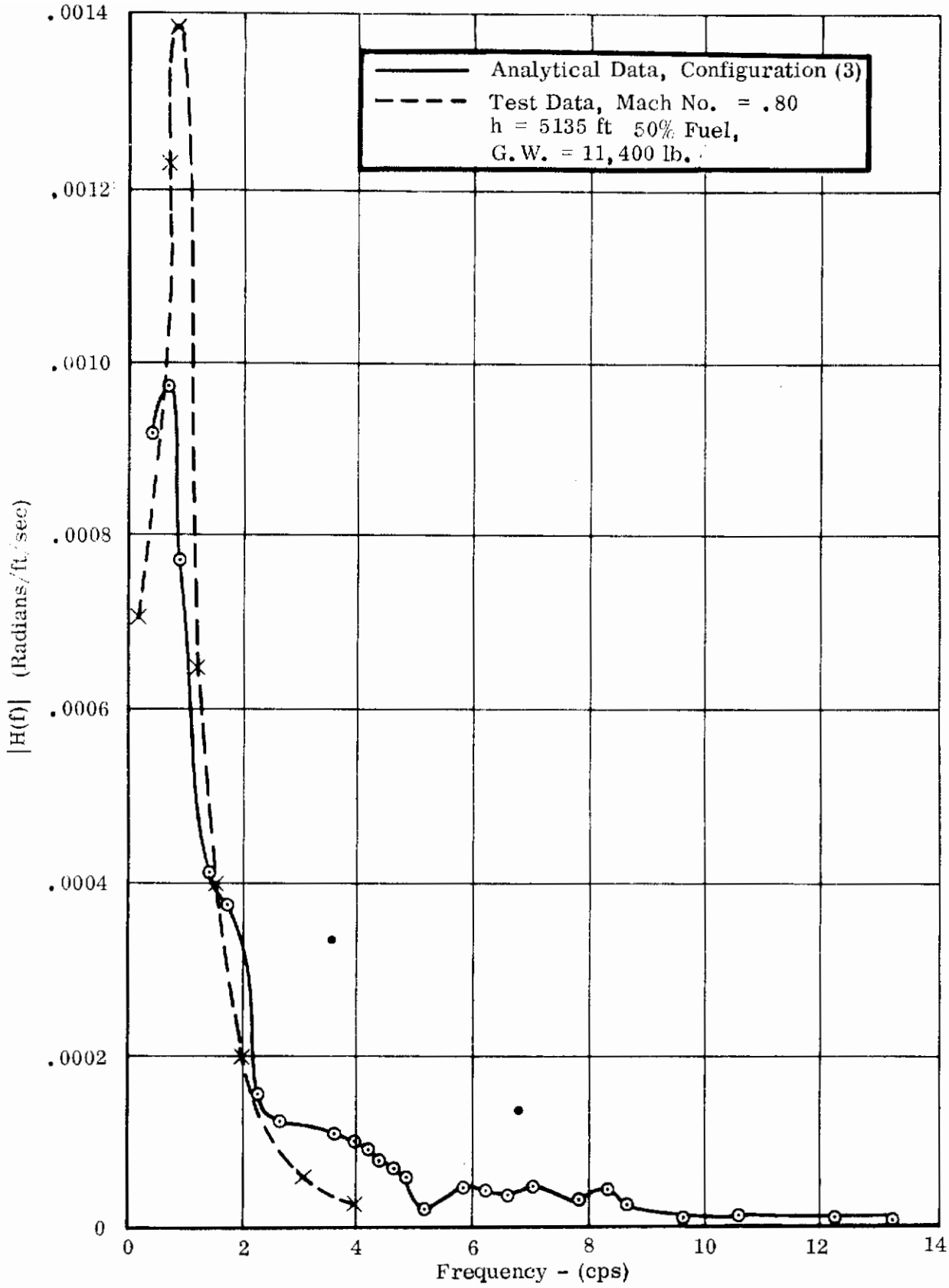

FIGURE 59 F-5A TRANSFER FUNCTION FOR RIGID PITCH MOTION

SECTION III

CONCLUSIONS AND RECOMMENDATIONS

Extensive data are presented in the gust computation of the T-38 trainer and the F-5A fighter using the power spectral approach. The integrated $\bar{A}$ and N_o data reflect the relative sensitivity of the aircraft to gust excitation as well as the vulnerability of individual stress sensitive locations and elements. Since the spectral approach is in its essence different from the established discrete gust design method, careful processing and evaluation are in order to deal with some of the unique characteristics in the computation using the new approach. Among some of the more salient factors to be considered are the definition of the input power spectrum, the choice of the stress sensitive locations, as well as the aircraft gust sensitive configuration, the accurate computation of the response transfer functions, the determination of a reasonable cut-off frequency in the numerical integration, etc. After all the factors influencing the computation are resolved, hopefully, a final standard will be established which may serve as a criterion in the gust design using the power spectral approach.

1. General Discussion

The outstanding features of the frequency response functions are produced by aeroelastic resonances. These features are also reflected in the integrated response functions $\bar{A}$ and N_o as plotted against the cut-off frequency f_{co}. An analysis carried out for the F-5A Configuration (3) shows that the peak response values obtained are consistent with the modified rigid gust formula (Reference 12):

$$R_{peak} = (\text{const.})\ (\text{DMF})\ L_g(k) \qquad (1\text{-}1)$$

where

$L_g(k) = (\rho V)\, SC_{L\alpha}\, \varphi(k)\, w_g$

DMF (dynamic magnification factor) = $1/2\ (\zeta_s + \zeta_a)$

ζ_s = % critical structural damping

ζ_a = % critical aero damping for applicable aeroelastic mode

$\varphi(k)$ = Sears gust function

In the event that highly coupled aeroelastic modes are encountered, corresponding expressions for higher order systems can be employed to provide qualitative information.

Another point of interest is the influence of the scale of turbulence on the computed $\bar{A}$ and N_o data. Equations (4-13), (4-14) show that, at frequencies for aeroelastic peak response, the $\bar{A}$ and N_o functions will assume positive variations in slope when plotted against the cut-off frequency. Starting with the von Kármán power spectrum, Equation (4-2) may be rewritten as:

$$\Phi_w(f) = \left(\frac{2\sigma_w^2 L}{V}\right)\left[\frac{1 + \frac{8}{3}(1.339\ w\ L/V)^2}{[1 + (1.339 w\ L/V)^2]^{11/6}}\right] \qquad (1\text{-}2)$$

It is observed that for $f < V/(2\pi L)$,

$$\Phi_w(f) \cong \frac{2\sigma_w^2 L}{V}\ (1 + \epsilon) \qquad (1\text{-}3)$$

where ϵ is a number with a smaller order of magnitude as compared to unity. On the other hand, it is noted that for $f >> V/(2\pi L)$,

$$\Phi_w(f) \cong \frac{16}{3}\left(\frac{V}{L}\right)^{2/3} \sigma_w^2\ \frac{1}{(1.339 \times 2\pi f)^{5/3}} \qquad (1\text{-}4)$$

$$f^2\Phi_w(f) \cong \frac{16}{3}\left(\frac{V}{L}\right)^{2/3} \sigma_w^2\ \frac{f^{1/3}}{(1.339 \times 2\pi)^{5/3}} \sim f^{1/3} \qquad (1\text{-}5)$$

The function $(f^2\Phi_w)$, which forms part of the integrand in the numerator of (4-14), accentuates the variation of N_o versus f_{co} at higher frequencies. Alternatively, the bulk of the contribution to $\bar{A}(f_{co})$ is derived from the lower frequency range. Inspection of the above approximate expression (6-4) of Φ_w for $f \gg V/(2\pi L)$ shows that $\Phi_w \sim \frac{1}{L^{2/3}} \cdot \frac{1}{f^{5/3}}$.

Accordingly, omitting subscript w,

$$A^2(f_{co}) \cong \frac{\int_o^{V/2\pi L} \left[\frac{2\sigma^2 L}{V}\right] |H(f)|^2 \, df + \int_{V/(2\pi L)}^{f_{co}} \left[\frac{16}{3}\left(\frac{V}{L}\right)^{2/3} \sigma^2\right] \left[\frac{f^{-5/3}}{(2\pi \times 1.339)^{5/3}}\right] |H(f)|^2 \, df}{\int_o^{\infty} \Phi_w(f) \, df} \qquad (1\text{-}6)$$

Since the frequency response functions vanish at f = 0, the first term of the numerator is much smaller than the second in the majority of the cases. As a result, $\bar{A}^2(f_{co})$ may be given as:

$$\bar{A}^2(f_{co}) \cong \frac{\frac{16}{3}\left(\frac{V}{L}\right)^{2/3} \pi \int_{(V/2\pi L)}^{f_{co}} f^{-5/3} \, |H(f)|^2 \, df}{(2\pi \times 1.339)^{5/3}} \qquad (1\text{-}7)$$

which shows that for fixed H(f), V, etc., $\bar{A}$ is proportional to $1/L^{1/3}$. Thus, for L = 500 feet, 1000 feet, 3000 feet, and 5000 feet, the corresponding values of $\bar{A}$ are expected to assume the following ratios: 2.15, 1.71, 1.18, 1.0. This phenomenon, which was first described by Dr. J.C. Houbolt, is illustrated for a number of critical stress elements in Tables XXII and XXIII. In the tables, it may be observed that the integrated amplitudes $\bar{A}$ computed for various scales of turbulence assume ratios close to those predicted above.

Similarly, the numerator and denominator in Equation (4-14) may be approximated by omitting the integration range $0 < f < V(2\pi L)$ so that:

$$N_o^2(f) \cong \frac{\int_{V(2\pi L)}^{f_{co}} |H(f)|^2 f^{1/3} \, df}{\int_{V(2\pi L)}^{f_{co}} |H(f)|^2 f^{-5/3} \, df} \qquad (1\text{-}8)$$

Thus, $N_o^2(f)$ is independent of L to a good approximation.

TABLE XXII. AMPLITUDE RATIOS AS FUNCTIONS OF THE SCALES OF TURBULENCE, T-38 TRAINER

	Configuration (1)			Configuration (2)			Configuration (3)		
Element	$\bar{A}_{500'}/\bar{A}_{5000'}$	$\bar{A}_{1000'}/\bar{A}_{5000'}$	$\bar{A}_{3000'}/\bar{A}_{5000'}$	$\bar{A}_{500'}/\bar{A}_{5000'}$	$\bar{A}_{1000'}/\bar{A}_{5000'}$	$\bar{A}_{3000'}/\bar{A}_{5000'}$	$\bar{A}_{500'}/\bar{A}_{5000'}$	$\bar{A}_{1000'}/\bar{A}_{5000'}$	$\bar{A}_{3000^2}/\bar{A}_{5000^2}$
S-1	2.03	1.61	1.16	2.0	1.60	1.16	2.01	1.60	1.15
S-2	2.03	1.61	1.15				2.02	1.61	1.16
S-5	1.95	1.66	1.16	1.92	1.57	1.17	1.93	1.57	1.15
S-8				1.92	1.57	1.17			
S-9				1.92	1.58	1.17			
S-12				1.94	1.58	1.17			
S-13	2.02	1.60	1.16				2.00	1.60	1.15
S-14				1.94	1.58	1.17			

TABLE XXIII. AMPLITUDE RATIOS AS FUNCTIONS OF THE SCALES OF TURBULENCE, F-5A FIGHTER

	Configuration (1)			Configuration (2)			Configuration (3)			
Element	$\bar{A}_{500'}/\bar{A}_{5000'}$	$\bar{A}_{1000'}/\bar{A}_{5000'}$	$\bar{A}_{3000'}/\bar{A}_{5000'}$	$\bar{A}_{500'}/\bar{A}_{5000'}$	$\bar{A}_{1000'}/\bar{A}_{5000'}$	$\bar{A}_{3000'}/\bar{A}_{5000'}$	$\bar{A}_{500'}/\bar{A}_{5000'}$	$\bar{A}_{1000'}/\bar{A}_{5000'}$	$\bar{A}_{3000'}/\bar{A}_{5000'}$	
S-4	2.00	1.59	1.17	1.96	1.60	1.19				
S-7	2.01	1.61	1.17	1.98	1.60	1.19	2.03	1.61	1.16	
S-10	2.02	1.61	1.17				2.04	1.61	1.16	
S-12	2.02	1.61	1.17	1.99	1.61	1.19				
S-13										
S-15							2.05	1.61	1.16	
S-23	2.05	1.62	1.17				2.06	1.62	1.16	

2. Discussion of T-38 Trainer Gust Data

Frequency response functions are presented for T-38 trainer gust critical stress elements corresponding to three flight configurations: 5 percent fuel at sea level and at 30,000 feet, 100 percent fuel at sea level. The altitude variation is chosen to show effect of density and speed on the stress statistics and the weight variation is chosen to indicate the effects of fuel consumption on stress statistics.

Configuration (1)

The responding aeroelastic mode frequencies are given in Table XII, page 38. It is observed that for the sea level case, the aerodynamic effects on the response frequencies are considerable. All of the responding aeroelastic modes are present in the wing and fuselage stresses except for the horizontal tail bending mode. The horizontal tail stresses are affected by all modes (including wing modes) owing to the coupling between the wing and aft fuselage motion. Examination of Table XII shows that the aerodynamic spring effect is stiffening in the case of the first wing-fuselage bending mode. It has an opposite effect in the case of the first wing torsion mode. In the latter case, considerable response level attained near 32 cps is due to the strongly coupled second wing bending and first wing torsion modes which have virtually equal aeroelastic resonant frequencies. The large positive slope exhibited by $\bar{A}(f_{co})$ and $N_o(f_{co})$ for the wing stresses between 18 and 35 cps is due to the second fuselage-wing bending mode peak response at 26.3 cps and the second wing fuselage, first wing torsion peak at 32.2 cps. The tail bending and fuselage bending mode frequencies are not significantly affected by aerodynamics.

Configuration (2)

Although the aeroelastic modes responding for this case are the same as those responding for the sea level case, the aerodynamic spring effects are considerably less (Table XII). Consequently, the aeroelastic resonances occur somewhat closer to the natural frequencies for the first two modes. The first wing bending peak at 30,000 feet occurs 3 cps lower than the corresponding peak sea level response. Also, the second wing-fuselage bending and first torsion modes evidence distinct uncoupled response peaks which are reflected in slope changes in $\bar{A}(f_{co})$ and $N_o(f_{co})$. The $N_o(f_{co})$ plots should not be interpreted as evidencing a constant positive asymptotic slope beyond 43 cps. Inspection of Equations (4-13) and (4-14) shows that calculations at higher frequencies will result in a subsequent decrease in slope for $N_o(f_{co})$ due to the "trough" between the first torsion peak and the

succeeding peak. Another factor which may change the N_o plot pattern is the structural damping at higher frequencies. A higher damping factor will decrease the amplitude of N_o substantially in this frequency region. The 30 percent deviation for S-7 from the rigid gust formula (ρV) behavior is due to the fact that the principal S-7 response mode for the higher altitude is first wing torsion. Since this mode responds at 42 cps for the high altitude case and at 32 cps for the low altitude case, the gust power spectrum differs approximately by a factor of $(42/32)^{5/3} = 1.6$ for the contributing bands. Consequently, the rms sea level response differs from the rms 30,000 foot response approximately by the factor $\sqrt{1.6}\,\rho V$.

The $N_o(f_{max})$ values for Configuration (2) reflect the higher mode response in the case of S-7 and S-13. However, the higher modes have a pronounced effect on $N_o(f_{max})$ for Configuration (1) in the cases of S-7, S-13, and S-2. The wing-fuselage modes which tend to produce high values for $N_o(f_{max})$ for S-2 are not strongly excited at high altitudes. This is indicative of the lack of the stiffening effect of the wing lift in these modes which, at lower altitudes, is sufficient to counteract the energy dissipation due to fuselage structural damping. Similar conclusions may be drawn for the relative sensitivity of the critical fuselage stress elements at different altitudes for both T-38 and F-5A which are reflected in the N_o versus $x/\bar{A}$ plots. Examination of the response functions for the 5 percent fuel sea level and 30,000 foot cases shows that the pitch (short period) mode response frequencies are 1.35 cps and 0.8 cps respectively. This decrease with altitude is due to the aerodynamic spring stiffening increases produced by increased dynamic pressure.

Configuration (3)

The effect of increased fuselage weight on the aeroelastic frequencies is established by a comparison of frequency data for Configurations (1), (3) in Table XII. The first fuselage bending response drops 2 cps in the heavier configuration. The first wing bending response drops 3-4 cps. These changes are reflected in the $N_o(f_{max})$ for the two configurations. In all cases, the $N_o(f_{max})$ levels for the heavy configuration are reduced compared to the light configuration. The difference between $N_o(f_{max})$ for the light and heavy cases is reduced due to the aeroelastic coupling exhibited by second wing bending and first wing torsion. It is noted that these two elastic modes respond near the 33 cps second bending mode natural frequency for the light configuration. They respond near the 40.8 cps first torsion mode natural frequency for the heavy case. This mode pair

has a considerable effect on the high $N_o(f_{max})$ values in Configuration (3) attained for S-1, S-2, and S-13 which are comparable to those obtained for Configuration (1). Examination of the response function (S-15) for the horizontal stabilizer shows the considerable influence of mode pair (5, 6) arising from the aft fuselage slope present for both cases.

The pitch frequency for the 100 percent fuel case, Configuration (3), is not appreciably different from the pitch frequency for Configuration (1). This is due to the fact that the fuel cells are located near the airplane center of gravity. Consequently, changes in the fuel weight do not significantly affect the airplane center of gravity moment of inertia. However, the pitch dynamic magnification for the 5 percent fuel case exceeds the magnification for 100 percent case.

3. Discussion of F-5A Fighter Gust Data

Frequency response functions for the F-5A gust critical stress elements are presented for Configuration (1), (2) (sea level, 30,000 feet) and for Configuration (3) (sea level). The altitude variation between Configurations (1), (2) shows the effect of density and speed for the aircraft carrying pylons with empty tanks. The effects of varying store configuration are demonstrated by comparing results for Configurations (1) and (3). The latter configuration represents an aircraft with bare wing with tip-attached sidewinders.

Configuration (1)

The responding aeroelastic modes are shown in Table XIII. The aeroelastic frequencies are not appreciably different from the natural frequencies due to the prominance of inertial effects of the wing and stores relative to aerodynamic effects. All the responding wing modes are present for wing stresses inboard of Wing Station 85. Stresses outboard of Wing Station 85 are not appreciably affected by the 22.2 cps Wing Station 85 tank roll-yaw mode. Modes (6) and (7) are primarily horizontal tail bending; the tail tip motion is approximately 10 times the wing tip motion in both modes. Nevertheless, the wing stresses exhibit considerable response in these modes due to the small contribution of the tail to the generalized masses.

Configuration (2)

Due to the prominance of inertial effects, particularly at high altitudes, the responding aeroelastic modes for this configuration have virtually the same frequencies as the natural modes. The only exceptions are the strongly coupled set of modes 5, 6, and 7 (Table XIII). The rigid gust formula ratio for the two configurations

$$(\rho v)_{\substack{\text{S. L.} \\ \text{M.81}}} / (\rho v)_{\substack{30,000' \\ \text{M.81}}} \cong 3.3$$

in general, is slightly higher than the calculated ratios:

$$\bar{A}(f_{max})_{\substack{\text{S. L.} \\ \text{M.81}}} / \bar{A}(f_{max})_{\substack{30,000' \\ \text{M.81}}}$$

The $N_o(f_{max})$ values for the F-5A are generally lower than the values obtained for comparable cases of the T-38. For Configuration (3) of T-38, (100 percent fuel at sea level) approximately 1/3 of the critical stresses exhibit $N_o(f_{max})$ values exceeding 10 cps. The values of $N_o(f_{max})$ for Configurations (1), (2) of F-5A are essentially independent of altitude. However, for the T-38 trainer Configuration (3) (5 percent fuel, 30,000 feet), the values obtained for $N_o(f_{max})$ are considerably less than the sea level values. Both of these differences are due to the heavy wing-store combination which results in lower aeroelastic frequencies as well as lessened aerodynamic and altitude effects which arise from the prominance of inertia forces for Configurations (1), (2) of the F-5A.

Configuration (3)

The important aeroelastic modes for Configuration (3), M.92 at sea level are shown in Table XIII. The first wing torsion and first fuselage are aerodynamically coupled and the resultant aeroelastic mode occurs at 8.5 cps. In addition, there is significant aerodynamic coupling between modes (3) and (5). This coupling can be attributed to the similarity of the wing motions for these two modes (Figure 21).

Further information can be deduced from Figure 21 by comparing the ratios of the nose motion to wing tip motion for modes (3) and (5). These ratios are approximately 4 1 and 1.4 respectively. Accordingly, a much larger fraction of the energy developed by gust forces is converted into kinetic energy for wing motion for mode (5) as compared to mode (3). Consequently, the coincidence of this factor and the strong coupling leads to the result that the majority of the wing stress responses

at 8.5 cps are principally derived from mode (5). This situation supplies an excellent example of the fallacy of a priori omission (from the structural mode model) of higher natural modes. In this case, considerable error would result for 8.5 cps responses if mode (5) (natural frequency = 17.32 cps) were omitted. The statistical implications of such an error are apparent in the $\bar{A}(f_{co})$, $N_o(f_{co})$ plot for the cases of S-23. Inspection of these plots reveals significant increases are derived from the band neighboring 8.5 cps.

The $N_o(f_{max})$ results for Configuration (3) generally exceed those of Configuration (1). This is attributable to a number of factors. The first wing bending and wing torsion modes occur at higher structural frequencies for Configuration (1) as compared to Configuration (3). Nevertheless, the higher modes of Configuration (1), such as second wing bending, second wing torsion, occur at frequencies lower than those exhibited by Configuration (3). Since the product $f^2\Phi_w(f)$ is proportional to $f^{1/3}$ in Equation (5-14) for large f, these higher modes are more heavily weighted than the lower modes. Secondly, Configuration (1) exhibits considerable pitch response compared to that of Configuration (3). Thirdly, Configuration (3) higher mode wing responses generally exceed those of (1) due to the transfer of energy to the stores as in the case of the Wing Station 85 store yaw-second wing bending aeroelastic mode. This energy is developed from the work done by the gust generalized forces in the second wing bending component. In the case of Configuration (3), no under-wing stores are present to absorb this energy. Hence, a greater fraction of the energy goes into kinetic energy represented by wing surface motion.

4. Concluding Remarks

The foregoing review of the results clearly indicates the importance of aerodynamic effects in determining the characteristics of frequency response functions and the derived statistical data. Indeed, aerodynamic effects play a decisive role in pinpointing the fuselage stress elements as gust critical at low altitudes. Another important factor in establishing gust load statistics is the structural model, i.e., modal description of the airplane analyzed. It was shown that modes with natural frequencies considerably higher than the anticipated response range must be included to predict the response for situations where aeroelastic coupling significantly lowers the response frequencies. The interpretation of the

data is materially enhanced by the scaling laws illustrated in subsection 1 and is aided by the employment of free-free airplane modes. Comparison of the computed data with flight test data whenever possible, also strengthens the analytical approach. In conclusion, it is to be anticipated that the quality of the design based on the spectral-statistical approach advocated in this report will be no better than the quality of the aeroelastic model used to calculate the frequency response functions.

The statement about the intercoupling of the higher modes should not be construed as a recommendation to include as many modes as permitted by available computer storage. It is known that the wing gust admittance function modulus squared is asymptotically proportional to 1/f. The above behavior, coupled with the fact that nondimensional structural damping factor ζ increases as the number of node lines increases, indicates that the numerator integral in Equation (4-14) contributes little above some moderate cutoff frequency despite the adverse factor $f^2 \Phi_{in} \sim f^{1/3}$ in the integrand. This point may be resolved through additional evaluation of the flight test data and a more critical examination of the aircraft structural damping behavior (as a function of the number of slip planes, associated with modal inflection points) along the frequency range.

APPENDIX I

METHOD OF FREQUENCY RESPONSE CALCULATION

In this Appendix, a detailed derivation of the equations of motion and the response quantities (deflection, acceleration, load, and stress) are presented. The equations are developed by the collocation method extended to the approximate modal solution using Galerkin's method. Frequency response functions due to a sinusoidal gust field or an external sinusoidal force may be determined through the use of these equations.

In the analysis, the following sign conventions are used. The coordinates (x, y, z), the forces and deflections are positive aft, outboard port, and downward. Gust velocity is positive downward if specified as a downwash. Shear, bending moment, yaw moment, and torque positive sign conventions are consistent with the requirements for structural analysis and are accounted for in the load integration matrices. Shear is positive up, outboard, and aft. Bending moment for the wing, tail, and fuselage is positive for compression in the upper fibers; yaw moment is positive for nose inboard on the left wing; torque on the wing is positive nose up.

Nomenclature

b_r	Reference semichord, feet
g	Structural damping coefficient
$k_r=\omega b_r/V$	Reduced frequency
S	Reference length, feet
t	Time, seconds
V	Vehicle velocity, feet/second
w_g	Local spanwise downwash velocity of gust, foot/second
W_g	Reference downwash velocity of gust, foot/second
x, y, z	Cartesian coordinates
ϵ	Error in series solution, pounds
ρ	Air density, slug/foot^3
ω	Circular frequency, radian/second

Subscripts and Signs

$(\ )_e$	Denotes external
$(\ )_F$	Refers to flexible modes

$( )_g$	Denotes gust
$( )_m$	Denotes motion
$( )_R$	Refers to rigid modes
$( )'$	Denotes use of free-free modes
$\bar{( )}$	Denotes complex amplitude, in general; in the case of mass terms, denotes complex mass which includes oscillatory aerodynamic effects.

Matrix Convention and Size Index

$[\ ]$	Square or rectangular matrix
$\{\ \}$	Column matrix
$\lceil\ \rfloor$	Diagonal matrix
$[\ ]^*$	Transposed matrix
$[\ ]^{-1}$	Inverse matrix
$[I]$	Unit matrix
R	Number of rigid modes. In the analysis R = 2, which consists of the rigid translation and the pitch motion at the reference point.
P	Number of control points
n	Number of elastic modes
L	Number of load or stress locations
f	Number of aerodynamic sections on a rigid fuselage

MATRIX	SIZE	UNITS	DESCRIPTION
$\left[A'_F\right]$	n x n	pound/inch	Flutter characteristic matrix
$\left\{\bar{a}'_F\right\}$	n x 1	inch	Amplitude coefficient of free-free modal series
$\left\{\bar{a}_G\right\}$	R x 1	$\left\{\frac{\text{inch}}{\text{radian}}\right\}$	Generalized coordinates describing rigid response of the reference element
$\left\{\bar{a}_R\right\}$	R x 1	$\left\{\frac{\text{inch}}{\text{radian}}\right\}$	Generalized coordinates describing total (rigid plus elastic) response of the reference element
$\left[a_{RF}\right]$	R x n	$\left[\frac{\text{ND}}{\text{radian/inch}}\right]$	Reference point modal series matrix

MATRIX	SIZE	UNITS	DESCRIPTION
$\left[\overline{B}_F'\right]$	n x P	ND	Generalized work coefficient matrix due to gust or external forces acting at control points
$\left[c\right]$	P x P	pound-second/ inch	Damping coefficient matrix corresponding to control point velocity
$\left[C_F'\right]$	n x n	pound-second/ inch	Generalized damping matrix
$\left[C_g\right]$	P x P	ND	Harmonic gust aerodynamic influence coefficient matrix for control point angle of attack due to gust
$\left[C_{gR}\right]$	f x f	ND	Harmonic gust aerodynamic influence coefficient matrix for a rigid fuselage with "f" aerodynamic sections
$\left[C_h\right]$	P x P	ND	Oscillatory aerodynamic influence coefficient matrix for control point motion
$\left[C_{hR}\right]$	f x f	ND	Oscillatory aerodynamic influence coefficient matrix due to rigid fuselage motion
$\left[\overline{D}_F'\right]$	n x R	$\left[\text{ND} \vdots 1/\text{inch}\right]$	Generalized work coefficient matrix due to gust or external forces acting at the reference point
$\left\{\overline{F}_e\right\}$	P x 1	pound	Externally applied forces at control points
$\left\{\overline{F}_g\right\}$	P x 1	pound	Control point force matrix due to gust
$\left\{\overline{F}_m\right\}$	P x 1	pound	Control point force matrix due to motion
$\left\{\overline{F}_s\right\}$	P x 1	pound	Control point load response matrix
$\left[g_F\right]$	n x n	ND	Structural damping coefficient matrix
$\left[h_F\right]$	P x n	ND	Cantilever modal series matrix
$\left[h_F'\right]$	P x n	ND	Free-free modal series matrix
$\left\{\overline{h}_1\right\}$	P x 1	inch	Absolute control point deflection response

MATRIX	SIZE	UNITS	DESCRIPTION
$[h_R]$	P x R	[ND | inch]	Rigid body modal matrix for control points
$[h_{R_o}]$	f x R	[ND | inch]	Rigid body modal matrix for rigid fuselage motions
$[\bar{h}_o]$	P x 1	inch	Control point motion due to reference point motion
$[k]$	P x P	pound/inch	Cantilever spring constant matrix
$[K'_F]$	n x n	pound/inch	Generalized spring matrix
$[\Delta m]$	R x R	$\left[\begin{array}{c\|c} \text{lb sec}^2/\text{in} & \text{lb sec}^2 \\ \hline \text{lb sec}^2 & \text{lb in sec}^2 \end{array}\right]$	Generalized mass matrix of reference point mass
$[\Delta \bar{m}]$	R x R	"	Generalized mass plus aero matrix for reference point motion
$[\bar{M}]$	L x 1	inch-pound	Bending moment response
$[M]$	P x P	pound second^2/ inch	Mass Matrix
$[\bar{M}]$	P x P	pound second^2/ inch	Mass plus aero matrix
$[M/F]$	L x P	inch	Bending moment coefficient matrix
$[m'_{FF}]$	n x n	pound second^2/ inch	Generalized mass matrix
$[\bar{m}'_{FF}]$	n x n	pound second^2/ inch	Generalized mass plus aero matrix
$[m'_{FR}]$	n x R	[lb sec^2/in | lb sec^2]	Rigid body and elastic mass coupling matrix
$[\bar{m}'_{FR}]$	n x R	[lb sec^2/in | lb sec^2]	Rigid body and elastic mass plus aero coupling matrix
$[\bar{m}_{RR}]$	R x R	$\left[\begin{array}{c\|c} \text{lb sec}^2/\text{in} & \text{lb sec}^2 \\ \hline \text{lb sec}^2 & \text{lb in sec}^2 \end{array}\right]$	Generalized airplane rigid mass plus aero matrix

MATRIX	SIZE	UNITS	DESCRIPTION
$\left\|\overline{Q}_e\right\|$	R x 1	$\left\|\frac{\text{pound}}{\text{inch pound}}\right\|$	External force acting at the reference point
$\left\|\overline{Q}_g\right\|$	R x 1	$\left\|\frac{\text{pound}}{\text{inch pound}}\right\|$	Aerodynamic force due to gust acting at the reference point
$\left\|\overline{Q}_m\right\|$	R x 1	$\left\|\frac{\text{pound}}{\text{inch pound}}\right\|$	Generalized aerodynamic force due to motion of the reference point
$\left\|\overline{T}\right\|$	L x 1	inch pound	Torque response
$\left\|T/F\right\|$	L x P	inch	Torque coefficient matrix
$\left\|\overline{V}\right\|$	L x 1	pound	Shear response matrix
$\left\|V/F\right\|$	L x P	ND	Shear coefficient matrix
$\left\|W\right\|$	P x P	ND	Aerodynamic weighting matrix for motion of control points
$\left\|W'\right\|$	P x P	ND	Gust weighting matrix for control points
$\left\|W_R\right\|$	f x f	ND	Aerodynamic weighting matrix for fuselage sections due to reference point motion (rigid fuselage)
$\left\|W'_R\right\|$	f x f	ND	Gust weighting matrix for fuselage sections (rigid fuselage)
$\left\|w_g/W_g\right\|$	P x 1	ND	Gust input column matrix
$\left\|\overline{YM}\right\|$	P x 1	inch pound	Yaw moment response matrix
$\left\|YM/F\right\|$	L x P	inch	Yaw moment coefficient matrix
$\left\|\epsilon\right\|$	P x 1	pound	Error in series solution
$\left\|\omega^2_F\right\|$	n x n	$1/\text{second}^2$	Frequency matrix

I.1 General Formulation

The equation of motion of a damped elastic system free in space is

$$\left[M\right]\left\{\ddot{h}_1\right\} + \left[c\right]\left\{\dot{h}_1 - \dot{h}_o\right\} + \left[k\right]\left\{h_1 - h_o\right\} = \left\{F(t)\right\} \tag{I-1}$$

in which h_1 is the matrix of absolute control point deflections, $\{h_o\}$ is the matrix of control point deflections due to rigid body motion, M is the mass matrix, c is the damping matrix, k is the spring matrix for the system cantilevered from the reference point of the rigid body motion, and F(t) is the matrix of external control point forces. Either viscous damping or structural damping may be considered. For the case of the structural damping, $c = kg/\omega$. The deflections due to the rigid body motion may be found by defining a rigid body modal matrix, $[h_R]$.

$$\left\{h_o\right\} = \left[h_R\right]\left\{a_R\right\} \tag{I-2}$$

where a_R is the rigid motion generalized coordinate matrix. The rigid body modal matrix may be used to specify the boundary conditions of the free-free system,

$$\left[h_R\right]^* \left[M\right]\left\{\ddot{h}_1\right\} + \left[\Delta m\right]\left\{\ddot{a}_R\right\} = \left[h_R\right]^* \left\{F(t)\right\} + \left\{Q(t)\right\} \tag{I-3}$$

where Δm is an incremental generalized mass matrix necessary to account for the rigid portion of the system not considered in the formulation of the basic mass matrix, and Q(t) is the generalized external force applied to the rigid portion of the system. The external forces may arise from three sources, namely, from the motion, from a gust, or from some arbitrary external source. Thus,

$$\left\{F(t)\right\} = \left\{F_m\right\} + \left\{F_g\right\} + \left\{F_e\right\} \tag{I-4}$$

$$\left\{Q(t)\right\} = \left\{Q_m\right\} + \left\{Q_g\right\} + \left\{Q_e\right\} \tag{I-5}$$

Considering the case of harmonic motion, the following transformations are introduced:

$$\left\{h\right\} = \mathrm{Re}\left\{\bar{h}e^{i\omega t}\right\} \tag{I-6}$$

$$\left\{F\right\} = \mathrm{Re}\left\{\bar{F}e^{i\omega t}\right\} \tag{I-7}$$

Transforming to the complex domain, Equations (I-1), (I-3) are reduced to:

$$-\omega^2 \left[M\right]\left|\bar{h}_1\right| + i\omega \left[c\right]\left|\bar{h}_1 - \bar{h}_o\right| + \left[k\right]\left|\bar{h}_1 - \bar{h}_o\right| = \left|\bar{F}\right| \tag{I-8}$$

$$-\omega^2 \left[h_R\right]^* \left[M\right] \left|\bar{h}_1\right| - \omega^2 \left[\Delta m\right]\left|\bar{a}_R\right| = \left[h_R\right]^* \left|\bar{F}\right| + \left|\bar{Q}\right| \tag{I-9}$$

The complex aerodynamic forces are known from the definitions of the aerodynamic influence coefficients (AIC's). The forces due to motion are given in terms of the oscillatory AIC's, while the gust forces are given in terms of the harmonic gust AIC's:

$$\left|\bar{F}_m\right| = (1/12)\ \rho\omega^2 b_r^2 S \left[W\right]\left[C_h\right]\left|\bar{h}_1\right| \tag{I-10}$$

$$\left|\bar{F}_g\right| = \rho V W_g b_r S \left[W'\right]\left[C_g\right]\left|{}^{w_g}/_{W_g}\right| \tag{I-11}$$

The weighting matrices W and W' are based on experimental data and may differ for data originated from different aerodynamic theories. The generalized forces on the rigid component are found based on expressions similar to Equations (I-10), (I-11) except that the AIC's are for the rigid component geometry.

$$\left|\bar{Q}_m\right| = (1/12)\,\rho\omega^2 b_{rR}^2 S_R \left[h_{Ro}\right]^* \left[W_R\right]\left[C_{hR}\right]\left[h_{Ro}\right]\left|\bar{a}_R\right| \tag{I-12}$$

$$\left|\bar{Q}_g\right| = \rho V W_g b_{rR} S_R \left[h_{Ro}\right]^* \left[W_R'\right]\left[C_{gR}\right]\left|{}^{w_g}/_{W_g}\right| \tag{I-13}$$

Combining Equations (I-2), (I-4), (I-5), (I-8), (I-9) and (I-10), the equation of motion is reduced to:

$$\left(-\omega^2\left[\bar{M}\right] + i\omega\left[c\right] + \left[k\right]\right)\left|\bar{h}_1\right| - \left(i\omega\left[c\right] + \left[k\right]\right)\left[h_R\right]\left|\bar{a}_R\right| = \left|\bar{F}_g\right| + \left|\bar{F}_e\right| \tag{I-14}$$

while the boundary conditions are

$$-\omega^2 \left[h_R\right]^* \left[\overline{M}\right]\left|\overline{h}_1\right| - \omega^2 \left[\Delta\overline{m}\right]\left|\overline{a}_R\right| = \left[h_R\right]^*\left(\left|\overline{F}_g\right| + \left|\overline{F}_e\right|\right) + \left|\overline{Q}_g\right| + \left|\overline{Q}_e\right| \quad \text{(I-15)}$$

where the complex mass terms are defined below to include aerodynamic terms

$$\left[\overline{M}\right] = \left[M\right] + (1/12)\,\rho b_r^2 S \left[W\right]\left[C_h\right] \quad \text{(I-16)}$$

$$\left[\Delta\overline{m}\right] = \left[\Delta m\right] + (1/12)\,\rho b_{rR}^2 S_R \left[h_R\right]^* \left[W_R\right]\left[C_{hR}\right]\left[h_{Ro}\right] \quad \text{(I-17)}$$

solving for $\overline{a}_R$ from Equation (I-15) yields

$$\left|\overline{a}_R\right| = -(1/\omega^2)\left[\Delta\overline{m}\right]^{-1}\left(\omega^2\left[h_R\right]^*\left[\overline{M}\right]\left|\overline{h}_1\right| + \left[h_R\right]^*\left(\left|\overline{F}_g\right| + \left|\overline{F}_e\right|\right) + \left|\overline{Q}_g\right| + \left|\overline{Q}_e\right|\right) \quad \text{(I-18)}$$

Substituting Equation (I-18) into Equation (I-14) and solving for $\left|\overline{h}_1\right|$ yields the final frequency response equation

$$\left|\overline{h}_1\right| = \left[\overline{A}\right]^{-1}\left(\left[\overline{B}\right]\left(\left|\overline{F}_g\right| + \left|\overline{F}_e\right|\right) - \left[\overline{D}\right]\left(\left|\overline{Q}_g\right| + \left|\overline{Q}_e\right|\right)\right) \quad \text{(I-19)}$$

where

$$\left[\overline{A}\right] = -\omega^2\left[\overline{M}\right] + \left(i\omega\left[c\right] + \left[k\right]\right)\left(\left[I\right] + \left[h_R\right]\left[\Delta m\right]^{-1}\left[h_R\right]^*\left[\overline{M}\right]\right) \quad \text{(I-20)}$$

$$\left[\overline{B}\right] = \left[I\right] - (1/\omega^2)\left(i\omega\left[c\right] + \left[k\right]\right)\left[h_R\right]\left[\Delta\overline{m}\right]^{-1}\left[h_R\right]^* \quad \text{(I-21)}$$

and

$$\left[\overline{D}\right] = (1/\omega^2)\left(i\omega\left[c\right] + \left[k\right]\right)\left[h_R\right]\left[\Delta\overline{m}\right]^{-1} \quad \text{(I-22)}$$

The structural load response is found from the spring term of Equation (I-8)

$$\left|\overline{F}_s\right| = \left[k\right]\left(\left|\overline{h}_1\right| - \left[h_R\right]\left|\overline{a}_R\right|\right) \quad \text{(I-23)}$$

or from its equivalent

$$\left|\overline{F}_s\right| = \left|\overline{F}_g\right| + \left|\overline{F}_e\right| + \omega^2 \left[\overline{M}\right]\left|h_1\right| - i\omega\left[c\right]\left(\left|\dot{\overline{h}}_1\right| - \left[h_R\right]\left|\dot{\overline{a}}_R\right|\right) \qquad \text{(I-24)}$$

The structural shear, moment, and torque responses are defined below based on the control point forces and the respective integration matrices:

$$\left|\overline{V}\right| = \left[V/F\right]\left|\overline{F}_s\right| \qquad \text{(I-25)}$$

$$\left|\overline{M}\right| = \left[M/F\right]\left|\overline{F}_s\right| \qquad \text{(I-26)}$$

$$\left|\overline{T}\right| = \left[T/F\right]\left|\overline{F}_s\right| \qquad \text{(I-27)}$$

$$\left|\overline{YM}\right| = \left[YM/F\right]\left|\overline{F}_s\right| \qquad \text{(I-28)}$$

I. 2 Modal Solution

In order to reduce the size of the frequency response equation (I-19), a modal solution is used. In one approach, a number of cantilever modes of the aircraft sub-assemblies are used as the input modal shapes to build up the overall response of the aircraft. An alternative to the use of the cantilever modes is to apply a series of free-free vibration modes, $\left[h_f\right]$, with the option of including a few arbitrary modes. Such a series solution usually yields a more rapidly covergent result as compared to the cantilever mode approach. In this case, the deformation at the control points and the reference element are respectively

$$\left|\overline{h}_1\right| = \left[h'_F\right]\left|\overline{a}'_F\right| + \left[h_R\right]\left|\overline{a}_G\right| \qquad \text{(I-29)}$$

$$\left|\overline{a}_R\right| = \left[a_{RF}\right]\left|\overline{a}'_F\right| + \left|\overline{a}_G\right| \qquad \text{(I-30)}$$

and the accelerations are found from the following equations

$$\left|\ddot{\overline{h}}_1\right| = -\omega^2 \left|h_1\right| \qquad \text{(I-31)}$$

$$\left|\ddot{a}_R\right| = -\omega^2 \left|a_R\right| \tag{I-32}$$

where the prime denotes the free-free condition, $\left|\bar{a}_G\right|$ is the matrix of centroidal coordinates, and $\left[a_{RF}\right]$ is the reference point modal matrix. To find $\left[a_{RF}\right]$, a distinction has to be made between the modes that are orthogonal and the arbitrary cantilever modes that are included in the solution. For this purpose, h'_F and a_{RF} are divided into submatrices as shown below:

$$\left[h'_F\right] = \left[\begin{array}{c|c} h'_{F_o} & h_{F_o} \end{array}\right] \tag{I-33}$$

$$\left[a_{RF}\right] = \left[\begin{array}{c|c} a_{RF_o} & O \end{array}\right] \tag{I-34}$$

where a_{RF} is found from the boundary conditions for free vibration

$$\left[a_{RF_o}\right] = -\left[\Delta m\right]^{-1} \left[h_R\right]^* \left[M\right] \left[h'_{F_o}\right] \tag{I-35}$$

Substituting Equations (I-2), (I-4), (I-29), and (I-30) into Equation (I-8) yields the equation of motion of the flexible components:

$$\begin{aligned} \left(-\omega^2 \left[\overline{M}\right] \left[h'_F\right] + \left(i\omega\left[c\right] + \left[k\right]\right) \left[h''_F\right]\right)\left|\bar{a}'_F\right| - \omega^2 \left[\overline{M}\right] \left[h_R\right] \left|\bar{a}_G\right| \\ = \left|\overline{F}_g\right| + \left|\overline{F}_e\right| + \left|\epsilon_F\right| \end{aligned} \tag{I-36}$$

where

$$\left[h''_F\right] = \left[h'_F\right] - \left[h_R\right] \left[a_{RF}\right] \tag{I-37}$$

Premultiplying Equation (I-8) by $\left[h_R\right]^*$ and then subtracting from Equation (I-9) yields the equation of motion of the rigid component. Upon substitution of Equations (I-2), (I-4), (I-5), (I-29) and (I-30), the equation is further reduced to:

$$-\omega^2 \left[\Delta\bar{m}\right]\left|\bar{a}_G\right| - \left(\omega^2 \left[\Delta\bar{m}\right]\left[a_{RF}\right] + \left[h_R\right]^* \left(i\omega\left[c\right] + \left[k\right]\right)\left[h''_F\right]\right)\left|\bar{a}'_F\right| = \left|\bar{Q}_g\right| + \left|\bar{Q}_e\right| + \left|\epsilon_R\right| \tag{I-38}$$

In the above, $\left|\epsilon_F\right|$ and $\left|\epsilon_R\right|$ are the errors in the respective equations of motion as a result of the modal solutions. Substituting Equation (I-29) and (I-30) into Equation (I-9) yields the boundary condition:

$$-\omega^2 \left[\bar{m}'_{RF}\right]\left|\bar{a}'_F\right| - \omega^2 \left[\bar{m}_{RR}\right]\left|\bar{a}_G\right| = \left[h_R\right]^* \left(\left|\bar{F}_g\right| + \left|\bar{F}_e\right|\right) + \left|\bar{Q}_g\right| + \left|\bar{Q}_e\right| \tag{I-39}$$

where

$$\left[\bar{m}_{RF}\right] = \left[h_R\right]^* \left[\bar{M}\right]\left[h'_F\right] + \left[\Delta\bar{m}\right]\left[a_{RF}\right] \tag{I-40}$$

$$\left[\bar{m}_{RR}\right] = \left[h_R\right]^* \left[\bar{M}\right]\left[h'_F\right] + \left[\Delta\bar{m}\right] \tag{I-41}$$

Applying the Galerkin principle to the equations of motion, Equations (I-36) and (I-38), the following equation is established:

$$\left[h'_F\right]^* \left|\epsilon_F\right| + \left[a_{RF}\right]^* \left|\epsilon_R\right| = 0 \tag{I-42}$$

Equation (I-42) leads to the generalized equation of motion:

$$\left(-\omega^2 \left[\bar{m}'_{FF}\right] + i\omega\left[c'_F\right] + \left[k'_F\right]\right)\left|\bar{a}'_F\right| - \omega^2 \left[\bar{m}'_{FR}\right]\left|\bar{a}_G\right| = \left[h'_F\right]^* \left(\left|\bar{F}_g\right| + \left|\bar{F}_e\right|\right) + \left[a_{RF}\right]^* \left(\left|\bar{Q}_g\right| + \left|\bar{Q}_e\right|\right) \tag{I-43}$$

where

$$\left[\bar{m}_{FF}\right] = \left[h'_F\right]^* \left[\bar{M}\right] \left[h'_F\right] + \left[a_{RF}\right]^* \left[\Delta\bar{m}\right]\left[a_{RF}\right] \quad \text{(I-44)}$$

$$\left[\bar{m}_{FR}\right] = \left[h'_F\right]^* \left[\bar{M}\right] \left[h_R\right] + \left[a_{RF}\right]^* \left[\Delta\bar{m}\right] \quad \text{(I-45)}$$

$$\left[c'_F\right] = \left[h''_F\right]^* \left[c\right] \left[h''_F\right] \quad \text{(I-46)}$$

$$\left[k'_F\right] = \left[h''_F\right] \left[k\right] \left[h''_F\right] \quad \text{(I-47)}$$

The deformations at the centroid are found by solving Equation (I-39):

$$\left[\bar{a}_G\right] = -(1/\omega^2) \left[\bar{m}_{RR}\right]^{-1} \left(\omega^2 \left[\bar{m}'_{RF}\right] \bar{a}'_F + \left[h_R\right]^* \left(\left[\bar{F}_g\right] + \left[\bar{F}_e\right]\right) + \left[\bar{Q}_g\right] + \left[\bar{Q}_e\right]\right) \quad \text{(I-48)}$$

Substituting Equation (I-48) into Equation (I-43) leads to the final response equation:

$$\left[\bar{a}'_F\right] = \left[\bar{A}'_F\right]^{-1} \left(\left[\bar{B}'_F\right] \left(\left[\bar{F}_g\right] + \left[\bar{F}_e\right]\right) - \left[\bar{D}'_F\right] \left(\left[\bar{Q}_g\right] + \left[\bar{Q}_e\right]\right)\right) \quad \text{(I-49)}$$

where

$$\left[\bar{A}'_F\right] = -\omega^2 \left(\left[\bar{m}'_{FF}\right] - \left[\bar{m}'_{FR}\right] \left[\bar{m}_{RR}\right]^{-1} \left[\bar{m}'_{RF}\right]\right) + i\omega \left[C'_F\right] + \left[K'_F\right] \quad \text{(I-50)}$$

$$\left[\bar{B}'_F\right] = \left[h'_F\right]^* - \left[\bar{M}'_{FR}\right] \left[\bar{m}_{RR}\right]^{-1} \left[h_R\right]^* \quad \text{(I-51)}$$

$$\left[\bar{D}'_F\right] = \left[\bar{m}'_{FR}\right] \left[\bar{m}_{RR}\right]^{-1} - \left[a_{RF}\right]^* \quad \text{(I-52)}$$

The generalized spring matrix is a diagonal matrix which is found from the diagonal elements of the generalized mass matrix and the corresponding free-free frequencies, ω'_F:

$$\left[K'_F\right] = \text{diagonal elements of } \left[m'_{FF}\right]\left[\omega'^2_F\right] \quad \text{(I-53)}$$

where

$$\left[m'_{FF}\right] = \left[h'_F\right]^* \left[M\right] \left[h'_F\right] + \left[a_{RF}\right]^* \left[\Delta M\right] \left[a_{RF}\right] \tag{I-54}$$

The generalized damping matrix representing structural damping also takes a diagonal form:

$$\omega \left[C'_F\right] = \left[K'_F\right] \left[g'_F\right] \tag{I-55}$$

where g'_{F_i} is the structural damping coefficient in the i^{th} free-free mode. The response of the control points if found from Equation I-29):

$$\left\{\bar{h}_1\right\} = \left[h'_F\right] \left\{\bar{a}'_F\right\} + \left[h_R\right] \left\{\bar{a}_G\right\} \tag{I-56}$$

The structural load response is found from the spring term of Equation (I-36):

$$\begin{aligned} \left\{\bar{F}_s\right\} &= \left[k\right] \left[h''_F\right] \left\{\bar{a}'_F\right\} \\ &= \left[M\right] \left[h'_F\right] \left[\omega'^2_F\right] \left\{\bar{a}'_F\right\} \\ &= \left\{\bar{F}_g\right\} + \left\{\bar{F}_e\right\} + \omega^2 \left[\bar{M}\right] \left[h_R\right] \left\{\bar{a}_G\right\} + \left(\omega^2 \left[\bar{M}\right] \left[h'_F\right]\right. \\ &\quad \left. - i\omega \left[c\right] \left[h''_F\right]\right) \left\{\bar{a}_G\right\} \end{aligned} \tag{I-57}$$

Substituting Equation (I-57) into Equations (I-25)-(I-28) yields the aircraft responses in terms of structural shear, moment, and torque.

1.3 Equations for Stress Transfer Functions

Stress may be found in two ways. One method is described in Reference 10, page 51 and is expressed as follows:

$$\bar{\sigma} = a\ \overline{BM} + b\bar{V} + c\bar{T} + d\ \overline{YM} \tag{I-58}$$

where a, b, c, and d are stress coefficients.

The other method employs the use of a stress influence coefficient matrix, $\left[S\right]$, which is defined as the stress at a specified location due to a unit load applied at each of the control points independently:

$$\left\{\bar{\sigma}\right\} = \left[S\right] \left\{\bar{F}_s\right\}$$

I. 4 Collocation Equations for Obtaining Aircraft Elastic Modes

The equations of motion for computing aircraft elastic modes may be derived as a special case of the general formulation of I. 1. Omitting the external forces and the damping matrix, Equation (I-14) is reduced to:

$$(-\omega_F^2 \left[M\right] + \left[K\right])\left|h_F\right| - \left[K\right]\left[h_R\right]\left|a_{FR}\right| = 0 \qquad \text{(I-60)}$$

In the above equation, ω_F is an unknown frequency eigenvalue. From Equation (I-15):

$$\left[h_R\right]^* \left[M\right]\left|h_F\right| + \left[\Delta m\right]\left|a_{FR}\right| = 0 \qquad \text{(I-61)}$$

the motion of the reference station is expressed as follows with the aid of (I-60):

$$\left|a_{FR}\right| = -\omega_F^2 \left(\left[\Delta m\right] + \left[h_R\right]^* \left[M\right]\left[h_R\right] \right)^{-1} \left[h_R\right]^* \left[M\right]\left[K\right]^{-1}\left[M\right]\left|h_F\right| \qquad \text{(I-62)}$$

Substituting Equation (I-62) into (I-60), the free vibration equation is obtained:

$$\left|h_F\right| = \omega_F^2 \left[K\right]^{-1}\left[M\right]\left|h_F\right| - \omega_F^2 \left[h_R\right]\left(\left[\Delta m\right] + \left[h_R\right]^* \left[m\right]\left[h_R\right]\right)^{-1}\left[h_R\right]^*\left[M\right]\left[K\right]^{-1}\left[M\right]\left|h_F\right| \qquad \text{(I-63)}$$

Equation (I-63) may be rewritten in the following form where the vibration modes and the corresponding frequencies are solved through iteration:

$$\left[U\right]\left|h_F\right| = \left(\frac{1}{\omega_F^2}\right)\left|h_F\right| \qquad \text{(I-64)}$$

where: $\left[U\right]$, the dynamical matrix, is defined as follows:

$$\left[U\right] = \left[A^{FF}\right]\left[M\right] \equiv \left[E\right]\left[K\right]^{-1}\left[M\right] \qquad \text{(I-65)}$$

$$\left[E\right] = \left[I\right] - \left[h_R\right]\left[m_{RR}\right]^{-1}\left[h_R\right]^*\left[M\right] \qquad \text{(I-66)}$$

$$\left[m_{RR}\right] = \left[h_R\right]^*\left[M\right]\left[h_R\right] + \left[\Delta m\right] \qquad \text{(I-67)}$$

The $\left[E\right]$ matrix (P x P) frees the restrained system (Reference 16).

APPENDIX II

REAL TIME GUST DATA PROCESSING

In the aircraft gust design using the spectral approach, the input spectral function is the gust power spectrum. To carry out the computation, the particular type of the gust spectrum used has a significant influence on the final statistical data. In order to establish a rational gust design criterion, it is then essential to acquire some standard gust spectra which are consistent with both the aerodynamic turbulence theory and the actual gust data obtained in aircraft flight tests. The present appendix describes the background of establishing the analytical gust spectra as well as the processing of the real time air turbulence data obtained in flight tests of the F-5A fighter. Some related information on the aircraft gust response data and their processing are also presented.

II.1 Gust Flight Tests

A flight test program for the F-5A fighter is established to acquire atmospheric turbulence data and to correlate analytically determined load and stress transfer functions with those determined experimentally. The airplane is instrumented to measure the gust input and selected responses. These data are converted into input-output cross spectra functions by use of the Tukey method modified to handle special problems relating to the F-5A airplane (Reference 13). From these data, transfer functions in the form of modulus and phase to the gust are determined.

The fighter flight test program is designed to establish the effect of Mach number, altitude, and weight configuration on the gust transfer function. Some typical correlations of analytical and experimentally determined transfer functions are shown in Subsection 4.

Two flights are required to obtain a pacer airspeed calibration of the modified A/S boom. The calibration is obtained in the clean configuration over the range of test Mach numbers. The gust load survey consists of a substantial number of flights to obtain airplane response and gust velocity input data in turbulent air.

The test instrumentation is selected and tested to ensure that the response characteristics of each component are compatible with the over-all system requirements.

An airborne, pulse-code-modulated (PCM) magnetic tape recording system is installed in the airplane to record all the test parameters. The pulse-code-modulated magnetic tape recording system is capable of recording at a rate of 133 samples per second in 93 separate channels.

A Gianninni boom-mounted differential pressure type angle of attack and sideslip indicator and suitable instrumentation for measuring the deflection of the boom assembly are installed in the airplane. It is necessary to conduct both a low and high speed wind-tunnel calibration of the angle of attack and sideslip sensor. An error analysis is conducted to determine the airplane up-wash effects of gust velocity measurement. A computing flow diagram indicating the processing of the flight test data is shown in Figure 60.

II. 2 Gust Data Processing

Based on the flight test data, the vertical gust velocity is computed by the equation:

$$w(t) = V_T (\alpha - \bar{\alpha}) - V_T \left[\int_0^t \dot{\Theta}(s)\, ds - \bar{\Theta} \right] + \int_0^t a_z(s)\, ds - \bar{\dot{z}} + \ell_x (\dot{\Theta} - \bar{\dot{\Theta}}) \qquad (II-1)$$

where

$$\alpha = \frac{1}{2} \sin^{-1} \left(\frac{k_o \Delta p_\alpha}{q} \right) + k_1 \left(\frac{\Delta p_\alpha}{q} \right)^2 + \frac{k_2 \Delta p_\beta}{q}$$

$$\beta = \frac{1}{2} \sin^{-1} \left(\frac{k_3 \Delta p_\beta}{q} \right) + k_4 \frac{\Delta p_\alpha}{q}$$

$\dot{\Theta}$ = pitch rate

a_z = normal acceleration

$\bar{\dot{z}}$ = mean vertical velocity

$w(t)$ = unfiltered gust velocity

q = dynamic pressure

V_T = true airspeed

Δp_α = angle of attack differential pressure at gust sensor

Δp_β = angle of sideslip differential pressure at gust sensor

Phase I: Calculation of Vertical or Lateral Gust Velocity

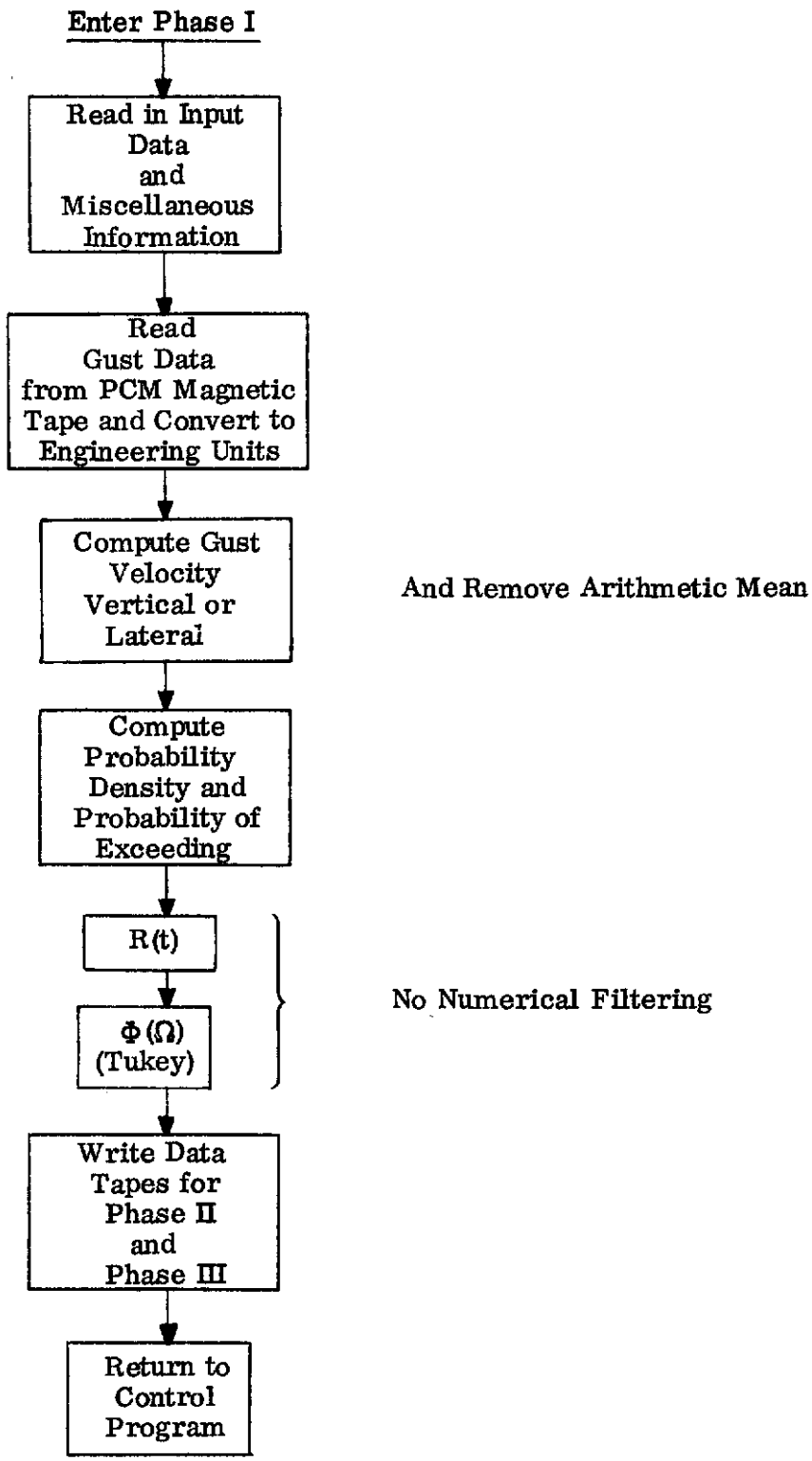

FIGURE 60. COMPUTER FLOW FOR PROCESSING GUST FLIGHT DATA

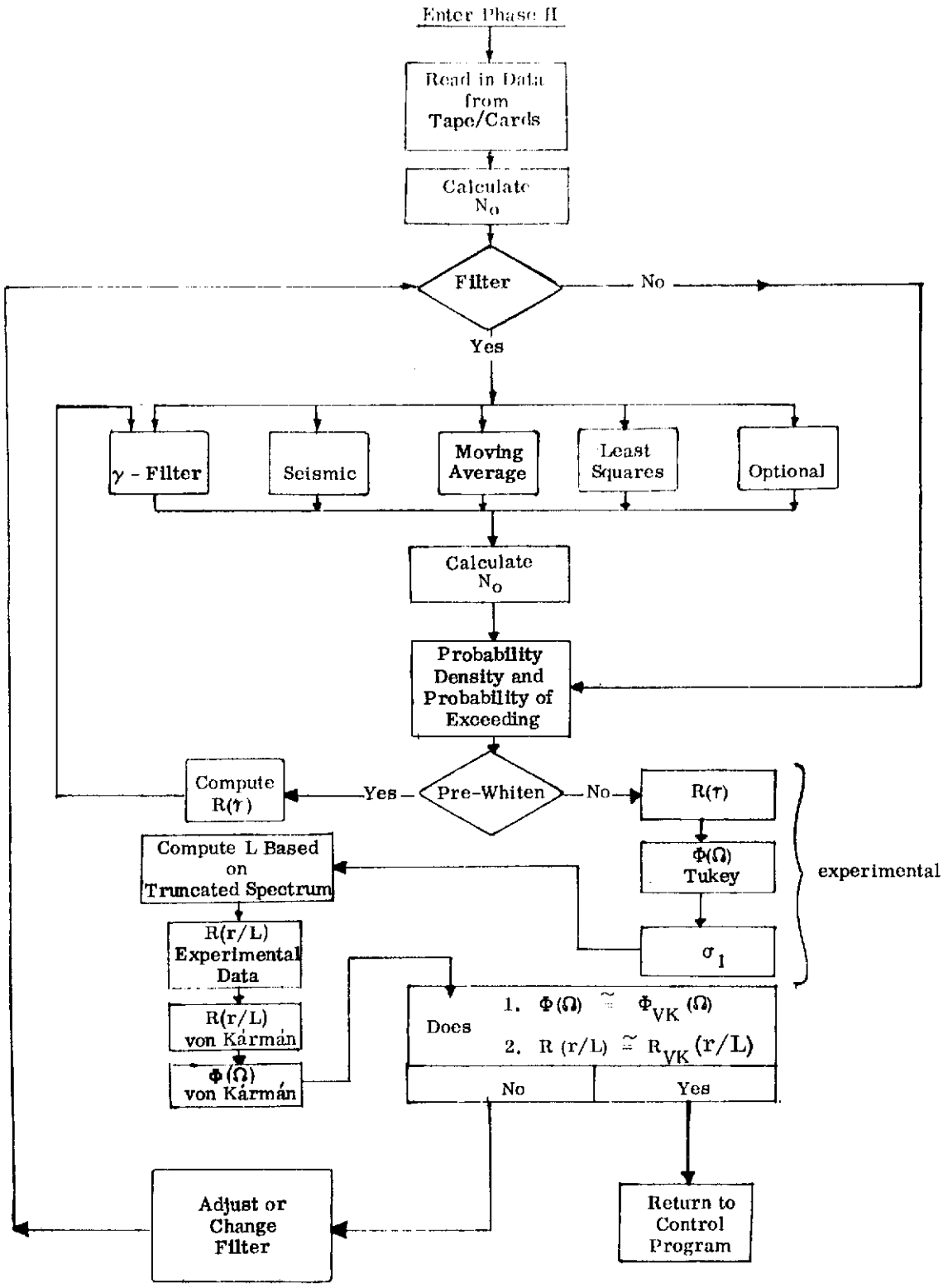

FIGURE 60. COMPUTER FLOW FOR PROCESSING GUST FLIGHT DATA (CONTINUED)

Phase III: Cross Spectral Analysis and Transfer Function Computation

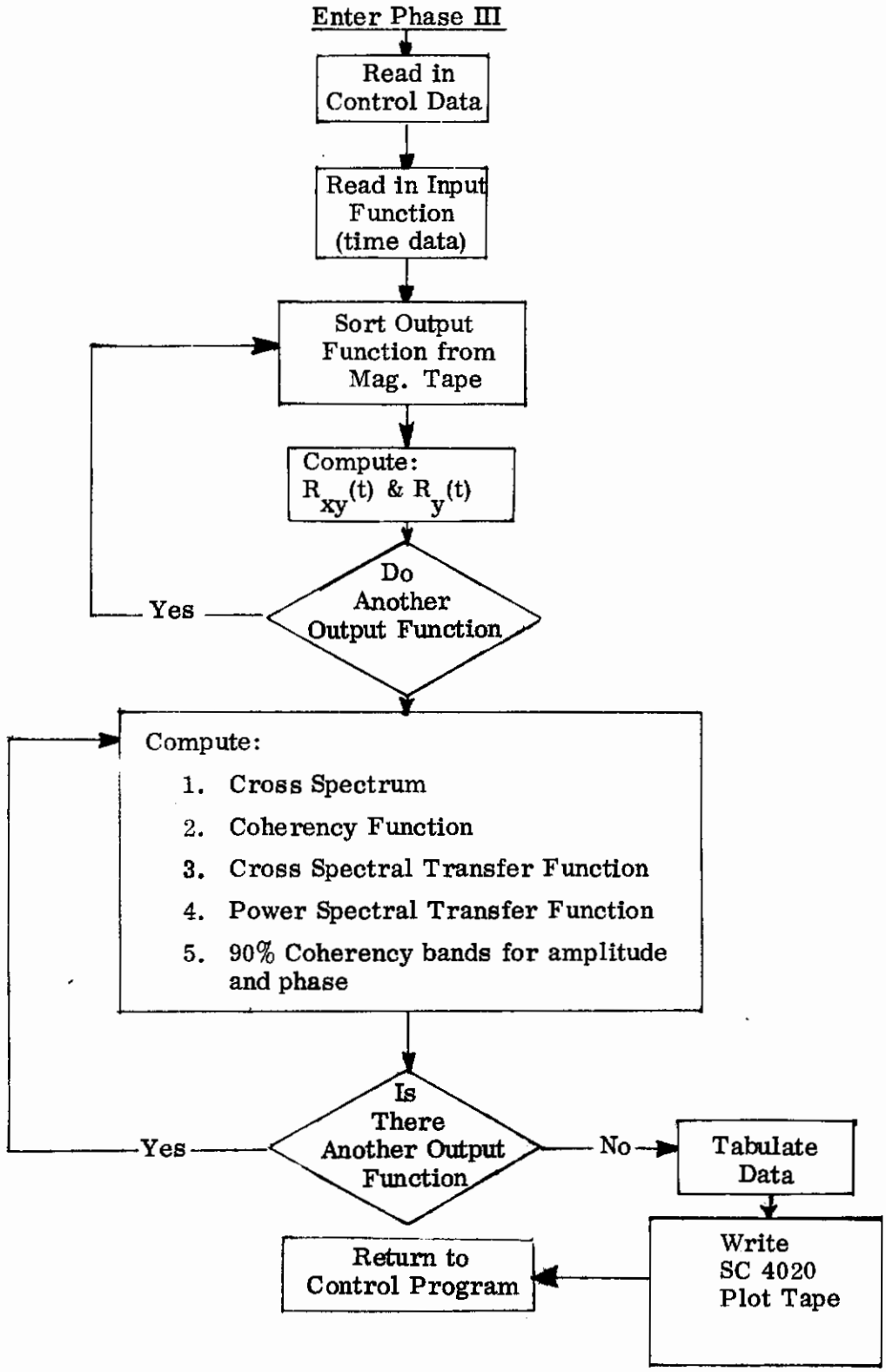

FIGURE 60. COMPUTER FLOW FOR PROCESSING GUST FLIGHT DATA (CONTINUED)

ℓ_x = longitudinal distance from gust sensor to airplane center of gravity

NOTE: all barred quantities denote mean values

Three sets of flight gust data are processed and converted into power spectra. Appropriate filter process is used to remove the linear trends and the low frequency drift components before the conversion. The spectra are curve fitted to von Kármán spectra. The scales of turbulence are determined based on the rms gust velocity and the truncated gust velocity. A brief summary of the processed gust data is shown in Table XXIV. Typical real time gust data before filtering is shown in Figure 61.

TABLE XXIV. Summary of Flight Gust Data

Case	Flight No.	γ- Filter Value	Sampling Time ϵ (sec.)	No. of Samples n	Scales of Turbulence L (ft.)	Rms Gust Velocity σ_w (ft/sec.)
1	275	.002	.0075	16,000	1780	5.1
2	276	.002	.0075	16,000	818	4.1
3	277	.008	.0075	16,000	902	7.0

In case 3 shown in Table XXIV, it is necessary to remove a large amplitude, low frequency pitch oscillation from the time series. Therefore, a slightly higher gamma value is required. Following the filtering operation, the data are pre-whitened by the operation,

$$\hat{w}(t) = w(t) - w(t-\epsilon) \qquad (II-2)$$

Since the pre-whitening operation results in a pre-whitened auto-correlation function, two auto-correlation functions are computed. One function, $R_w(t)$, corresponds to the gamma-filtered time series. The other $\hat{R}_w(t)$, is the pre-whitened auto-correlation function used to compute the smoothed power spectral density estimates. The pre-whitened auto-correlation functions are not shown here. However, the normalized, gamma-filtered, functions, $R_w(r/L)/R(0)$, are exhibited in Figures 62-64. These data are computed with ϵ = 0.15 second and m = 133 time lags for a period of 120 seconds.

In order to apply an appropriate filter function for each set of gust data, the distributions of the filtered data subject to various degrees of filtering are studied. The idea behind the process is that a properly filtered set of air gust data is expected to have

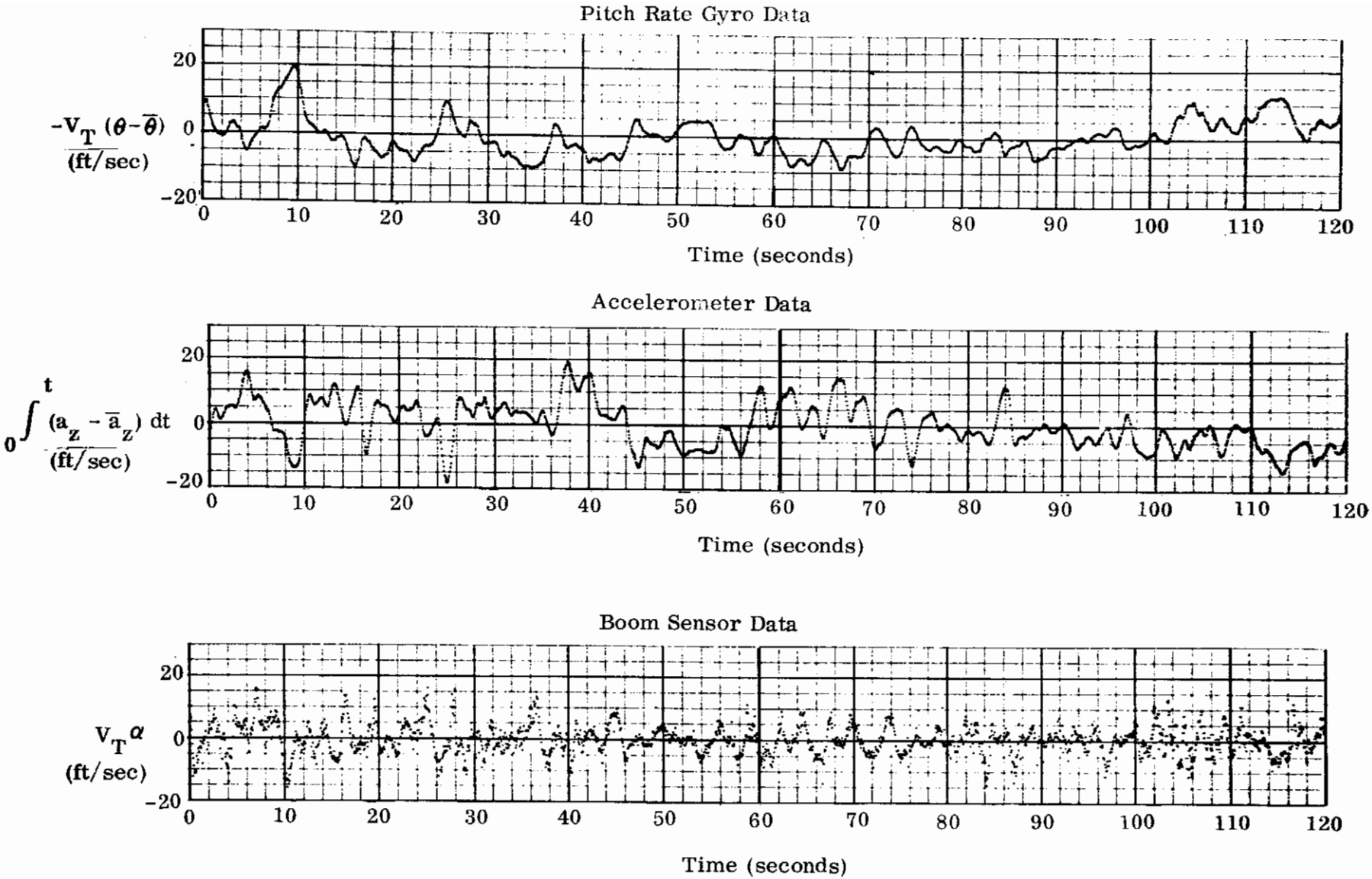

FIGURE 61 TYPICAL REAL TIME GUST DATA, FLIGHT 275

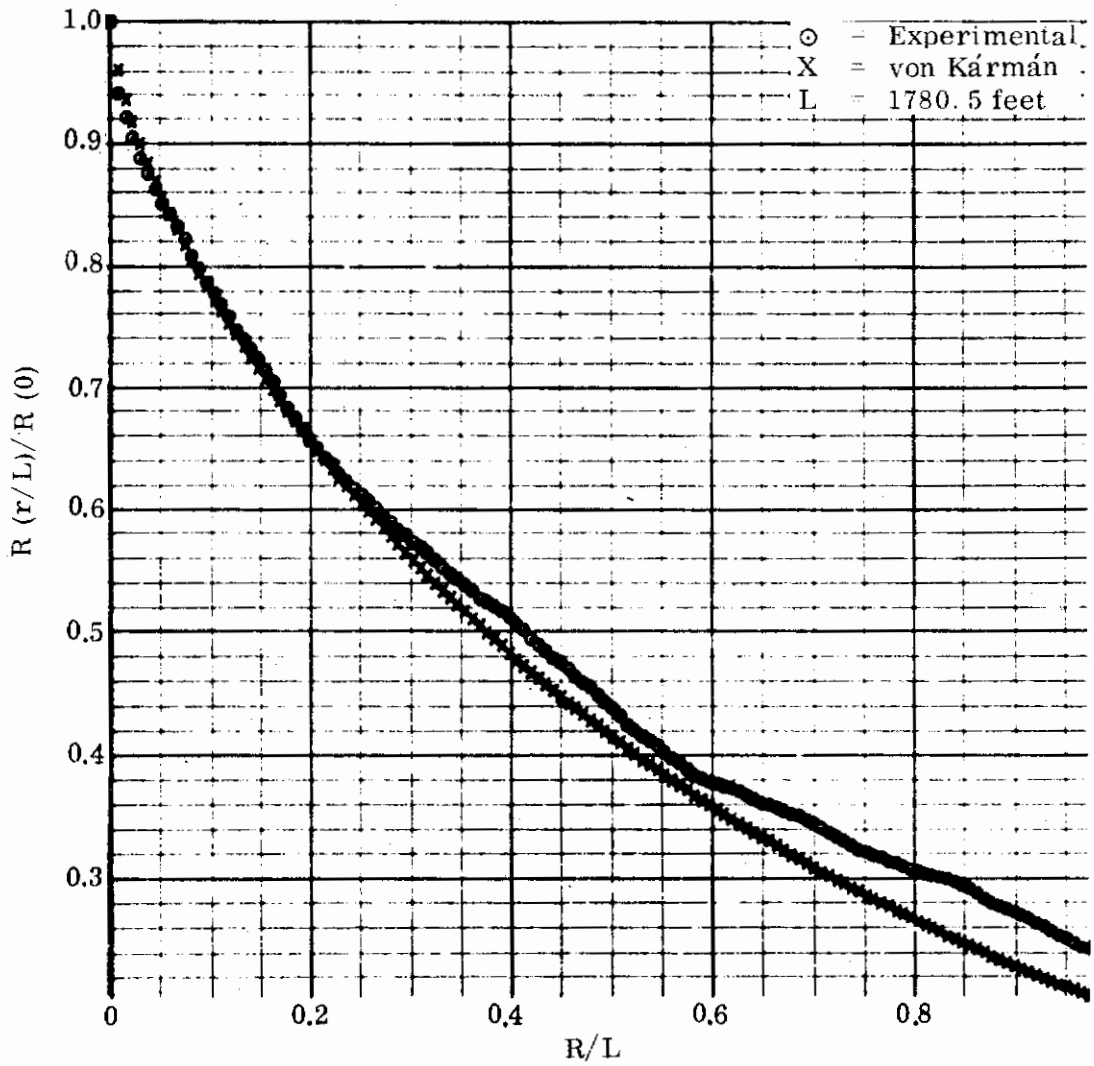

FIGURE 62 COMPARISON OF AUTO-CORRELATION FUNCTIONS, FLIGHT 275

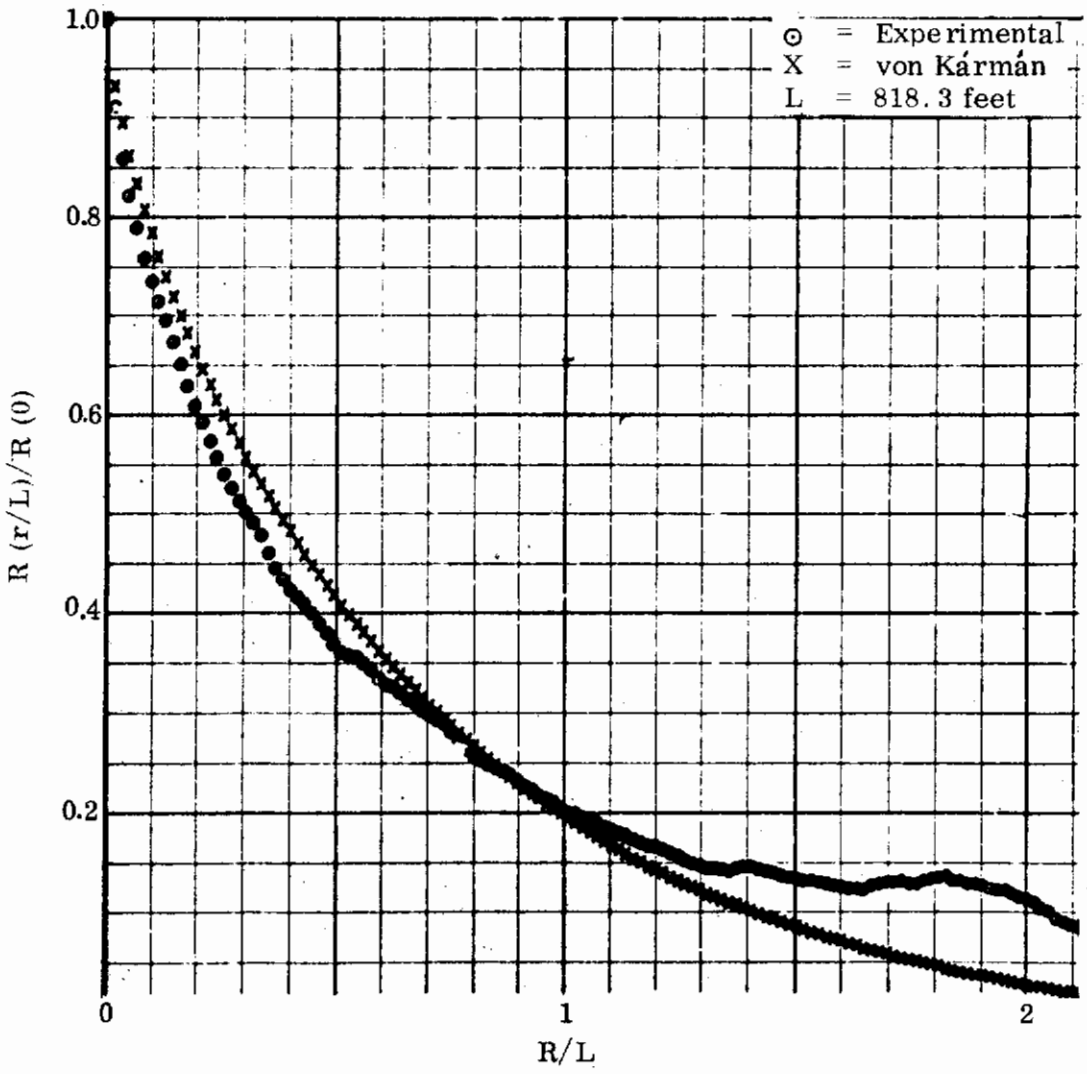

FIGURE 63 COMPARISON OF AUTO-CORRELATION FUNCTIONS, FLIGHT 276

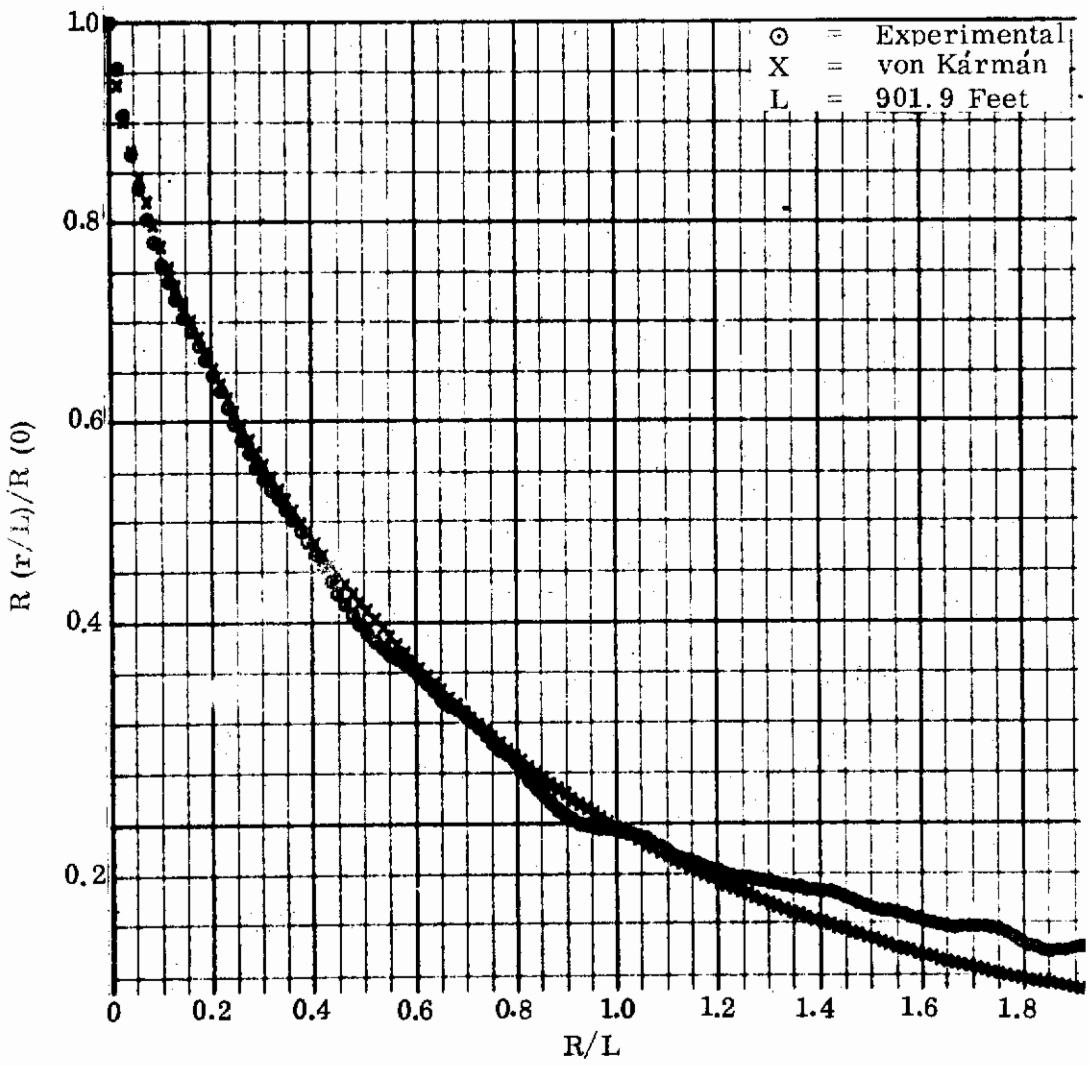

FIGURE 64 COMPARISON OF AUTO-CORRELATION FUNCTIONS, FLIGHT 277

Gaussian distribution. Thus, the distributions of various sets of the filtered data may be used as a basis to select a proper filter. The data shown in Figures 65-67 are obtained by partitioning the velocity amplitude (-25 to + 25 feet/second) into 200 equal intervals. The total numbers of gust velocity digital points falling in the intervals are plotted for each set of gamma-filtered data. Prior to computing the probability distributions above, the arithmetic mean is removed from the unfiltered gust velocity data. The unfiltered data are then gamma-filtered for the values, $\gamma = .001$, $.002$, $.004$, $.006$, and $.008$ for 16,000 points with $\epsilon = .0075$ seconds. The filter transfer function data are plotted in Figure 68 for a number of values.

The distribution curves obtained above are integrated and the probability of exceeding is computed for $\gamma = 0$, $.004$, and $.008$:

$$e(s, \gamma) = \frac{\int_{-\infty}^{s} p(w, \gamma)\, dw}{\int_{-\infty}^{\infty} p(w, \gamma)\, dw} \qquad (II-3)$$

These data are shown in Figures 69-71. In the figures, the coordinate system is such that the plot corresponding to a Gaussian distribution is a straight line. The standard Tukey procedure is applied to the smoothed pre-whitened auto-correlation functions, $\hat{R}_w(t)$. The post-darkening operator $\frac{1}{2}(1-\cos \omega\epsilon)^{-1}$ is combined with the digitalization compensation operator $2(1-\cos \omega\epsilon)/(\omega\epsilon)^2$ to obtain the vertical gust velocity power spectral density:

$$\Phi(\omega) = \frac{\hat{\Phi}(\omega)}{(\omega\epsilon)^2} \qquad (II-4)$$

These data are shown in Figures 72-74 together with the fitted von Kármán spectra.

II.3 Fitting of the von Kármán Spectrum

The gust spectral data are fitted with von Kármán spectra. The scales of turbulence L are determined through truncated integration of the power spectrum:

$$L = 0.692\left(\frac{\sigma_w}{\sigma_1}\right)^3 \left(\frac{1}{\Omega_1^{2/3}} - \frac{1}{\Omega_0^{2/3}}\right)^{3/2} \qquad (II-5)$$

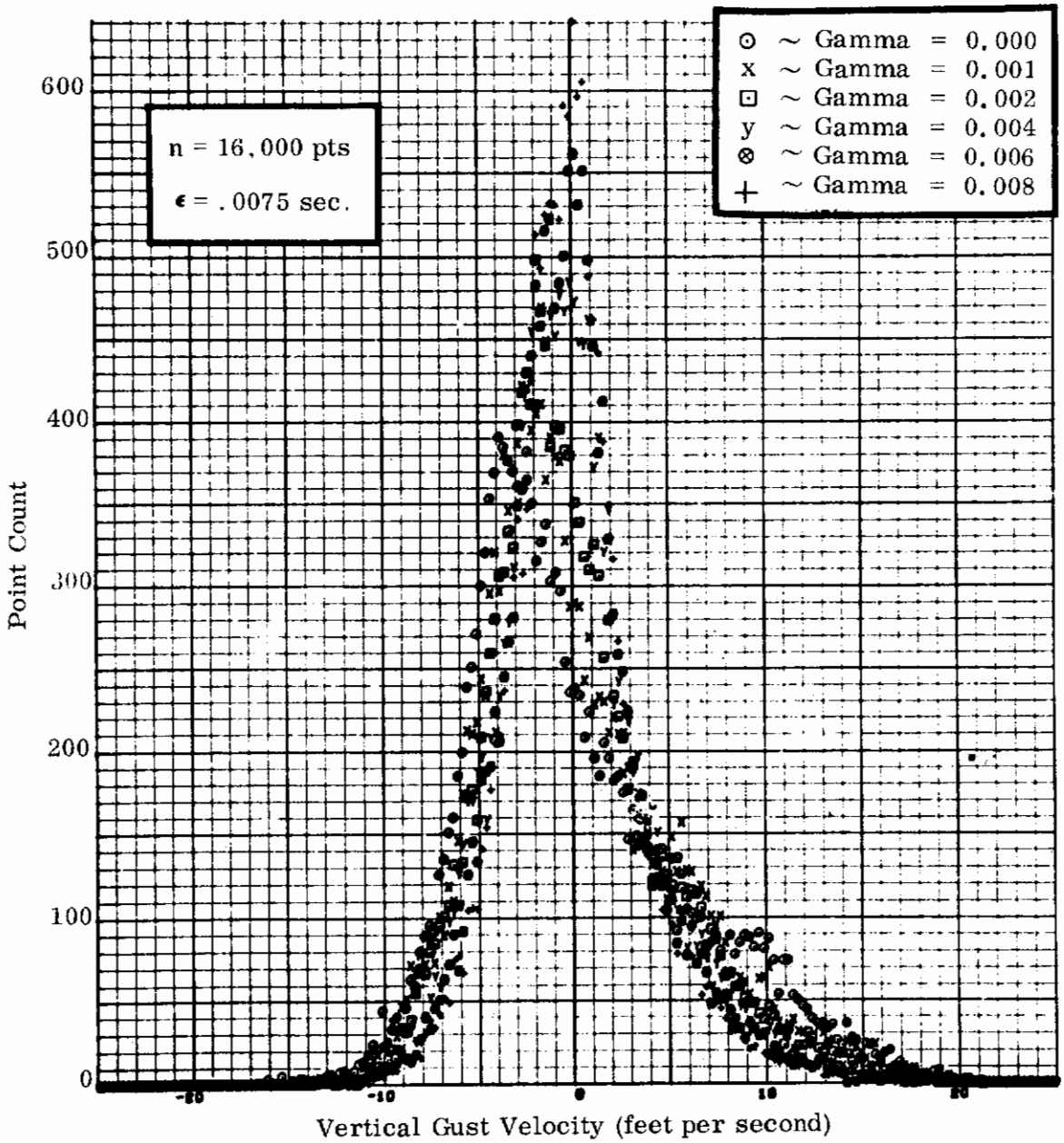

FIGURE 65 POINT DISTRIBUTION OF VERTICAL GUST VELOCITY, FLIGHT 275

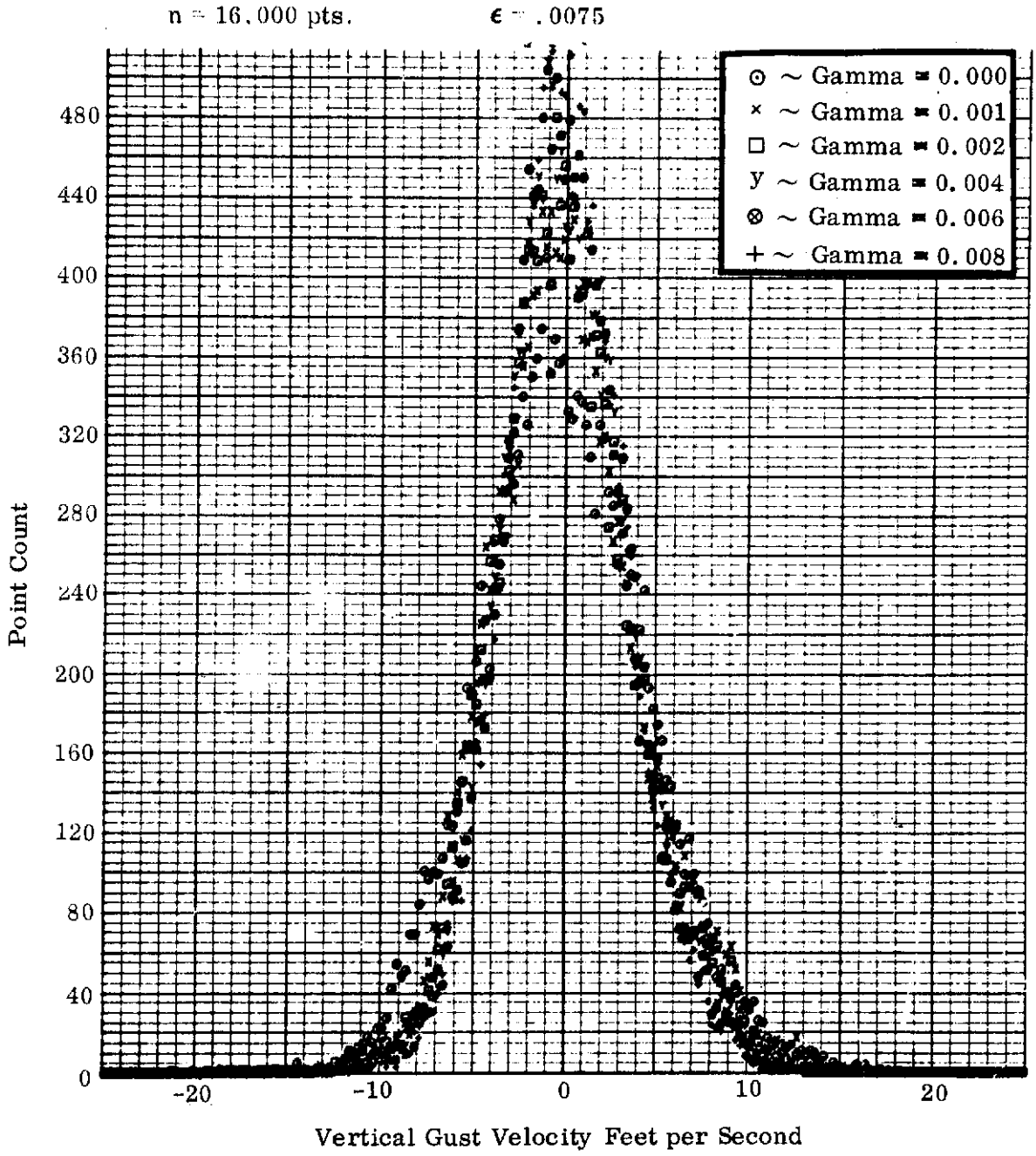

FIGURE 66 POINT DISTRIBUTION OF VERTICAL GUST VELOCITY, FLIGHT 276

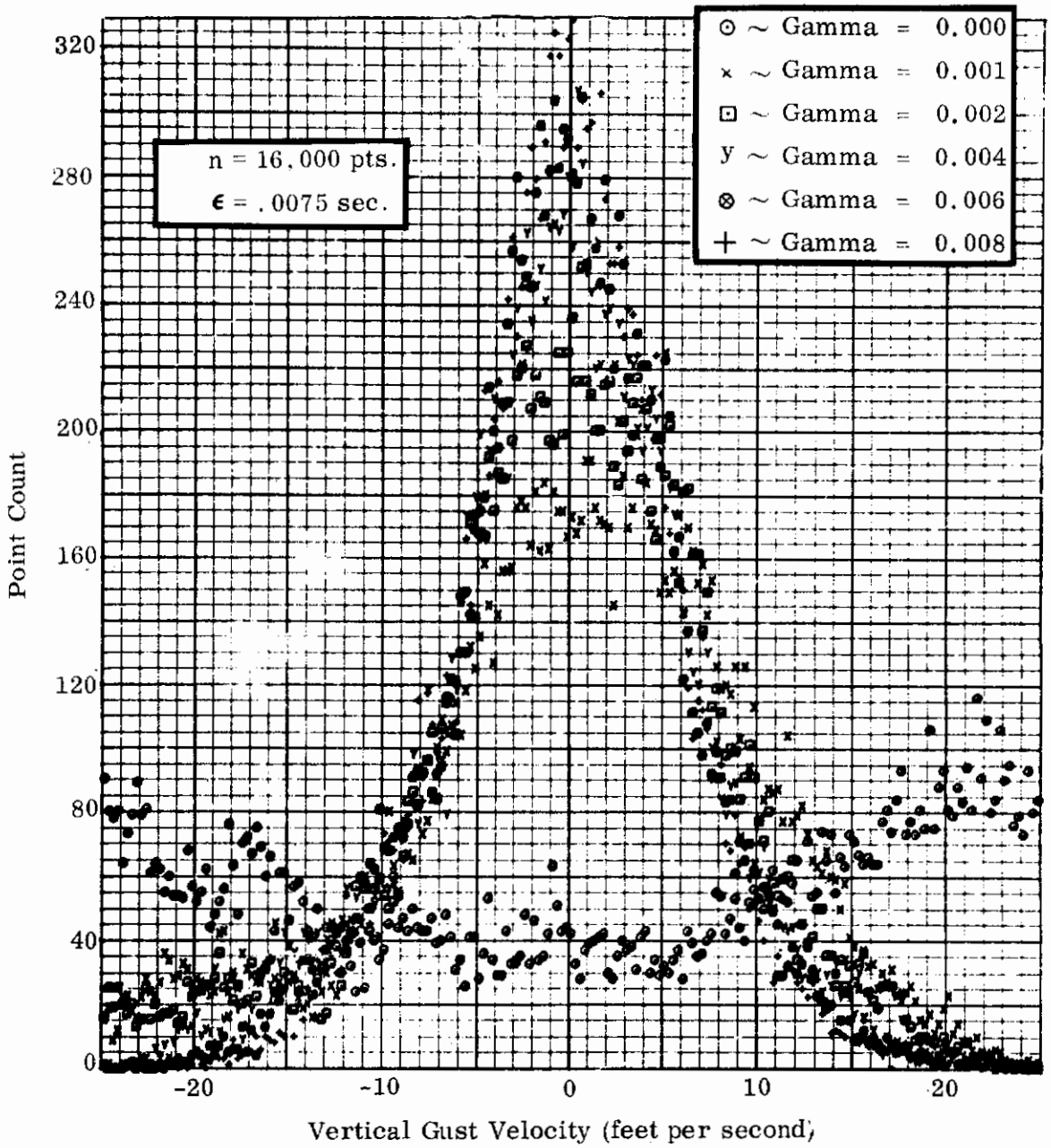

FIGURE 67 POINT DISTRIBUTION OF VERTICAL GUST VELOCITY, FLIGHT 277

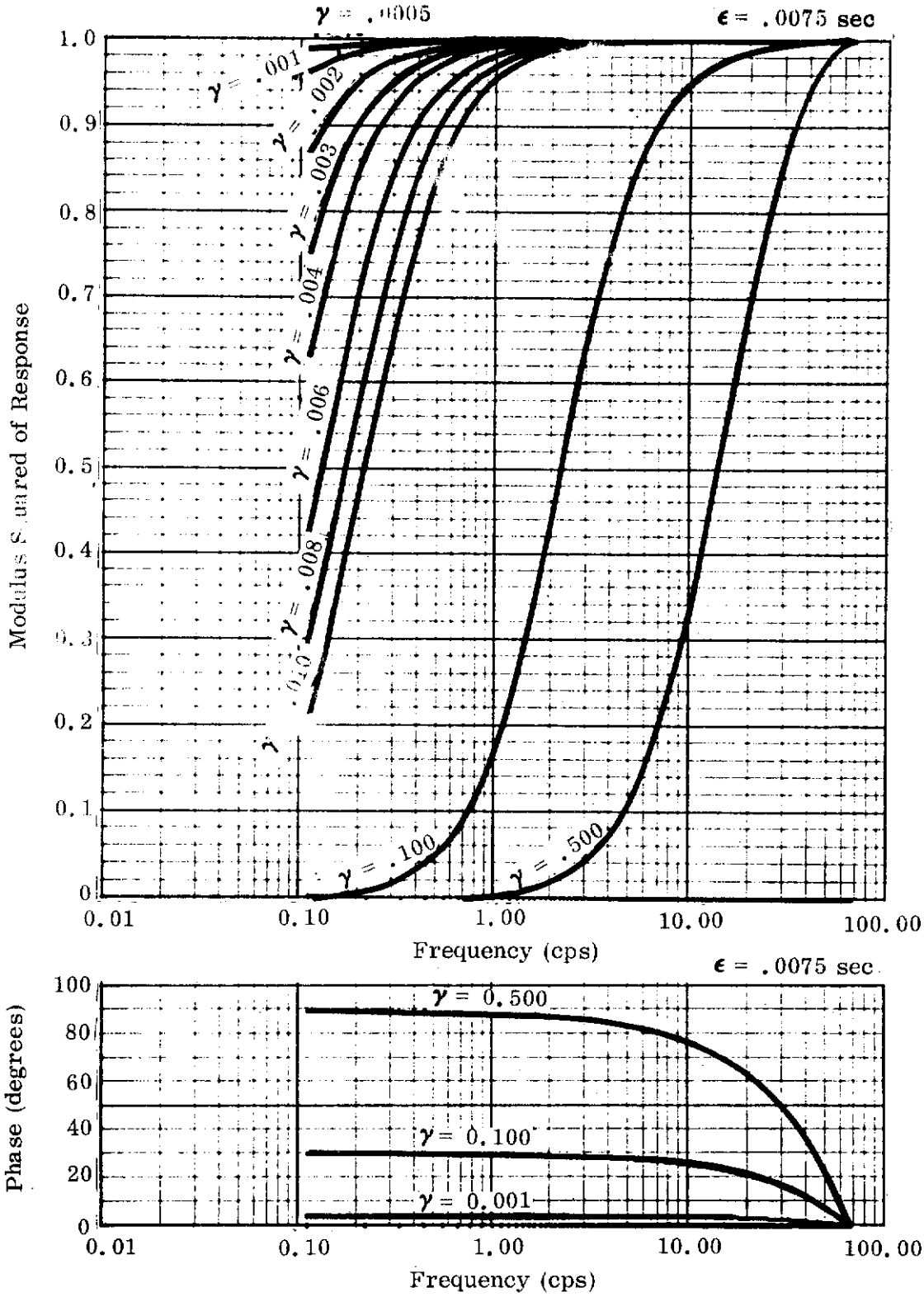

FIGURE 68 GAMMA FILTER TRANSFER FUNCTION

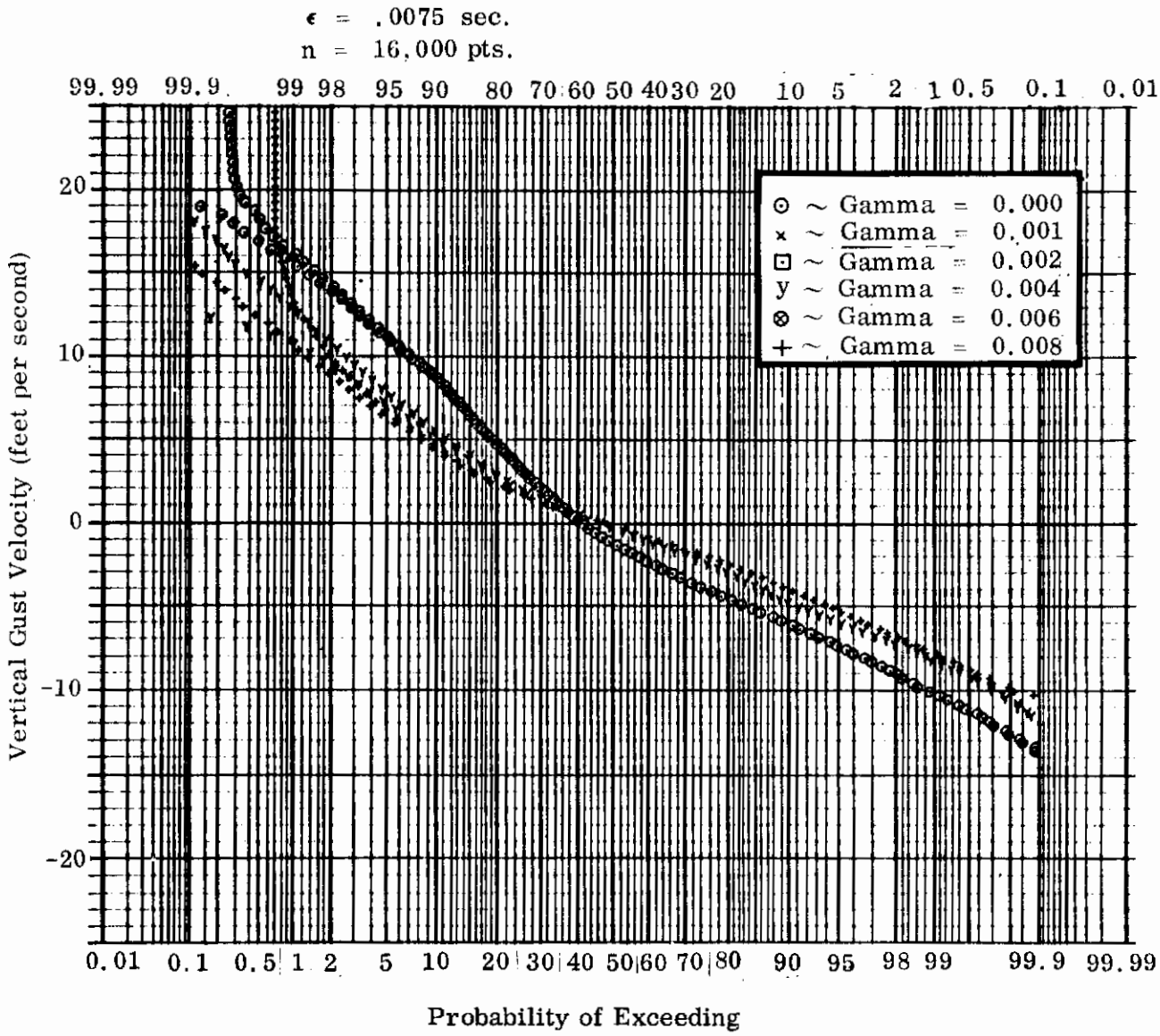

FIGURE 69 PROBABILITY GRAPH, FLIGHT 275

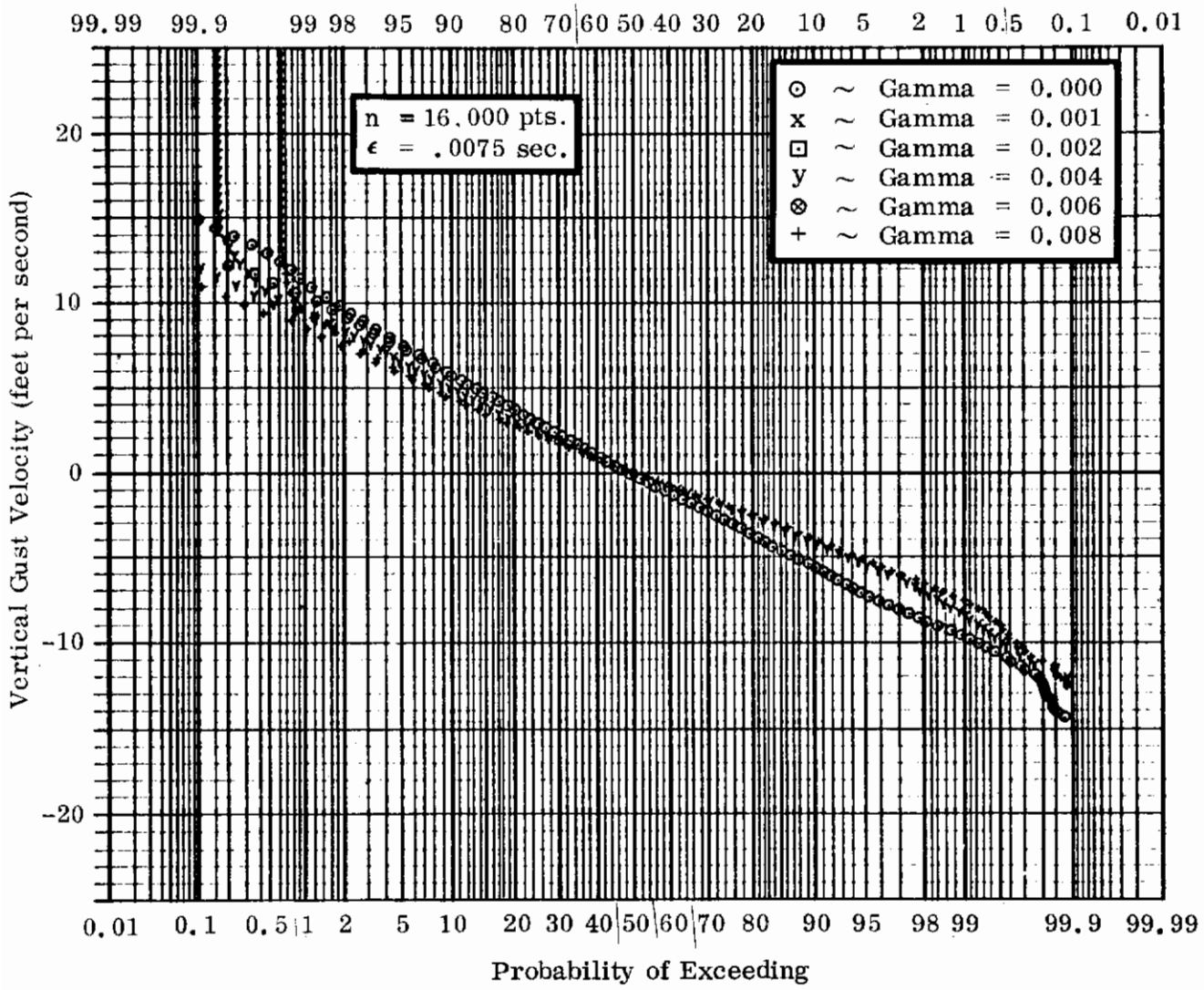

FIGURE 70 PROBABILITY GRAPH, FLIGHT 276

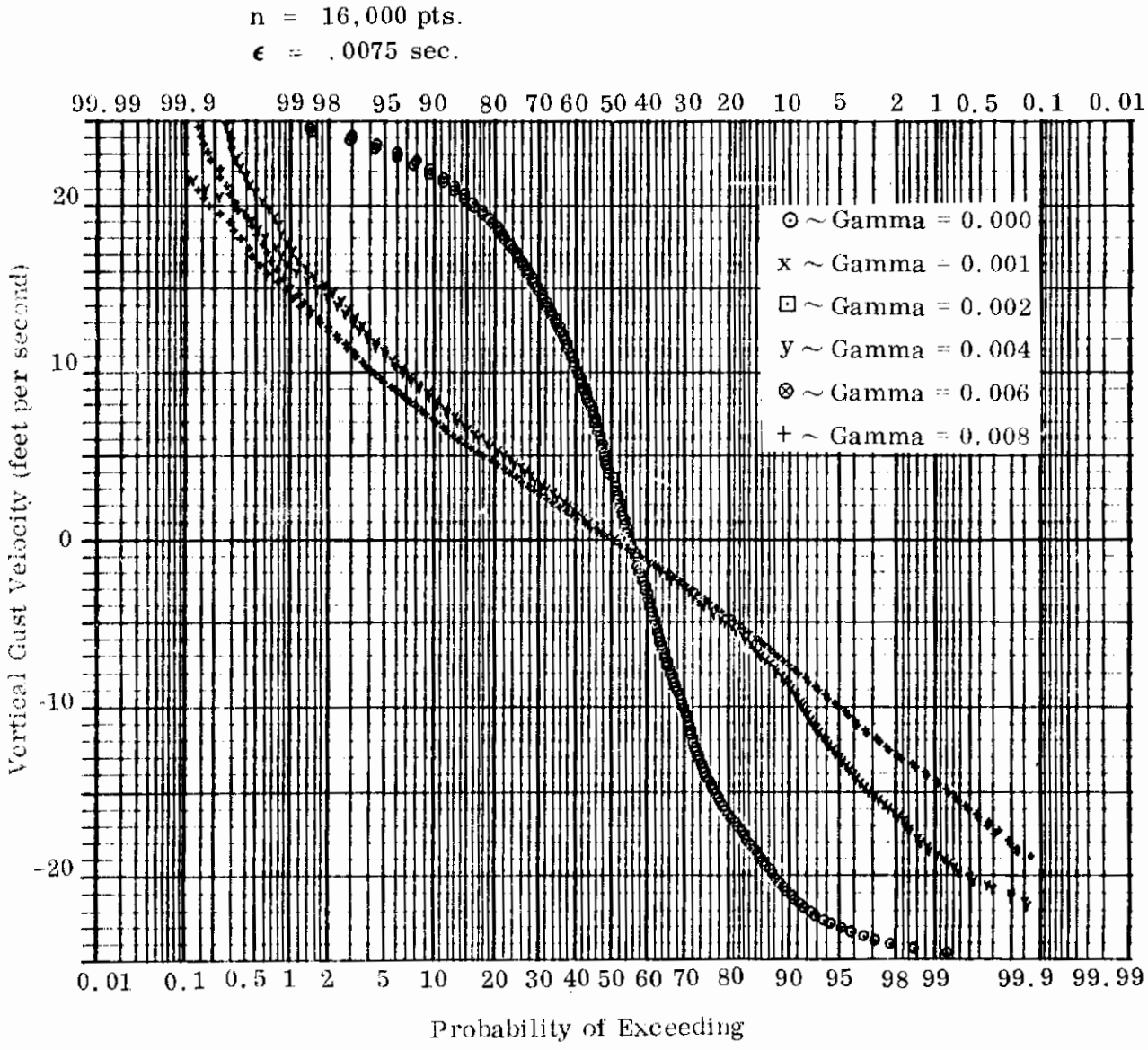

FIGURE 71 PROBABILITY GRAPH, FLIGHT 277

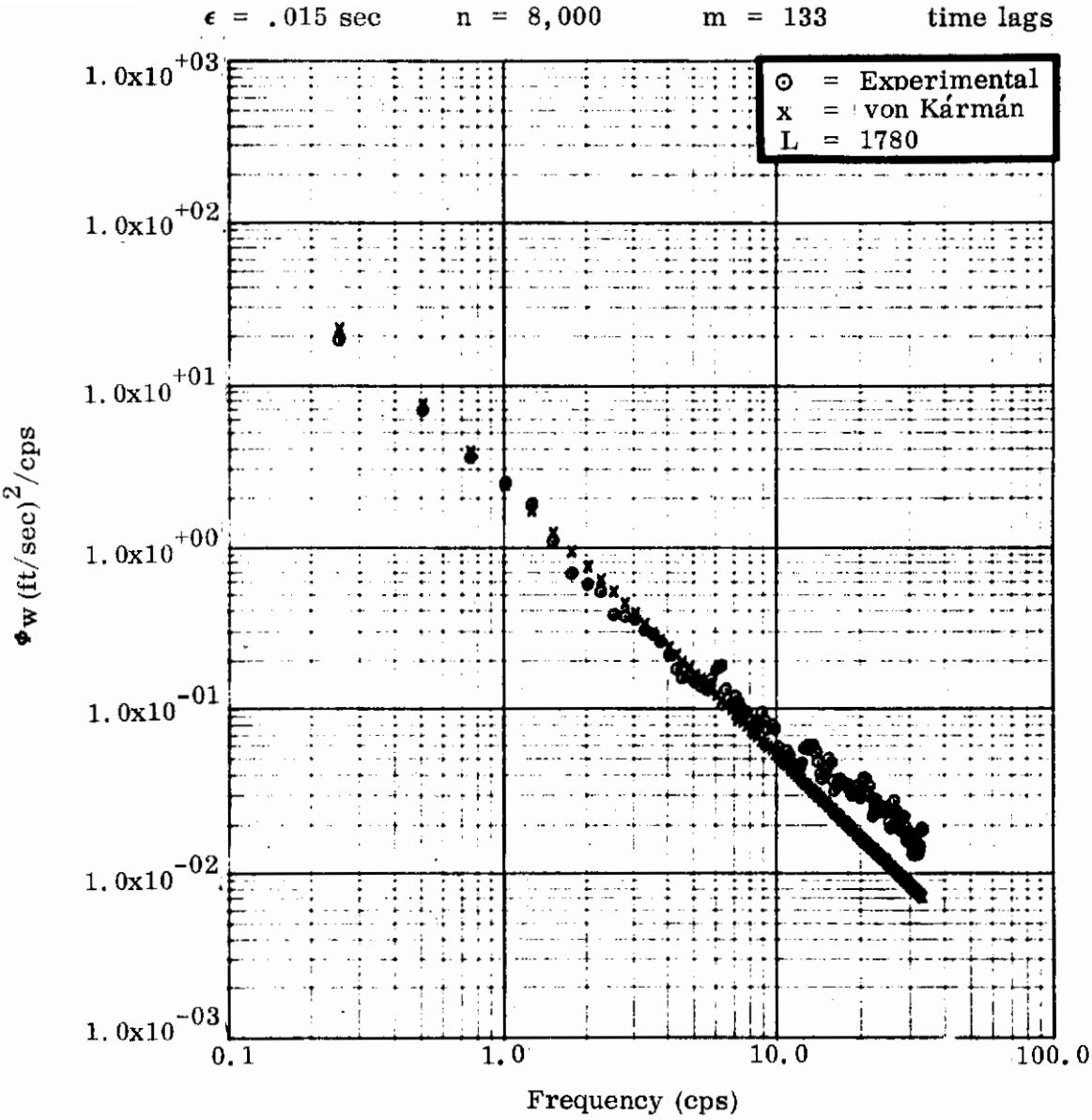

FIGURE 72 POWER SPECTRAL DENSITY OF VERTICAL GUST VELOCITY, FLIGHT 275

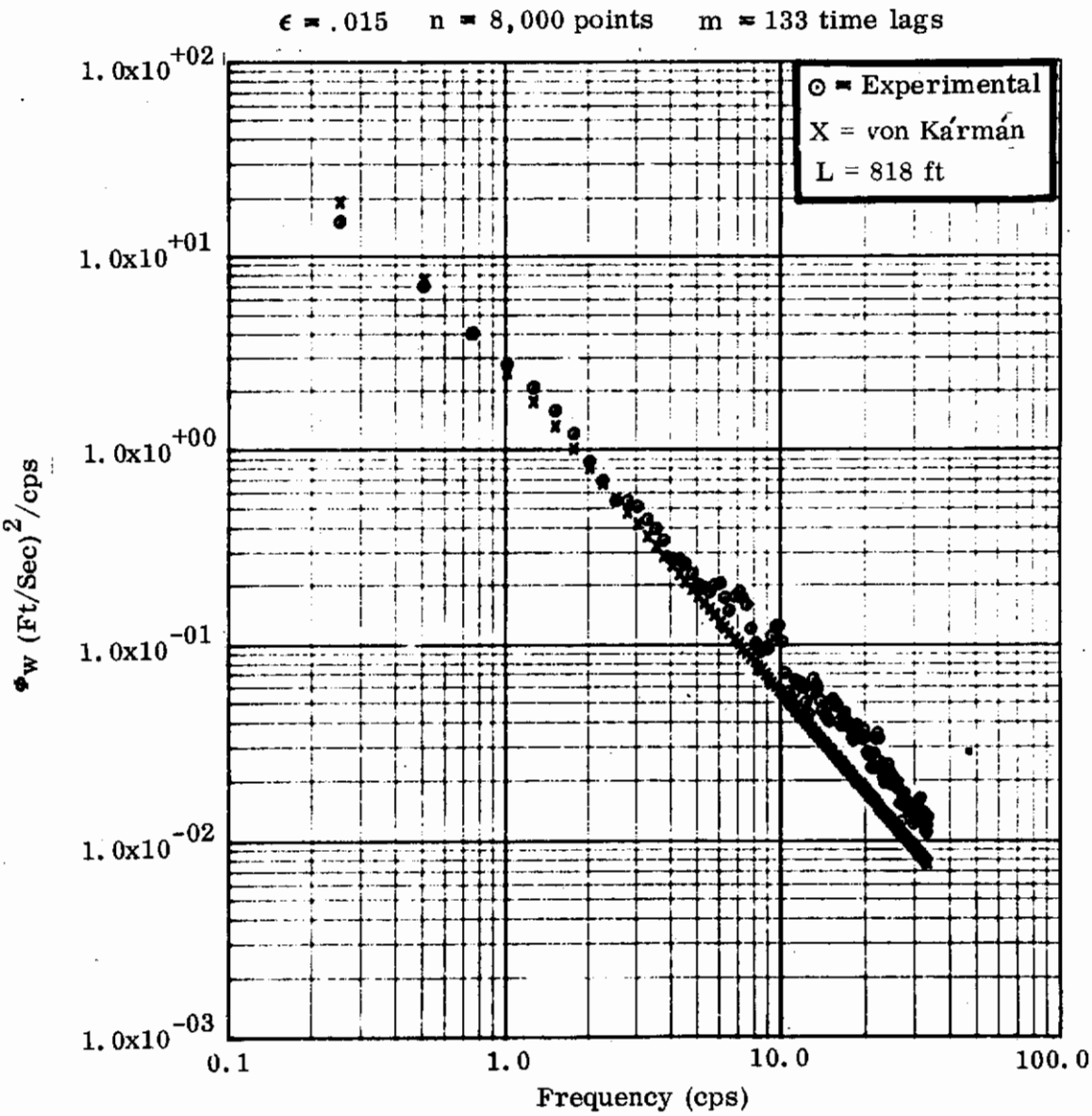

FIGURE 73 POWER SPECTRAL DENSITY OF VERTICAL GUST VELOCITY, FLIGHT 276

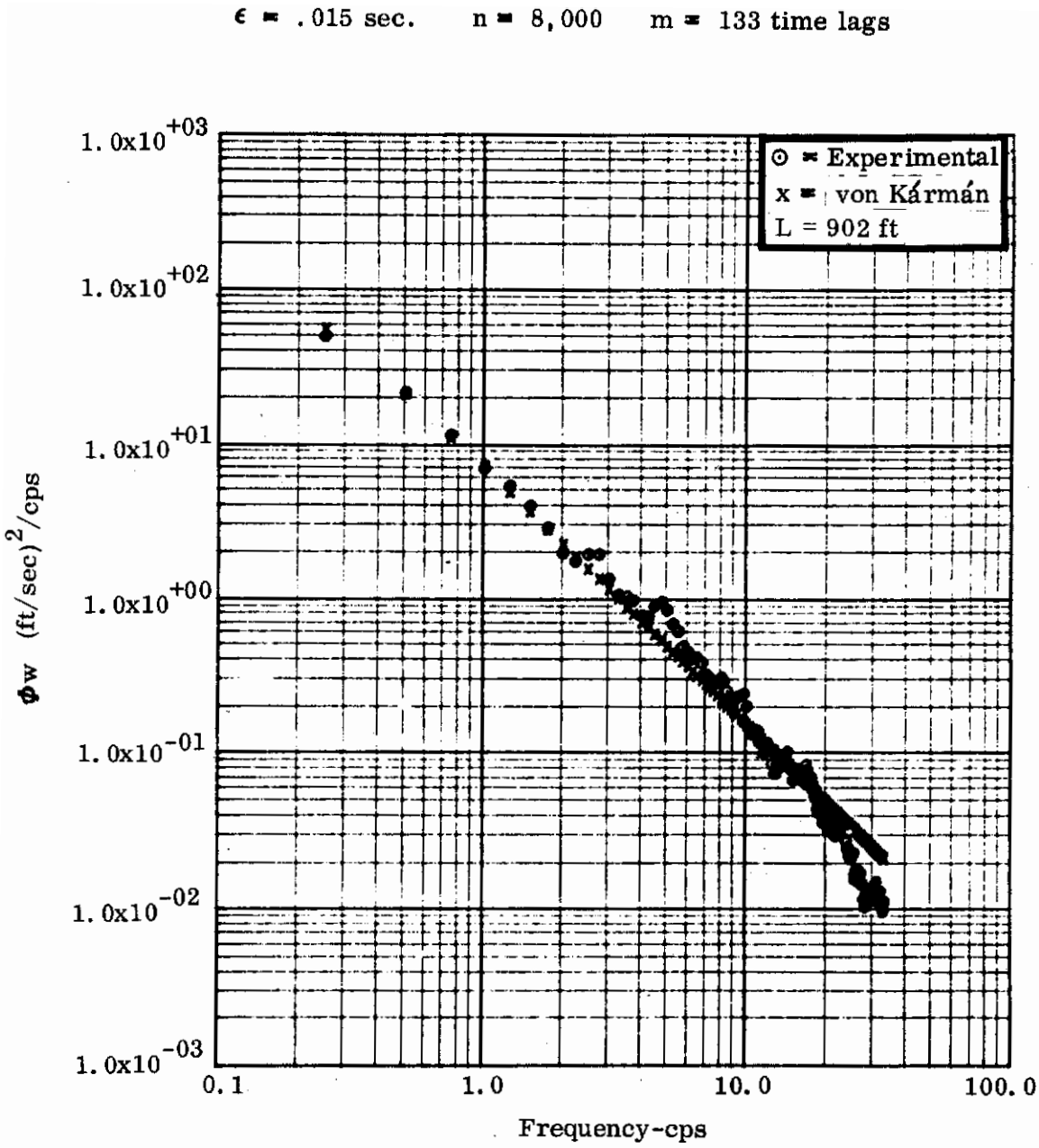

FIGURE 74 POWER SPECTRAL DENSITY OF VERTICAL GUST VELOCITY, FLIGHT 277

where σ_w is equal to $R^{1/2}(0)$, Ω_1 and Ω_0 are the truncated and the upper limit of the spatial frequencies used in the integration:

$$\sigma_1^2 = \int_{\Omega_1}^{\Omega_0} \Phi_w(\Omega)\, d\Omega \qquad (II\text{-}6)$$

The scales of turbulence derived in this manner are given in Table XXIV and Figures 72-74. The same scale data is substituted into the von Kármán auto-correlation function:

$$R(r/L) = \frac{\sqrt[3]{4}}{\Gamma\left(\frac{1}{3}\right)} \sigma_w^2 \left[\frac{r}{1.339L}\right]\left[K_{1/3}\left(\frac{r}{1.339L}\right) - \frac{1}{2}\left(\frac{r}{1.339L}\right) K_{2/3}\left(\frac{r}{1.339L}\right)\right] \qquad (II\text{-}7)$$

These data are shown in Figures 62-64. Similarly, the scale of turbulence values were substituted into the von Kármán power spectral density equation which are shown in Figures 72-74:

$$\Phi(\Omega) = \frac{\sigma_w^2 L}{\pi} \frac{1 + \frac{8}{3}(1.339L\,\Omega)^2}{\left[1 + (1.339L\,\Omega)^2\right]^{11/6}} \qquad (II\text{-}8)$$

II.4 Seismic Type Filter Function

In order to gain flexibility in amplitude attenuation and cutoff frequency in processing the gust data, a new filter function is proposed by Dr. J. C. Houbolt. The filter is based on the dynamic characteristics of a mass-spring-damper system with a low natural frequency which may be represented symbolically in Figure 75.

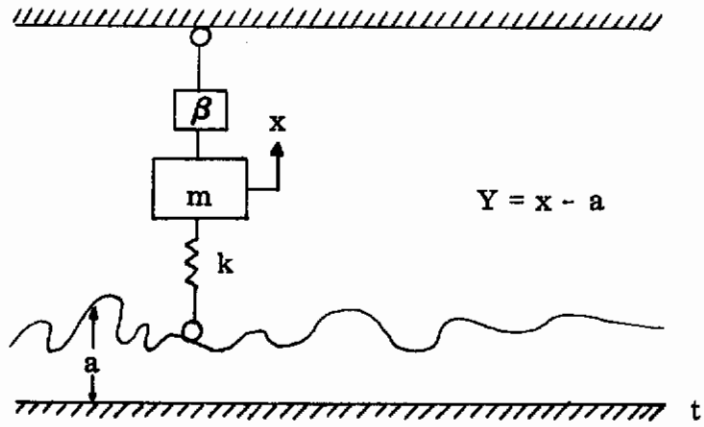

FIGURE 75. A SEISMIC SYSTEM

The system is moving along the horizontal direction so that the displacement input is a(t). Assume a(t) to be the original function, Y(t) = (x - a) the filtered function. The system is arranged in such a manner that the mass motion x(t) is responsive only to low frequency components of a(t). The net result is that Y(t) retains the high frequency components of a(t). In other words, the system works as a high pass filter with controllable filter pattern. In the time domain, the operation may be represented as:

$$m \frac{d^2Y}{dt^2} + \beta \frac{dY}{dt} + k Y = - m \frac{d^2a}{dt^2} - \beta \frac{da}{dt} \qquad \text{(II-9)}$$

In digital processing, after reversing the sign of a(t), the following recurrence formula is used:

$$(Y_{n+1} - 2Y_n + Y_{n-1}) + \frac{\beta\epsilon}{2m}(Y_{n+1} - Y_{n-1}) + \frac{k\epsilon^2}{m} Y_n = (a_{n+1} - 2a_n + a_{n-1}) + \frac{\beta\epsilon}{2m}(a_{n+1} - a_{n-1}) \qquad \text{(II-10)}$$

where ϵ is the sampling time interval. To start the computation, the following initial values are used:

$$Y_o = 0, \quad Y_1 = a_1 - \frac{2}{1 + \frac{\beta\epsilon}{2m}} a_o \qquad \text{(II-11)}$$

This same filter function may be represented as a transfer function between the input and output power spectra:

$$\Phi_Y = \frac{(\cos\omega\epsilon - 1)^2 + \left(\frac{\beta\epsilon}{2m}\right)^2 \sin^2 \omega\epsilon}{\left[\cos\omega\epsilon - 1 + \frac{K\epsilon^2}{2m}\right]^2 + \left(\frac{\beta\epsilon}{2m}\right)^2 \sin^2 \omega\epsilon} \Phi a \qquad \text{(II-12)}$$

The corresponding phase shift is

$$\theta = \arctan\left(\frac{\frac{\beta\epsilon}{2m}\sin\omega\epsilon}{\cos\omega\epsilon - 1}\right) - \arctan\left(\frac{\frac{\beta\epsilon}{2m}\sin\omega\epsilon}{\cos\omega\epsilon - 1 + \frac{k\epsilon^2}{2m}}\right) \qquad \text{(II-13)}$$

The parameters which determine the filtering range and the shape of the filter may be presented in the following manner.

$$\frac{k\epsilon^2}{2m} = \frac{\pi^2}{2} \frac{\omega_1^2}{\omega_o^2} , \frac{\beta\epsilon}{2m} = \pi \frac{\beta}{\beta_{cr}} \frac{\omega_1}{\omega_o} \qquad \text{(II 14)}$$

where

$$\omega_1 = \sqrt{\frac{k}{m}} , \quad \beta_{cr} = 2\sqrt{km}$$

$$\omega_o = \frac{\pi}{\epsilon} = \text{the folding frequency}$$

Typical filter response data based on (II-12), (II-13) are plotted in Figures 76-78 for various values of ω_1 and β/β_{cr}. In the figures, the (β/β_{cr}) values used are .65, .66, .67, .68, .70, .80.

The vertical gust velocity data from flight 392-10 are numerically processed through seismic type filter and gamma filter. In the case of the gamma-filter $\gamma = .002$ is found to be a satisfactory value. The data are processed with cut-off values of $\omega_1/2\pi = 0.0088$, 0.049, and 0.088 cps with $\epsilon = 0.015$ second. Appropriate (β/β_{cr}) value is chosen to minimize the filter amplitude function overshoot. The analytical von Karman auto-correlation function (II-7) and Tukey power spectral densities are computed for these data and are exhibited in Figures 79 and 80 respectively A comparison of the filter gain characteristics is shown in Figure 81. From the above-mentioned data, it can be seen that the seismic type filter serves the same general purpose of the gamma filter, while the former has the freedom to determine a specific cutoff frequency. Indeed, as evidenced in Figure 80, the low frequency gust power density is very sensitive to the choice of the cutoff frequency of the seismic type filter

II.5 Coherence Functions and Confidence Limits

The coherence function γ^2 (f) is known to play a central role in establishing the statistical reliability of measured frequency response functions. This function is given by the relation

$$\gamma^2(f) = \left|\Phi_{xz}(f)\right|^2 \Big/ \left[\Phi_{xx}(f)\ \Phi_{zz}(f)\right] \qquad \text{(II-15)}$$

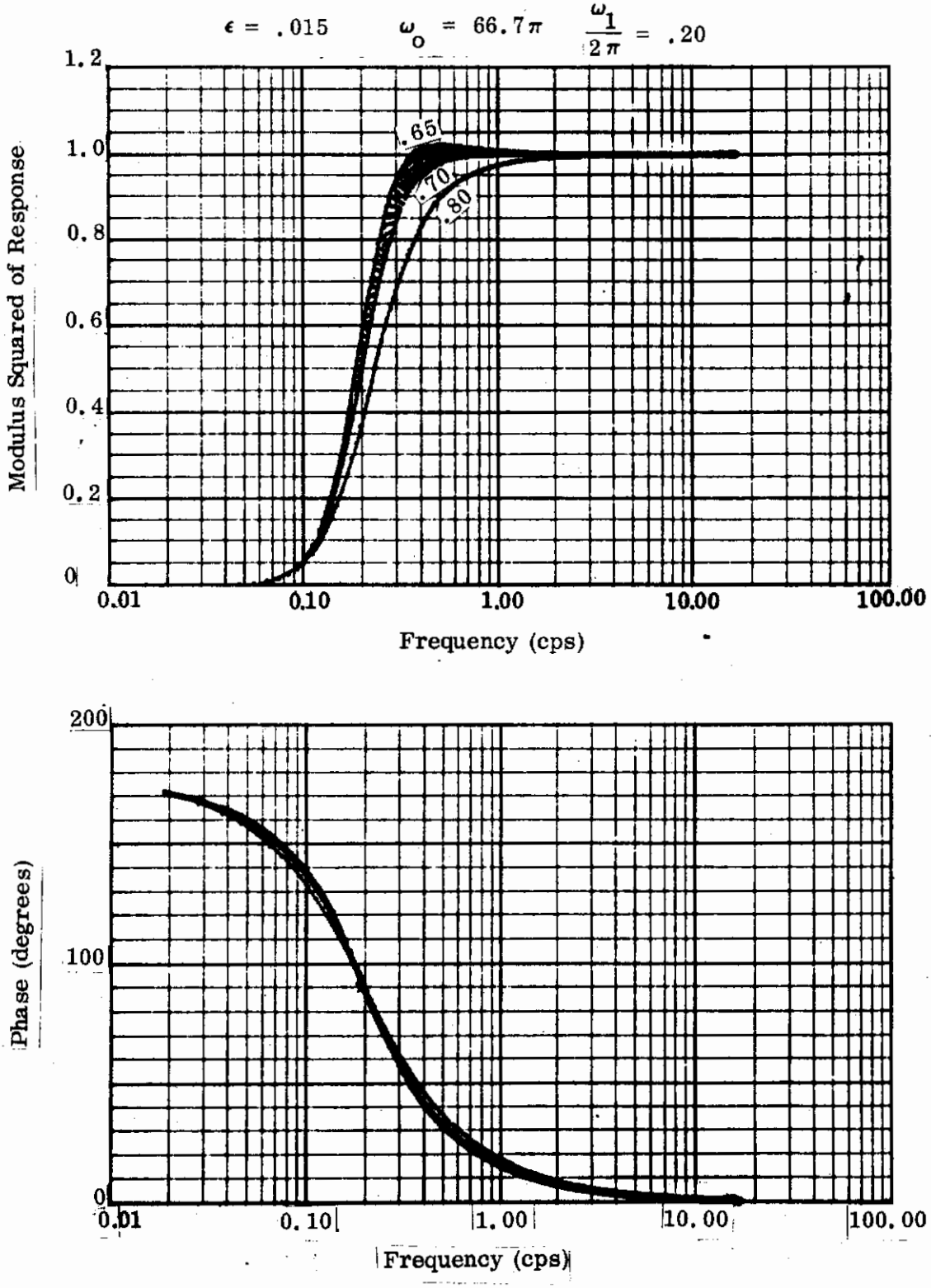

FIGURE 76 SEISMIC FILTER RESPONSE DATA

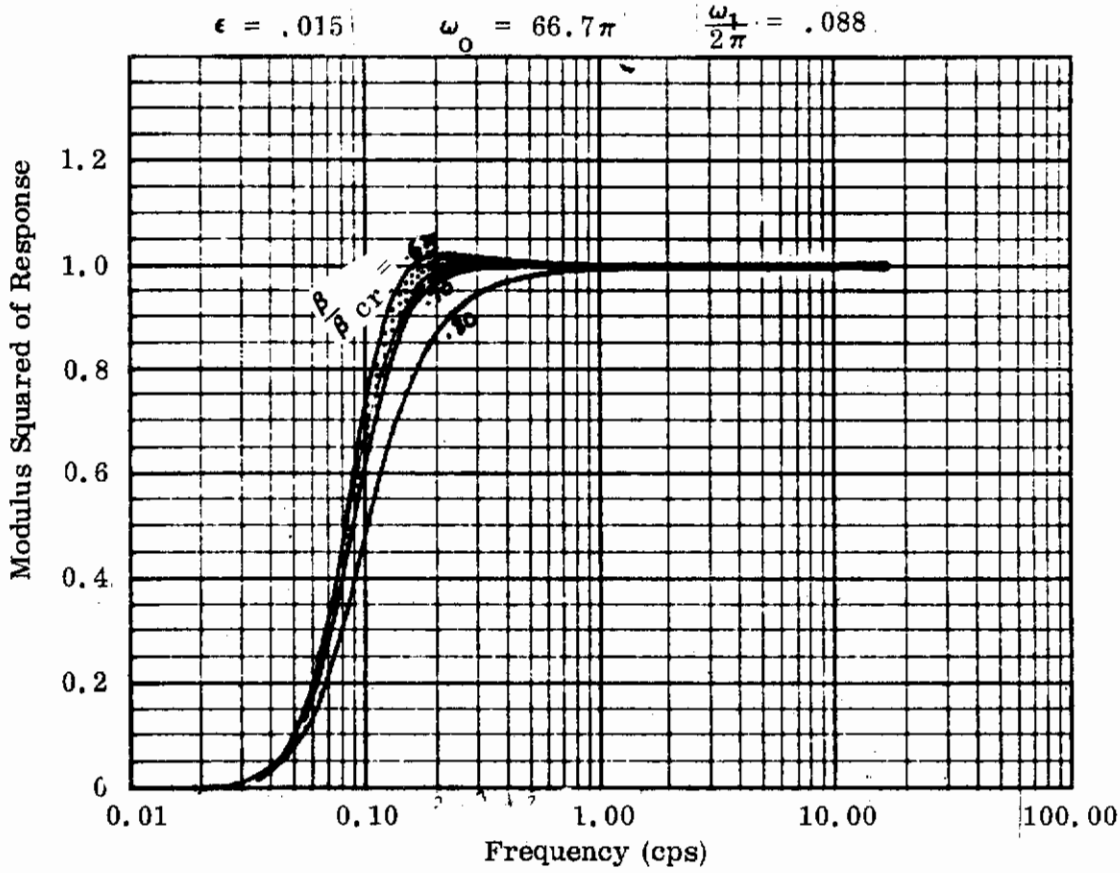

Phase Shift of Filter Response Function
Seismic Filter Type II

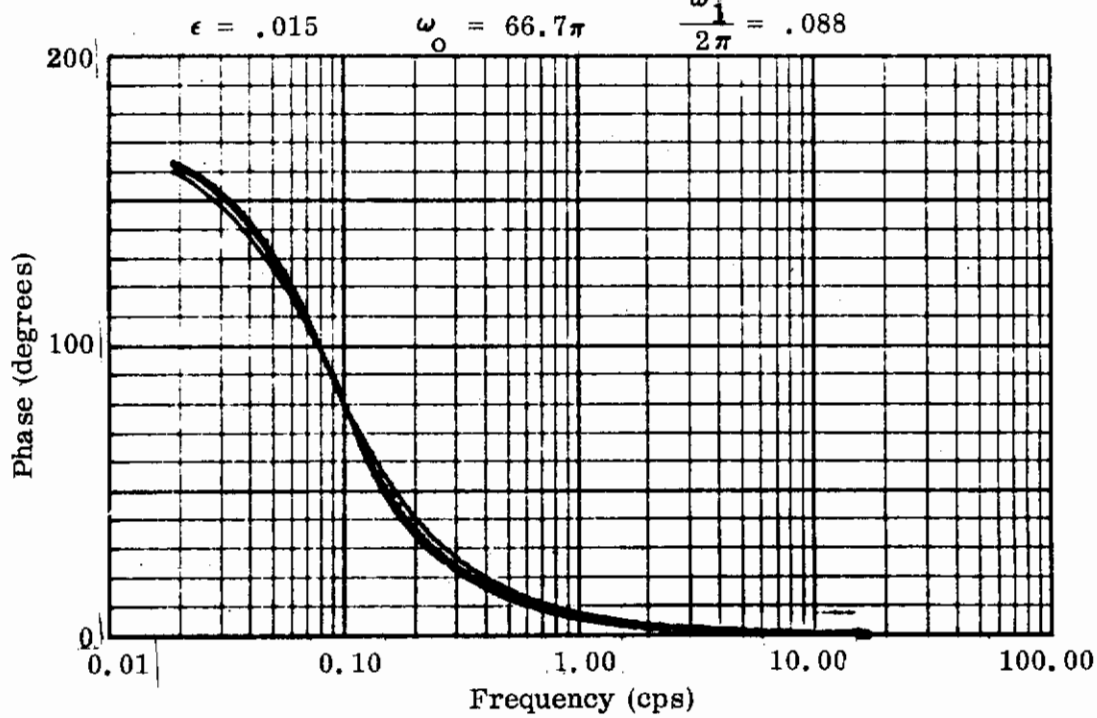

FIGURE 77 SEISMIC FILTER RESPONSE DATA

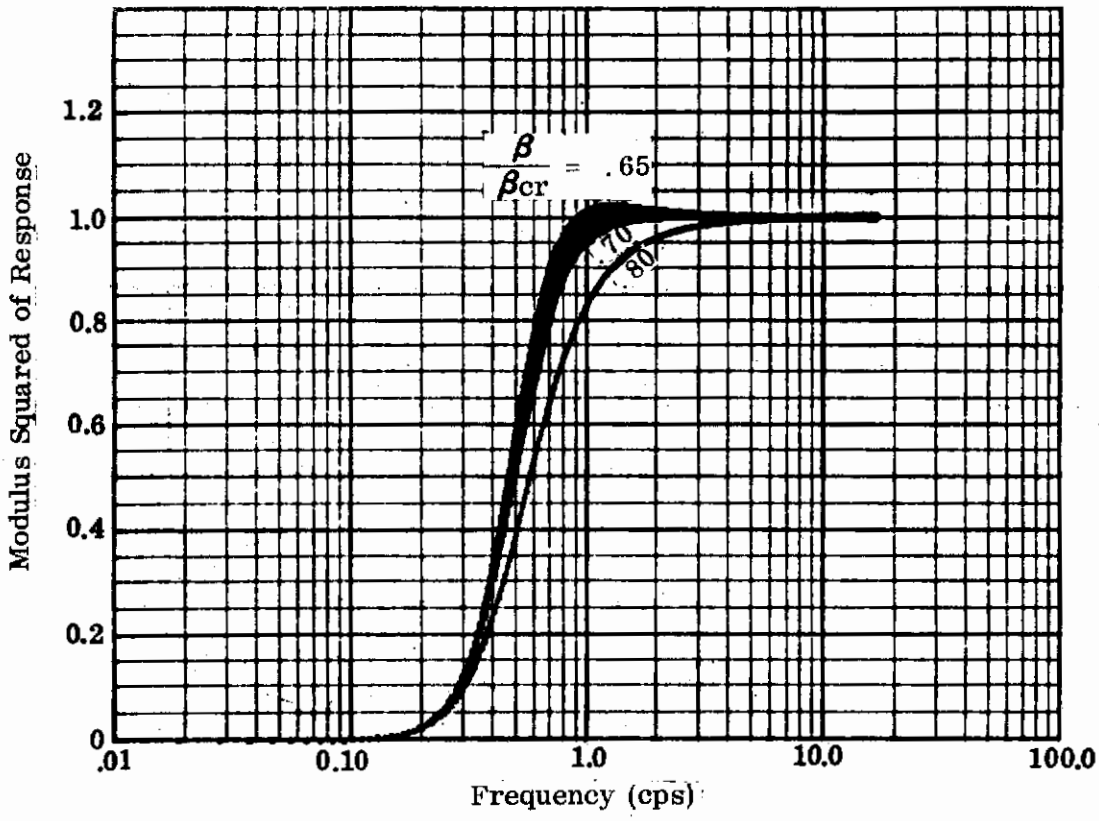

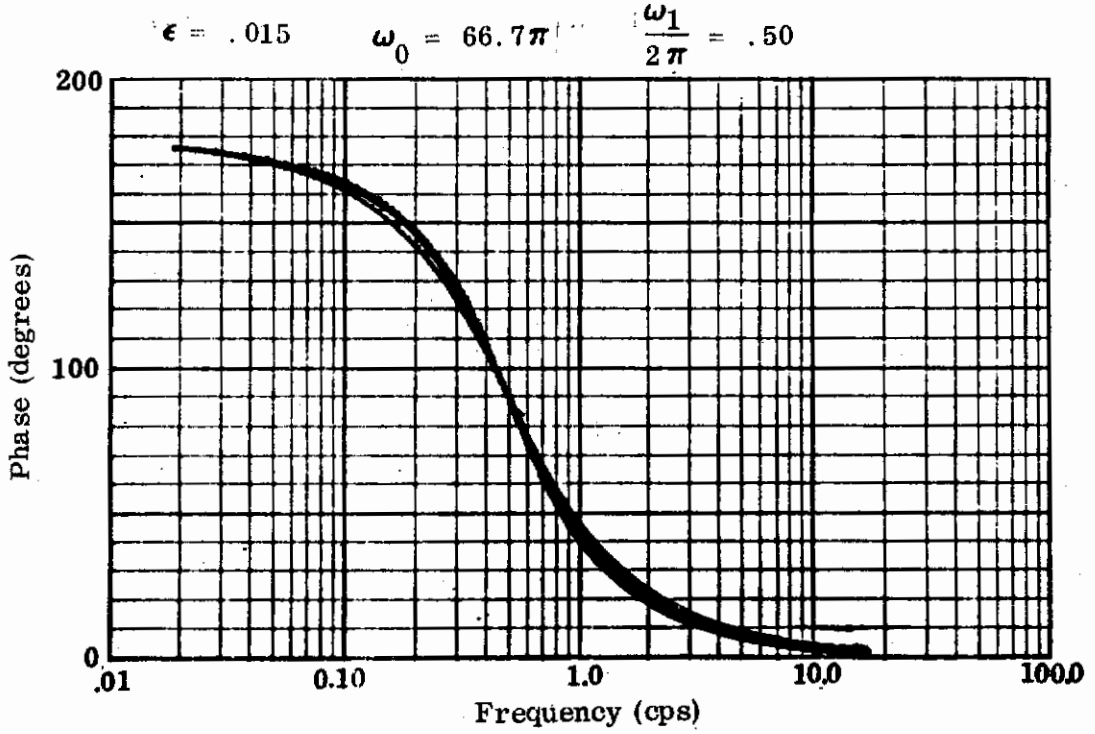

FIGURE 78 SEISMIC FILTER RESPONSE DATA

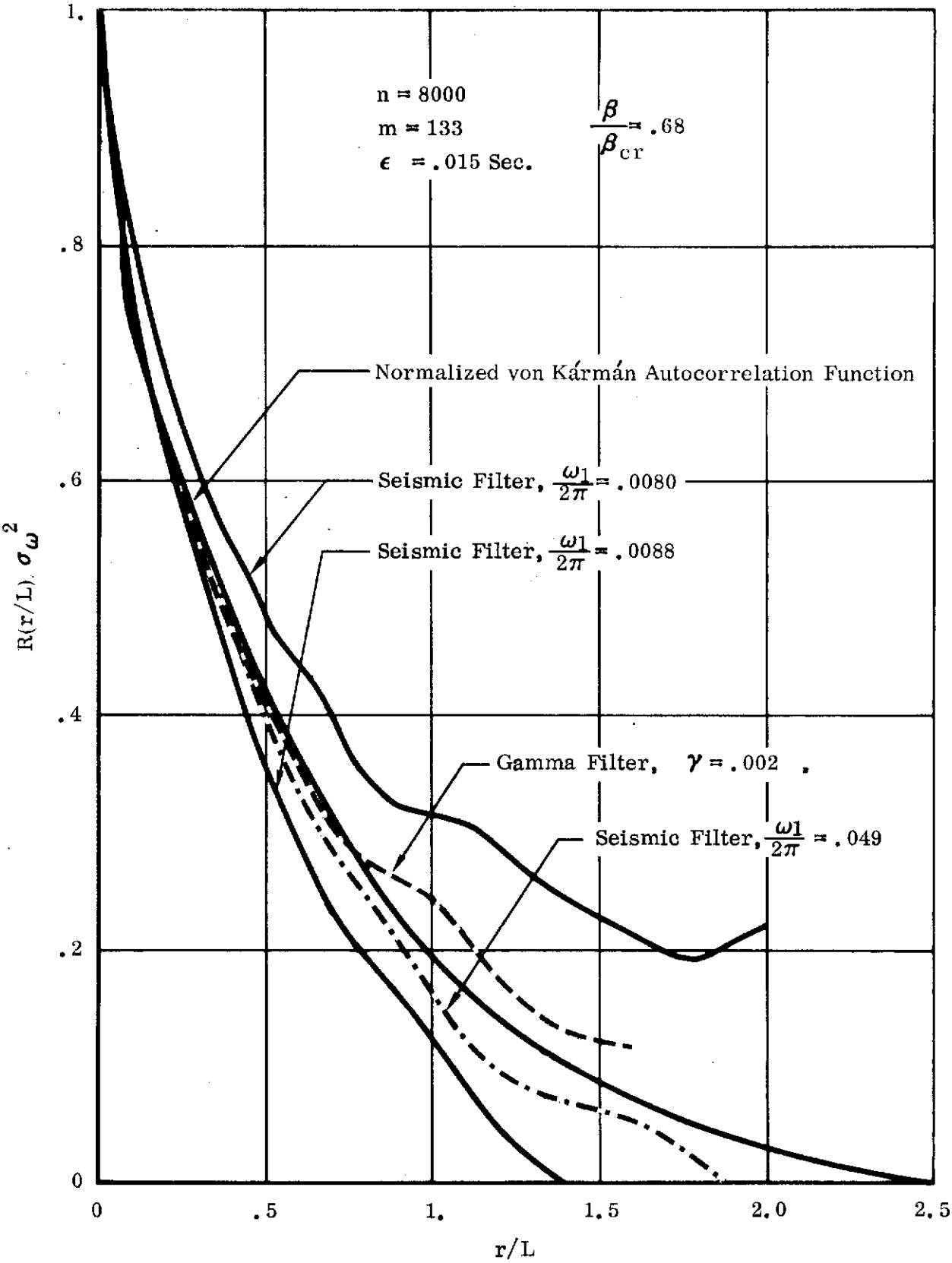

FIGURE 79 COMPARISON OF THE VON KARMAN NORMALIZED AUTOCORRELATION FUNCTION WITH EXPERIMENTAL NORMALIZED AUTOCORRELATION FUNCTIONS

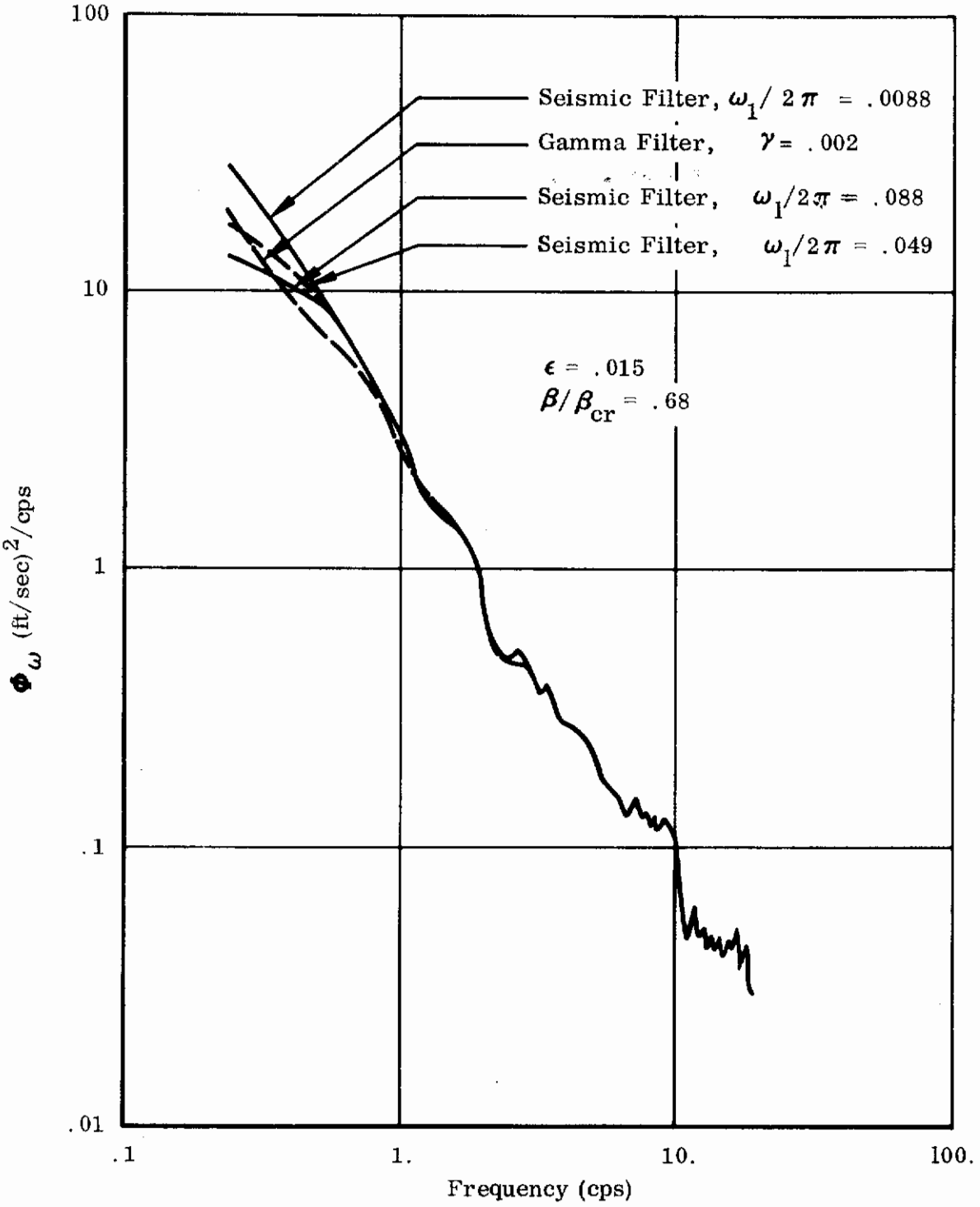

FIGURE 80 COMPARISON OF VERTICAL GUST VELOCITY POWER SPECTRA FOR DATA PROCESSED THROUGH HIGH-PASS SEISMIC AND GAMMA FILTERS

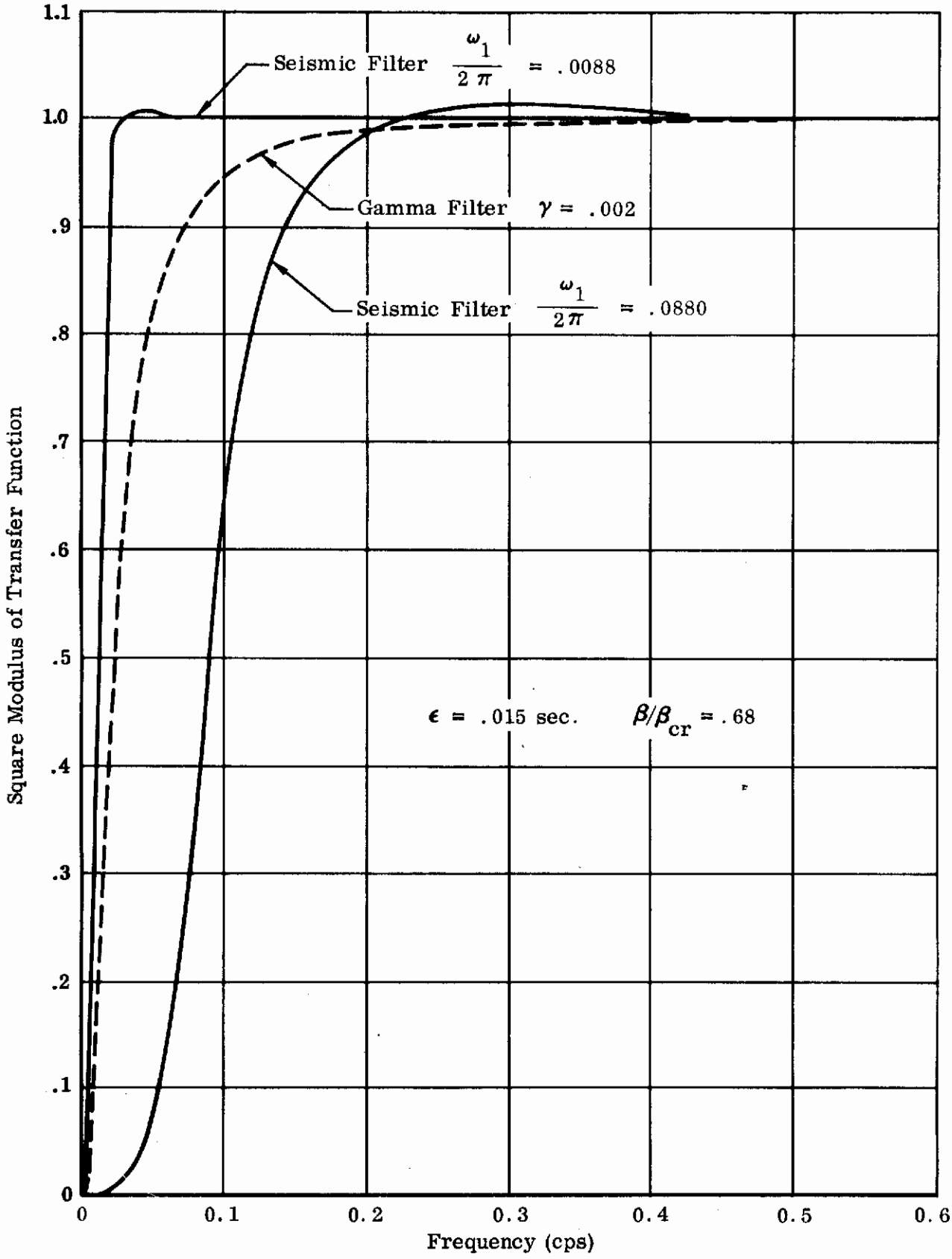

FIGURE 81 COMPARISON OF NUMERICAL FILTER CHARACTERISTICS

where Φ_{xx} (f), Φ_{zz} (f) and Φ_{xz} (f) denote the input, response and cross power spectra respectively. It can be shown by the Cauchy-Schwarz inequality that $\gamma^2 \leq 1$ (Reference 14).

The relationship between the confidence limits and coherence has been derived by Goodman (Reference 15):

$$\text{Probability}\left[\begin{array}{l}(1 - \sin \Delta\varphi) \quad < \dfrac{\text{Sample } H_c\text{ (f)}}{\text{True } H_c\text{ (f)}} < (1 + \sin\Delta\varphi) \\ \\ -\Delta\varphi < \Big[(\text{Sample phase}) - (\text{True phase})\Big] < \Delta\varphi\end{array}\right] \leq P \qquad \text{(II-16)}$$

The errors $\Delta\varphi$ is given in terms of γ^2 (f) by the relation:

$$\Delta\varphi = \text{arc sin}\left[\frac{1-\gamma^2}{\gamma^2}\left((1-P)^{-\frac{m}{N'}} - 1\right)\right]^{1/2} \qquad \text{(II-17)}$$

where

N	=	length of record (number of samples)
m	=	highest order lagged products used in computing the sample H_c (f)
N'	=	N-m = effective length of record
r^2	=	a priori estimate of coherency
P	=	confidence level

Thus, the upper and lower confidence limits coincide at frequencies for which γ^2 (f) = 1.0.

The complex frequency response function H_c (f) is defined as:

$$H_c\text{ (f)} = \Phi_{xz}\text{ (f)} \Big/ \Phi_{xx}\text{ (f)} \qquad \text{(II-19)}$$

This relation can be combined with the relation defining the spectral frequency response functions H_s^2 (f) = Φ_{zz} (f) / Φ_{xx} (f) to yield

$$\gamma^2 (f) = \left| \Phi_{xz}(f) \right|^2 / \Phi_{xx}(f)\, \Phi_{zz}(f) = \left| H_c(f) \right|^2 / H_s^2(f)$$

Accordingly, the statistical reliability of measured frequency response functions can be determined by comparison of the estimates $| H_c (f)|$ and $H_s (f)$.

The effect of changing the record length is shown in the following example. With $P = 0.75$, $\gamma^2 = 0.50$, $m = 30$, $N' = 1000$, one has $\sin \Delta\varphi \approx 0.21$, $\Delta\varphi \approx 12^o$. With a record twice as long, the following data are obtained: $P = 0.75$, $\gamma^2 = 0.50$, $m = 30$, $N' = 2000$; $\sin \Delta\varphi \approx 0.15$, $\Delta\varphi \approx 8^o$.

The exponent in (II-17) is usually defined as one half the number of statistical degrees of freedom $k = 2N'/m = 2 (N-m)/m$. Figure 82 illustrates the effect of variations in $\gamma^2 (f)$ and confidence level P on statistical reliability for $k = 238$.

Figures 83 and 84 illustrate typical measured spectral and cross spectral frequency response function estimates. It will be noted that $H_c (f)$ and $H_s (f)$ exhibit differences which increase with frequency. This can be attributed to data contamination at higher frequencies arising from spanwise variations in the vertical gust velocity, lateral and head-on gusts, and non-steady aerodynamic effects due to nose boom vibrations, noises in instrumentation etc. These noise sources are reflected in the decrease of coherence function levels with frequency in Figure 84.

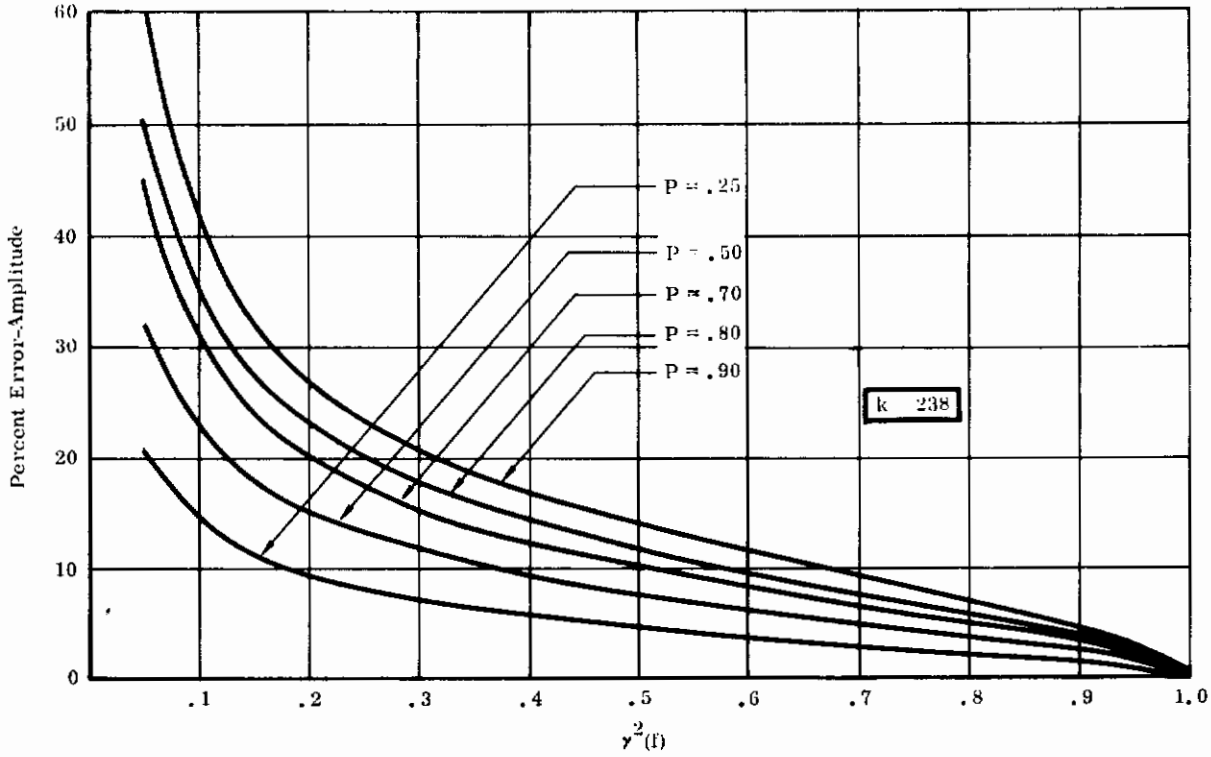

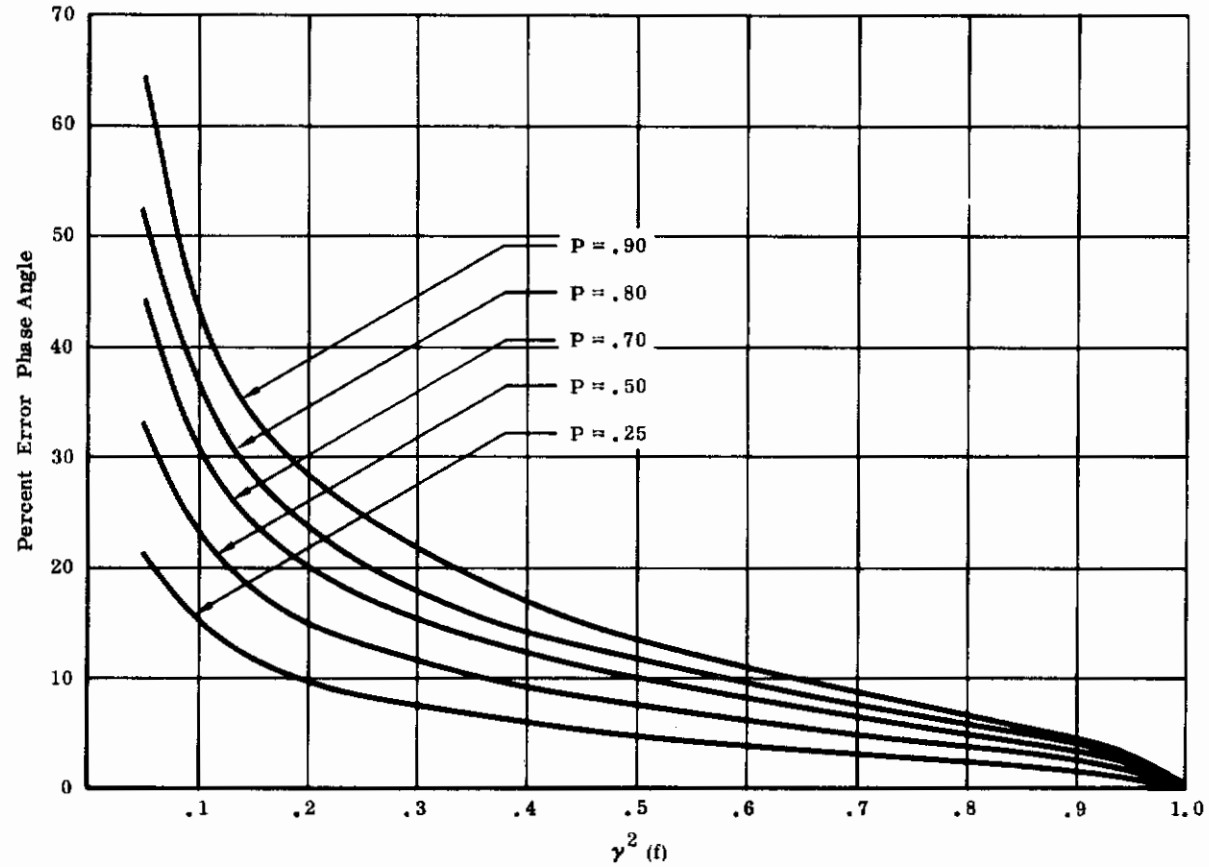

FIGURE 82 PERCENT ERROR VS. THE COHERENCE FUNCTION γ^2 (f) FOR SEVERAL CONFIDENCE LEVELS

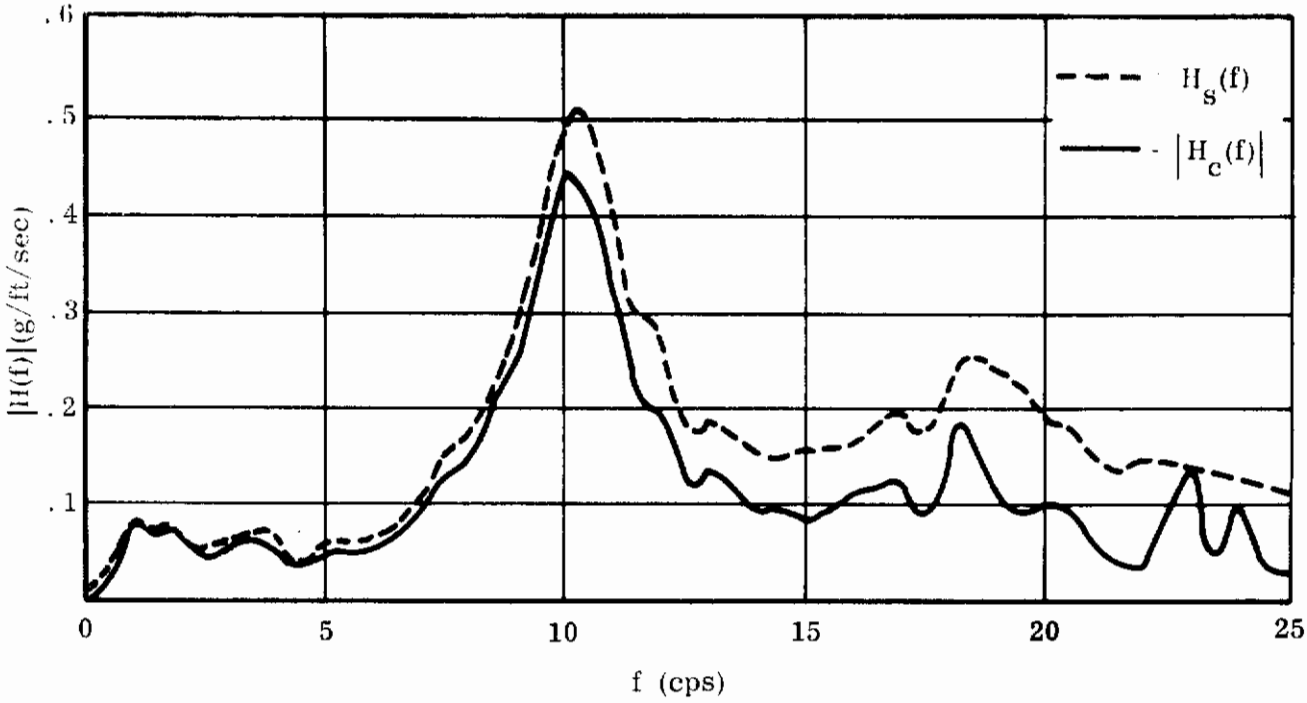

FIGURE 83 COMPARISON OF $|H_c(f)|$ AND $H_s(f)$ FOR F-5A NORMAL ACCELERATION FUS. STA. 92

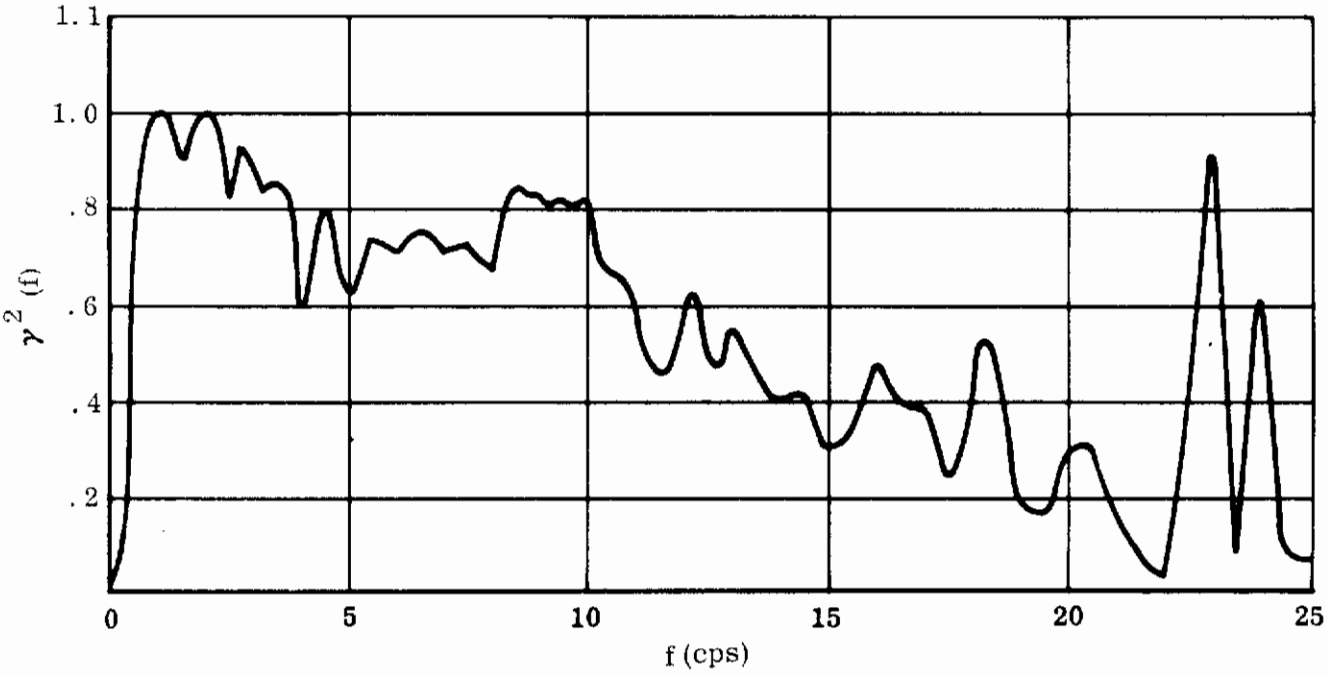

NOTES:

(1) These figures are based on a folding frequency 33 cps.
(2) An anti-foldback RLC filter with a cutoff at 25 cps is applied to both input and output channels.

FIGURE 84 COHERENCE FUNCTION VERSUS FREQUENCY FOR F-5A NORMAL ACCELERATION FUS. STA. 92

REFERENCES

1. Watkins, C. E., Runyan, H. L., and Woolston, D. S., "On the Kernel Function of the Integral Equations Relating the Lift and Downwash Distributions of Oscillating Finite Wings in Subsonic Flow," NASA Report 1234, 1955.

2. Runyan, H. L. and Woolston, D. S., "Method of Calculating the Aerodynamic Loading on Oscillating Finite Wing in Subsonic and Sonic Flow," NASA Report 1322, 1957.

3. Rodden, W. P., and Revell, J. D., "The Status of Unsteady Aerodynamic Influence Coefficients," SMF Fund Paper No. FF-55, January 1962.

4. Rodden, W. P., Farkas, E. F., Oyama, R. K., "Subsonic and Sonic Aerodynamic Influence Coefficients from Unsteady Lifting Surface Theory: Analytical Development and Procedure for IBM 7090 Computer," NOR 61-056, Northrop Corporation, Norair Division, April 1961.

5. Rodden, W. P., Farkas, E. F., Slack, F. C., "Harmonic Gust Aerodynamic Influence Coefficients by Incompressible Strip Theory: Analytical Development and Procedure for the IBM 7090 Computer," NOR 61-059, Northrop Corporation, Norair Division, April 1961.

6. Bennett, F. V. and Pratt, K. G., "Calculated Responses of a Large Sweptwing Airplane to Continuous Turbulence with Flight-Test Comparisons," NASA Technical Report R-69, 1960.

7. Nielsen, J. N., "Missile Aerodynamics," McGraw-Hill Book Company, Inc., New York, New York, 1960.

8. Bisplinghoff, R. L., Ashley, H., and Halfman, R. L., "Aeroelasticity," Addison-Wesley Publishing Company, Inc., Cambridge, Massachusetts, 1955.

9. Cross, A. K., "T-38 Dynamic Response Gust Loads, Comparison Between Flight Test and Analytical Results," NOR 60-306, Northrop Corporation, Norair Division, March, 1964.

10. Houbolt, J. C., Steiner, R., and Pratt, C. P., "Dynamic Response of Airplanes to Atmospheric Turbulence Including Flight Data on Input and Response," NASA Technical Report R-199, 1964.

11. Batchelor, G. K., "The Theory of Homogeneous Turbulence," Cambridge University Press, Cambridge, Massachusetts, 1958.

12. Fung, Y. C., "An Introduction to the Theory of Aeroelasticity," John Wiley and Sons, Inc., New York City, New York, 1955.

13. Press, H., and Tukey, J. W., "Power Spectral Methods of Analysis and Their Application in Airplane Dynamics," Volume IV, AGARD Flight Test Manual, Part IV C, Durbin, E. J., editor, North Atlantic Treaty Organization, Paris, France.

14. Bendat, J. S., "Principles and Applications of Random Noise Theory," John Wiley and Sons, Inc., New York City, New York, 1958.

15. Goodman, N. R., "On the Joint Estimation of the Spectra, Cospectrum and Quadrature Spectrum of a Two Dimensional Stationary Gaussian Process," Scientific Paper No. 10, Engineering Statistics Laboratory, College of Engineering, New York University.

16. Cross, A. K., "Generalized Spectral Representation in Aeroelasticity: Part II," Journal of the Aerospace Sciences, Volume 28, No. 5, May 1961, pp 420, 421.

UNCLASSIFIED
Security Classification

DOCUMENT CONTROL DATA - R&D

(Security classification of title, body of abstract and indexing annotation must be entered when the overall report is classified)

1. ORIGINATING ACTIVITY *(Corporate author)*
Northrop Corporation
Norair Division
Hawthorne, California 90250

2a. REPORT SECURITY CLASSIFICATION
Unclassified

2b. GROUP

3. REPORT TITLE
DESIGN CALCULATIONS ON PROVEN TRAINER AND FIGHTER AIRCRAFT FOR THE VERIFICATION OF A GUST DESIGN PROCEDURE

4. DESCRIPTIVE NOTES *(Type of report and inclusive dates)*
Final Report, April 1965 - April 1966

5. AUTHOR(S) *(Last name, first name, initial)*
Hwang, Chintsun
Kamberg, B.D.
Pi, W.S.
Cross, A.K.

6. REPORT DATE	7a. TOTAL NO. OF PAGES	7b. NO. OF REFS
July 1966	170	16

8a. CONTRACT OR GRANT NO.	9a. ORIGINATOR'S REPORT NUMBER(S)
AF33(615)-2625	AFFDL-TR-66-82
b. PROJECT NO. 1367	
c. Task No. 136702	9b. OTHER REPORT NO(S) *(Any other numbers that may be assigned this report)* NOR 66-149
d.	

10. AVAILABILITY/LIMITATION NOTICES
This document is subject to specific export controls and each transmittal to foreign governments or foreign nations may be made only with prior approval of AFFDL (FDTR), Wright-Patterson AFB, Ohio 45433.

11. SUPPLEMENTARY NOTES	12. SPONSORING MILITARY ACTIVITY
	AFFDL (FDTR) Wright-Patterson AFB, Ohio

13. ABSTRACT Design calculations are performed on proven trainer and fighter aircraft for the purpose of verifying a new gust design procedure based on power spectral techniques. The aircraft used in the computation are Northrop Norair T-38 trainer and F-5A fighter. The new gust design procedure uses a gust power spectrum as the input in aircraft response calculation, as against the present discrete gust approach, where the input is a gust velocity profile with a single frequency determined by the aircraft speed and the gust gradient distance. The report describes the specific aircraft weight and flight configurations used in the computation. The choice of stress sensitive locations is explained and illustrated. Also presented is the computation procedure for obtaining the aircraft transfer functions to be used in both the discrete gust and power spectral approaches. Based on the gust input spectrum and the aircraft transfer functions, a number of aircraft gust response power spectra are generated. These latter spectral data are integrated along the frequency band to obtain the mean aircraft response levels and the average zero crossing counts which are the final results of the computation. Through the computation various scales of turbulence and cut-off frequencies are used to study their effects on the end results of the new gust design procedure. Also presented in the report is supplementary study on the digital processing of the real time gust data and their conversion into the power spectral data.

DD FORM 1 JAN 64 1473

UNCLASSIFIED
Security Classification

14 KEY WORDS	LINK A		LINK B		LINK C	
	ROLE	WT	ROLE	WT	ROLE	WT
gust loads power spectra stresses response parameters zero crossinngs analysis transfer functions gust design criteria						

INSTRUCTIONS

1. ORIGINATING ACTIVITY: Enter the name and address of the contractor, subcontractor, grantee, Department of Defense activity or other organization *(corporate author)* issuing the report.

2a. REPORT SECURITY CLASSIFICATION: Enter the overall security classification of the report. Indicate whether "Restricted Data" is included. Marking is to be in accordance with appropriate security regulations.

2b. GROUP: Automatic downgrading is specified in DoD Directive 5200.10 and Armed Forces Industrial Manual. Enter the group number. Also, when applicable, show that optional markings have been used for Group 3 and Group 4 as authorized.

3. REPORT TITLE: Enter the complete report title in all capital letters. Titles in all cases should be unclassified. If a meaningful title cannot be selected without classification, show title classification in all capitals in parenthesis immediately following the title.

4. DESCRIPTIVE NOTES: If appropriate, enter the type of report, e.g., interim, progress, summary, annual, or final. Give the inclusive dates when a specific reporting period is covered.

5. AUTHOR(S): Enter the name(s) of author(s) as shown on or in the report. Enter last name, first name, middle initial. If military, show rank and branch of service. The name of the principal author is an absolute minimum requirement.

6. REPORT DATE: Enter the date of the report as day, month, year; or month, year. If more than one date appears on the report, use date of publication.

7a. TOTAL NUMBER OF PAGES: The total page count should follow normal pagination procedures, i.e., enter the number of pages containing information.

7b. NUMBER OF REFERENCES: Enter the total number of references cited in the report.

8a. CONTRACT OR GRANT NUMBER: If appropriate, enter the applicable number of the contract or grant under which the report was written.

8b, 8c, & 8d. PROJECT NUMBER: Enter the appropriate military department identification, such as project number, subproject number, system numbers, task number, etc.

9a. ORIGINATOR'S REPORT NUMBER(S): Enter the official report number by which the document will be identified and controlled by the originating activity. This number must be unique to this report.

9b. OTHER REPORT NUMBER(S): If the report has been assigned any other report numbers *(either by the originator or by the sponsor)*, also enter this number(s).

10. AVAILABILITY/LIMITATION NOTICES: Enter any limitations on further dissemination of the report, other than those imposed by security classification, using standard statements such as:

(1) "Qualified requesters may obtain copies of this report from DDC."

(2) "Foreign announcement and dissemination of this report by DDC is not authorized."

(3) "U. S. Government agencies may obtain copies of this report directly from DDC. Other qualified DDC users shall request through _____."

(4) "U. S. military agencies may obtain copies of this report directly from DDC. Other qualified users shall request through _____."

(5) "All distribution of this report is controlled. Qualified DDC users shall request through _____."

If the report has been furnished to the Office of Technical Services, Department of Commerce, for sale to the public, indicate this fact and enter the price, if known.

11. SUPPLEMENTARY NOTES: Use for additional explanatory notes.

12. SPONSORING MILITARY ACTIVITY: Enter the name of the departmental project office or laboratory sponsoring *(paying for)* the research and development. Include address.

13. ABSTRACT: Enter an abstract giving a brief and factual summary of the document indicative of the report, even though it may also appear elsewhere in the body of the technical report. If additional space is required, a continuation sheet shall be attached.

It is highly desirable that the abstract of classified reports be unclassified. Each paragraph of the abstract shall end with an indication of the military security classification of the information in the paragraph, represented as *(TS), (S), (C), or (U)*.

There is no limitation on the length of the abstract. However, the suggested length is from 150 to 225 words.

14. KEY WORDS: Key words are technically meaningful terms or short phrases that characterize a report and may be used as index entries for cataloging the report. Key words must be selected so that no security classification is required. Identifiers, such as equipment model designation, trade name, military project code name, geographic location, may be used as key words but will be followed by an indication of technical context. The assignment of links, rules, and weights is optional.

GPO 886-551